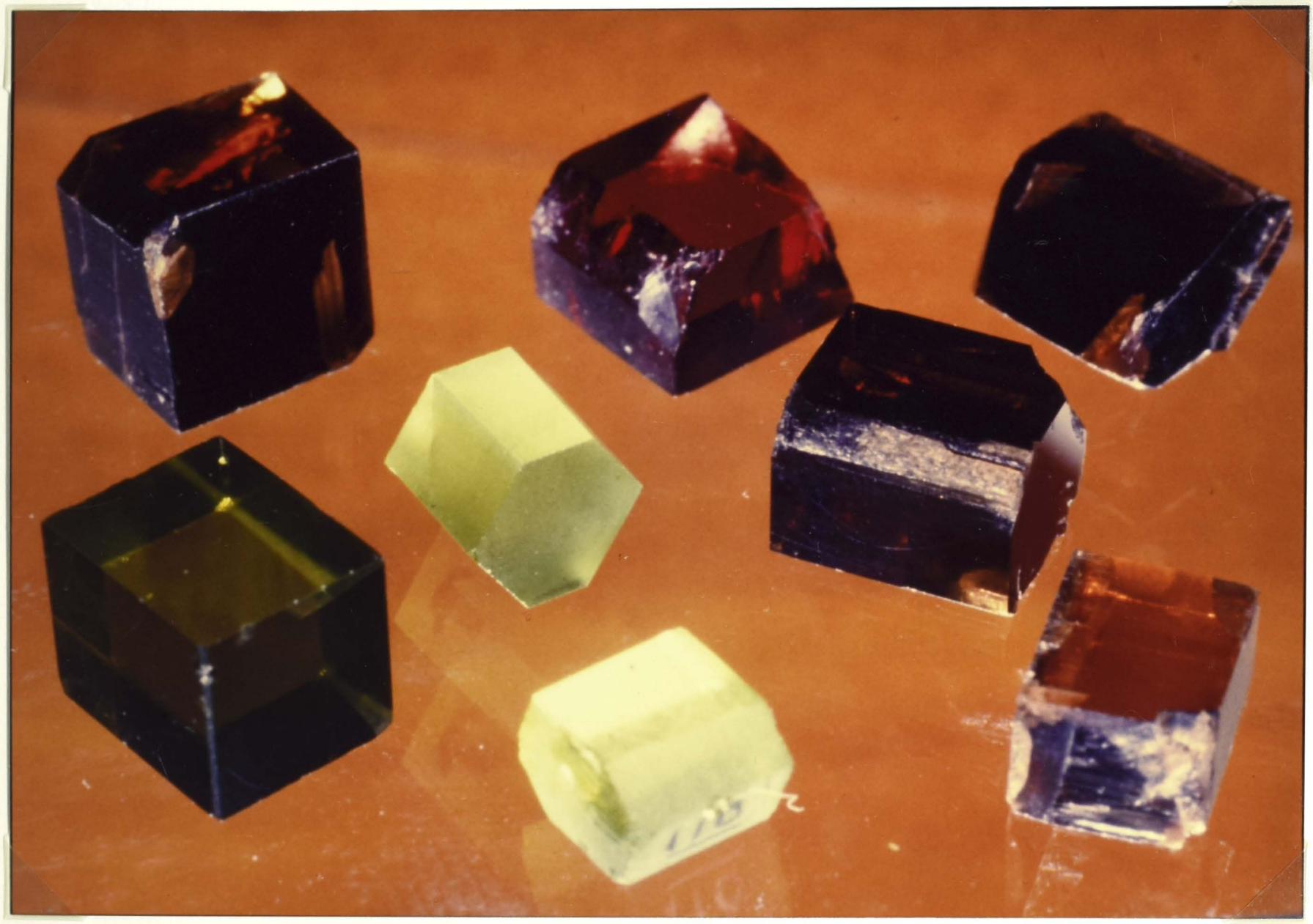

ELASTICITY OF

SOME MANTLE MINERALS

A thesis submitted for the degree of

DOCTOR OF PHILOSOPHY

at the

AUSTRALIAN NATIONAL UNIVERSITY

by

SHARON LYNETTE WEBB

March 1985

STATEMENT

The work in this thesis was carried out while I was a full-time research scholar in the Research School of Earth Sciences, at the Australian National University, during the period of February 1981 to March 1985. Dr. Ian Jackson is responsible for a large amount of the thought in the discussion of shear-mode softening in Chapter 3, and also for the geometrical analyses of the structures discussed in Chapter 5. Otherwise, except where mentioned in the text or the acknowledgements, the research described in this thesis is my own. No part of this thesis has been submitted to any other university or similar institution.

S.L. Webb

March 1985, Canberra

ACKNOWLEDGEMENTS

First, and foremost, I must thank my supervisor, Dr. Ian Jackson for his continuing guidance and encouragement, and his untiring supervision over the past four years.

Herbert Niesler has been invaluable in keeping the hi-tech gremlins at bay, and fixing the innumerable 'slight technical hitches' by knowing where to kick the rig. I must also thank Bill Hibberson, Alan Major and Kevin Morris for managing to keep up the supply of pressure vessels and pistons; with Graeme Horwood also managing to turn out fresh batches of mitre rings every few weeks.

Most of the computer programs were written (and maintained) by Herbert Niesler, with Herb McQueen and Tim Williams lending their expertise to the occassional problems.

Dr. John Fitz Gerald spent a considerable amount of time characterizing the microstructure of my crystals, particularly the orthopyroxenes. Nick Ware also helped with the electron microprobe analyses of the crystals.

A number of people participated in the preparation of this thesis. To my friend Cath Clarke (better known as 'Slave'), I extend my profound gratitude for the hours she spent on my pictures and typing. I must also thank my friends Ian and Kathleen for their assistance with the illustrations. The photographs were all courtesey of Paul Brugman and his off-sider Jan Bitmead.

A number of people were interested in the writing of the thesis. Steve Mackwell lent me his olivine crystals before he deformed them, and left; bequeathing his office and peace and quiet in which to work. Drs. M. Paterson and K. Muirhead also dropped in once or twice to see if the thesis was progressing.

Frontpiece: The garnet (top centre), orthopyroxene (right, top left), and some of the olivine (bottom left) crystals whose elastic moduli are presented in this thesis.

ABSTRACT

The elastic moduli of large single crystals of olivine, orthopyroxene and garnet of approximate upper mantle compositions have been measured over a 3 GPa range of hydrostatic pressure at room temperature. The greater pressure capability, and the use of improved ultrasonic interferometric techniques including the incorporation of explicit corrections for transducer-bond phase shifts, have enabled the measurement of more reliable first pressure derivatives (±1%) of the elastic moduli than has previously been possible. In addition, second pressure derivatives (±10%) of the elastic moduli of these relatively incompressible minerals have been resolved for the first time.

The present measurements confirm the magnitudes of the first pressure derivatives of the elastic moduli of olivine, garnet and orthopyroxene of similar compositions determined in previous studies over much reduced (≦1 GPa) pressure ranges. In particular, the first pressure derivatives of the elastic moduli of orthopyroxene were found to be very large with respect to those of olivine and garnet - in accord with the findings of Frisillo and Barsch (1972). The second pressure derivatives of the elastic moduli determined in this study however, illustrate the importance of accurate high pressure measurements in the extrapolation of single crystal elasticities to mantle conditions. Curvature in the pressure dependence of the bulk and shear moduli of the olivine and garnet crystals reduces the pressure derivatives from those observed at zero pressure by ~20% over the 3 GPa pressure range. The pressure dependences of the bulk and shear moduli of orthopyroxene, however, decrease by 38% and 53% respectively over this pressure range.

The anomalous pressure dependence of the elastic moduli of orthopyroxene is due to the kinked and puckered chains of SiO_4 tetrahedra in this structure - in contrast to the isolated tetrahedra in both the olivine and garnet structures. The ability of these chains to kink and pucker accommodates the large distortions of the M2 octahedra in orthopyroxene. The large first and second pressure derivatives observed for orthopyroxene are a direct result of the distorted octahedra becoming more regular with increasing pressure and consequently straining the chains of tetrahedra. The large second pressure derivatives are a measure of the small pressure range required for an equilibrium to be reached between forces associated with deformation of the chains of tetrahedra and with distortion of the M2 octahedra.

The determination of the first and second pressure derivatives of the elastic moduli of olivine, garnet and especially orthopyroxene has facilitated the extrapolation of the measured elastic properties to greater pressures. Velocity profiles for specific upper mantle assemblages have been calculated via aggregate theory using these new elasticity data, previously determined temperature derivatives of the elastic moduli, and an average upper mantle geotherm. The compressional velocity profiles calculated with oceanic and shield geotherms bound the average upper mantle compressional velocity of the PREM model of Dziewonski and Anderson (1981). The shear velocities calculated with these two geotherms however, are up to 5% higher than the shear velocities of the PREM model. The incorporation of the large negative second pressure derivatives of the bulk modulus of orthopyroxene reduces the compressional velocity calculated for 200 km depth assuming a linear pressure dependence of the bulk modulus, by 2%.

The measurement of the elastic moduli of the wüstite analogue MnO over the 3 GPa pressure range has facilitated the incorporation of the crystal-field stabilization energy in existing systematics by providing a realistic value for the pressure derivative of the bulk modulus of MnO, where previously $\partial K/\partial P$ was estimated on the basis of the observed elasticity of other minerals. This has enabled the calculation of the bulk moduli for the 3d transition-metal monoxides, providing a more reliable estimate of the bulk modulus for stoichiometric FeO. A negative pressure derivative of the shear modulus C_{44} has been observed (at pressures $\geqq$1 GPa) in this study. Such reduction in the magnitude of the modulus C_{44} will tend to increase the thermodynamic competitiveness of any structure related to B1 by C_{44}-controlled shear deformation. The softening of this modulus has previously been associated with the paramagnetic→antiferromagnetic transition in MnO at low temperature, and the B1→B2 transition in the alkali halides and the alkaline-earth monoxides at high pressures. These phases are therefore two of the possible high pressure phases of MnO which are related to the original phase by C_{44}-controlled shear.

The shear modulus C_{55} of fayalite has been measured to pressures in excess of the equilibrium olivine→spinel transition pressure (~2 GPa). This modulus is the one which might have been expected to soften significantly prior to a martensitic transformation. No such softening of the modulus C_{55} was observed over this pressure range. Furthermore, the pressure dependences of the modulus C_{55} for fayalite and C_{55} for the forsteritic olivine discussed earlier are comparable, despite the much closer proximity of fayalite to the high pressure boundary of its stability field. Thus, there is no evidence for pressure-induced shear-mode softening in fayalite prior to a martensitic olivine→spinel transition.

TABLE OF CONTENTS

CHAPTER 1

INTRODUCTION

Information concerning the composition of the Earth's mantle is supplied indirectly through sampling of the mantle to depths of about 200 km by basaltic magmas and kimberlite pipes. The xenoliths from both sources range in composition from eclogite to peridotite. The observed compositions however, are predominantly peridotitic. Peridotitic nodules from depths greater than 70 km are generally variably depleted garnet lherzolites. Magmas from shallower depths carry xenoliths which are also dominantly peridotitic but these xenoliths exhibit a spinel lherzolite mineralogy.

The realization that the material represented by the peridotitic xenoliths is complementary to and not parental to the basaltic magmas led to the development of compositional models for the parent mantle (Ringwood, 1962;Green and Ringwood, 1963;Clark and Ringwood, 1964;Ringwood, 1966). These models were given the non-specific name

pyrolite, indicating a pyroxene-olivine mineralogy capable of yielding basaltic magmas on partial melting with a peridotite residue (Ringwood, 1962). This pyrolite composition has been refined by extensive petrological and geochemical modelling (Green and Ringwood, 1967;Green, 1971;Ringwood, 1975;Green et al., 1979), and has been shown to crystallize as a mixture of olivine, Al-poor pyroxene and pyrope-rich garnet at pressures corresponding to the depth interval ~70 to ~200 km. Below ~200 km, progressive transformation of the pyroxenes to garnets with partial octahedral co-ordination of Si results in the formation of complex garnet solid solutions.

Further phase changes occur in this mineralogy with increasing depth. A major phase change occurs at about 400 km where olivine transforms to the ß-phase (Ringwood and Major, 1970;Akimoto et al., 1976); at greater depths, 500-550 km, the Ca silicate component of garnet transforms to the perovskite phase (Ringwood and Major, 1971;Liu and Ringwood, 1975), while ß-phase completes the transformation to spinel (Ito et al., 1974). At 650 km this spinel phase disproportionates into orthorhombic perovskite, $MgSiO_3$, plus rocksalt structured MgO (Liu, 1975), and the remaining pyrope-rich garnet transforms first to an ilmenite (Ringwood and Major, 1968;Ito et al., 1972) and then to a perovskite phase (Liu, 1975).

The most important source of information on the physical properties of the mantle is provided by seismology. The phase transformations observed in the model pyrolite mantle occur at depths which are consistent with the observed discontinuities in the velocity profiles of the mantle. The range of possible olivine-pyroxene-garnet mineralogies for the upper mantle can be narrowed by comparing the measured wave-velocities for natural samples of proposed mineralogies

at mantle conditions with the compressional- and shear-wave seismic profiles. However, it is technically difficult to measure velocities through specimens of mantle material in the laboratory at conditions approaching those of the mantle - simultaneous high pressures and temperatures being limited to the range < 1 GPa and < 700 K (eg Christensen, 1979). Higher pressures and temperatures are separately attainable and the purpose of the present high pressure experiments is to reduce the lengthy extrapolation from laboratory to upper mantle pressures. In particular the combination of improved ultrasonic techniques and greater pressure capability provide for more reliable characterization of the pressure dependence of elastic wave velocities than has previously been possible.

The present study is concerned primarily with the mantle from ~70 to 200 km depth. The natural samples of rocks from these depths together with the experimentally observed mineralogy of the pyrolite compositional model indicate a mineralogy for this region of the mantle dominated by olivine, with lesser volumes of orthopyroxene and clinopyroxene, and a small volume of pyrope-rich garnet. In view of this proposed garnet-pyrolite/garnet-lherzolite mineralogy, the elastic moduli of single crystals of olivine, orthopyroxene and pyrope-rich garnet with well characterized micro-structure, will be measured at high pressure and room temperature.

There have been previous studies of the elastic properties of single crystals of olivine, orthopyroxene and garnet of similar compositions. These earlier measurements however, were conducted over smaller (≤1 GPa) pressure ranges and linear pressure dependences of the moduli were generally observed.

The pressure dependence of the elastic moduli of the present crystal of pyrope-rich garnet has been previously determined by Bonczar et al. (1977) to 1 GPa. Their measured moduli appear somewhat anomalous when compared to the elastic moduli computed from the garnet solid solution systematics of Babuska et al. (1978) and Leitner et al. (1980) for a crystal of this composition. Resolution of this discrepancy is a goal of this study.

The elastic moduli of orthopyroxene have been determined to 1 GPa by Frisillo and Barsch (1972). The value of $\partial K/\partial P$ (9.6) deriving from their study is anomalously high relative to $\partial K/\partial P$ for most silicate minerals including olivine ($\partial K/\partial P$=5.13, Kumazawa and Anderson, 1969) and garnet ($\partial K/\partial P$=4.74, Bonczar et al., 1977; $\partial K/\partial P$=5.43, Soga, 1967) The determination of the high-pressure elastic moduli of orthopyroxene is therefore a major priority in this study.

The present 3 GPa pressure capability together with the accuracy of the measured travel-times allows the determination of reliable first pressure derivatives (±1%) and the measurement of second pressure derivatives (±10%) of the elastic moduli for these minerals for the first time. The elasticity data for these three mantle minerals may be combined with the aid of aggregate theory to produce upper and lower bounds to the bulk and shear moduli of various model mineralogies for an isotropic, homogeneous mantle (Voigt, 1928;Reuss, 1929;Hashin and Shtrikman, 1962a, 1962b;Watt, 1979). These model mantle elasticities require only a modest extrapolation from the observed 3 GPa pressure range to ~6.5 GPa (200 km). Velocity profiles for specific olivine, garnet and orthopyroxene mineralogies may then be calculated from the bulk and shear moduli of composites of these minerals together with the

previously determined temperature derivatives of the elastic moduli and an average upper mantle geotherm.

The single-crystal elastic moduli of a range of silicates have previously been discussed, particularly by Weidner and his colleagues (Vaughan and Weidner, 1978;Au and Weidner, 1985) in terms of the polyhedral lattice models. The relative magnitudes of the elastic moduli and their pressure derivatives measured in this study for olivine, garnet and orthopyroxene may be rationalized in this manner. In particular, it may be possible to provide a qualitative explanation for the anomalous pressure dependence of the orthopyroxene moduli.

The physical properties of phases representative of the mantle at greater depths may also be investigated with the present high-pressure ultrasonic interferometer. The pronounced discontinuity in seismic wave velocities near 400 km depth is attributable to the onset of the olivine(α)→spinel(γ) transformation, which, for compositions near $(Mg_{0.9}Fe_{0.1})_2SiO_4$ is actually a complex sequence of reactions which occur progressively with increasing pressure: $\alpha \rightarrow (\alpha+\gamma) \rightarrow (\alpha+\beta) \rightarrow \beta \rightarrow (\beta+\gamma) \rightarrow \gamma$ (Ringwood and Major, 1970;Akimoto et al., 1976). The geophysical importance of the kinetics of this transformation with its possible contribution to the driving force for plate tectonics (Schubert and Turcotte, 1971;Toksöz et al., 1971; Ringwood, 1975) and to deep-focus earthquakes (Sung and Burns, 1976) has focussed attention on the transformation mechanism - for which two alternatives have been suggested. The first is a nucleation and growth mechanism (Sung and Burns, 1976). The second is a martensitic diffusionless mechanism which achieves the conversion of the hexagaonal-close-packed anion array of the olivine lattice into the face-centred-cubic geometry of spinel by the actions of partial dislocations associated with the (100)[001] slip

system (Poirier, 1981a). Such a transformation would probably be accompanied by premonitory shear mode softening of the elastic stiffness moduli C_{55} and C_{66} governing shear parallel to the (100) plane (Poirier, 1981a). The availability of a single crystal of fayalite together with the (room temperature) 3 GPa pressure capability of the ultrasonic interferometer affords an opportunity to study the pressure sensitivity of the key shear moduli of an olivine to pressures in excess of its metastable olivine≠spinel transition pressure (~2 GPa for Fe_2SiO_4, Ringwood, 1975).

Finally, the high pressure polymorphism of the transition-metal oxides is of considerable current interest in connection with element patitioning among the ferromagnesian phases of the Earth's lower mantle and the solubility of oxygen in the outer core (Ringwood, 1977; McCammon et al., 1983). However, there is confusion concerning both the elastic properties (eg Jeanloz and Hazen, 1983) and the high pressure polymorphism of wüstite, and given the availability a single crystal of the FeO analogue MnO, the elastic moduli of MnO will be measured at room temperature to 3 GPa.

CHAPTER 2

EXPERIMENTAL TECHNIQUES

2.1 Introduction

The most direct method of determining the elastic moduli of a single-crystal is to measure the velocities of elastic waves travelling through the crystal. For each direction in a single-crystal, three independent waves with mutually orthogonal displacements may be propagated. In general, no one of these displacements coincides with either the normal to the wave front or a direction parallel to the wave front. There are however, special directions in any crystal (depending upon its symmetry) in which one of the waves is a compressional mode with the displacement vector coinciding with the wave front normal, and the other two waves are transverse modes with displacement vectors perpendicular to each other and in the plane of the wave front.

The equation of motion for an elastic medium in the absence of body

forces is

$$\sigma_{ij,j} = \rho \ddot{U}_i \qquad i = 1,2,3 \qquad (2.1)$$

where ρ is the density, σ_{ij} is the stress tensor, the comma notation implies differentiation and the repeated suffix implies summation. We seek a plane wave solution for the particle motion, of the form

$$U_\ell = U_{0\ell} \exp i(\omega t - \underline{k}.\underline{r}) \qquad \ell = 1,2,3. \qquad (2.2)$$

Introducing the elastic stiffness tensor $C_{ijk\ell}$, and the stress-strain relationship

$$\sigma_{ij} = C_{ijk\ell}\, \varepsilon_{k\ell} \qquad i,j = 1,2,3 \qquad (2.3)$$

where $\varepsilon_{k\ell} = (U_{\ell,k} + U_{k,\ell})/2$, the equation of motion (Eqn. 2.1) becomes

$$C_{ijk\ell}\, U_{\ell,kj} = \rho \ddot{U}_i \qquad i = 1,2,3. \qquad (2.4)$$

This equation can be solved for any direction of propagation through a crystal of any symmetry (see Truell et al., 1969). For the particle displacement vector $\underline{U}$ and the wave vector $\underline{k} = (\omega/v)\,\underline{n}$, the term $U_{\ell,kj}$ (in Eqn. 2.4) is

$$U_{\ell,kj} = - n_k\, n_j\, U_{0\ell}\, (\omega/v)^2 \exp i(\omega t - \underline{k}.\underline{r}) \qquad (2.5)$$

and the equation of motion (Eqn. 2.4) can be rewritten as

$$(C_{ijk\ell}\, n_k\, n_j - \rho\, v^2\, \delta_{i\ell})\, U_{0\ell} = 0 \qquad i = 1,2,3, \qquad (2.6)$$

for $\delta_{i\ell}=1$ $(i=\ell)$, and $\delta_{i\ell}=0$ $(i\neq\ell)$.

For the special case of cubic symmetry, where the elastic constant matrix is

$$\begin{matrix} C_{11} & C_{12} & C_{12} & \cdot & \cdot & \cdot \\ C_{12} & C_{11} & C_{12} & \cdot & \cdot & \cdot \\ C_{12} & C_{12} & C_{11} & \cdot & \cdot & \cdot \\ \cdot & \cdot & \cdot & C_{44} & \cdot & \cdot \\ \cdot & \cdot & \cdot & \cdot & C_{44} & \cdot \\ \cdot & \cdot & \cdot & \cdot & \cdot & C_{44} \end{matrix} , \qquad (2.7)$$

the equation of motion (Eqn. 2.6) reduces to

$$\begin{aligned} (C_{11}-C_{44})U_{01}n_1n_1 + (C_{12}+C_{44})U_{02}n_1n_2 + (C_{12}+C_{44})U_{03}n_1n_3 &= (\rho v^2-C_{44})U_{01} \\ (C_{12}+C_{44})U_{01}n_2n_1 + (C_{11}-C_{44})U_{02}n_2n_2 + (C_{12}+C_{44})U_{03}n_2n_3 &= (\rho v^2-C_{44})U_{02} \\ (C_{12}+C_{44})U_{01}n_3n_1 + (C_{12}+C_{44})U_{02}n_3n_2 + (C_{11}-C_{44})U_{03}n_3n_3 &= (\rho v^2-C_{44})U_{03} \end{aligned} \qquad (2.8)$$

with the direction of propagation being described by the direction cosines n_i, and

$$n_1^2 + n_2^2 + n_3^2 = 1. \qquad (2.9)$$

There is a solution to the equation of motion (Eqn. 2.6 in general, and Eqn. 2.8 in particular) if and only if the secular determinant is zero:

$$|C_{ijk\ell}\, n_k\, n_\ell - \rho\, v^2\, \delta_{i\ell}| = 0. \qquad (2.10)$$

For a wave propagating along [100] in a cubic crystal, with $n_1=1$, and $n_2=n_3=0$, the roots of Eqn. 2.10 are

$$\begin{aligned} \rho v^2_{[100]} &= C_{11} \\ \rho v^2_{[100]} &= C_{44} \\ \rho v^2_{[100]} &= C_{44}. \end{aligned} \qquad (2.11)$$

A pure compressional wave is propagated when the wave front normal coincides with the displacement vector $\underline{U}$; or

$$\underline{U}\times\underline{n} = 0, \tag{2.12a}$$

and a pure transverse wave is propagated when the wave front normal is perpendicular to the displacement vector $\underline{U}$; or

$$\underline{U}.\underline{n} = 0. \tag{2.12b}$$

Hence

$$\rho v^2_{[100]} = C_{11} \tag{2.13}$$

is the solution for a compressional wave, and

$$\rho v^2_{[100]} = C_{44} \qquad \text{with any polarization} \tag{2.14}$$

is the solution for the transverse waves propagating in the [100] direction.

For the propagation direction [110] in a crystal of cubic symmetry, with $n_1=n_2=1/\sqrt{2}$ and $n_3=0$, the roots of Eqn. 2.10 are

$$\rho v^2_{[110]} = (C_{11} + C_{12} + 2C_{44})/2$$

$$\rho v^2_{[110]} = C_{44} \qquad \text{polarization [001]}$$

and $$\rho v^2_{[110]} = (C_{11} - C_{12})/2 \qquad \text{polarization } [1\bar{1}0]. \tag{2.15}$$

Figure 2.1 illustrates the propagation and polarization directions for the pure shear and compressional waves described by Eqns. 2.13-2.15,

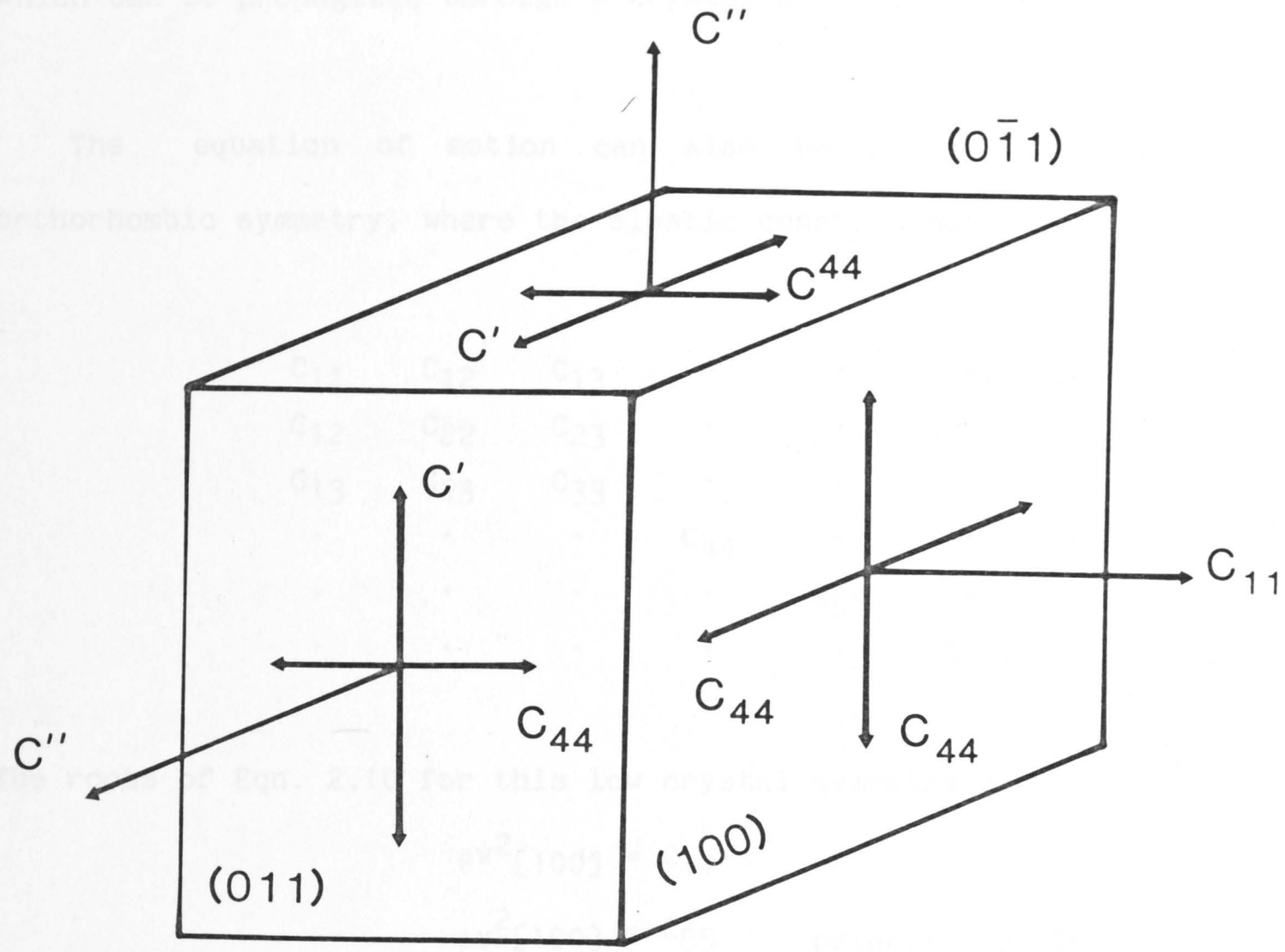

$$C' = (C_{11}-C_{12})/2$$

$$C'' = (C_{11}+C_{12}+2C_{44})/2$$

Figure 2.1 The principal propagation and polarization directions for the pure shear and pure compressional waves which propagate through a crystal of cubic symmetry.

which can be propagated through a crystal of cubic symmetry.

The equation of motion can also be solved for crystals of orthorhombic symmetry, where the elastic constant matrix is:

$$\begin{matrix} C_{11} & C_{12} & C_{13} & \cdot & \cdot & \cdot \\ C_{12} & C_{22} & C_{23} & \cdot & \cdot & \cdot \\ C_{13} & C_{23} & C_{33} & \cdot & \cdot & \cdot \\ \cdot & \cdot & \cdot & C_{44} & \cdot & \cdot \\ \cdot & \cdot & \cdot & \cdot & C_{55} & \cdot \\ \cdot & \cdot & \cdot & \cdot & \cdot & C_{66}. \end{matrix} \qquad (2.16)$$

The roots of Eqn. 2.10 for this low crystal symmetry are:

$$\begin{aligned} \rho v^2_{[100]} &= C_{11} \\ \rho v^2_{[100]} &= C_{55} && \text{polarization } [001] \\ \rho v^2_{[100]} &= C_{66} && \text{polarization } [010] \\ \rho v^2_{[010]} &= C_{22} \\ \rho v^2_{[010]} &= C_{44} && \text{polarization } [001] \\ \rho v^2_{[010]} &= C_{66} && \text{polarization } [100] \\ \rho v^2_{[001]} &= C_{33} \\ \rho v^2_{[001]} &= C_{44} && \text{polarization } [010] \\ \rho v^2_{[001]} &= C_{55} && \text{polarization } [100] \\ \rho v^2_{[110]_c} &= (C_{44} + C_{55})/2 && \text{polarization } [001] \end{aligned} \qquad (2.17)$$

$$\rho v^2_{[110]_c} = K_{12}(P) \qquad \text{polarization } \sim[110]_c$$

$$= (C_{11}+C_{22}+2C_{66})/4+\sqrt{(C_{11}-C_{22})^2+4(C_{12}+C_{66})^2}/4$$

$$\rho v^2_{[110]_c} = K_{12}(S) \qquad \text{polarization } \sim[1\bar{1}0]_c$$

$$= (C_{11}+C_{22}+2C_{66})/4-\sqrt{(C_{11}-C_{22})^2+4(C_{12}+C_{66})^2}/4$$

$$\rho v^2_{[011]c} = (C_{55} + C_{66})/2 \qquad \text{polarization } [100]$$

$$\rho v^2_{[011]c} = K_{23}(P) \qquad \text{polarization } \sim[011]_c$$

$$= (C_{22}+C_{33}+2C_{44})/4+\sqrt{(C_{22}-C_{33})^2+4(C_{23}+C_{44})^2}/4$$

$$\rho v^2_{[011]c} = K_{23}(S) \qquad \text{polarization } \sim[01\bar{1}]_c$$

$$= (C_{22}+C_{33}+2C_{44})/4-\sqrt{(C_{22}-C_{33})^2+4(C_{23}+C_{44})^2}/4 \qquad (2.17)$$

$$\rho v^2_{[101]c} = (C_{44} + C_{66})/2 \qquad \text{polarization } [010]_c$$

$$\rho v^2_{[101]c} = K_{13}(P) \qquad \text{polarization } \sim[101]_c$$

$$= (C_{11}+C_{33}+2C_{55})/4+\sqrt{(C_{11}-C_{33})^2+4(C_{13}+C_{55})^2}/4$$

$$\rho v^2_{[101]c} = K_{13}(S) \qquad \text{polarization } \sim[10\bar{1}]_c$$

$$= (C_{11}+C_{33}+2C_{55})/4-\sqrt{(C_{11}-C_{33})^2+(C_{13}+C_{55})^2}/4$$

where the $[101]_c$ notation describes a direction of propagation with respect to a hypothetical cubic lattice isoaxial with the orthorhombic lattice. (Thus $[101]_c$ is a direction at 45° to [100] and [001] and 90° to [010]). The compressional and shear modes $K_{ij}(P)$ and $K_{ij}(S)$ are not pure modes but are quasi-compressional and quasi-shear modes of approximately the polarizations indicated. Figure 2.2 illustrates the propagation and polarization directions for these solutions to the equation of motion for a crystal of orthorhombic symmetry. (Note the symmetry relations for the shear modes C_{ii}, i=4,5,6.)

McSkimin and his colleagues in the 1950's pioneered the ultrasonic pulse interferometric methods of measuring accurate travel-times of elastic waves propagating through single crystals. Today these

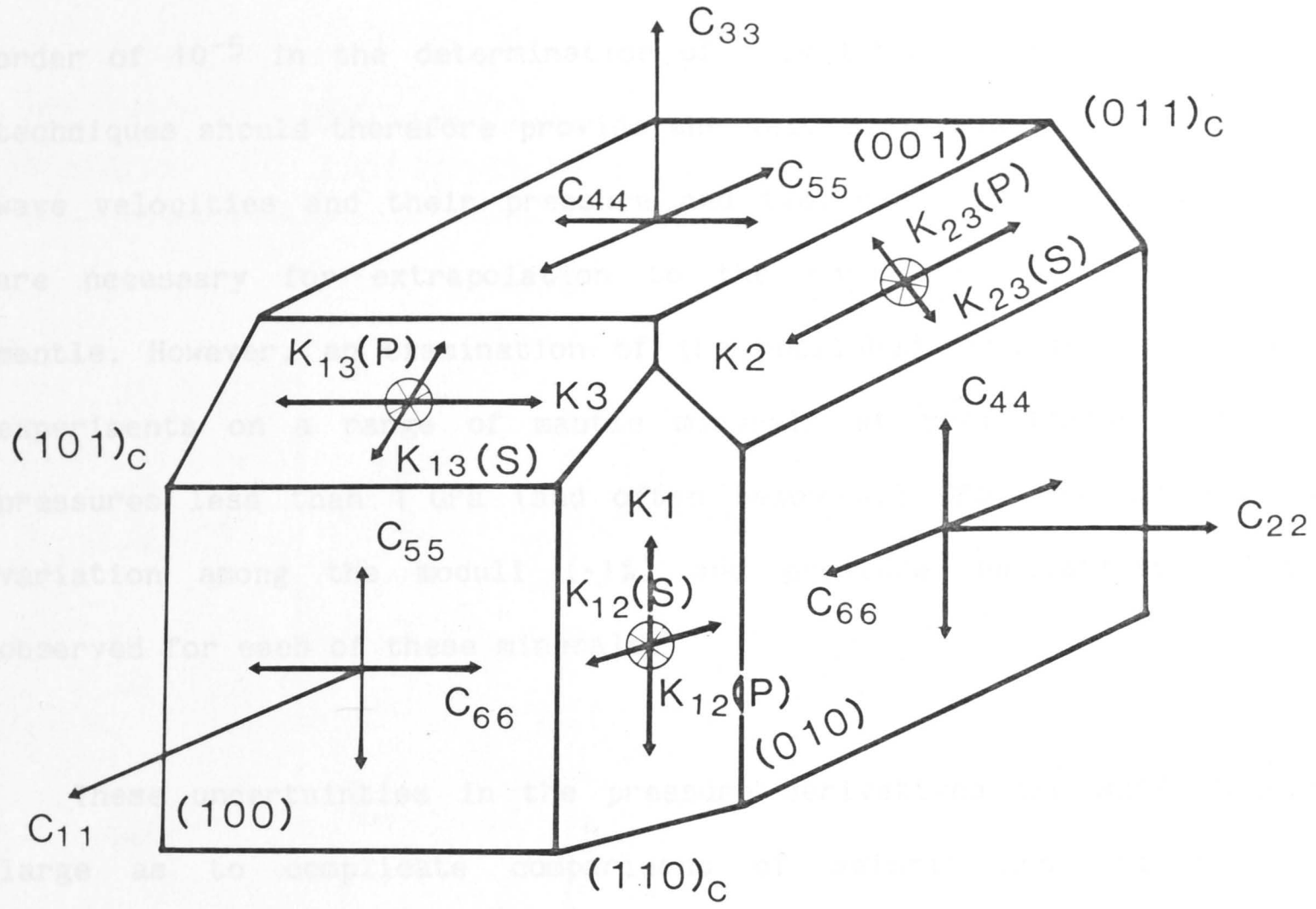

$$K1 = (C44 + C55)/2$$

$$K2 = (C55 + C66)/2$$

$$K3 = (C44 + C66)/2$$

Figure 2.2 The principal propagation and polarization directions for the pure shear and pure compressional waves, together with the quasi-shear and quasi-compressional waves which propagate through a crystal of orthorhombic symmetry.

techniques are capable, in principle, of an absolute accuracy of the order of 10^{-5} in the determination of travel-times. These ultrasonic techniques should therefore provide the well constrained values of the wave velocities and their pressure and temperature derivatives which are necessary for extrapolation to the conditions of the Earth's mantle. However, an examination of the published data for ultrasonic experiments on a range of mantle minerals at room temperature, to pressures less than 1 GPa (and often below 0.5 GPa) reveals a wide variation among the moduli (~1%) and pressure derivatives (~10%) observed for each of these minerals.

These uncertainties in the pressure derivatives are sufficiently large as to complicate comparisons of seismic and extrapolated laboratory velocities for the Earth's mantle, and have thus provided strong motivation for both the reassessment of potential sources of error in the ultrasonic pulse interferometric techniques and also the extension of the pressure capability (Davies and O'Connell, 1977; Jackson et al., 1981;Jackson and Niesler, 1982).

2.2 Transducer-bond phase shift

In the conventional bonded-transducer configuration (Figure 2.3) there arises a phase shift due to the interference between the direct reflection from the crystal-bond interface and other reflected waves which return to the crystal after multiple reverberations within the transducer and bond. Previously, the procedure has been to use theoretical models of this reflection phase shift to separate the propagation and phase shift components of the measured travel-times. The major conclusion from such analyses is that the transducer-bond

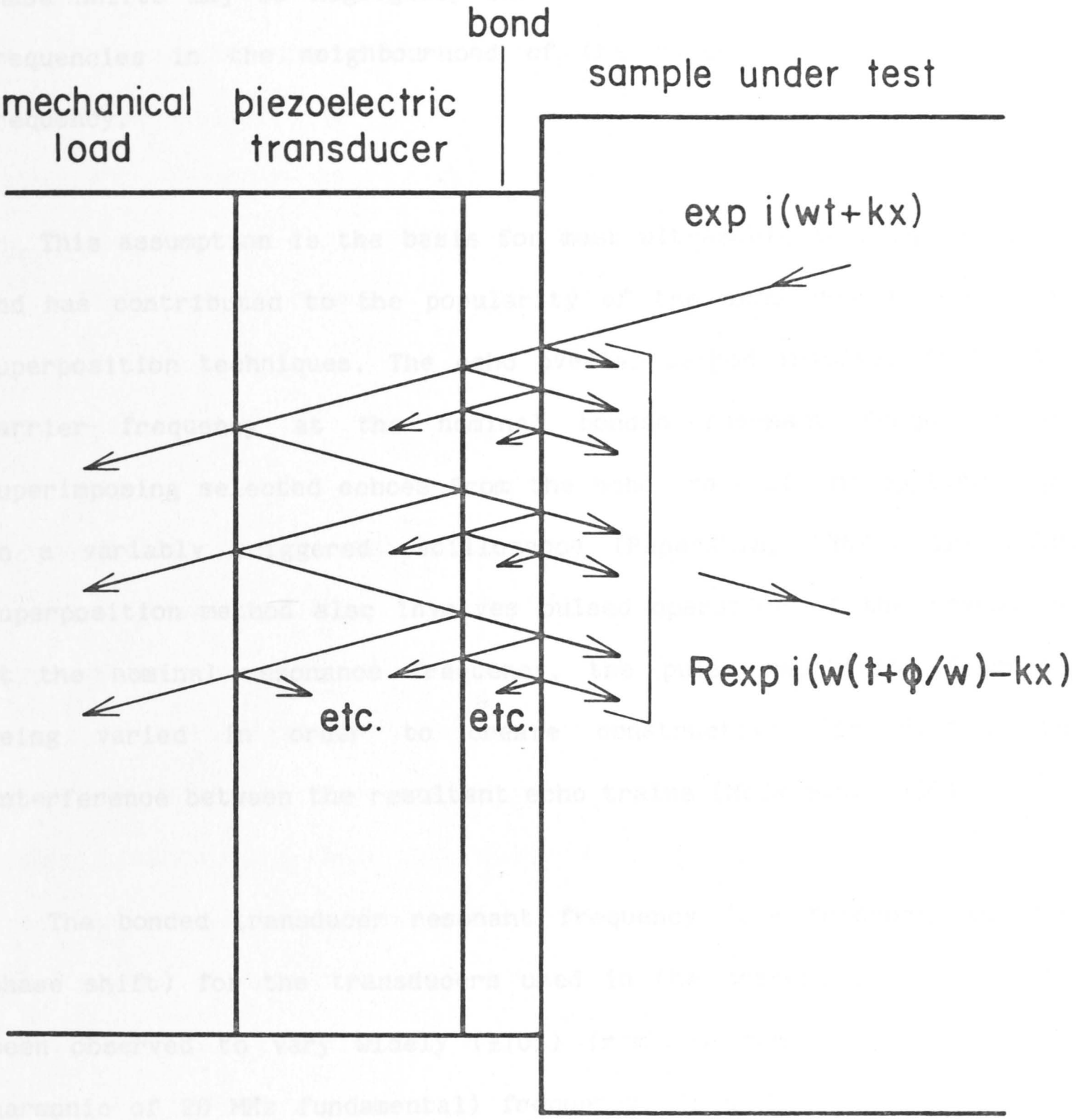

Transducer - bond phase shifts in ultrasonics

Figure 2.3 The creation of phase shift effects due to multiple reverberations of the applied signal within the transducer and bond.

phase shifts may be negligibly small for sufficiently thin bonds at frequencies in the neighbourhood of the bonded transducer resonant frequency.

This assumption is the basis for most ultrasonic techniques in use and has contributed to the popularity of the echo overlap and pulse superposition techniques. The echo overlap method involves fixing the carrier frequency at the nominal bonded resonant frequency and superimposing selected echoes from the echo train of the applied pulse on a variably triggered oscilloscope (Papadakis, 1967). The pulse superposition method also involves pulsed operation of the transducer at the nominal resonance frequency, the pulse repetition frequency being varied in order to create constructive (or destructive) interference between the resultant echo trains (McSkimin, 1950).

The bonded transducer resonant frequency (the frequency of zero phase shift) for the transducers used in the present experiments has been observed to vary widely (±10%) from the nominal 60 MHz (third harmonic of 20 MHz fundamental) frequency. This factor, together with the pressure dependence of the appropriate elastic modulus and hence of the resonant frequency of the transducers (approximately +1 MHz per GPa) makes it difficult to operate consistently under conditions of zero phase shift.

2.3 Phase comparison technique

Thus the apparent round-trip travel-time measured by ultrasonic interferometry will in general be the sum of a propagation contribution $2L/v$ and a contribution $\Phi/2\pi f$ associated with the reflection phase

shift (see Figure 2.3). These terms can be separated by varying the relative contributions of the propagation and reflection phase shifts. This was accomplished by performing comparative one- and two-transducer experiments (Jackson et al. 1981) which enable direct measurement of the transducer-bond phase shift and thus permit explicit correction of the measured travel-times.

2.3.1 Transducers

Coaxially plated quartz transducers of 20 MHz (±1%) nominal resonance frequency were used in the present experiments. The X-cut compressional mode transducers and the AC-cut shear mode transducers were 6.35 mm in diameter. These transducers were employed in preference to the 20 MHz $LiNbO_3$ transducers used by Jackson et al. (1981) as the former produce pure shear and compressional modes of propagation. The transducers used in the one- and two-transducer comparative experiments were always chosen from the same batch in order to minimize any possible variation in the transducer resonance frequencies.

It was occassionally necessary to reshape the transducers in order to match the irregular faces of the crystals used. This entailed shaving off some of the coaxial plating and reducing the size of the inactive area of the transducer, but always leaving the 3.2 mm diameter active area of the inner electrode untouched. This process was shown experimentally to have no effect on the quality of the signal produced, and no effect on the measured travel-times.

2.3.2 Bonds

The transducers were bonded to the crystals with a 9:1 molar

mixture of glycerine and phthalic anhydride. This mix was sufficiently mobile at 3 GPa to accommodate the deviatoric stresses occurring at the crystal-bond-transducer interfaces which could otherwise have cracked either the crystals or the transducers. However, at low pressures (<1 GPa) the bond was often too fluid to allow efficient transmission of shear waves. Most room pressure measurements, for both compressional and shear waves were conducted using a stiffer bond of 1:1 glycerine and phthalic anhydride. The bonding of the transducer with this viscous mixture was accomplished by repeated heating and clamping of the transducer, bond and crystal in order to thin the bond sufficiently, and to ensure uniform thickness of the bond. The mobile 9:1 mixture could be adequately thinned by repeated clamping at room temperature. After some initial experimentation it was demonstrated that bonds of reproducible quality could be prepared via these methods.

2.3.3 Measurement of travel-times

The phase comparison technique used in the present experiments is based on the procedure of Jackson et al. (1981) and Jackson and Niesler (1982) (see Figure 2.4). Application of a pair of appropriately spaced phase coherent pulses to the transducer results in interference between the respective echo trains. In particular, The first echo from the second pulse overlaps with the second echo from the first pulse. For an applied pulse $A(\omega)\sin\omega t$, the resultant overlapped echo is

$$R(\omega,t) = A(\omega)\sin\omega t + r(\omega)A(\omega)\sin(\omega t + 2\omega L/v + \Phi(\omega)) \qquad (2.18)$$

where $A(\omega)$ is the transducer response function and $r(\omega)$ is the reflection coefficient at the transducer-bond-crystal interface (see Figure 2.3). For any given ω, $R(\omega,t)$ is a sinusoid of the form

Figure 2.4 Block diagram of the ultrasonic interferometer.

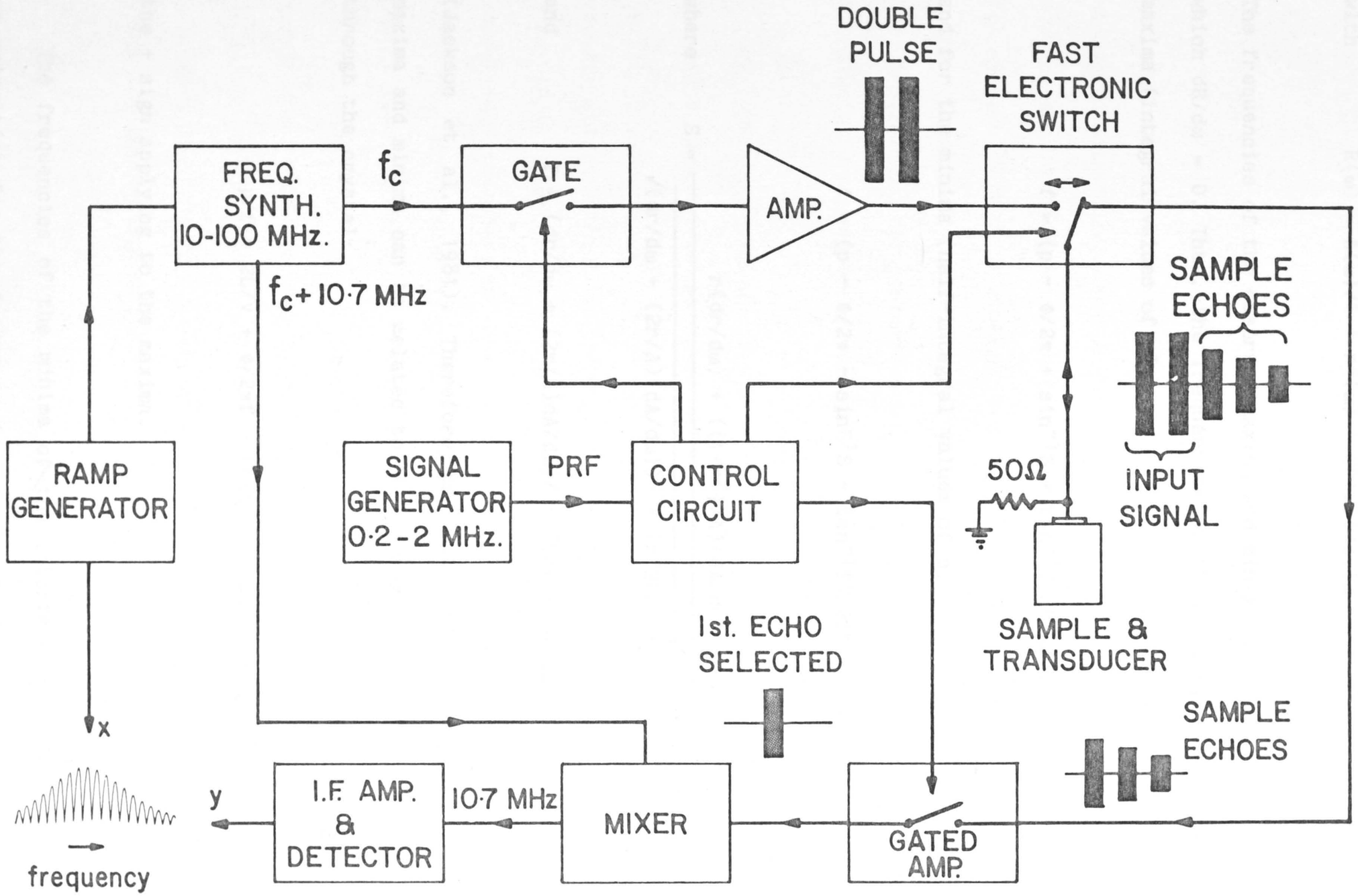
DOUBLE PULSE
FAST ELECTRONIC SWITCH
FREQ. SYNTH. 10-100 MHz.
f_c
GATE
AMP.
f_c + 10·7 MHz
SAMPLE ECHOES
RAMP GENERATOR
SIGNAL GENERATOR 0·2 - 2 MHz.
PRF
CONTROL CIRCUIT
50Ω
INPUT SIGNAL
SAMPLE & TRANSDUCER
1st. ECHO SELECTED
SAMPLE ECHOES
x
y
I.F. AMP. & DETECTOR
10·7 MHz
MIXER
GATED AMP.
frequency

$$R(\omega,t) = R(\omega)\sin(\omega t + \delta(\omega)) \tag{2.19}$$

$$\text{with} \qquad R(\omega) = A(\omega)\sqrt{1 + r^2(\omega) + 2r(\omega)\cos(2\omega L/v + \Phi(\omega))} \tag{2.20}$$

The frequencies of the observed maxima and minima of $R(\omega)$ are those for which $dR/d\omega = 0$. Thus, the frequencies of these extrema are, for the maxima (integral values of p)

$$f = (p - \Phi/2\pi + \sin^{-1}S + \tan^{-1}T)/(2L/v) \tag{2.21}$$

and for the minima (half-integral values of p)

$$f = (p - \Phi/2\pi - \sin^{-1}S + \tan^{-1}T)/(2L/v) \tag{2.22}$$

$$\text{where} \qquad S = \frac{r(dr/d\omega) + ((1+r^2)/A)(dA/d\omega)}{\sqrt{(dr/d\omega + (2r/A)(dA/d\omega))^2 + (r(2L/v + d\Phi/d\omega))^2}} \tag{2.23}$$

$$\text{and} \qquad T = (dr/d\omega + (2r/A)dA/d\omega)/(r(2L/v + d\Phi/d\omega)), \tag{2.24}$$

(Jackson et al., 1981). Therefore the observed frequencies of the maxima and minima can be related to the propagation travel-time (2L/v) through the crystal:

$$p/f = 2L/v + \Phi/2\pi f - (\tan^{-1}T \pm \sin^{-1}S)/f, \tag{2.25}$$

the + sign applying to the maxima.

The frequencies of the minima of the interference pattern require no correction for the frequency dependence of the transducer response

function $A(\omega)$ and the reflection coefficient $r(\omega)$ as $(\tan^{-1}T - \sin^{-1}S) = 0$ to at least four significant figures, and thus Eqn. 2.25 can be expressed as

$$p/f = 2L/v + \Phi/2\pi f \qquad (2.26)$$

for half-integral values of p. Furthermore, the frequencies of the minima are less subject to perturbation by noise than those of the maxima, as the minima are sharper by a factor $(1+r)/(1-r)$ (Jackson et al., 1981). This term becomes very large as the reflection coefficient r approaches 1. Consequently, we have measured only the frequencies of the minima of the interference pattern, in an effort to avoid introducing unwanted errors into the measured travel-times.

The overlapped echo $R(\omega,t)$ (Eqn. 2.19) is gated to remove the transient effects at each end of the pulse due to the finite time needed to build up a steady state phase contribution from the reverberations within the bond and transducer. The carrier frequency is then tuned through a frequency range of 10 MHz centred on the approximate frequency of zero phase shift at either the fundamental or the third harmonic of the transducer resonance frequency. The analogue output (see Figure. 2.4) illustrates the resulting maxima and minima of the interference pattern modulated by the response envelope of the transducer. The flatness of this response envelope is a sensitive indicator of the bond quality. For the high quality bonds achieved at pressure, the envelope is essentially frequency independent for ±4 MHz about the bonded transducer resonant frequency.

The minima of the interference pattern were located automatically and the frequencies were recorded digitally. A 5 MHz range about the

zero phase shift frequency includes at least ten minima for travel-times >1 μsec (see Eqn. 2.26). The frequency measurements were then repeated with a second passive transducer bonded to the other end of the crystal. This second transducer was earthed in order to produce an electrical termination equivalent to that of the first transducer.

Most of the experiments were conducted within the third harmonic response envelope (centred near 60 MHz) of the 20 MHz transducers. The phase shift contribution $\Phi/2\pi f$ at this frequency is one third of that which would be incurred near the fundamental resonance frequency. Hence, the phase shift correction term is smaller for travel-times measured at the third harmonic, and any associated errors are also smaller.

The assumption that the total transducer-bond phase shift associated with the two-transducer configuration is twice that for the one-transducer configuration can now be used to calculate the desired propagation travel-time

$$t_o(f) = 2L/v = 2t_1(f) - t_2(f) \qquad (2.27)$$

and the transducer-bond phase shift

$$\Phi(f)/2\pi = f\times(t_2(f) - t_1(f)) \qquad (2.28)$$

where $t_1(f)$ and $t_2(f)$ are the apparent travel-times at frequency f for the one- and two-transducer configurations. Figure 2.5 illustrates a typical set of travel-times calculated across the frequency range, and the associated phase shift calculated from the apparent travel-times. The frequency independence of the corrected travel-time $t_o(f)$ is an

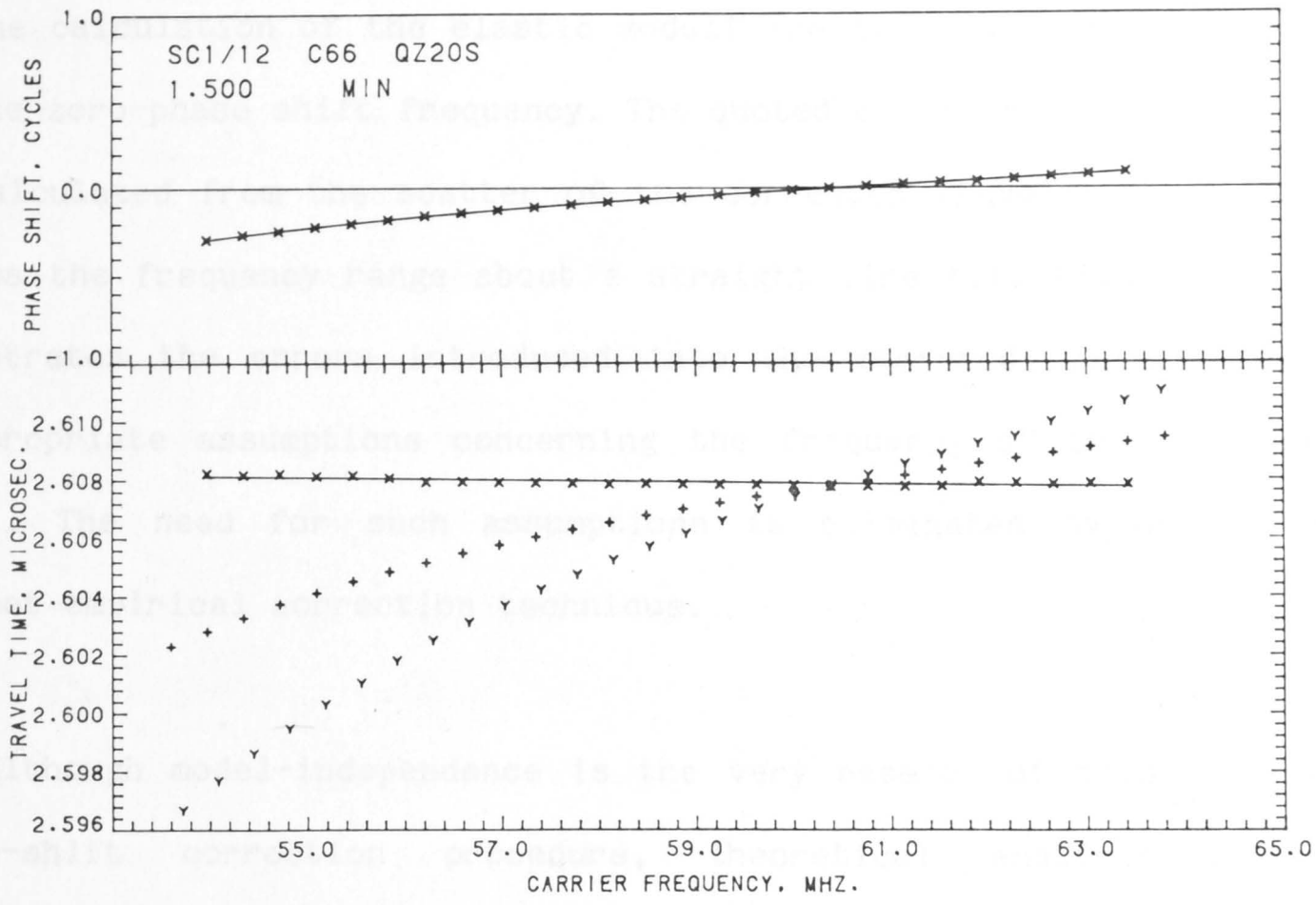

Figure 2.5 Phase comparison data at 1.5 GPa for a shear-mode ($C_{66}(12)$ of olivine - see Chapter 4). The plotting symbols (+), (Y) and (X) in the lower part of the figure denote respectively, apparent travel-times for one- and two-transducer configurations, and travel-times corrected for the transducer-bond phase shifts, for all interference minima in the displayed frequency range. The lines superimposed on the phase shift and corrected travel-times are, respectively, the best fitting quadratic and linear representation of the data.

indicator of the success of this method of analysis, and an illustration of the reproducibility of the bonds. The travel-times used in the calculation of the elastic moduli are the travel-times measured at the zero-phase shift frequency. The quoted error in this travel-time is calculated from the scatter of the corrected travel-times measured across the frequency range about a straight line fit. Figure 2.5 also illustrates the errors introduced into the measured travel-times by inappropriate assumptions concerning the frequency of the zero phase shift. The need for such assumptions is eliminated by use of the present empirical correction technique.

Although model-independence is the very essence of this empirical phase-shift correction procedure, theoretical analysis of the transducer performance provides useful insight into the effects of possible transducer and bond variability. The transmission-line approach of Berlincourt (1964) and Sittig (1967) has been used by Niesler (1985) to calculate the effect of a 0.2-0.5 μm thick gold layer on a disc of quartz with a free resonance frequency of 20 MHz. A 0.2 μm thick layer of gold decreases the resonance frequency by approximately 1.25 MHz. The further increase in thickness of the plating from 0.2 to 0.5 μm however, has little effect on the resonance frequency. The bonds between the crystal and transducer in the present study are 0.2-0.5 μm thick. Bonds of this thickness were calculated (Niesler, 1985) to have no significant effect on the zero phase-shift frequency of the transducers. However, these bonds were calculated to effect the phase-shift components of the observed travel-times in the opposite sense to that calculated for the addition of a layer of gold.

Although we have attempted to avoid the mismatching of the transducer resonance frequencies within pairs of transducers used in

the one- and two-transducer comparative experiments, the measured free resonance frequencies of the transducers have been observed to range from 20.5-22.0 MHz (or 61.8-66.1 MHz). A mismatch in the zero phase shift frequencies of a pair of transducers displaces the corrected travel-times by a constant amount (either positive or negative) throughout the pressure range. This displacement is of the order of 1 nsec per MHz mismatch of the fundamental frequencies. This would result in a systematic error of order 0.1% in the measured elastic modulus, but the first and second pressure derivatives of the modulus would be unaffected. A further irregularity observed in the plots of travel-times versus frequency is the positive frequency dependence of the travel-times - attributable to be dispersion effects associated with the non-planar nature of the propagating wave (Niesler, pers. comm., 1984).

The frequencies of the interference minima for each mode of propagation were measured at room temperature. The deviations (~1 K) from this temperature (295 K) were monitored with a calibrated thermistor in intimate contact with the pressure vessel.

2.4 Crystal preparation

The single crystals used in these experiments were oriented to within 0.5° using X-ray Laue back-reflection techniques. Pairs of parallel faces of the required orientation were then cut and ground, and polished with 8 μm and 3 μm diamond paste, and 1 μm alumina powder. The faces were checked with optical flats and found to be flat to within $\lambda/2$ of sodium light.

The crystal densities were measured within an uncertainty ±0.1% by immersion in ethanol at 295 K. The compositions of the crystals were determined by electron-microprobe analysis, and the microstructure of each crystal was investigated via both optical and electron microscopy.

2.5 Pressure generation and measurement

Hydrostatic pressures up to 3 GPa were routinely generated at room temperature in a piston-cylinder apparatus (see Figure 2.6) following the method of Boehler et al. (1977). The bore of the pressure vessel was 12.7 mm in diameter and was sealed with Bridgman unsupported area seals. The liquid pressure medium used was a 1:1 (by volume) mixture of pentane and isopentane.

A coil of manganin wire of nominally 40 Ω resistance wound around the upper (immobile) seal was used as the pressure sensor (see Figure 2.6). The resistance of this wire increases at a rate of ~1 Ω per GPa. The pressure dependence of the gauge resistance was calculated from the known room- pressure resistance, and the resistance observed at the melting pressure of mercury at room temperature (Lloyd et al., 1969) given by

$$P = 3.8227((T/234.29)^{1.1772} - 1), \qquad (2.29)$$

and at the centre of the 'region of indifference' for the Bi I→II transition (Zeto and Vanfleet, 1971) from the equation

$$P = 2.550 - 0.00482(T - 298.16) \qquad (2.30)$$

(Peerdeman et al., 1980).

EXPERIMENTAL CONFIGURATION FOR ULTRASONIC VELOCITY MEASUREMENT TO 3 GPA

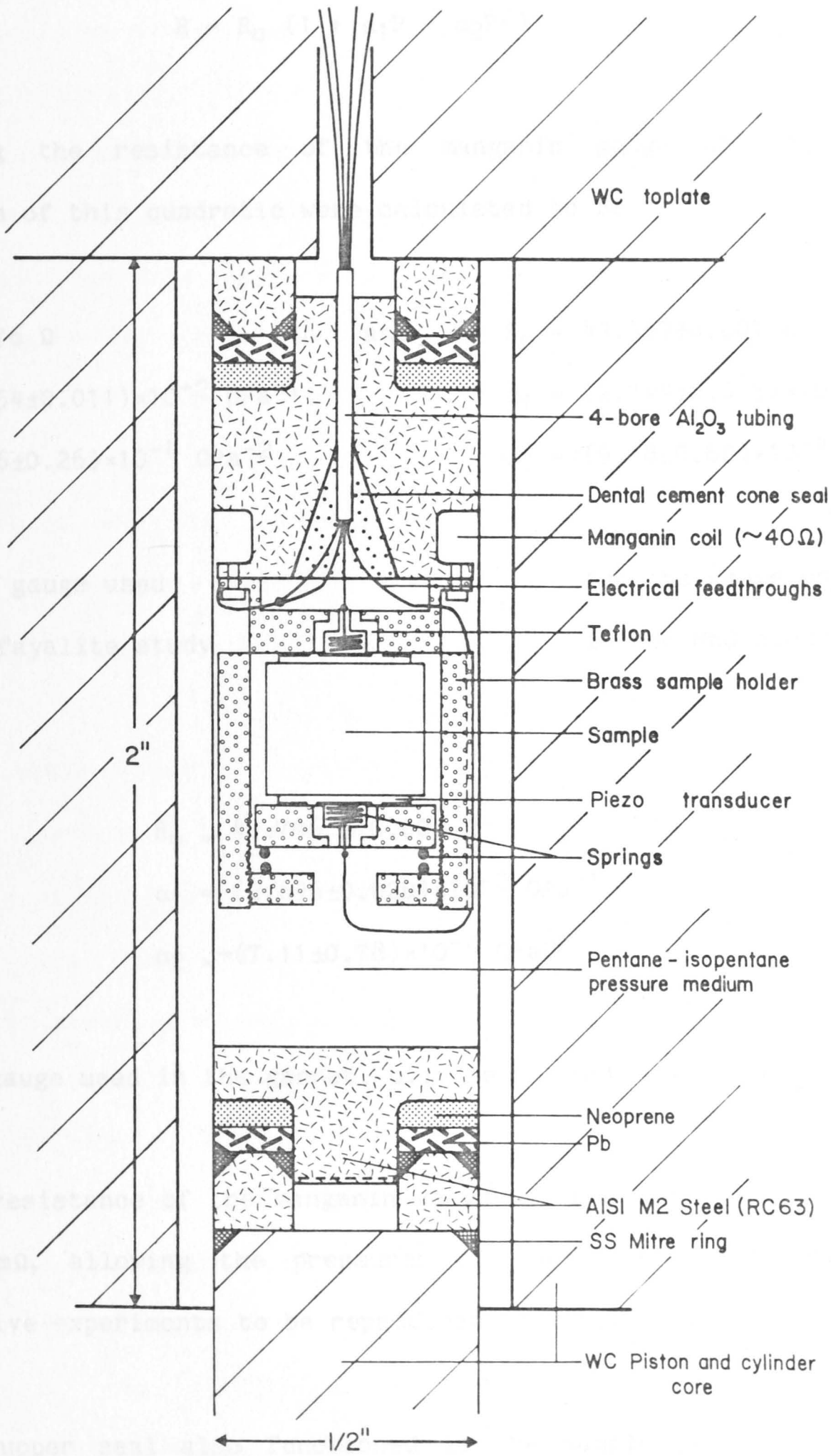

Figure 2.6 Experimental configuration for ultrasonic velocity measurement to 3 GPa as a function of hydrostatic pressure within a conventional piston-cylinder apparatus.

These three points can be used to define a quadratic

$$R = R_o (1 + \alpha_1 P + \alpha_2 P^2) \qquad (2.31)$$

describing the resistance of the manganin gauge at 295 K. The parameters of this quadratic were calculated to be

$R_o = 42.376\ \Omega$	$R_o = 43.369 \pm 0.001\ \Omega$
$\alpha_1 = (2.654 \pm 0.011) \times 10^{-2}\ GPa^{-1}$	$\alpha_1 = (2.744 \pm 0.015) \times 10^{-2}\ GPa^{-1}$
$\alpha_2 = -(5.76 \pm 0.26) \times 10^{-4}\ GPa^{-2}$	$\alpha_2 = -(9.18 \pm 0.80) \times 10^{-4}\ GPa^{-2}$
for the gauge used in the fayalite study	for the gauge used in the MnO study

and

$$R_o = 42.796 \pm 0.001\ \Omega$$
$$\alpha_1 = (2.696 \pm 0.020) \times 10^{-2}\ GPa^{-1}$$
$$\alpha_2 = -(7.11 \pm 0.78) \times 10^{-4}\ GPa^{-2} \qquad (2.32)$$

for the gauge used in the garnet, olivine and orthopyroxene studies.

The resistance of the manganin gauge was measured with an accuracy of 0.5 mΩ, allowing the pressures of the one- and two-transducer comparative experiments to be reproduced to within 2 mΩ, or 2×10^{-3} GPa.

The upper seal also functioned as the sample holder (see Figure 2.6). The 0.13 mm diameter electrical connections for the manganin gauge and the transducer contacts were fed through a four bore alumina tube which was embedded in a dental cement cone-seal. This sample holder could accommodate crystals as large as an 8 mm cube.

2.6 Data reduction

The crystals investigated in this study were of either cubic or orthorhombic symmetry. The elastic properties of crystals of cubic symmetry are described by three independent elastic constants which can be determined from the travel-times of elastic waves travelling through the crystal (see Eqns. 2.13-2.15). There are seven simple modes of propagation through a crystal of cubic symmetry. These are the compressional and shear modes propagating in the [100] and [111] directions, and the compressional and two independent shear modes propagating in the [110] direction. Only three of these modes need to be measured in order to determine the three independent elastic constants of a crystal of cubic symmetry.

The elastic properties of the crystals of orthorhombic symmetry are described by nine independent elastic constants. There are 18 relatively simple modes of propagation through crystals of this symmetry (see Eqn. 2.17). These are the compressional and two independent shear modes which propagate in the axial directions, and the shear waves and the quasi-shear and quasi-compressional waves which propagate in the $[110]_c$-type directions. The symmetry relations of the elastic stiffness matrix are such that the three on-diagonal shear-mode constants can be determined from the travel-times of waves propagating in two different axial directions (ie $C_{2323} = C_{3232}$). The symmetry relations of the elastic stiffness matrix also allow the same information to be gained from the quasi-shear mode and from the quasi-compressional mode propagating in the same direction.

In calculating the elastic constants from the travel-times determined at different pressures it is necessary to take into account

the effects of pressure on the length and density of the crystal. The calculations in the present study have been performed using Cook's algorithm for the separation of the effects due to variations in the elastic moduli from the effects due to static strains in crystals subjected to hydrostatic pressures. A detailed account of this procedure was originally given for crystals of cubic or hexagonal symmetry (Cook, 1957), however the algorithm can also be extended to accommodate crystals of orthorhombic symmetry. This treatment of the pressure dependence of the elastic moduli of an orthorhombic crystal requires the travel-times of 12 modes of propagation to be measured.

2.6.1 Cook's method for crystals of cubic symmetry

Consider a crystal having pairs of plane parallel faces, the direction of propagation of an ultrasonic pulse being perpendicular to the faces. The pressure P reduces the distance l_0 between the faces to

$$l(P) = l_0/s \qquad \text{where } s \geqq 1, \tag{2.33}$$

and the subscript 0 refers to zero pressure. In the case of a crystal with cubic symmetry, s is independent of the direction of propagation within the crystal. The density of such a crystal is

$$\rho(P) = \rho_o \, s^3 \tag{2.34}$$

where ρ_o is the zero-pressure density. The general equation for an adiabatic elastic modulus is

$$C = 4 \, (l_0)^2 \, \rho_o \, f^2 \, s \tag{2.35}$$

where f is the reciprocal of the round-trip travel-time.

The eigenvalues associated with wave propogation in the [100] direction of a cubic crystal are

$$C_{11} = 4\,\rho_o\,(l_{10})^2\,(f_1)^2\,s$$
$$C_{44} = 4\,\rho_o\,(l_{10})^2\,(f_4)^2\,s \qquad \text{with any polarization} \tag{2.36}$$

and for a wave propogating in the [011] direction

$$(C_{11} + C_{12} + 2C_{44})/2 = 4\,\rho_o\,(l_{20})^2\,(f_3)^2\,s$$
$$(C_{11} - C_{12})/2 = 4\,\rho_o\,(l_{20})^2\,(f_2)^2\,s \qquad \text{polarized in the } [0\bar{1}1] \text{ direction}$$
$$C_{44} = 4\,\rho_o\,(l_{20})^2\,(f_5)^2\,s \qquad \text{polarized in the [100] direction} \tag{2.37}$$

For a cubic crystal, the equation for the shortening of a length within the crystal due to increasing pressure can be expressed as

$$\frac{ds}{s\,dP} = S_{11}{}^T + 2S_{12}{}^T \tag{2.38}$$

where the $S_{ij}{}^T$ are the isothermal stiffnesses. These isothermal terms can be related to the adiabatic measurements (Nye, 1957)

$$\frac{ds}{s\,dP} = \left(1 + \frac{3\,\alpha^2\,T}{\rho_o\,c_p\,(S_{11} + 2S_{12})}\right)\,(S_{11} + 2S_{12})$$

$$= (1 + \Delta)(S_{11} + 2S_{12}) \tag{2.39}$$

for α, the linear thermal expansion coefficient and c_p, the specific heat. For crystals of cubic symmetry, the elastic stiffnesses in Eqn 2.39 are simply related to the elastic compliances

$$C_{11} + 2C_{12} = S_{11} + 2S_{12}. \tag{2.40}$$

The substitution of Eqns. 2.36 and 2.37 into Eqn. 2.39 enables the term s to be evaluated by numerical integration (ignoring the pressure dependence of the term Δ)

$$s = 1 + (1 + \Delta)\frac{1}{4\rho_o}\int_0^P \frac{dP}{3(l_{10})^2(f_1)^2 - 4(l_{20})^2(f_2)^2} \tag{2.41}$$

and used in Eqns. 2.36 and 2.37 to calculate the pressure dependence of the adiabatic elastic constants of a crystal of cubic symmetry.

2.6.2 Cook's method for crystals of orthorhombic symmetry

For a crystal of orthorhombic symmetry with pairs of faces cut perpendicular to the axes Ox, Oy, and Oz, the distances between the (100), (010), and (001) faces can be written as

$$l_1(P) = l_{10}/s_1$$
$$l_2(P) = l_{20}/s_2 \tag{2.42}$$
and $$l_3(P) = l_{30}/s_3 \qquad \text{for } s_1, s_2, s_3 \geq 1$$

respectively. For faces cut at 45° to two of the orthogonal axes and parallel to the third, the distances between the $(110)_c$, $(011)_c$, and $(101)_c$ faces can be written as

$$l_6(P) = \frac{\sqrt{2}\, l_{60}}{\sqrt{s_1^2 + s_2^2}} \quad , \quad l_4(P) = \frac{\sqrt{2}\, l_{40}}{\sqrt{s_2^2 + s_3^2}}$$

and
$$l_5(P) = \frac{\sqrt{2}\, l_{50}}{\sqrt{s_1^2 + s_3^2}} \tag{2.43}$$

respectively. The density of an orthorhombic crystal is

$$\rho(P) = \rho_o s_1 s_2 s_3, \tag{2.44}$$

and the equations for the adiabatic elastic constants are

$$\begin{aligned} C_{11} &= 4\ \rho_o\ (l_{10})^2\ (f_1)^2\ s_2 s_3 / s_1 \\ C_{55} &= 4\ \rho_o\ (l_{10})^2\ (f_5)^2\ s_2 s_3 / s_1 \\ C_{66} &= 4\ \rho_o\ (l_{10})^2\ (f_6)^2\ s_2 s_3 / s_1, \end{aligned} \tag{2.45}$$

and
$$\begin{aligned} C_{22} &= 4\ \rho_o\ (l_{20})^2\ (f_2)^2\ s_1 s_3 / s_2 \\ C_{44} &= 4\ \rho_o\ (l_{20})^2\ (f_{11})^2\ s_1 s_3 / s_2 \\ C_{66} &= 4\ \rho_o\ (l_{20})^2\ (f_{12})^2\ s_1 s_3 / s_2, \end{aligned} \tag{2.46}$$

and
$$\begin{aligned} C_{33} &= 4\ \rho_o\ (l_{30})^2\ (f_3)^2\ s_1 s_2 / s_3 \\ C_{44} &= 4\ \rho_o\ (l_{30})^2\ (f_4)^2\ s_1 s_2 / s_3 \\ C_{55} &= 4\ \rho_o\ (l_{30})^2\ (f_{10})^2\ s_1 s_2 / s_3, \end{aligned} \tag{2.47}$$

and
$$K_{12} = 8\ \rho_o\ (l_{60})^2\ (f_7)^2\ s_1 s_2 s_3 / (s_1^2 + s_2^2) \tag{2.48}$$
$$K_{13} = 8\ \rho_o\ (l_{50})^2\ (f_8)^2\ s_1 s_2 s_3 / (s_1^2 + s_3^2) \tag{2.49}$$
$$K_{23} = 8\ \rho_o\ (l_{40})^2\ (f_9)^2\ s_1 s_2 s_3 / (s_2^2 + s_3^2), \tag{2.50}$$

where f_i is the reciprocal of the round-trip travel-time. The relationships for K_{ij} (Eqns. 2.48, 2.49 and 2.50) hold for the travel-times of either the quasi-shear or the quasi-compressional modes measured in each direction. The redundancy in the measurement of the shear modes C_{ii} (i=4,5,6) allows the introduction of the relationships

$$\frac{(l_{10})\ (f_6)}{(l_{20})\ (f_{12})} = \frac{s_1}{s_2} = \lambda_6$$

$$\frac{(l_{10})\ \ (f_5)}{(l_{30})\ (f_{10})} = \frac{s_1}{s_3} = \lambda_5$$

$$\frac{(l_{20})\ (f_{11})}{(l_{30})\ (f_4)} = \frac{s_2}{s_3} = \lambda_4. \qquad (2.51)$$

from Eqns. 2.45, 2.46 and 2.47. The substitution of these equalities in Eqns 2.45-2.50 allows the modulus for each mode to be expressed in terms of either s_1, s_2 or s_3 only. It follows from the form of the expressions

$$C_{12} = \sqrt{(C_{22} + \lambda_6^2 C_{66} - (1+\lambda_6^2)K_{12})(\lambda_6^2 C_{11} + C_{66} - (1+\lambda_6^2)K_{12})}/\lambda_6 - C_{66}$$

$$C_{13} = \sqrt{(C_{33} + \lambda_5^2 C_{55} - (1+\lambda_5^2)K_{13})(\lambda_5^2 C_{11} + C_{55} - (1+\lambda_5^2)K_{13})}/\lambda_5 - C_{55}$$

$$C_{23} = \sqrt{(C_{33} + \lambda_4^2 C_{44} - (1+\lambda_4^2)K_{23})(\lambda_4^2 C_{22} + C_{44} - (1+\lambda_4^2)K_{23})}/\lambda_4 - C_{44}.$$

(2.52)

relating the C_{ij} $(i \neq j)$ to the moduli of the measured modes that <u>each</u> of the C_{ij} (whether or not i=j) may be expressed as the product of any one of the unknown s_k (k=1,2 or 3) and a corresponding function F_k of the known zero-pressure density and dimensions and the mode frequencies. Thus each of the C_{ij} is expressible in the form

$$C = s_k\ F_k(\rho_o, l_{jo}(j=1,2...6), f_j(j=1,2...6)) \qquad (2.53)$$

The application of hydrostatic pressure causes independent

shortening of each of the directions parallel to the orthogonal axes of the orthorhombic lattice. This shortening due to isothermal compression can be expressed as

$$\frac{ds_i}{s_i\ dP} = \sum_{j=1}^{3} S_{ij}^T \qquad i=1,2,3 \qquad (2.54)$$

where the S_{ij}^T are the isothermal elastic compliance terms. The relationship between the measured adiabatic compliance terms and the isothermal terms is (Nye, 1957)

$$\sum_{j=1}^{3} S_{ij}^T = \left(1 + \frac{\alpha_i \sum_{j=1}^{3} \alpha_j \quad T}{\rho_o\ c_p \sum_{j=1}^{3} S_{ij}} \right) \sum_{j=1}^{3} S_{ij} \qquad i=1,2,3 \qquad (2.55)$$

for α_i, the thermal linear expansion in directions Ox, Oy, and Oz, and c_p, the specific heat, and thus Equation 2.53 becomes

$$\frac{ds_i}{s_i\ dP} = (1 + \Delta_i) \sum_{j=1}^{3} S_{ij} \qquad i=1,2,3. \qquad (2.56)$$

The compliance matrix S_{ij} is simply the inverse of the stiffness matrix C_{ij}, and the elastic compliance terms can easily be related to the elastic stiffnesses:

$$S_{11} = (C_{22}C_{33} - C_{23}C_{23})/\Gamma$$
$$S_{12} = (C_{13}C_{23} - C_{12}C_{33})/\Gamma$$
$$S_{13} = (C_{12}C_{23} - C_{13}C_{22})/\Gamma$$
$$S_{22} = (C_{11}C_{33} - C_{13}C_{13})/\Gamma$$
$$S_{23} = (C_{13}C_{12} - C_{11}C_{23})/\Gamma$$
$$S_{33} = (C_{11}C_{22} - C_{12}C_{12})/\Gamma$$

and
$$S_{44} = C_{44}^{-1}$$
$$S_{55} = C_{55}^{-1} \qquad (2.57)$$
$$S_{66} = C_{66}^{-1}$$

where $\Gamma = C_{11}C_{22}C_{33} - C_{11}C_{23}C_{23} - C_{33}C_{12}C_{12} + 2C_{12}C_{13}C_{23} - C_{22}C_{13}C_{13}$.

These pressure dependent values of s_i can now be substituted into Eqns. 2.45-2.52 to calculate the elastic moduli C_{ij} over the 3 GPa pressure range.

2.7 Curve fitting and estimation of errors

Successively higher-order polynomials were fitted to the compressional- or shear-mode moduli calculated with Cook's algorithm, using a multiple linear regression technique (Bevington, 1969) and an F-test (with a 99.5% confidence level) to test the statistical significance of each added term. At this confidence level a polynomial of at least second order was required to fit the modulus - pressure data for every mode. These polynomials were restricted to quadratics as the calibration of the manganin pressure gauge is not sufficiently accurate to justify inclusion of higher order terms. This produces a quadratic of the form

$$C = a_0 \pm \sigma_t(a_0) + (a_1 \pm \sigma_t(a_1))\, P + (a_2 \pm \sigma_t(a_2))\, P^2 \qquad (2.58)$$

where the uncertainties $\sigma_t(a_i)$ in the parameters a_i reflect the departures of the data from the model.

The variances in the terms a_i (i=0,1,2) for each such quadratic were calculated from

$$\sigma^2(a_i) = (\sigma_t(a_i))^2 + (\partial a_i/\partial L_0)^2\ \sigma^2(L_0) + (\partial a_i/\partial \rho_0)^2\ \sigma^2(\rho_0) + (\partial a_i/\partial \alpha_1)^2\ \sigma^2(\alpha_1) + (\partial a_i/\partial \alpha_2)^2\ \sigma^2(\alpha_2) \quad (2.59)$$

(Jackson and Niesler, 1982) where

$$\partial a_i/\partial L_0 = 2a_i/L_0$$

and

$$\partial a_i/\partial \rho_0 = a_i/\rho_0. \quad (2.60)$$

The last two terms in Eqn. 2.61 are associated with the uncertainties in the calibration of the manganin gauge. The partial derivatives can be calculated from the polynomial expansions of the moduli as functions of the manganin resistance, which in turn is a function of pressure, to give;

$$\partial a_0/\partial \alpha_1 = 0 \qquad \partial a_0/\partial \alpha_2 = 0$$

$$\partial a_1/\partial \alpha_1 = a_1/\alpha_1 \qquad \partial a_1/\partial \alpha_2 = 0$$

$$\partial a_2/\partial \alpha_1 = a_2/\alpha_1 - a_1\ \alpha_2/(\alpha_1)^2 \qquad \partial a_2/\partial \alpha_2 = a_1/\alpha_1 \quad (2.61)$$

The elastic constants C_{ij} $i \neq j$, which can only be obtained via a combination of the simple C_{ii} modes and the K_{ij} modes were calculated from the measured travel-times of the K_{ij} modes and the quadratics which have been fitted to the other modes (ie C_{ii}) involved, with the errors in the fits of the quadratics being propagated through the calculation of the C_{ij} $(i \neq j)$ quadratics.

CHAPTER 3

PRESSURE-INDUCED SHEAR-MODE SOFTENING AND PHASE TRANSFORMATIONS

3.1 Introduction: criteria for lattice stability

The stability of a crystal lattice relative to all alternative configurations attainable by infinitesimal homogeneous deformations requires the strain energy density $C_{ij}\varepsilon_i\varepsilon_j/2$ to be positive definite. This condition, known as the Born stability criterion (Born, 1940), is met if each of the principal minors of the elastic stiffness matrix is positive.

It is important to emphasize that the Born criterion is a necessary but not sufficient condition for the stability of a lattice. It obviously does not guarantee stability relative to alternative configurations which may be attained by infinitesimal non-homogeneous deformations, or by finite deformation of the lattice. Thus ferroelectric transitions, which occur as one of the optic mode

frequencies approaches zero, involve no anomalous behaviour of the elastic moduli which are associated with long wavelength acoustic modes. In some special cases, the transformational strain may take the form of a finite shear (as in the B1-B2 transformation discussed below) or alternatively the transformation may require complete disruption of the lattice and proceed by a nucleation and growth mechanism. The large atomic displacements required by both of these transformation mechanisms are beyond the scope of elasticity theory and the vanishing of a principal minor of the stiffness matrix would not be expected.

The sufficient condition for the stability of a particular crystal structure under given conditions of temperature and pressure is that the Gibbs free energy be a minimum relative to all alternative configurations. The positive strain energy density condition (ie the Born criterion) for the mechanical stability of a lattice against infinitesimal homogeneous deformations is a special case of the more general thermodynamic stability criterion.

Of particular importance in this chapter are phase transformations which may be accomplished by a finite shear deformation of the original structure. For crystal structures which are related in this way, any reduction (softening) of the appropriate shear modulus (for example with increasing pressure) will reduce both the free energy of the deformed lattice relative to the original lattice and the height of the energy barrier between the two phases. Such pressure-induced shear-mode softening might therefore have implications for the nature and kinetics of high pressure phase transformations.

3.2 Shear-mode softening and B1 lattice instability

General relationships for the elastic moduli of crystals with cubic symmetry can be obtained from simple static lattice calculations. Weidner and Simmons (1972) formulated equations for the elastic moduli of a B1 lattice for a general interatomic central-force model with nearest-neighbour and next-nearest-neighbour interactions, to obtain the following relationships for the moduli C_{11}, C_{12} and C_{44}, the bulk modulus K and hydrostatic pressure P:

$$C_{11} = \frac{1}{r}\left(f(r) + g(r\sqrt{2}) - \frac{G(r\sqrt{2})}{r\sqrt{2}}\right) + \frac{\alpha(C_{11})}{r^4} \qquad (3.1)$$

$$C_{12} = P + \frac{1}{2r}\left(g(r\sqrt{2}) + \frac{G(r\sqrt{2})}{r\sqrt{2}}\right) + \frac{\alpha(C_{44})}{r^4} \qquad (3.2)$$

$$C_{44} = -P + \frac{1}{2r}\left(g(r\sqrt{2}) + \frac{G(r\sqrt{2})}{r\sqrt{2}}\right) + \frac{\alpha(C_{44})}{r^4} \qquad (3.3)$$

$$K = \frac{2}{3}P + \frac{1}{3r}\left(f(r) + 2\,g(r\sqrt{2})\right) + \frac{\alpha(K)}{r^4} \qquad (3.4)$$

$$P = \frac{1}{r^2}\left(F(r) + \sqrt{2}G(r\sqrt{2})\right) + \frac{\alpha(P)}{r^4}\,, \qquad (3.5)$$

where r is the anion-cation distance and α represents the Madelung-type summations of the electrostatic contributions. The interatomic forces between anions and cations are represented by the general force relationships

$$f(r) = -(\partial f^*_{ij}/\partial r_{ij})(r_{ij})$$

and $$F(r) = f^*_{ij}(r_{ij}), \tag{3.6}$$

and between anions and anions;

$$g(r\sqrt{2}) = -(\partial f^*_{ij}/\partial r_{ij})(r_{ij})$$

and $$G(r\sqrt{2}) = f^*_{ij}(r_{ij}) \tag{3.7}$$

for f^*, the non-electrostatic force between atoms. Substitution of Eqn. 3.5 into Eqn. 3.3 yields

$$r^2\, C_{44}(P) = \frac{\alpha(C_{44}) - \alpha(P)}{r^2} - F(r) + \frac{1}{2}\left(r\, g(r\sqrt{2}) - \frac{3G(r\sqrt{2})}{\sqrt{2}}\right) \tag{3.8}$$

where the nearest-neighbour repulsive forces contribute negatively, and the electrostatic attraction and next-nearest-neighbour repulsion contribute positively to $C_{44}(P)$. For a simplified central-force model in which $F(r)$ and $G(r)$ both have the same form $\sim A(r_o/r)^{-n}$, Eqns. 3.6 and 3.7 become

$$f(r) = -\frac{\partial F}{\partial r} = n\frac{F(r)}{r},$$

and $$g(r\sqrt{2}) = n\frac{G(r\sqrt{2})}{r\sqrt{2}} \tag{3.9}$$

For this simple model, the modulus $C_{44}(P)$ (Eqn. 3.8) becomes

$$r^2\ C_{44}(P) = \frac{\alpha(C_{44}) - \alpha(P)}{r^2} - F(r) + (n-3)\frac{G(r\sqrt{2})}{2\sqrt{2}} \tag{3.10}$$

$$= \frac{\alpha(C_{44}) - \alpha(P)}{r^2} - A(r_o/r)^n\left(1 - \frac{n-3}{2^{(n+3)/2}}\right). \tag{3.11}$$

For all plausible values of n ($3 < n < 12$) (see Anderson and Liebermann, 1970), the negative nearest-neighbour contribution to $C_{44}(P)$ is off-set only slightly by the positive contribution of the next-nearest-neighbour repulsion. Equation 3.11 illustrates that for $n \geq 3$, the negative contribution from the nearest-neighbour repulsive forces will increase in magnitude at a faster rate with increasing pressure (decreasing r) than the electrostatic contribution. Thus, the pressure derivative of the modulus C_{44} in this simple model will decrease with increasing pressure and eventually become negative. Anderson and Liebermann (1970) considered electrostatic forces and nearest-neighbour interactions of the form $A(r_o/r)^{-n}$, and found

$$\left.\frac{\partial C_{44}}{\partial P}\right|_0 = \frac{5.776 - n}{n - 1} \qquad (3.12)$$

where $\partial C_{44}/\partial P$ is small and positive for $n < 5.776$, becoming negative for larger n. The magnitude of the term n is defined by the pressure dependence of the bulk modulus, with $\partial K/\partial P=(n+7)/3$. Demarest (1972) fitted the known pressure dependence of the elastic moduli of a number of alkali halides to a central-force model which included not only electrostatic and nearest-neighbour forces, but also a next-nearest-neighbour Lennard-Jones interaction. The next-nearest-neighbour contribution to the pressure dependence of the modulus C_{44} in this model ranged from the negligibly small terms predicted in Eqn. 3.11 for the simplified central-force model, to half the absolute magnitude of the negative nearest-neighbour contribution. These central force models indicate the likelihood of C_{44} mode softening at sufficiently high pressures for any B1 structure. Such reduction in the magnitude of C_{44} will tend to increase the thermodynamic competitiveness of any structure related to B1 by C_{44}-controlled shear deformation.

The B2 phase to which most B1-structured alkali halides transform at sufficiently high pressures is a case in point. Demarest et al. (1977) have shown that this transition can be accomplished by compression of the B1 lattice along the [111] axis. This mode of compression is a simple combination of finite ε_4-type shears (see Fig. 3.1). Demarest et al.'s (1977) simple model for the energy of a continuously deforming B1 lattice results in a relationship for the Gibbs free energy of the deformed lattice as a function of strain. This energy is calculated for a central-force model, with the energy of the lattice being given by

$$U = \frac{z^2 e^2 A_r}{r} + \sum_{i=1}^{8} \frac{b}{r_i^n} \qquad (3.13)$$

where z is the ionicity term, e is the charge on each atom, A_r is the Madelung-like sum for the B1 and B2 phases and the intermediate states between these two phases, and r_i is the interatomic distance. The repulsive term is summed over the six nearest-neighbours in the B1 lattice and the extra two atoms which become the additional nearest-neighbours in the B2 lattice. The height of the energy barrier between the two states was found to be proportional to C_{44}/K. Therefore it is instructive to observe the behaviour of this ratio $\Upsilon = C_{44}/K$ for the alkali halides as they approach the B1→B2 transition. The model of Demarest et al. (1977) suggests a critical value for Υ of 0.15-0.20 associated with the pressure induced phase transformation of the alkali halides.

Of the B1 structured oxides, SrO and CaO are known to undergo the B1→B2 transformation at high pressures. Values of C_{44}, C_{44}/K and $\partial(C_{44}/K)/\partial P$ for the alkali halides and these simple oxides are

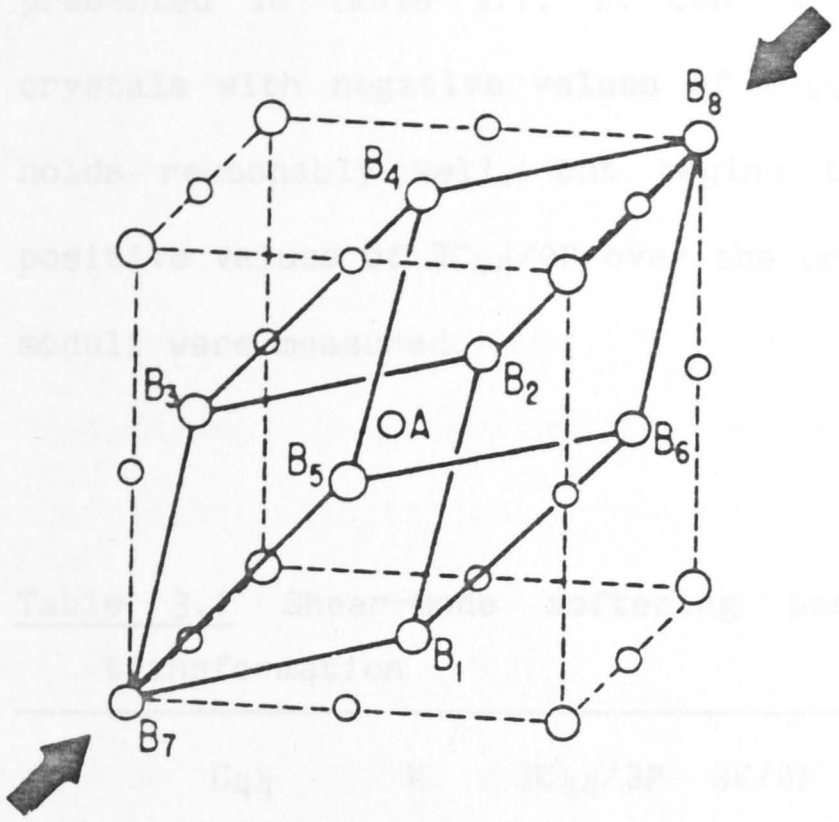

NaCl

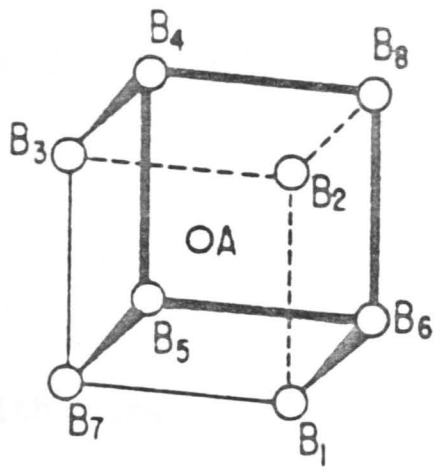

CsCl

Figure 3.1 Transformation from the B1(NaCl) to the B2(CsCl) lattice by compression along [111] (after Demarest et al., 1977).

presented in Table 3.1. It can be seen from this table, that for crystals with negative values of $\partial C_{44}/\partial P$, Demarest et al.'s criterion holds reasonably well, but begins to fail for crystals which have positive values of $\partial C_{44}/\partial P$ over the pressure range in which the elastic moduli were measured.

Table 3.1 Shear-mode softening associated with the B1→B2 phase transformation

	C_{44} GPa	K GPa	$\partial C_{44}/\partial P$	$\partial K/\partial P$	C_{44}/K	$\partial(C_{44}/K)/\partial P$ GPa^{-1}	P_{tr}* GPa	Ref.
RbI	2.79	11.09	-0.49	5.41	0.25	-0.17	0.4	1,2
RbBr	3.84	13.66	-0.56	5.30	0.28	-0.15	0.4	1,2
RbCl	4.75	16.30	-0.61	5.35	0.29	-0.13	0.5	1,2
KI	3.73	12.15	-0.23	5.10	0.31	-0.15	1.7	3,4
KBr	5.08	14.86	-0.33	5.38	0.34	-0.15	1.7	5,4
KCl	6.33	17.89	-0.41	4.78	0.35	-0.12	1.9	6,4
KF	12.81	31.13	-0.45	5.02	0.41	-0.081	4	7,8
NaCl	12.80	25.21	0.37	5.26	0.51	-0.091	30	9,10
NaF	28.22	48.20	0.21	5.18	0.59	-0.059	27	11,12
SrO	55.87	91.21	-0.21	5.18	0.61	-0.037	36	13,14
CaO	80.32	112.50	0.20	4.83	0.71	-0.029	65	13,15
MgO	155.8	162.5	1.11	4.13	0.96	-0.018	>200	16,17

* B1→B2 transformation pressures at room temperature.

References:

1. Chang and Barsch, 1971;2. Pistorious, 1965a;3. Barsch and Shull, 1971;4. Pistorious, 1965b;5. Reddy and Ruoff, 1965;6. Demarest et al., 1977;7. Koliwad et al., 1967;8. Yagi et al., 1978;9. Spetzler et al., 1972;10. Bassett et al., 1968;11. Bartels and Schuele, 1965;12. Yagi et al., 1983;13. Chang and Graham, 1977;14 Sato and Jeanloz, 1981;15. Jeanloz et al., 1979;16. Jackson and Niesler, 1982;17. Vassilou and Ahrens, 1981;18. present study and Sumino, 1979;19. Akimoto et al., 1967.

There exists another class of simple oxides, the transition metal monoxides, which experience shear-mode softening prior to a phase change. Each of these oxides undergoes a paramagnetic→antiferromagnetic phase change with decreasing temperature, at room pressure. A slight lattice distortion accompanies this phase change. In the case of CoO, this distortion is tetragonal, but NiO, MnO and FeO all experience a rhombohedral distortion equivalent to compression along the [111] axis. Measurements of the elastic constants of MnO (Cracknell and Evans, 1970;Seino, 1982;Sumino et al., 1980) and $Fe_{1-x}O$ (Berger et al. 1983) have been performed over a range of temperatures from ~300 K to the respective Néel temperatures (118 K and 189 K) at which the paramagnetic→antiferromagnetic phase change occurs. Each of these studies showed normal behaviour of the moduli C_{11} and $(C_{11}-C_{12})/2$. For both MnO and $Fe_{1-x}O$ however, the onset of shear-mode softening of the modulus C_{44} was observed about 100 K above the respective Néel temperatures.

The high pressure polymorphism of the transition metal monoxides is of considerable current interest in connection with element partitioning among the ferromagnesian phases of the Earth's lower mantle and the solubility of oxygen in the Earth's outer core (e.g. Ringwood, 1977;McCammon et al., 1983). Of particular importance is the evidence for a shock-induced phase transformation in wüstite ($Fe_{0.94}O$) near 70 GPa (Jeanloz and Ahrens, 1980). This phase transformation appears to involve a density increase of 5-9% of the 70 GPa density, or 10-28% of the zero pressure density. However, the nature of this high-pressure phase remains uncertain.

Navrotsky and Davies (1981) have predicted the transformation pressure of FeO from thermochemical systematics. Their preferred

transformation to the hexagonal NiAs(B8) phase is calculated to occur for a pressure ~30 GPa, while the CsCl(B2) transformation favoured by Jeanloz and Ahrens (1980) is predicted to occur for pressures ~300 GPa. Jackson and Ringwood (1981) have discussed the possibilities of a B1→B8 transition accompanied by spin-pairing. Static compression studies, however, have revealed only an essentially rhombohedral distortion of the B1 phase at pressures above 5-12 GPa (Zou et al. 1981; Heinz and Jeanloz, 1983; Yagi et al., 1985). It is possible that this high-pressure distortion has the same origin as that accompanying the paramagnetic→antiferromagnetic transition observed at low temperatures.

In view of the current state of confusion concerning both the elastic properties (e.g. Sumino et al., 1980;Berger et al., 1981: Jeanloz and Hazen, 1983) and the high-pressure polymorphism of wüstite, and the wide range of possible structural, electronic and magnetic transitions, it seems that a systematic study of the high pressure behaviour of the transition-metal monoxides might be fruitful. Accurate equations of state derived from high pressure ultrasonic measurements of the B1 phases will help in the interpretation of static and shock compression data. Furthermore, any pressure-induced shear-mode softening might provide insight into possible modes of transformation. As part of this broader program, the three independent elastic moduli of MnO have been measured to 3 GPa.

3.3 The elasticity of MnO

3.3.1 Specimen description

A large single crystal of MnO was kindly made available by Professor T.J. Ahrens of the California Institute of Technology. This crystal was opaque with a metallic-black lustre. Pairs of parallel (±0.5°) (100) and (011) faces were prepared, leaving a crystal with the dimensions 7.803±0.003 mm, 6.035±0.003 mm, and ~8 mm in the [100], [011] and [01$\bar{1}$] directions respectively (see Figure 3.2). The density of the crystal was measured to be 5.346±0.004 g cm^{-3}. This is slightly less than the X-ray density of 5.365 g cm^{-3} (Sumino et al., 1980). This low measured density was due to the presence of ~4% (volume) Mn_3O_4 which was observed with both reflected light microscopy and electron-microprobe analysis as thin (~5 μm × ~30 μm) bone shaped surface features lying in axial orientations.

3.3.2 Data reduction

The elastic moduli were calculated using Cook's (1957) algorithm to determine the isothermal length and density changes for a crystal of cubic symmetry (see Chapter 2) due to increasing hydrostatic pressure. The coefficient of linear thermal expansion used in this calculation was

$$\alpha = 11.5\times10^{-6}\ K^{-1} \qquad (3.14)$$

from Suzuki et al. (1979), and the specific heat was taken as

$$c_p = 617\ J\ kg^{-1}\ K^{-1} \qquad (3.15)$$

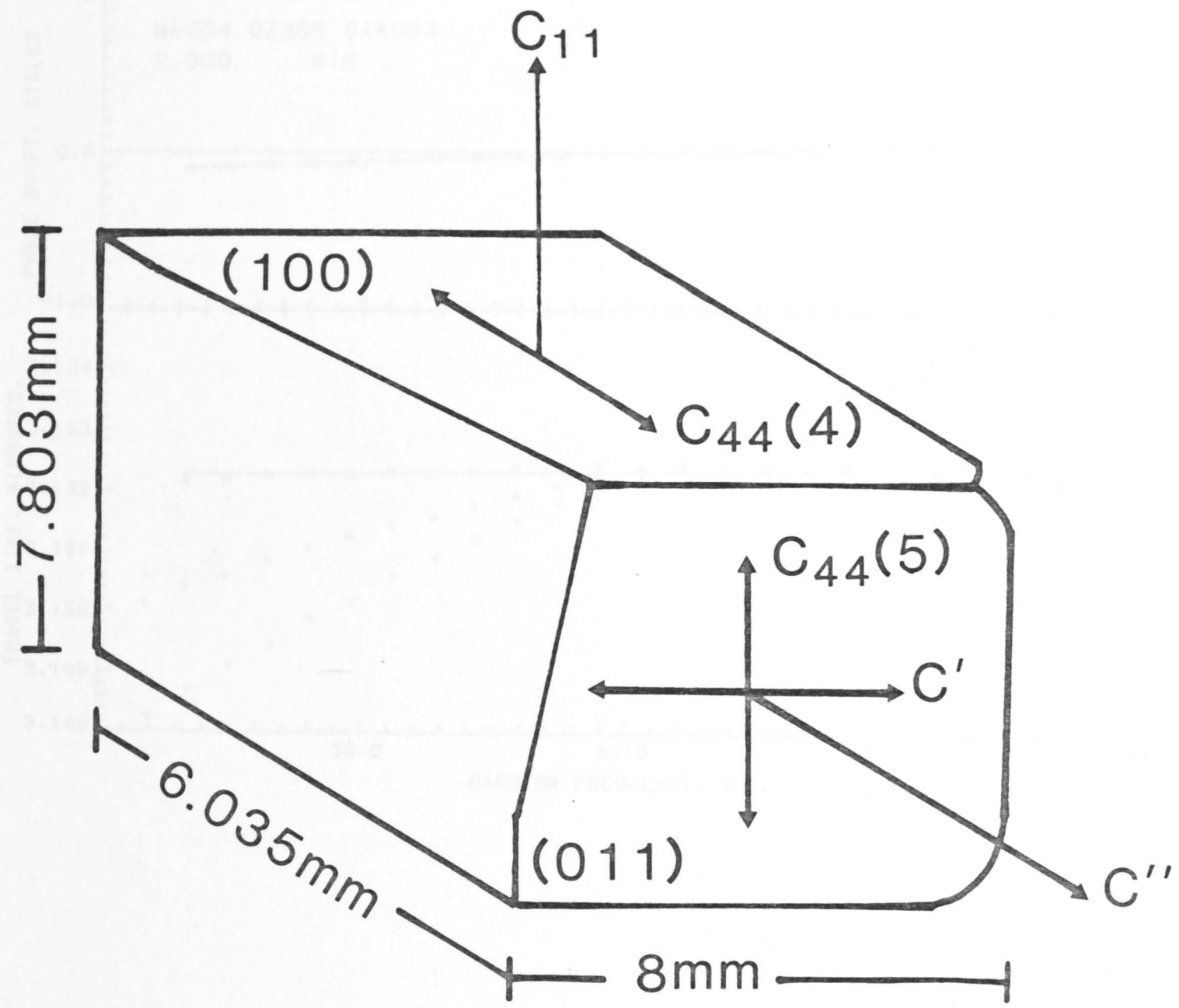

$$C' = (C_{11} - C_{12})/2$$

$$C'' = (C_{11} + C_{12} + 2C_{44})/2$$

MnO

Figure 3.2 Propagation and polarization directions for the elastic moduli of MnO.

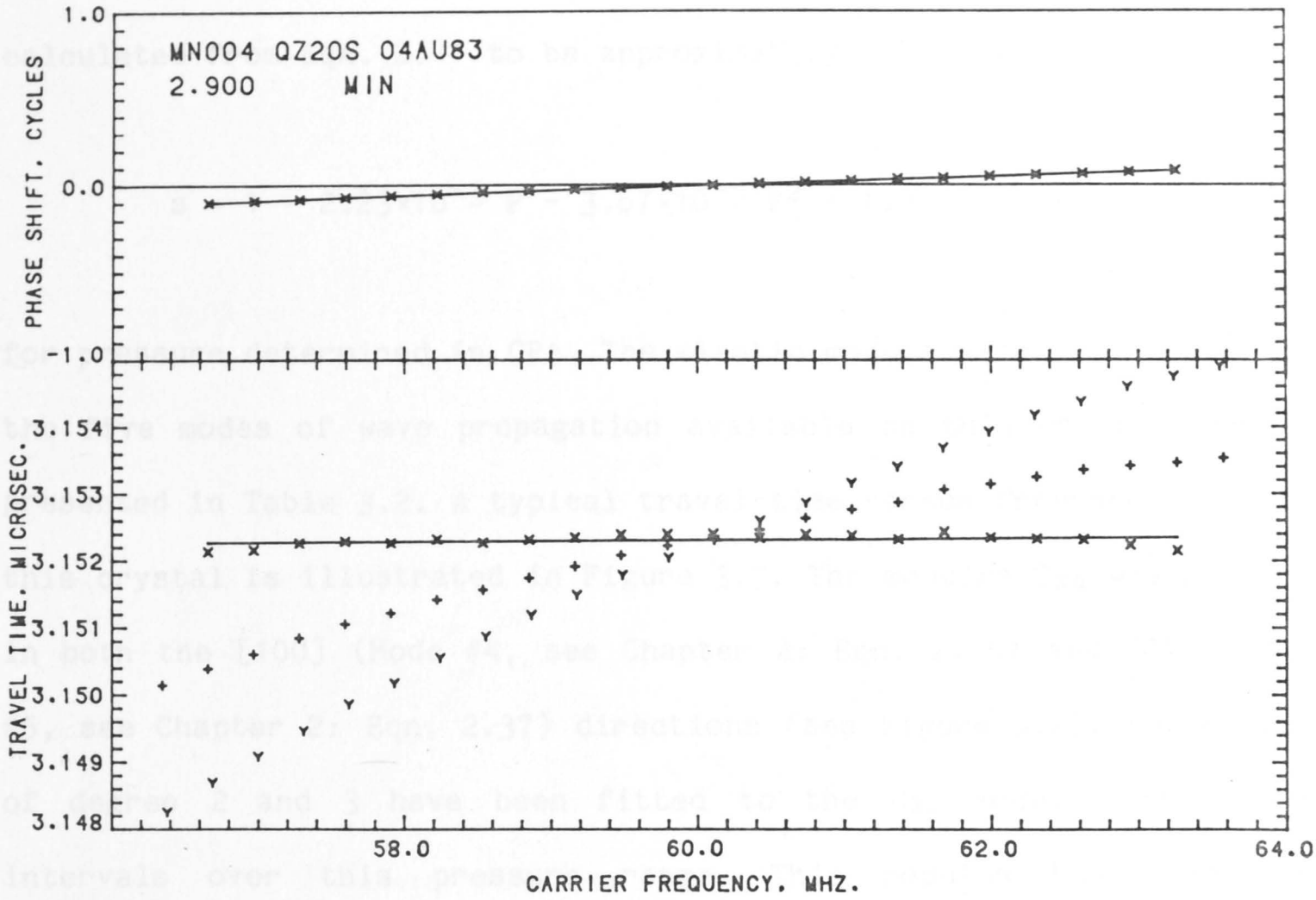

Figure 3.3 Phase comparison data at 2.90 GPa for the shear modulus $C_{44}(4)$ of MnO.

from JANAF Thermochemical Tables (1971). The length correction term was calculated from Eqn. 2.41 to be approximately

$$s = 1 + 2.23\times10^{-3}\ P - 3.67\times10^{-5}\ P^2 + 1.98\times10^{-6}\ P^3 \qquad (3.16)$$

for pressure determined in GPa. The elastic moduli were calculated from the five modes of wave propagation available on this crystal and are presented in Table 3.2. A typical travel-time versus frequency plot for this crystal is illustrated in Figure 3.3. The modulus C_{44} was measured in both the [100] (Mode #4, see Chapter 2: Eqn. 2.36) and [011] (Mode #5, see Chapter 2: Eqn. 2.37) directions (see Figure 3.2). Polynomials of degree 2 and 3 have been fitted to the C_{44} moduli measured at intervals over this pressure range. This modulus has also been calculated as a combination of the moduli associated with the the modes C_{11}, $(C_{11}-C_{12})/2$ and $(C_{11}+C_{12}+2C_{44})/2$.

The large differences between the pressure dependence of the modulus C_{44} calculated form the combination of C_{11}, C' and C'', and the dependence of the measured C_{44} modes are due to the difficulty in fitting a quadratic (or cubic) to the measured observed variation of C_{44} with pressure. The zero pressure measurements and the pressure dependences of the moduli $C_{44}(4)$ and $C_{44}(5)$ agree within the quoted errors for either the quadratic or cubic fits. The pressure dependences of these moduli are illustrated in Figures 3.4 and 3.5.

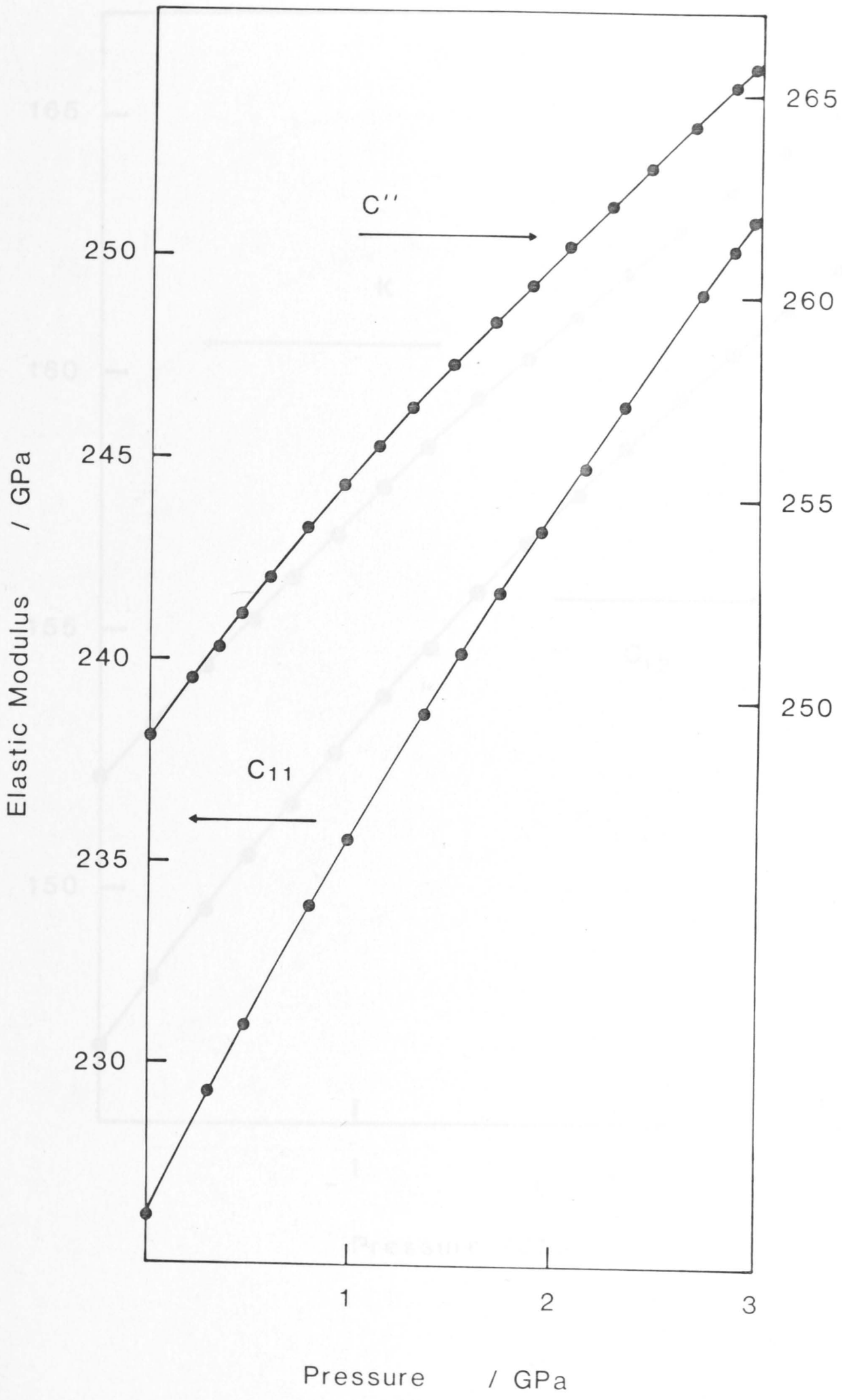

Figure 3.4a The variation with pressure of the compressional moduli C_{11} and C" of MnO. The uncertainties in modulus are everywhere less than the diameter of the plotting symbols.

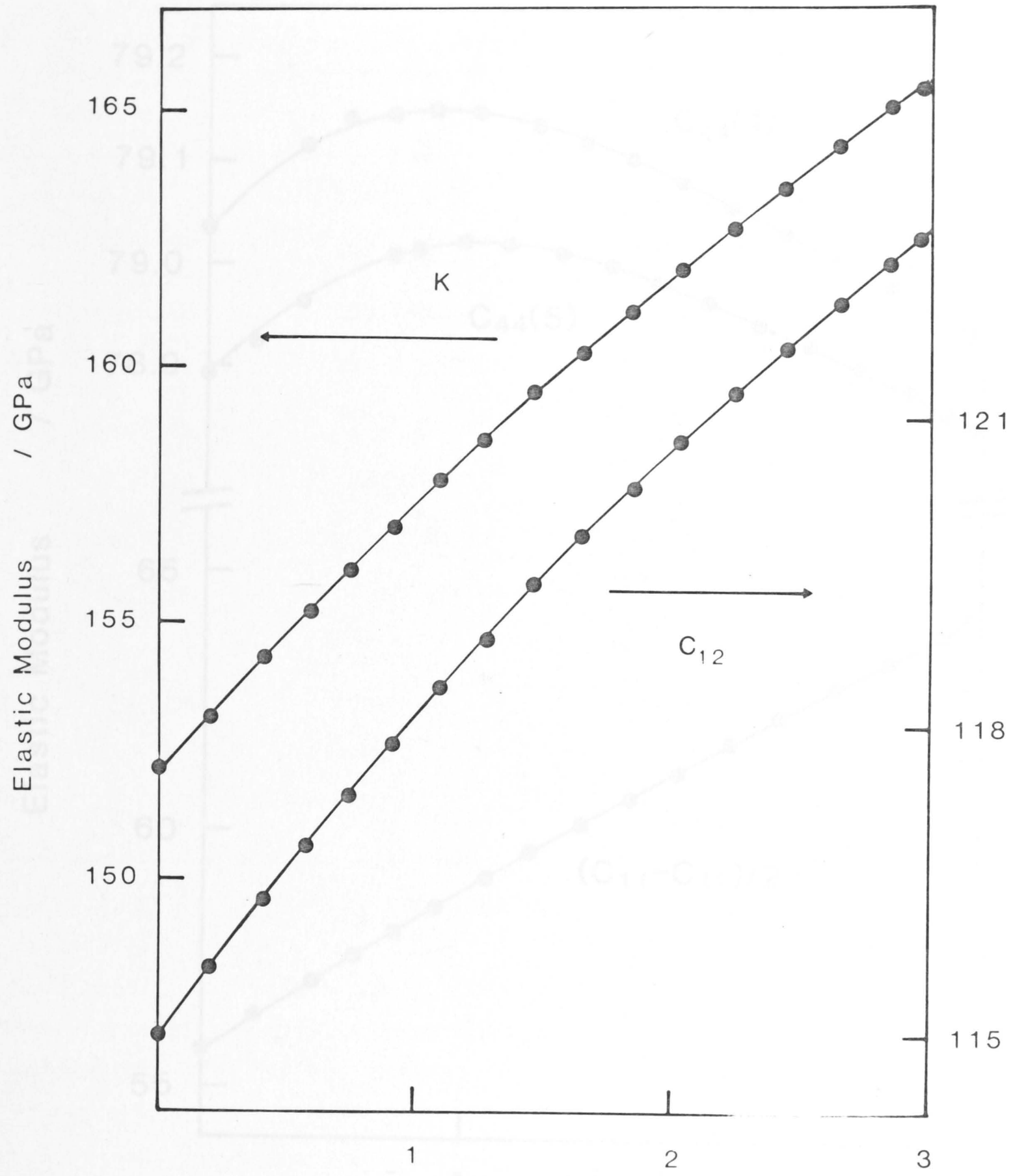

Figure 3.4b The variation with pressure of the modulus C_{12} and the bulk modulus of MnO. The uncertainties in modulus are everywhere less than the diameter of the plotting symbols.

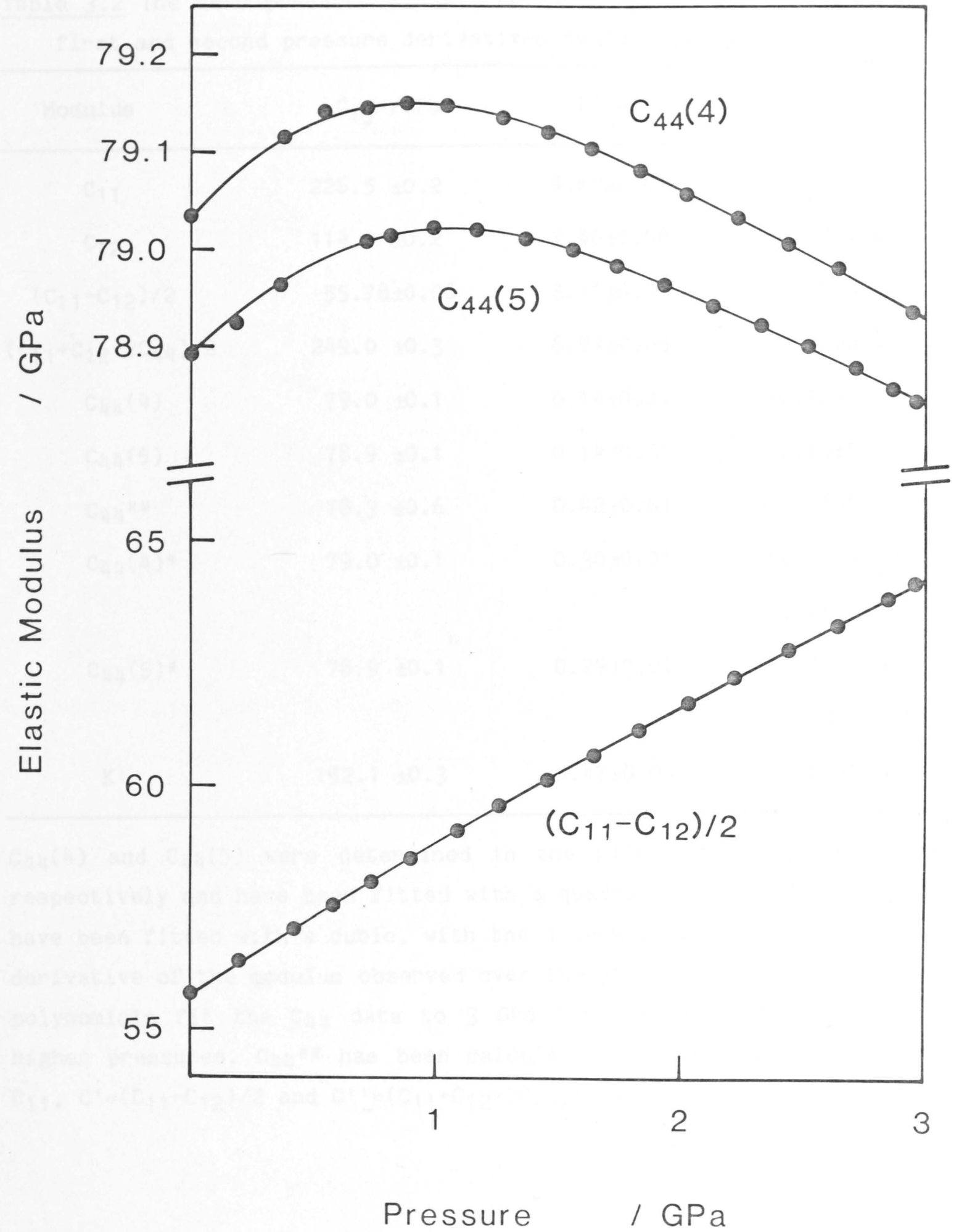

Figure 3.5 The variation with pressure of the shear moduli $C_{44}(4)$, $C_{44}(5)$ and C' of MnO. The uncertainties in modulus are everywhere less than the diameter of the plotting symbols.

Table 3.2 The zero pressure elastic moduli of MnO together with their first and second pressure derivatives calculated at zero pressure.

Modulus	C_{ij} /GPa	$\partial C/\partial P$	$\partial^2 C/\partial P^2$ /GPa^{-1}
C_{11}	226.5 ±0.2	9.63±0.07	-0.94±0.06
C_{12}	114.9 ±0.2	3.40±0.08	-0.52±0.08
$(C_{11}-C_{12})/2$	55.78±0.06	3.11±0.02	-0.21±0.01
$(C_{11}+C_{12}+2C_{44})/2$	249.0 ±0.3	6.94±0.05	-0.91±0.05
$C_{44}(4)$	79.0 ±0.1	0.14±0.01	-0.12±0.02
$C_{44}(5)$	78.9 ±0.1	0.14±0.01	-0.10±0.02
C_{44}**	78.3 ±0.6	0.42±0.01	-0.18±0.02
$C_{44}(4)$*	79.0 ±0.1	0.30±0.01	-0.40±0.02
			0.18±0.03†
$C_{44}(5)$*	78.9 ±0.1	0.29±0.01	-0.36±0.02
			0.18±0.03†
K	152.1 ±0.3	5.47±0.09	-0.66±0.05

$C_{44}(4)$ and $C_{44}(5)$ were determined in the [100] and [011] directions respectively and have been fitted with a quadratic. $C_{44}(4)$* and $C_{44}(5)$* have been fitted with a cubic, with the † term being the third pressure derivative of the modulus observed over the 3 GPa pressure range. These polynomials fit the C_{44} data to 3 GPa but cannot be extrapolated to higher pressures. C_{44}** has been calculated from a combination of the C_{11}, $C'=(C_{11}-C_{12})/2$ and $C''=(C_{11}+C_{12}+2C_{44})/2$ moduli.

The room pressure elastic constants of MnO which have previously been measured by Oliver (1969) using the echo overlap technique, Uchida and Sato (1973) using both the pulse superposition and echo overlap techniques, and Sumino (1980) using the rectangular parallelopiped resonance technique, are tabulated in Table 3.3. The elastic moduli determined in these previous studies are comparable (±7%) with the present measurements.

Table 3.3 The zero pressure elastic moduli of MnO.

Modulus GPa	Sumino et al. (1980)	Uchida and Saito (1973)	Oliver (1969)	Present Study
C_{11}	233 ±3	222 ±1	223± 6	226.5 ±0.2
C_{12}	122 ±4	110 ±2	120±10	114.9 ±0.2
$(C_{11}-C_{12})/2$	55.8±0.2	56.1±0.9	52± 5	55.78±0.06
$(C_{11}+C_{12}+2C_{44})/2$	257 ±4	244 ±2	251± 8	249.0 ±0.3
C_{44}	79.4±0.2	78 ±3	79± 2	78.9 ±0.1
K	159 ±4	147 ±3	154±19	152.1 ±0.3

The anomalous high-pressure behaviour of the modulus C_{44} is of particular interest. It is evident from Table 3.2 and from Figure 3.5 that C_{44} increases at a modest rate with increasing pressure, attains a maximum value near 1 GPa, and thereafter decreases with further increase of pressure. Such mode softening is indicative of lattice instability at sufficiently high pressures of the paramagnetic B1 phase of MnO (eg Born, 1940;Demarest et al., 1977). The connection between the observed shear-mode softening and high-pressure lattice instability will be discussed in Section 3.5 below.

3.3.3 Elasticity systematics among the transition-metal monoxides

The present elastic moduli of MnO can be used to predict the elastic properties of other transition-metal monoxides from the first transition series. Anderson and Nafe (1965) and Anderson and Anderson (1970) have demonstrated that the simple relationship

$$K_0 V_0 = \text{constant} \qquad (3.17)$$

adequately describes the covariation of molar volume (V_0) and bulk modulus (K_0) for non-transition-metal monoxides in the B1 structure. The effects of the crystal-field energy associated with transition-metal ions in octahedral co-ordination with oxygen anions can be introduced into this systematic treatment of the bulk moduli of the simple rock-salt structured oxides following the theory of Hush and Pryce (1958) and Ohnishi and Mizutani (1978).

The transition-metal atoms of the Fe series have partially filled 3d shells. The most immediately obvious effect of these partially filled shells on the physical properties of the transition-metal monoxides is illustrated in Figure 3.6 in which the metal-oxygen distance is plotted with respect to increasing atomic number. The interatomic distance shows a marked periodic variation with atomic number. This phenomenon can be explained in terms of the periodic variation of the crystal-field stabilization energy (CFSE) with the increasing population of electrons in the 3d shell of the transition-metal ion (Hush and Pryce, 1958).

The bulk modulus of the transition-metal monoxides is also influenced by the crystal-field stabilization energy. Hush and Pryce (1958) and Ohnishi and Mizutani (1978) have discussed the effect of the crystal-field potential on the bulk modulus. The bulk modulus is defined as

$$K_0 = V_0 \left. \frac{\partial^2 U}{\partial V^2} \right|_{P=0} \qquad (3.18)$$

where K_0 and V_0 are the zero pressure bulk modulus and molar volume, and U is the internal energy of a crystal.

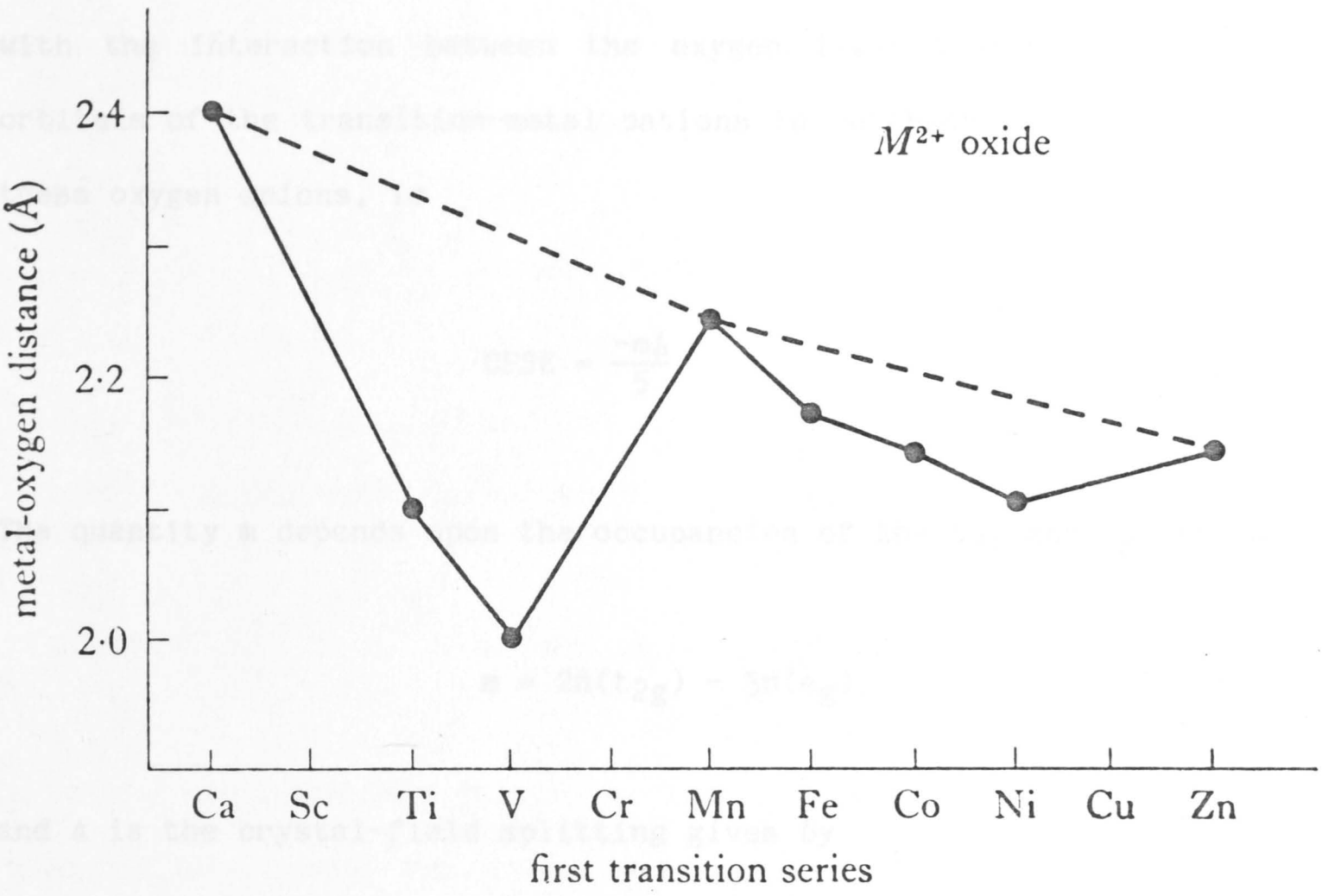

Figure 3.6 The metal-oxygen distances in transition-metal monoxides (after Burns 1970).

The crystal-field stabilization energy (e.g. Burns, 1970) associated with the interaction between the oxygen ligands and the e_g and t_{2g} orbitals of the transition-metal cations in octahedral coordination with these oxygen anions, is

$$CFSE = \frac{-m\Delta}{5} \tag{3.19}$$

The quantity m depends upon the occupancies of the t_{2g} and e_g orbitals:

$$m = 2n(t_{2g}) - 3n(e_g) \tag{3.20}$$

and Δ is the crystal-field splitting given by

$$\Delta \propto R^{-5} \tag{3.21}$$

where R is the metal-ligand separation. It follows that the total molar internal energy of the transition-metal monoxide may be written as:

$$\begin{aligned} U(V) &= F(V) + CFSE \\ &= F(V) - CV^{-5/3} \end{aligned} \tag{3.22}$$

where F(V) is the conventional lattice energy of a crystal and is assumed to be of the form

$$F(V) = -\frac{Az_1z_2e^2}{V^{1/3}} + \frac{B}{V^{n/3}} \tag{3.23}$$

where the first term on the right is the attractive Coulombic term, and the second term is the repulsive potential. From Eqn. 3.23, the bulk

modulus

$$K_0^* = \frac{Az_1z_2e^2(n-1)}{9\ V_0^{*4/3}} \tag{3.24}$$

and its pressure derivative

$$\left.\frac{\partial K_0^*}{\partial P}\right|_{P=0} = \frac{n+7}{3} \tag{3.25}$$

can be calculated; where K_0^* and V_0^* are the zero pressure bulk modulus and molar volume in the absence of the crystal-field stabilization energy. The effects of the CFSE on the molar volume and the bulk modulus of a transition-metal monoxide can now be calculated from Eqns. 3.18, 3.21 and 3.22:

$$C = \frac{9}{5} K_0^* (V_0^* V_e)^{4/3} \frac{(V_0^*/V_e)^{(n-1)/3} - 1}{n-1} \tag{3.26}$$

and

$$K_e = \frac{4K_0^*}{n-1} \left|\frac{V_0^*}{V_e}\right|^{4/3} \left(\frac{n-5}{4} \times \left|\frac{V_0^*}{V_e}\right|^{(n-1)/3} + 1\right) \tag{3.27}$$

for K_e and V_e the bulk modulus and molar volume of the crystal with the crystal-field effects incorporated (Ohnishi and Mizutani, 1978).

The distribution of the 5 electrons in the 3d shell of an Mn atom in octahedral coordination produces an almost spherical atom with zero crystal-field stabilization energy. Hence, the elastic properties of MnO are unaffected by the crystal-field stabilization energy, with the result that the lattice parameter of MnO and the bulk modulus with its pressure derivative can be used in Eqns. 3.17, 3.25 and 3.27 to

calculate the bulk moduli of the other Fe series transition-metal monoxides.

This model of Ohnishi and Mizutani (1978) incorporates a $K_0^*(V_0^*)^{4/3}$=constant relationship (Eqn. 3.24) in contrast to the K_0V_0=constant relationship observed by Anderson and Anderson (1970) (Eqn. 3.17) for the rock-salt structured oxides MgO, CaO and SrO. The present calculations of the bulk moduli of the transition-metal monoxides have been based upon the K_0V_0=constant relationship which appears to adequately describe the variation of the bulk moduli of the B1 structured monoxides. The predicted bulk moduli for the transition-metal monoxides are listed in Table 3.4 and compared with previous measurements of the bulk moduli for these crystals in Figure 3.7.

The present predicted value of 177 GPa for the bulk modulus of stoichiometric FeO is comparable with Yagi et al's (1984) bulk modulus of 172±10 GPa for $Fe_{0.98}O$ determined by X-ray diffraction, and the predicted 182±5 GPa of Jackson et al. (1978) extrapolated from the bulk moduli determined for polycrystalline $(Mg_xFe_{1-x})O$ aggregates. However, the bulk moduli of single crystals of non-stoichiometric $Fe_{0.95}O$ wüstite determined ultrasonically by Jackson et al. (1985) (K=155.2±0.2 GPa) and Berger et al.(1981) (K=153±1) are much lower than predicted for stoichiometric wüstite by the present model.

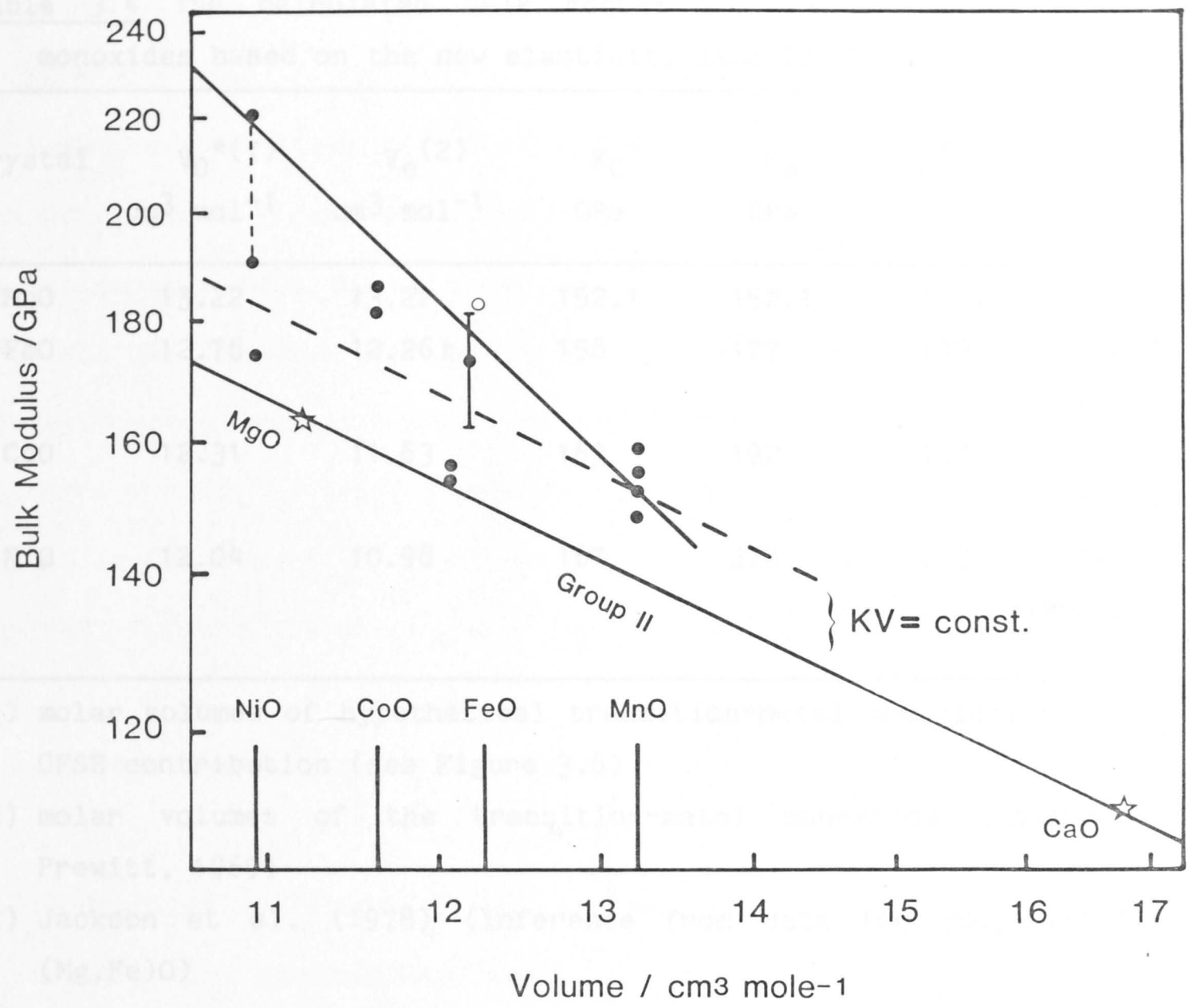

Figure 3.7 Relationship between bulk modulus and molar volume for the 3d transition-metal monoxides. The broken line is the $K_O^* V_O^*$ = constant trend while the steeper solid line represents the calculated covariation of bulk modulus (K_e) and molar volume (V_e) for the crystal-field stabilized oxides based on $K_O^* V_O^*$ = constant (see text and Table 3.4 for details). The measured bulk moduli of non-stoichiometric wüstite are those of Jackson et al. (1985), and Berger et al. (1981) for $Fe_{0.95}O$, and Yagi et al. (1984) for $Fe_{0.98}O$. The open symbol is the bulk modulus predicted for stoichiometric FeO from the polycrystalline data of Jackson et al. (1978). The MgO data point is from Jackson and Niesler (1982), and the CaO data point is from Chang and Graham (1977).

Table 3.4 The calculated bulk moduli of the 3d transition-metal monoxides based on the new elasticity data for MnO.

Crystal	V_0*(1) $cm^3\ mol^{-1}$	V_e(2) $cm^3\ mol^{-1}$	K_0* GPa	K_e GPa	$K_e(K_0 V_0^{4/3}=\text{const.})$ GPa	
MnO	13.22	13.22	152.1	152.1	152.1	
FeO	12.76	12.26†	158	177	179	182(3)
						155(4)
CoO	12.31	11.63	163	192	197	186(5)
						181(6)
NiO	12.04	10.98	167	218	225	173(5)
						190-220(7)

(1) molar volumes of hypothetical transition-metal monoxides without a CFSE contribution (see Figure 3.6)

(2) molar volumes of the transition-metal monoxides (Shannon and Prewitt, 1969)

(3) Jackson et al. (1978) (inference from data for polycrystalline (Mg,Fe)O)

(4) Jackson et al. (1985) $Fe_{0.95}O$

(5) Sumino et al. (1980)

(6) Uchida and Saito (1972)

(7) Notis et al. (1971) (polycrystal)

† stoichiometric FeO molar volume from McCammon (1983)

The zero pressure bulk modulus of MnO employed by Ohnishi and Mizutani (1978) in their calculations was that observed by Uchida and Saito (1972). This measurement of the bulk modulus of MnO is 3% lower than that of the present study; hence the zero pressure bulk moduli calculated for the hypothetical transition-metal monoxides in the present study are higher than those predicted by Ohnishi and Mizutani (1978). The pressure derivative of the bulk modulus of MnO was estimated to be between 4 and 5 for the purposes of Ohnishi and Mizutani's calculations, compared with the measured value of 5.47. The

bulk moduli calculated for the 3d transition-metal monoxides in the present study are 5-15% higher than those of Ohnishi and Mizutani due to the combined effects of the greater values of K and $\partial K/\partial P$ measured in this study. Figure 3.7 illustrates the predicted bulk moduli for stoichiometric FeO, NiO and CoO (with $K_0{}^*V_0{}^*$=constant) compared with previous measurements of the single crystal and polycrystal bulk moduli of these monoxides. The predicted moduli are generally higher than the measured moduli; however, given the range of previously determined bulk moduli for MnO, similar errors in the determinations of the bulk moduli for FeO, CoO and NiO are to be expected.

3.3.4 Shear-mode softening and lattice instability in MnO

Pronounced softening of the C_{44} modulus of MnO has previously been observed in the paramagnetic phase within a few tens of degrees of the room pressure Néel point T_N ~120K (Sumino et al., 1980;Seino, 1982). The development of antiferromagnetic ordering at T_N is accompanied by a slight rhombohedral distortion ~0.5° (Morosin, 1970) of the cubic lattice involving compression of the lattice along [111]. Whereas C_{11} and $C'=(C_{11}-C_{12})/2$ both increase monotonically with decreasing temperature between room temperature and T_N, C_{44} remains essentially constant (within 1%) between room temperature and 220K, but decreases at an exponentially increasing rate by a total of 30% between 220K and T_N. Seino (1982) has demonstrated that the anomalous temperature dependence of C_{44} may be quantitatively modelled in terms of nearest- and next-nearest-neighbour exchange interactions accompanying the development of pronounced short-range magnetic order. Significant short-range magnetic order has been shown to persist to temperatures as high as 700 K (Babić et al., 1976).

If instead of decreasing the temperature towards the room pressure Néel point, increasing pressure is used to raise the Néel point towards room temperature (295K) similar behaviour of the three independent elastic moduli, and especially of C_{44}, might be expected as the Néel point is approached. Bloch et al. (1980) have shown the Néel temperature of MnO to increase with hydrostatic pressure at a rate of 3 K GPa^{-1} over a pressure range of 4 GPa, suggesting that a pressure of ~60 GPa is required to raise T_N to room temperature. Thus, in the absence of other thermodynamically competitive phases, the paragmagnetic→antiferromagnetic transition would be expected to occur at ~60 GPa at room temperature. Under these circumstances, the low-temperature elasticity data would suggest that C_{44} might remain essentially independent of pressure, in general accord with our observations, to perhaps 40-50 GPa thereafter decreasing exponentially as the Néel point is approached and the effect of the increasing short-range order is felt.

However, we have already seen that negative $\partial C_{44}/\partial P$ is a rather general characteristic of B1 lattices at high pressure. The connection between C_{44} mode softening and the B1→B2 phase transformation in the alkali halides and alkaline earth oxides (Demarest et al., 1977;see Section 3.2 of this thesis) is well documented. With reference to Table 3.1, it is evident that the alkali halides which undergo this transformation below 4 GPa have markedly negative (<-0.2) pressure derivatives of the modulus C_{44}. In sharp contrast, halides with positive $\partial C_{44}/\partial P$ (NaF, NaCl) have B1→B2 transformation pressures of ~30 GPa. However, a more reliable indicator of an imminent B1→B2 transformation than C_{44} itself appears to be the ratio of C_{44} to the bulk modulus K. Demarest et al. (1977) have shown for the alkali halides that the B1→B2 transformation occurs when this ratio decreases

to a critical value in the range 0.15-0.20.

Data in Table 3.1 may be used to calculate critical values of C_{44}/K of 0.17 and 0.22, respectively, for the B1→B2 phase transformations in SrO (36 GPa, Sato and Jeanloz, 1981) and CaO (65 GPa, Jeanloz et al., 1979). For MnO, the ratio C_{44}/K decreases from 0.52 at zero pressure (C_{44}=79.0 GPa, K=152.1 GPa) to 0.24 at 30 GPa, and 0.17 at 50 GPa ($\partial C_{44}/\partial P$ assumed to be -0.12 from the straight line fit to the C_{44} curve for pressures in excess of 1.5 GPa (see Figure 3.5), $\partial K/\partial P \approx 5.5$). It is therefore predicted on the basis of the stability criterion proposed by Demarest et al. (1977) that MnO should undergo a B1→B2 transformation within the pressure interval 30-50 GPa at room temperature.

The softening of the C_{44} mode of a B1 phase does not necessarily lead to B1→B2 polymorphism. The nature of the B1→B2 transformational strain, along with pronounced C_{44} softening in the B1 phase, must imply a relatively low free energy for the B2 phase and a relatively low energy barrier between the two phases. However, it is always possible that an alternative phase might have an even lower free energy. Jackson and Ringwood (1981) and Navrotsky and Davies(1981) have suggested structures related to nickel arsenide as alternative high pressure phases for the transition-metal monoxides. The relatively spherical distribution of electron density associated with the Mn^{2+} d_5 configuration and the observation by McCammon et al. (1984) that pressure does not increase the solubility of MnS in NiAs-structured FeS may be consistent with B1→B2 polymorphism in both MnS and MnO.

Seino (1982) has shown that the development of short-range magnetic order in the paramagnetic phase causes anomalous softening of C_{44} over

an extended temperature range above T_N. Similar softening of C_{44} would therefore be expected with increasing pressure as the Néel temperature increases towards room temperature.

Simple lattice models for the NaCl structures predict that $\partial C_{44}/\partial P$ should become negative at sufficiently high pressures for all B1 phases. This is a consequence of the increased importance of the negative contribution of the short-range nearest-neighbour overlap interaction as the interatomic distance is reduced by compression. Similar softening of the C_{44} modulus might be expected to occur with decreasing interatomic distance in response to decreasing temperature at atmosperic pressure.

The effect of the short-range magnetic order on the magnitude of the elastic constants is simply to reinforce the existing effects of the central-force nearest-neighbour repulsions due to shortening of the interatomic distances with either pressure or temperature. This is apparent in the behaviour of C_{44} with decreasing temperature. The intrinsic lattice softening of C_{44} observed in the NaCl structured halides is illustrated by an almost linear C_{44} versus pressure curve with no catastrophic breakdown of this trend before the phase transition occurs. The C_{44} modulus of MnO with decreasing temperature begins to breakdown within ~50° of the Néel temperature as the added effect of the short-range magnetic order becomes much larger than that of the intrinsic lattice softening.

It is noted that the predicted B1→B2 transformation pressure for MnO of 30-50 GPa is intermediate between the observed transformation pressures of SrO (36 GPa) and CaO (65 GPa) despite the much smaller ionic radius of Mn^{2+}. This possible violation of the general trend

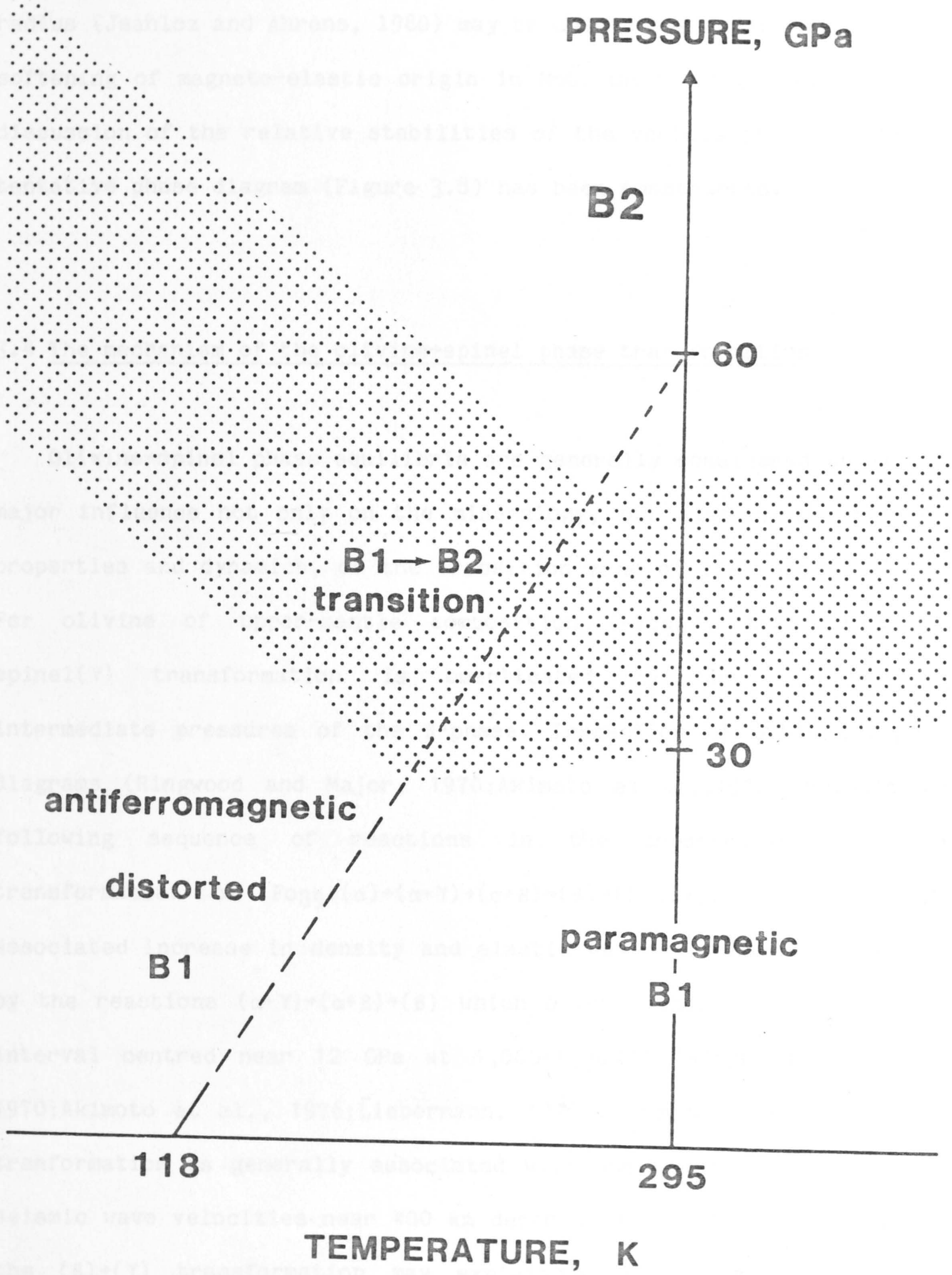

Figure 3.8 Tentative high-pressure phase diagram for MnO.

whereby B1→B2 transformation pressure increases with decreasing ionic radius (Jeanloz and Ahrens, 1980) may be due to the additional C_{44} mode softening of magneto-elastic origin in MnO. On the basis of the above discussion of the relative stabilities of the various phases of MnO, a tentative phase diagram (Figure 3.8) has been constructed.

3.4 The mechanism of the olivine→spinel phase transformation

Olivine→spinel phase equilibria are generally considered to exert a major influence not only on the mineralogy, but also on the physical properties and dynamics, of the transition zone of the Earth's mantle. For olivine of upper-mantle composition (~Fo_{89}), the olivine(α)→spinel(γ) transformation is complicated by the stability at intermediate pressures of the β-phase. Inspection of published phase diagrams (Ringwood and Major, 1970;Akimoto et al.,1976) reveals the following sequence of reactions in the pressure-induced phase transformation of Fo_{89}:(α)→(α+γ)→(α+β)→(β)→(β+γ)→(γ). Most of the associated increase in density and elastic wave velocities is achieved by the reactions (α+γ)→(α+β)→(β) which occur within a 1 GPa pressure interval centred near 12 GPa at 1,000-1,200°C (Ringwood and Major, 1970;Akimoto et al., 1976;Liebermann, 1975). Accordingly, the (α)→(β) tranformation is generally associated with the major discontinuity in seismic wave velocities near 400 km depth in the Earth's mantle, while the (β)→(γ) transformation may explain a more minor discontinuity sometimes observed in the depth range 500-550 km (Ringwood, 1975;Akimoto et al., 1976).

Elevation of these equilibria within relatively cool subducting lithosphere (by virtue of positive Clapeyron slopes dP/dT) may

contribute substantially to the driving force for plate tectonics (Schubert and Turcotte, 1971;Toksöz et al.,1971;Ringwood, 1975). Alternatively, sluggish transformation kinetics in the neighbourhood of the equilibrium boundary could result in significant olivine metastability, with potentially important implications not only for the dynamics of the lithospheric slab but also for its stress state and for the origin of deep-focus earthquakes (e.g. Sung and Burns, 1976). Any role for transformation plasticity in the rheology of subducting lithosphere or surrounding mantle is also dependent upon its kinetics of transformation relative to those for dynamic recovery (Paterson, 1983).

The very considerable geophysical importance of the kinetics of the $(\alpha)\rightarrow(\alpha+\gamma)\rightarrow(\alpha+\beta)\rightarrow(\beta)$ transformation has stimulated interest in the transformation mechanism. The observation that the $(\alpha)\rightarrow(\beta)$ transformation of Fo_{89} is initiated by the formation of spinel (γ, composition $\sim(Mg_{0.5}Fe_{0.5})_2SiO_4$), and the contraction of the β-phase field with decreasing temperature, have been cited as justification for emphasis of the olivine→spinel transformation mechanism (Sung and Burns, 1976;Poirier, 1981a), for which two radically different alternatives have been proposed. The first is a nucleation and growth mechanism (Sung and Burns, 1976) in which the olivine/spinel boundary propagates by a generally uncoordinated, thermally activated movement of atoms which is rate-controlled by the diffusion of oxygen ions.

The second possibility is a martensitic diffusionless mechanism (Poirier, 1981a) which would achieve the conversion of the hexagonally-close-packed anion array of olivine into the face-centred-cubic geometry of spinel by the action of dislocations. Specifically, it is suggested by Poirier that partial dislocations associated with the

(100)[001] slip system sweep across the basal plane of olivine creating layers of stacking faults with the spinel structure, which become more stable as the transition is approached. It is envisaged that the necessary cation rearrangement over atomic distances is accomplished by a coordinated shuffle known as syncroshear.

It is further suggested (Poirier,1981a) that such a transition would probably be accompanied by softening of the elastic stiffness moduli (C_{55} and C_{66}) governing shear on the (100) plane. In this connection, Poirier draws attention to the fact that pressure derivatives of the elastic moduli for single-crystal forsterite and ~Fo_{90} olivine are least for C_{55} and C_{66}. The availability of a single crystal of fayalite together with the high pressure capability of our ultrasonic interferometer, affords an opportunity for study of the pressure sensitivity of the key shear moduli of an olivine to pressures beyond its equilibrium olivine→spinel transition pressure (~2 GPa for Fe_2SiO_4, Ringwood, 1975).

3.5 Search for C_{55} mode softening in fayalite

3.5.1 Specimen description

The original objective of this study was measurement of the pressure dependence of all nine single-crystal elastic stiffness constants of a large crystal of fayalite (Fe_2SiO_4, space group Pbnm) grown by the floating zone technique (Takei, 1978). However, minor cracks which developed along the (010) cleavage plane during preparation of the crystal faces were found to seriously affect the propagation of certain modes (especially those with propagation vector

k parallel to [010], thereby eliminating the possibility of a comprehensive study (see also Sumino, 1979).

It was possible, however, to obtain high quality data for the shear-mode with propagation direction [001] and polarization direction [100], and thus measure the pressure dependence of the key shear modulus, C_{55}. Accordingly, a pair of parallel (001) faces was cut, ground and polished. The density of the virgin (uncracked) crystal boule was 4.400±0.003 g cm^{-3} which compares favourably with the X-ray density of 4.397 g cm^{-3} (Sumino, 1979). The orientation of the polished faces was within 1° of (001) and their spacing was 6.375±0.002 mm.

3.5.2 Data reduction

The high ultrasonic attenuation of fayalite dictated the use of $LiNbO_3$ (41° rotated X-cut) transducers as this shear-mode transducer has a higher electromechanical coupling factor and a higher impedance than the AC-cut quartz transducers employed in the present studies, resulting in a correspondingly higher signal/noise ratio. Unfortunately, this gain in signal level is at the expense of mode purity (Warner et al., 1967) and care must be exercised in the positioning of the receiver gate to avoid compressional mode interference (Jackson et al., 1981).

The modulus C_{55} may was calculated from the expression

$$C_{55}(P) = \rho(P)v^2(P) = 4\rho(P)L^2(P)/t^2(P) \qquad (3.28)$$

where ρ, L, v and t are respectively the density, length, wave velocity and travel-time. Figure 3.9 illustrates a typical travel-time versus

frequency plot for this mode of propagation. $\rho(P)$ and $L(P)$ were calculated from Murnaghan expressions of the form

$$\rho/\rho_0 = (L_0/L)^3 = (1 + K_0'P/K_0)^{1/K_0'}. \qquad (3.29)$$

The values of K_o and K_o' used in this calculation were, for $\rho(P)$, the single-crystal volume incompressibility and its pressure derivative and, for $L(P)$, the corresponding quantities for a hypothetical cubic crystal with the same linear incompressibility as fayalite parallel to [001] (see Nye, 1957, p.146, for details). The necessary K_o were calculated from the elastic moduli reported by Graham et al. (1982), whereas the K_o' were set equal to the pressure derivative of the bulk modulus of magnesian olivine presented in Chapter 4.

However, variation from this assumed value of $K_0'=4.87$ to that ($K_0'=3.62$) extrapolated from the pressure dependences of the bulk moduli of the ferro-magnesian olivines observed in the present study and the studies of Graham and Barsch (1969) and Kumazawa and Anderson (1969) (see Table 4.12) does not perturb the calculated pressure dependence of the modulus C_{55} beyond the limits of the quoted errors.

The pressure dependence of the modulus C_{55} calculated in this manner was found to be

$$\begin{aligned} C_{55} &= 46.9 \pm 0.1 \text{ GPa} \\ \partial C_{55}/\partial P &= 1.76 \pm 0.01 \\ \partial^2 C_{55}/\partial P^2 &= -0.14 \pm 0.01 \text{ GPa}^{-1} \end{aligned} \qquad (3.30)$$

Figure 3.10 illustrates the behaviour of this modulus over the 3 GPa pressure range.

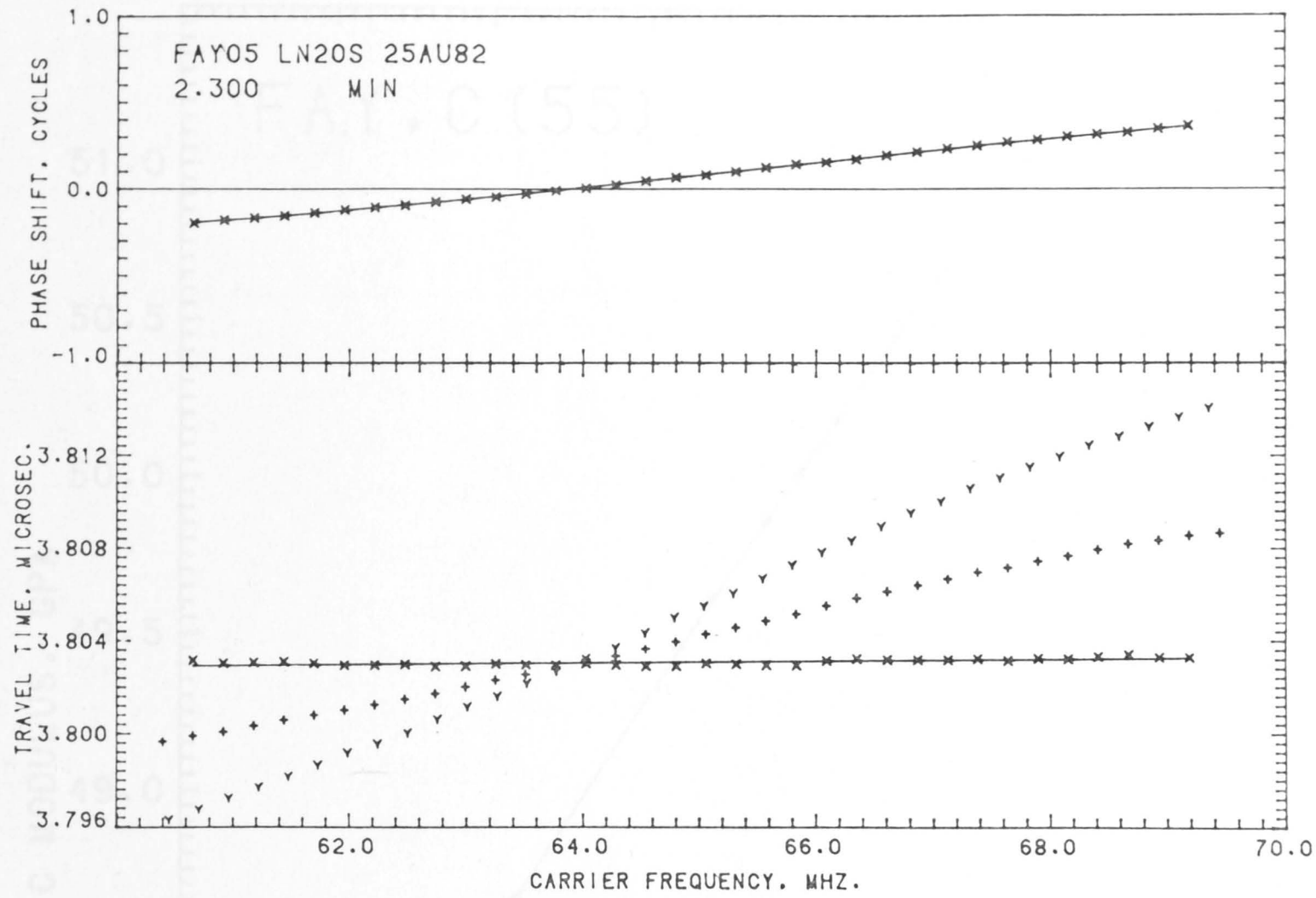

Figure 3.9 Phase comparison data at 2.30 GPa for the shear modulus C_{55} of fayalite.

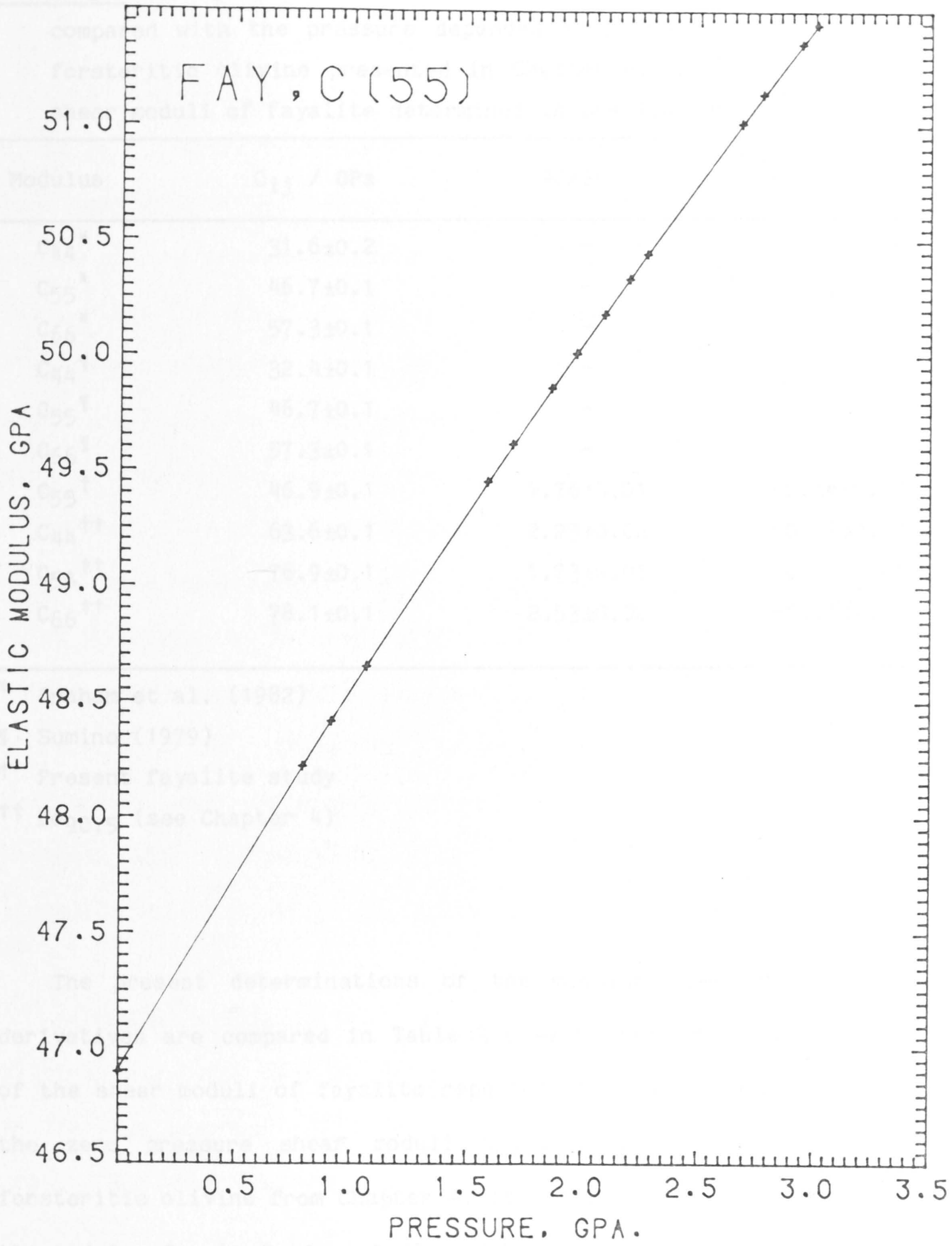

Figure 3.10 The variation with pressure of the modulus C_{55} of fayalite. The uncertainties in modulus are everywhere less than the diameter of the plotting symbols.

Table 3.5 The pressure dependence of the modulus C_{55} of fayalite compared with the pressure dependence of the shear moduli of the forsteritic olivine presented in Chapter 4, and the zero pressure shear moduli of fayalite determined in previous studies.

Modulus	C_{ij} / GPa	$\partial C/\partial P$	$\partial^2 C/\partial P^2$ /GPa^{-1}
C_{44}*	31.6±0.2	-	-
C_{55}*	46.7±0.1	-	-
C_{66}*	57.3±0.1	-	-
C_{44}¶	32.4±0.1	-	-
C_{55}¶	46.7±0.1	-	-
C_{66}¶	57.3±0.1	-	-
C_{55}†	46.9±0.1	1.76±0.01	-0.14±0.01
C_{44}††	63.6±0.1	2.23±0.02	-0.19±0.02
C_{55}††	76.9±0.1	1.73±0.01	-0.15±0.01
C_{66}††	78.1±0.1	2.53±0.02	-0.21±0.01

* Graham et al. (1982)

¶ Sumino (1979)

† Present fayalite study

†† $Fo_{90.5}$ (see Chapter 4)

The present determinations of the modulus C_{55} and its pressure derivatives are compared in Table 3.5 with room pressure measurements of the shear moduli of fayalite reported by previous authors, and with the zero pressure shear moduli and pressure derivatives for the forsteritic olivine from Chapter 4. The zero pressure determinations of the modulus C_{55} by Sumino et al. (1979) and Graham et al. (1982) agree within the quoted errors with the present measurement. Among the transition-metal silicate olivines, C_{55} decreases across the sequence Ni, Co, Mn, Fe in accord with the variation of C_{44} among the transition-metal monoxides with the B1 structure (Bass, 1982); and therefore, C_{55} of fayalite is expected to be less than those observed for the forsteritic and the transition-metal olivines.

3.5.3 On the absence of shear-mode softening

The measured first pressure derivative of the modulus C_{55} of fayalite is "normal" in the sense that it is positive and comparable in magnitude with $\partial C_{55}/\partial P$ of the forsteritic olivine presented in Chapter 4. The second pressure derivative is also comparable to that of the forsteritic olivine, in spite of the much closer proximity (at atmospheric pressure) of Fe_2SiO_4 to the high-pressure boundary of its stability field. it is also instructive to compare the value of C_{55}/K with corresponding quantities for the alkali halides (Table 3.6).

At room temperature and pressure, fayalite exhibits a value of C_{55}/K (0.37) which is comparable with C_{44}/K for the potassium halides and therefore suggestive of marginal stability of the olivine phase for 2 GPa < P < 4 GPa. There is, however, no comparable evidence for pressure-induced shear-mode softening of fayalite since $\partial C_{55}/\partial P$ is strongly positive, and $\partial(C_{55}/K)/\partial P$ is near zero and positive for all plausible values of $\partial K/\partial P$ (eg 3.6-4.9).

Although extrapolation of the high-pressure high-temperature olivine→spinel boundary for Fe_2SiO_4 (Akimoto et al., 1967) suggests an equilibrium pressure of ~2 GPa at room temperature, it is well known that the transformation (unlike the B1→B2 transitions) requires significant thermal activation. Thus, although the measurements reported here extend beyond the equilibrium boundary without showing any clearly anomalous behaviour of the shear modulus C_{55}, they are conducted under conditions which preclude the occurrence of the transformation. We note that the need for substantial thermal activation may be readily incorporated into a martensitic model for the olivine→spinel transformation via the temperature dependence of the

Peierls stresses acting on dislocations (Poirier, 1981b).

Table 3.6 Shear-mode softening associated with the B1→B2 phase transformation and the comparable calculations for the present fayalite crystal and the forsteritic olivine presented in Chapter4.

	C_{44} GPa	K GPa	$\partial C_{44}/\partial P$	$\partial K/\partial P$	C_{44}/K	$\partial(C_{44}/K)/\partial P$ GPa^{-1}	P_{tr}* GPa
RbI	2.79	11.09	-0.49	5.41	0.25	-0.17	0.4
RbBr	3.84	13.66	-0.56	5.30	0.28	-0.15	0.4
RbCl	4.75	16.30	-0.61	5.35	0.29	-0.13	0.5
KI	3.73	12.15	-0.23	5.10	0.31	-0.15	1.7
KBr	5.08	14.86	-0.33	5.38	0.34	-0.15	1.7
KCl	6.33	17.89	-0.41	4.78	0.35	-0.12	1.9
KF	12.81	31.13	-0.45	5.02	0.41	-0.081	4
NaCl	12.80	25.21	0.37	5.26	0.51	-0.091	30
NaF	28.22	48.20	0.21	5.18	0.59	-0.059	27
SrO	55.87	91.21	-0.21	5.18	0.61	-0.037	36
CaO	80.32	112.50	0.20	4.83	0.71	-0.029	65
MgO	155.8	162.5	1.11	4.13	0.96	-0.018	>200
Fe_2SiO_4†							
C_{55}	46.9	127.7	1.76	4.9**	0.37	0.000	
				3.6***		0.003	
$Fo_{90.5}$††							
C_{44}	63.6	129.1	2.23	4.87	0.49	-0.001	
C_{55}	76.9		1.73		0.60	-0.009	
C_{66}	78.1		2.53		0.61	-0.003	

* B1→B2 transformation pressures at room temperature.

** pressure dependence assumed from the forsteritic olivine in Chapter 4.

*** pressure dependence extrapolated from the data presented in Table (4.12)for the ferro-magnesian olivines.

† the C_{55} modulus of the present fayalite

†† the shear moduli for the forsteritic olivine in Chapter 4.

Under these circumstances, it is conceivable that shear-mode softening associated with a martensitic olivine→spinel transformation, like the transformation itself, might require thermal activation. However, Fukizawa and Kinoshita (1982) have recently measured the shear wave velocity of polycrystalline fayalite under conditions of simultaneous high pressure and high temperature to 5.2 GPa and 700° C, at which point the olivine→spinel transition began to occur, without observing an anomalous decrease in velocity. There is thus no evidence from either the present single-crystal study or the work of Fukizawa and Kinoshita on polycrystalline material, for pressure induced shear-mode softening in fayalite prior to a martensitic olivine→spinel transformation.

CHAPTER 4

ELASTICITY OF SOME MANTLE MINERALS

4.1 Introduction

The mineralogy of the upper mantle is dominated by olivine, with lesser volumes of orthopyroxene and clinopyroxene and a small volume of pyrope-rich garnet. The difficulties in measuring the elastic properties of whole rocks of this mineralogy has resulted in the development of techniques designed to measure the elastic properties of single crystals of mantle minerals at moderate pressure and temperature (see Chapter 2). The methods detailed in Chapter 2 have been applied to the determination of the pressure dependence of the elastic moduli of single crystals of olivine, garnet and orthopyroxene.

4.2 Garnet

4.2.1 Specimen description

A large natural single-crystal of pyrope-rich garnet (space group Ia3d) of composition $(Mg_{0.62}Fe_{0.36}Ca_{0.02})_3Al_2Si_3O_{12}$ was made available by Prof. E.K. Graham of Pennsylvania State University. This gem quality crystal was blood-red in colour and free from inclusions. The crystal had been prepared with parallel (±0.5°) pairs of (100) and (011) faces (see Figure 4.1). The density of the crystal was determined by immersion in ethanol to be 3.839±0.003 g cm^{-3}. Previous determinations of the density of this crystal by immersion in water have been quoted as 3.76±0.01 g cm^{-3} (Isaak and Graham, 1976) and 3.726±0.002 g cm^{-3} (Bonczar et al., 1977). These low densities were queried by Leitner et al. (1980) who calculated a density of 3.847 g cm^{-3} from the chemical composition of the crystal. This calculated density is in good agreement with the present measurement.

The three modes of propagation required to measure the elastic constants C_{11}, $(C_{11}-C_{12})/2$ and C_{44} (see Figure 4.1) were measured on this crystal. Figure 4.2 illustrates a typical set of travel-time data from the comparative one- and two-transducer experiments for these modes over the 3 GPa pressure range.

4.2.2 Data reduction

The elastic constants of this garnet were calculated from the measured travel-times using Cook's method for a crystal of cubic symmetry (see Chapter 2) to correct for the effects of hydrostatic pressure on length and density. The specific heat and the coefficient

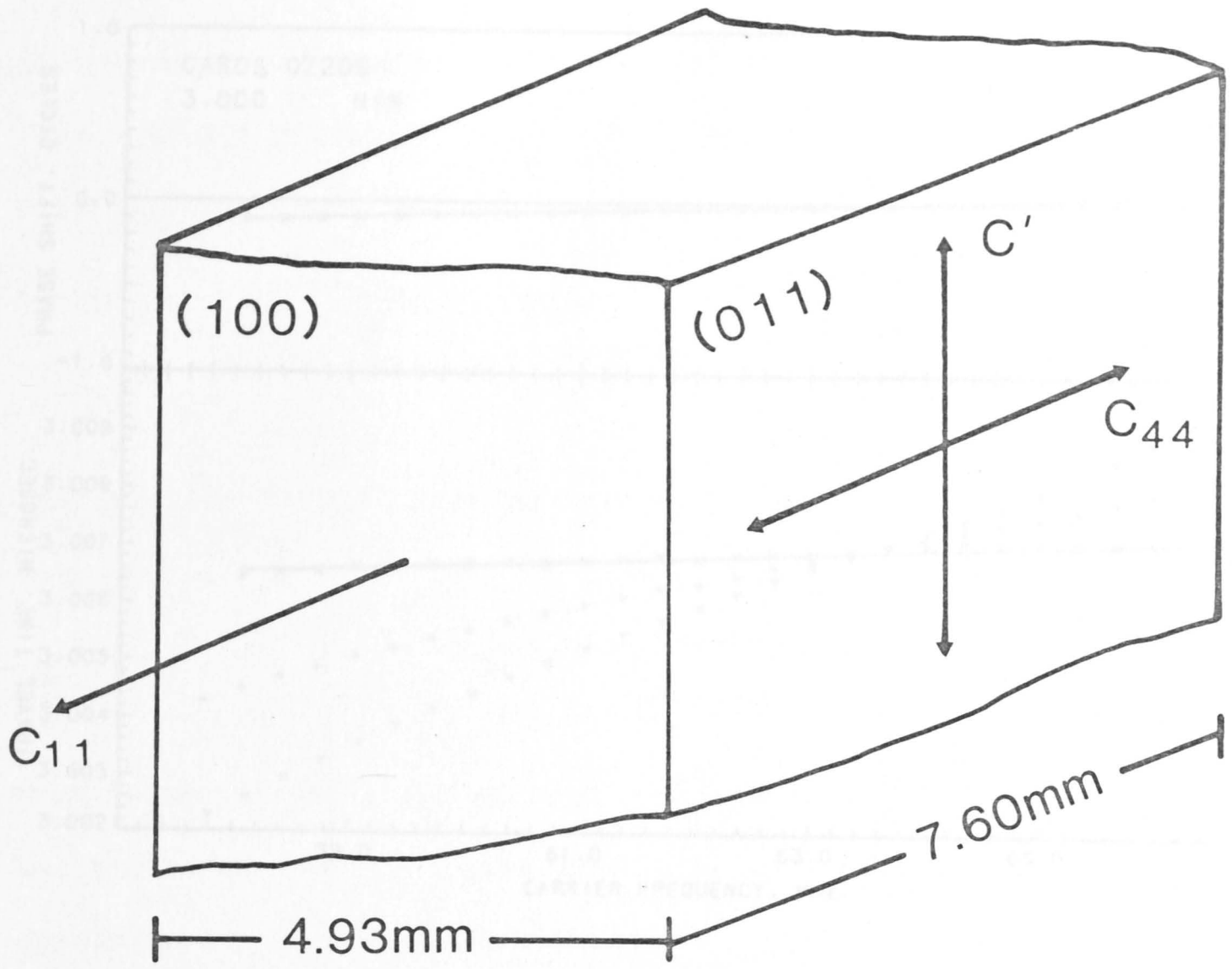

$$C' = (C_{11} - C_{12})/2$$

Garnet

Figure 4.1 Propagation and polarization directions for the elastic moduli of garnet.

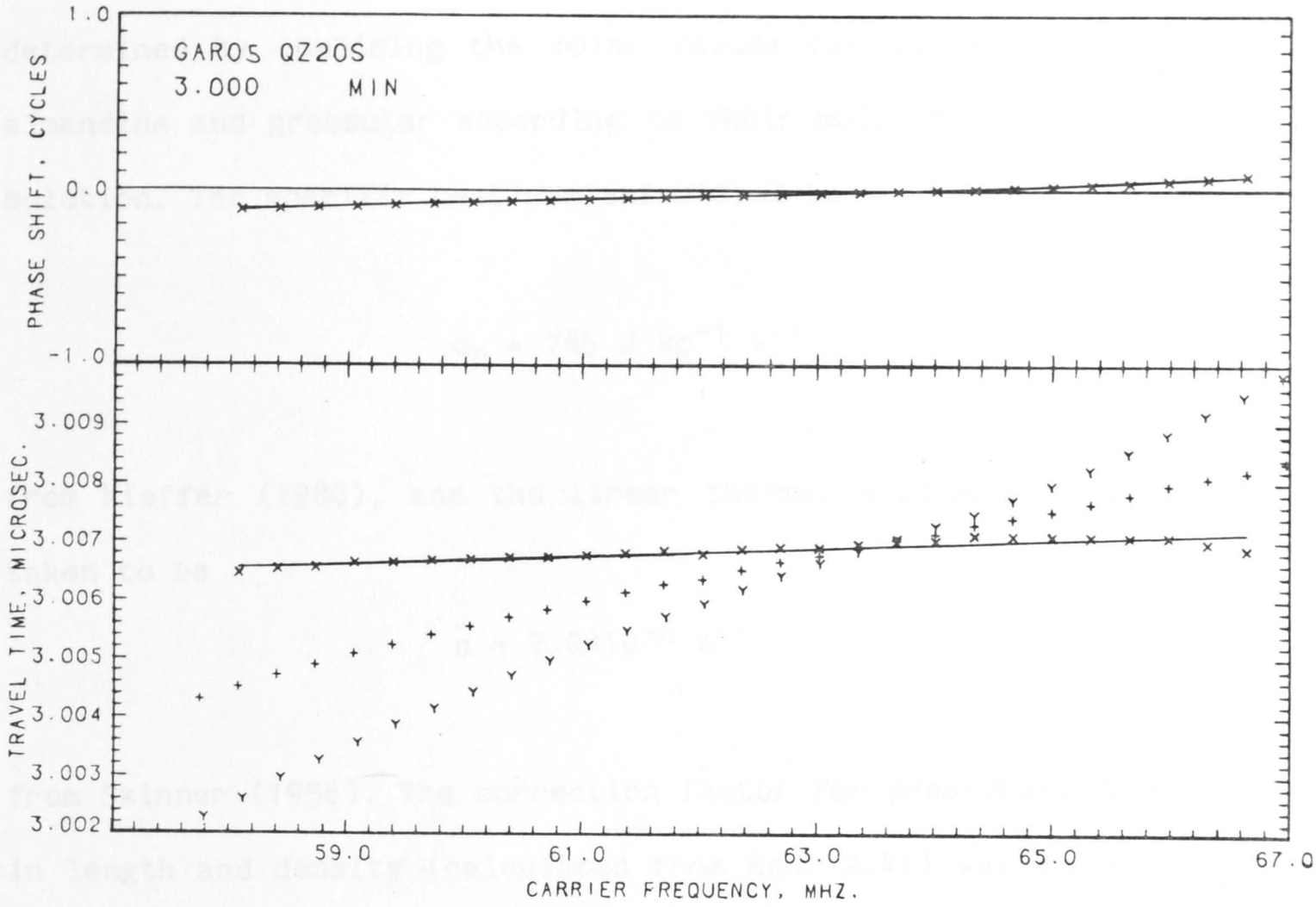

Figure 4.2 Phase comparison data at 3.00 GPa for the shear mode $C_{44}(5)$ of garnet.

of linear thermal expansion required for this calculation were determined by combining the molar values for the end-members pyrope, almandine and grossular according to their mole fractions in the solid solution. The specific heat was calculated to be

$$c_p = 745 \text{ J kg}^{-1} \text{ k}^{-1} \tag{4.1}$$

from Kieffer (1980), and the linear thermal expansion coefficient was taken to be

$$\alpha = 7.0\times10^{-6} \text{ K}^{-1} \tag{4.2}$$

from Skinner (1956). The correction factor for pressure-induced changes in length and density (calculated from Eqn. 2.41) was calculated to be approximately

$$s = 1 + 1.94\times10^{-3} P - 2.55\times10^{-5} P^2 + 8.96\times10^{-7} P^3, \tag{4.3}$$

for pressure measured in GPa. The resulting modulus versus pressure behaviour observed over the 3 GPa range is illustrated in Figures 4.3 and 4.4. The zero pressure elastic stiffnesses, together with their first and second pressure derivatives are presented in Table 4.1. It is evident that this crystal is only mildly anisotropic, with $C_{44} \approx (C_{11}-C_{12})/2$, and also $C_{11} \approx (C_{11}+C_{12}+2C_{44})/2$, throughout the 3 GPa pressure range. The elastic compliances calculated from the measured stiffnesses, together with their first and second pressure derivatives are tabulated in Table 4.2.

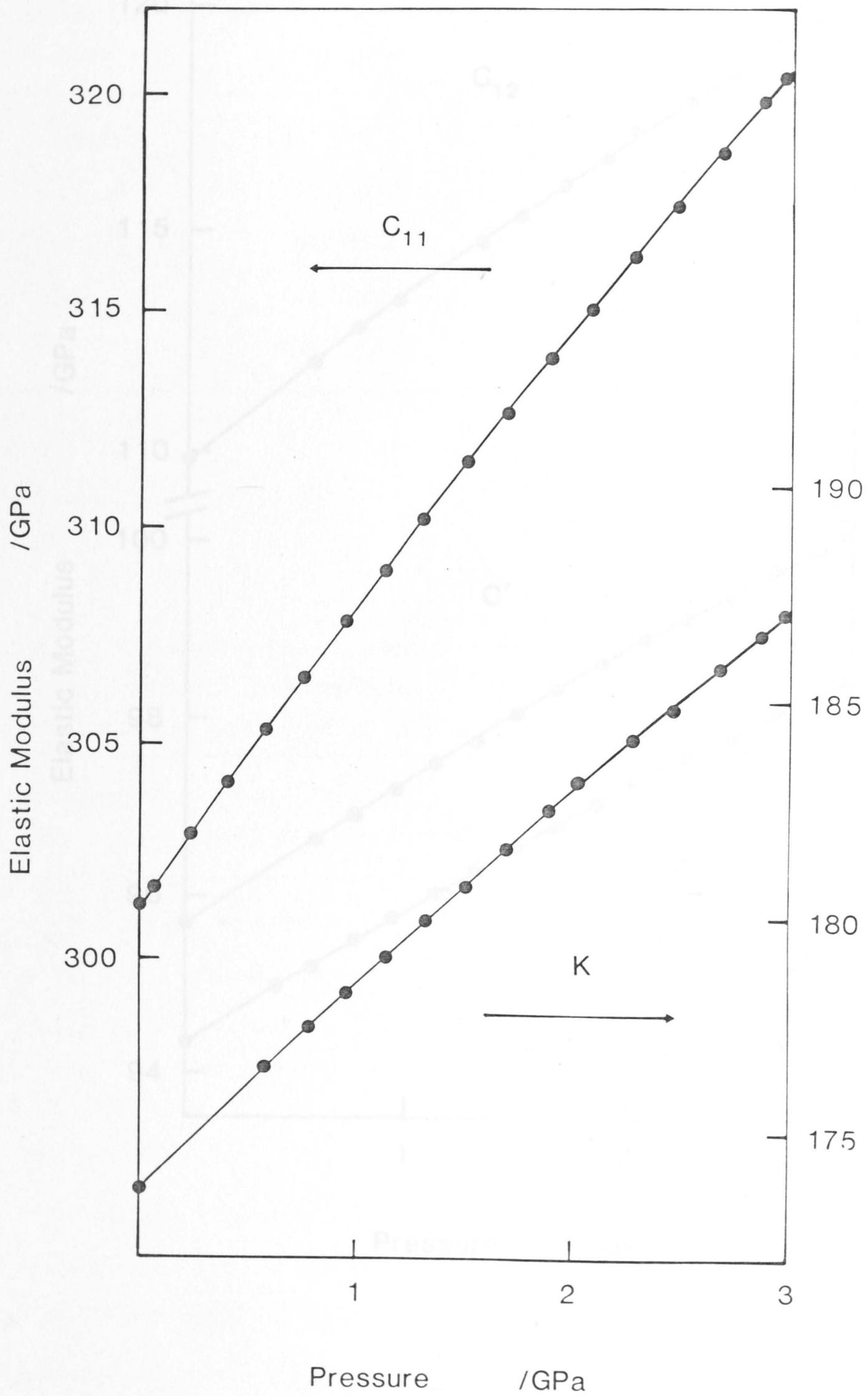

Figure 4.3 The variation with pressure of the compressional modulus C_{11} and the bulk modulus of garnet. The uncertainties in modulus are everywhere less than the diameter of the plotting symbols.

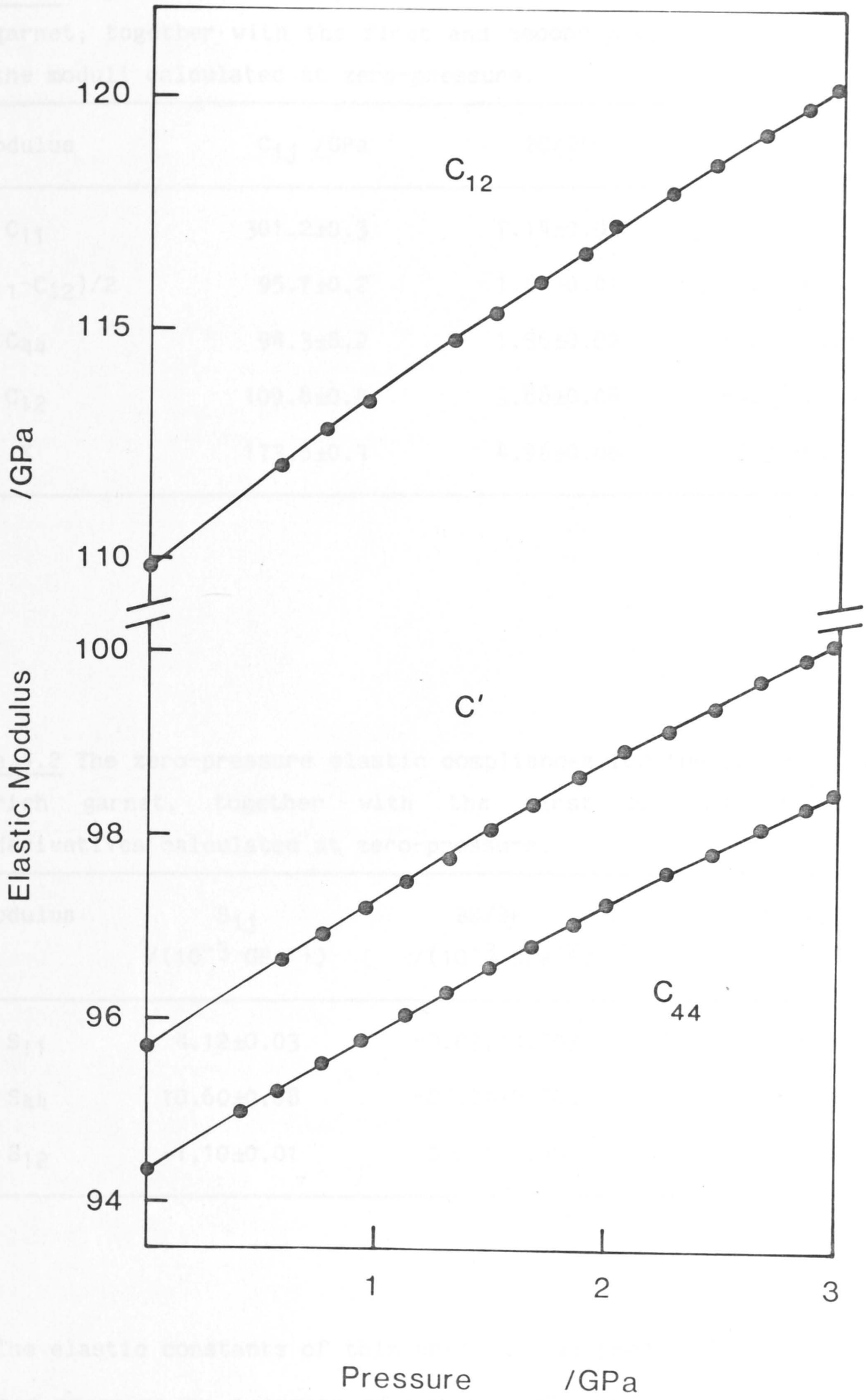

Figure 4.4 The variation with pressure of the shear moduli C_{44} and C', and also the modulus C_{12} of garnet. The uncertainties in modulus are everywhere less than the diameter of the plotting symbols.

Table 4.1 The measured zero-pressure elastic moduli of the pyrope-rich garnet, together with the first and second pressure derivatives of the moduli calculated at zero-pressure.

Modulus	C_{ij} /GPa	$\partial C/\partial P$	$\partial^2 C/\partial P^2$ /GPa^{-1}
C_{11}	301.2±0.3	7.14±0.05	-0.45±0.04
$(C_{11}-C_{12})/2$	95.7±0.2	1.64±0.01	-0.10±0.01
C_{44}	94.3±0.2	1.56±0.02	-0.13±0.01
C_{12}	109.8±0.4	3.88±0.06	-0.26±0.04
K	173.6±0.4	4.96±0.06	-0.31±0.04

Table 4.2 The zero-pressure elastic compliances for the present pyrope-rich garnet, together with the first and second pressure derivatives calculated at zero-pressure.

Modulus	S_{ij} /(10^{-3} GPa^{-1})	$\partial S/\partial P$ /(10^{-3} GPa^{-2})	$\partial^2 S/\partial P^2$ /(10^{-3} GPa^{-3})
S_{11}	4.12±0.03	-0.077±0.003	0.003±0.001
S_{44}	10.60±0.08	-0.174±0.006	0.009±0.003
S_{12}	-1.10±0.01	0.011±0.001	-0.001±0.001

The elastic constants of this crystal have previously been measured at room pressure by a number of authors. The preliminary measurements of Wang and Huang (1975) and Isaak and Graham (1976) have been superseded by the more extensive study of Bonczar et al. (1977) who measured the elastic stiffnesses of this garnet to ≤1 GPa, by the pulse superposition technique. In this study however, the calculations were

based upon a density measurement which has since been found to be incorrect. The room pressure moduli and the pressure derivatives calculated by Bonczar et al. (1977) have been recalculated using the present density measurment and are presented in Table 4.3.

Table 4.3 The zero-pressure moduli for the pyrope-rich garnet together with the first pressure derivatives of Bonczar et al. (1977), recalculated using the density determined in the present study.

Modulus	C_{ij} /GPa	$\partial C/\partial P$
C_{11}	301.1±0.4	7.0±0.2
$(C_{11}-C_{12})/2$	95.8±0.5	1.6±0.1
C_{44}	94.4±0.1	1.5±0.1
C_{12}	109.4±0.5	3.8±0.2
K	173.3±0.4	4.9±0.2

These corrected values of the elastic moduli and the first pressure derivatives determined for this crystal by Bonczar et al. (1977) at low pressures, agree within the errors quoted with the corresponding quantities measured in the present study. The importance of the second pressure derivatives determined in the present study is illustrated by the 18-25% decrease in the observed pressure dependence of the elastic moduli over the 3 GPa pressure range.

4.2.3 Elasticity and crystal chemistry

The general structural formula for silicate garnets is $A_3B_2Si_3O_{12}$. Extensive solid solutions occur in both the A and B sites, but only limited solid solutions occur between these two sites. The garnets can

be divided into two groups by the occupancy of these sites (Winchell, 1933). The pyralspite (pyrope-almandine-spessartine) series has either Fe^{+2}, Mg^{+2}, or Mn^{+2} cations in the A site, with an Al^{+3} cation in the B site. The second group is the ugrandite (uvarovite-grossular-andradite) series in which the A site is occupied by a Ca^{+2} cation while the B site is occupied by either a Cr^{+3}, Al^{+3}, or Fe^{+3} cation.

Of particular geophysical interest is the elasticity of the pyrope-almandine solid solution. However, systematic variation of elastic moduli associated with Fe-Mg substitution tends to be obscured to some extent by varying admixtures of the other end-members in the natural and synthetic garnet single crystals whose elastic properties have been measured. Simple elasticity-density systematics do not adequately describe the elasticity of these complex solid solutions. More rewarding is a multivariate analysis of the measured elasticities of the various solid solution members to calculate the elastic properties of the end-members of the series.

There have been a number of analyses of the end-member elasticities using this multivariate approach. The single crystals of garnet whose elastic properties have been measured range across both the pyralspite and ugrandite solid solutions. It is therefore necessary to invert the data for the elastic properties of the six end-member garnets of these solid solution series. Isaak and Graham (1976), Babuska et al. (1978) and Leitner et al. (1980) have assumed the elastic moduli C_{ij} of a solid solution to be related linearly to the mole fraction of the constituent end-members. Thus, the elastic modulus of a member of a solid solution can be given by

$$(C_{ij})_{ss} = \sum_{k=1}^{n} X_k \, (C_{ij})_k + e \qquad (4.4)$$

where $(C_{ij})_{ss}$ is the measured modulus of the solid solution member, $(C_{ij})_k$ is the same modulus for the k^{th} end-member, X_k is the mole fraction of the k^{th} component in the solid solution, and 'e' is a normally distributed error term with a mean of zero. The results of these analyses are listed in Table 4.4. Isaak and Graham (1976) constrained their calculations with the measured elastic properties of seven pyralspite garnets, while Babuska et al. (1978) used a data base comprising 23 garnets. Leitner et al. (1980) added a synthetic pyrope to the range of garnet compositions available for the calculation of the end-member elasticities. In this latter study both the elastic stiffnesses and the elastic compliances of the end-member compositions were calculated. No preference was shown for either method however, as they resulted in the calculation of similar end-member elasticities.

Isaak and Graham (1976) found an increase of ~8% in the bulk modulus with increasing Fe content between the pyrope and almandine end-members. However, Babuska et al. (1978) and Leitner et al. (1980) with the end-member elasticities constrained by extended data sets found only ~2% increase in the bulk modulus. Table 4.4 illustrates the effects of Fe (or Mn) substition for Mg on the elastic moduli of pyrope garnet. The moduli C_{11}, C' and C_{44} all increase by 5-11% with increasing of Fe (or Mn) content, while the modulus C_{12} decreases by ~6% with increasing Fe (or Mn) content.

Table 4.4 Least-squares solutions for end-member elastic moduli (GPa) (after Leitner et al., 1980) where the modulus $C'=(C_{11}-C_{12})/2$.

End member	Sol*	K	C_{11}	C'	C_{12}	C_{44}
Pyrope	1	175±1	294±1	89±1	116±1	91±1
$Mg_3Al_2Si_3O_{12}$	2	175±2	294±1	89±1	116±1	91±1
	3	173±1	297±1	93±1	111±1	92±1
	4	166±1	287±1	91±1	105±1	92±1
	5	174±1				
Almandine	1	176±1	309±1	100±1	109±1	97±1
$Fe_3Al_2Si_3O_{12}$	2	177±2	312±2	101±1	109±1	97±1
	3	178±1	309±1	98±1	113±1	96±1
	4	180±1	311±1	98±1	115±1	93±1
	5	178±1				
Spessartine	1	176±2	304±1	96±1	112±1	94±1
$Mn_3Al_2Si_3O_{12}$	2	175±3	303±1	96±1	111±1	93±1
	3	174±1	302±1	96±1	110±1	94±1
	4	172±1	301±1	97±1	107±1	96±1
	5	175±1				
Grossular	1	169±2	317±1	111±1	95±1	102±1
$Ca_3Al_2Si_3O_{12}$	2	160±3	297±1	103±2	91±1	94±2
	3	169±1	317±1	111±1	95±1	102±1
	4	170±1	319±1	112±3	95±1	102±1

* Solutions 1 (averaging of stiffnesses) and 2 (averaging of compliances) of Leitner et al. (1980) based on weighted pyrope data. Solution 3 by Babuska et al.(1978).Solution 4 by Isaak and Graham (1976).Solution 5 of Leitner et al. omits the data of Bonczar et al. (1977).

The end-member elasticities presented in Table 4.4 can now be used to calculate the zero pressure elastic properties of the present pyrope-almandine-grossular solid solution. Table 4.5 shows that the

elasticities calculated from the small data set of Isaak and Graham (1976) result in a reasonable approximation to the measured elastic moduli of this pyrope-rich garnet, while Babuska et al. (1978) achieve a closer approximation to the elastic properties of the present garnet. Solutions 1 and 2 for the end-member elasticities (Leitner et al., 1980) are only marginally affected by the inclusion of the Bonczar et al. (1977) data which were based on an erroneous density determination. This is a consequence of the weight given to the Brillouin scattering data for the pyrope end-member. These solutions, and solution 5 for the bulk moduli only, yield calculated moduli for the crystal of the present study which are in good agreement with the observed values.

Table 4.5 The zero pressure elastic moduli measured in the present study compared with the values predicted by the various systematic treatments.

Solution*	K /GPa	C_{11} /GPa	C_{12} /GPa	C_{44} /GPa	C'/GPa
present study	173.6±0.4	301.2±0.2	109.8±0.4	94.3±0.1	95.7±0.1
1	175.2±0.8	300 ±1	113 ±2	93.4±0.7	93.1±0.7
2	175 ±1	301 ±2	113 ±2	93 ±2	93.6±0.7
3	174.7±0.7	302 ±1	111 ±2	93.6±0.7	95.2±0.7
4	171.1±0.7	296 ±1	108 ±2	92.6±0.7	93.9±0.7
5	175.5±0.8				

* Solutions 1-5 have the same significance as in Table 4.4.

The anomaly which previously existed between the elastic moduli predicted for this garnet by the systematics of Leitner et al. (1980) and the elastic moduli measured by Bonczar et al. (1977) has been

removed by the present measurements. This linear addition of the elastic properties of the end-members of the solid solution appears to give reliable calculations of the solid solution elasticities, especially when a large pool of elasticity data is used to constrain the calculations (eg Leitner et al., 1980;Babuska et al., 1978).

Leitner et al. (1980) have calculated the end-member elasticities by summation of both the elastic compliances and the elastic stiffnesses of the solid solution garnets. There is no significant difference between the moduli calculated for the pyralspites using these two methods. The predictions for the end-member ugrandites however depends upon which equation is used. The calculations for the elasticity of the present pyrope-almandine garnet is almost independent of the grossular component, and there is no reason to prefer one method to the other for the calculation of the elastic properties of the present garnet.

The first pressure derivatives of the pyralspite garnets (see Table 4.6) at zero pressure, like the moduli themselves, are not strongly affected by changes in the Mg-Fe-Mn composition, with only a slight trend towards lower values of the pressure derivatives appearing with increasing cation radius. The addition of large Ca cations to the structure however tends to further decrease the values of the derivatives of the bulk modulus and the moduli C_{11} and C_{44} while increasing the derivative of the modulus C_{12}.

Table 4.6 The first pressure derivatives together with the lattice parameters of a number of pyralspite garnets.

∂C/∂P	Garnet #1	Garnet #2	Garnet #3	Garnet #4	Garnet #5
a (Å)	11.48	11.53	11.55	11.57	11.84
K	4.96	5.43	4.95	4.59	4.25
C_{11}	7.14	7.48	7.15	6.69	5.10
C_{12}	3.88	4.41	3.85	3.54	3.83
C_{44}	1.56	1.31	1.30	1.26	0.52

#1 $(Mg_{0.62}Fe_{0.36}Ca_{0.02})_3Al_2Si_3O_{12}$ present study
#2 $(Mg_{0.21}Fe_{0.76}Ca_{0.03})_3Al_2Si_3O_{12}$ Soga (1967)
#3 $(Fe_{0.46}Mn_{0.54})_3Al_2Si_3O_{12}$ Wang and Simmons (1974)
#4 $(Fe_{0.52}Mn_{0.46}Ca_{0.01})_3Al_2Si_3O_{12}$ Isaak and Graham (1976)
#5 $(Fe_{0.08}Mn_{0.07}Ca_{0.85})_3Al_2Si_3O_{12}$ Halleck (1973)

Tables 4.4 and 4.6 illustrate the effects of chemical composition on the elastic moduli of garnet. The variations in garnet chemistry across the pyralspite series do not substantially affect the magnitudes of the elastic moduli or their pressure derivatives. This indicates that the elasticity of the pyralspite garnets is controlled by the Al-O and Si-O bonds and the resultant coordination polyhedra, with the atom in the 8-fold coordination site having little effect on the elastic properties of the garnet lattice.

4.3 Olivine

4.3.1 Specimen description

The nine independent elastic constants of single-crystal olivine $(Mg,Fe)_2SiO_4$ (space group Pbnm) were determined over the 3 GPa pressure range. It was necessary to use four crystals of olivine in order to measure the travel-times of the twelve modes of wave propagation required in the calculation of the elastic constants. Four large crystals of San Carlos olivine were kindly provided by Prof. D.L. Kohlstedt of Cornell University. The presence of low-angle tilt and twist boundaries within these crystals (Ricoult and Kohlstedt, 1983) results in a small uncertainty in each wave propagation direction. The lattice rotations across such boundaries are random rather than cumulative with at most a 2° mismatch between grains, and a total misorientation across each crystal of less than 3°. Calculations based on the method of Waterman (1957) indicate that a crystal misorientation of 2° would perturb the measured elastic wave velocities by less than 0.1%.

The four olivine crystals of essentially the same composition (see Table 4.7) were prepared with pairs of parallel (±0.5°) faces oriented to enable the measurement of the twelve modes necessary for the calculation of the pressure dependence of the nine independent elastic constants. The six on-diagonal moduli were measured on crystal #1 (see Figure 4.5) which was a magnificent specimen with no visible flaws or inclusions, cut from a large single crystal of San Carlos olivine. The three off-diagonal moduli were measured on crystals #2-#4. Crystals #2 and #3 were both long rectangular prisms, while crystal #4 was a small hexagonal prism (see Figure 4.6). These three crystals all contained

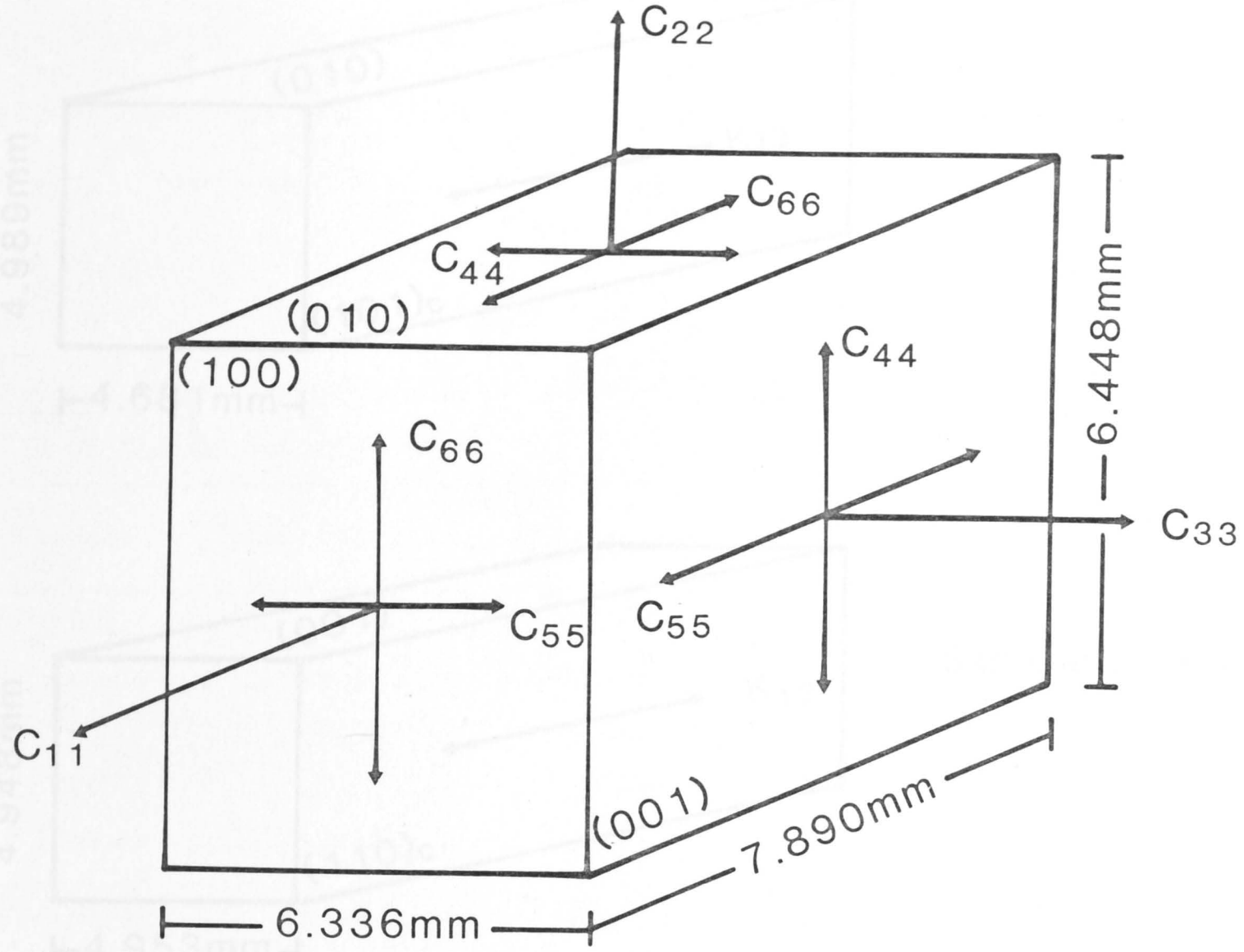

San Carlos # 1

Figure 4.5 Propagation and polarization directions for the elastic moduli determined on the San Carlos olivine crystal #1.

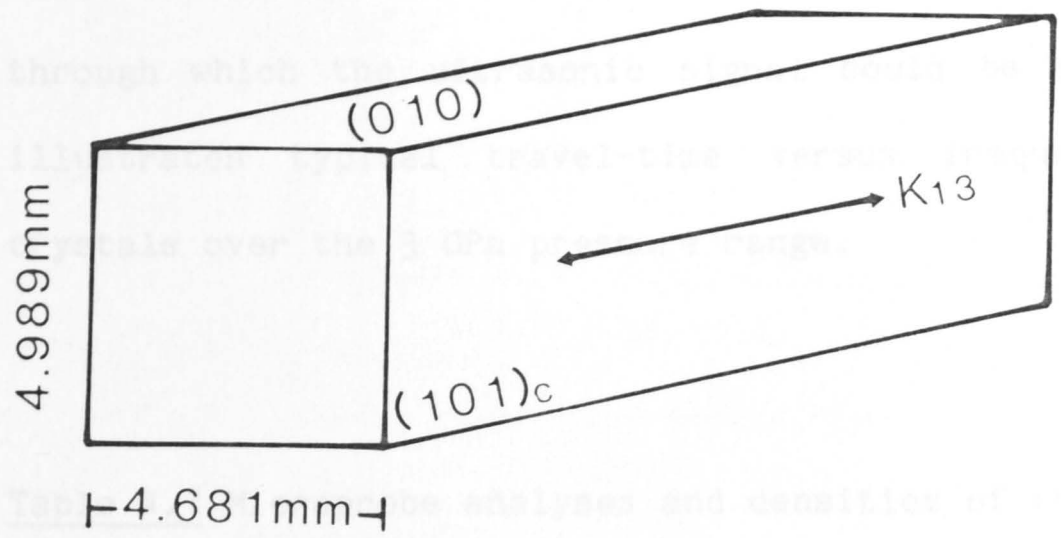

San Carlos # 2

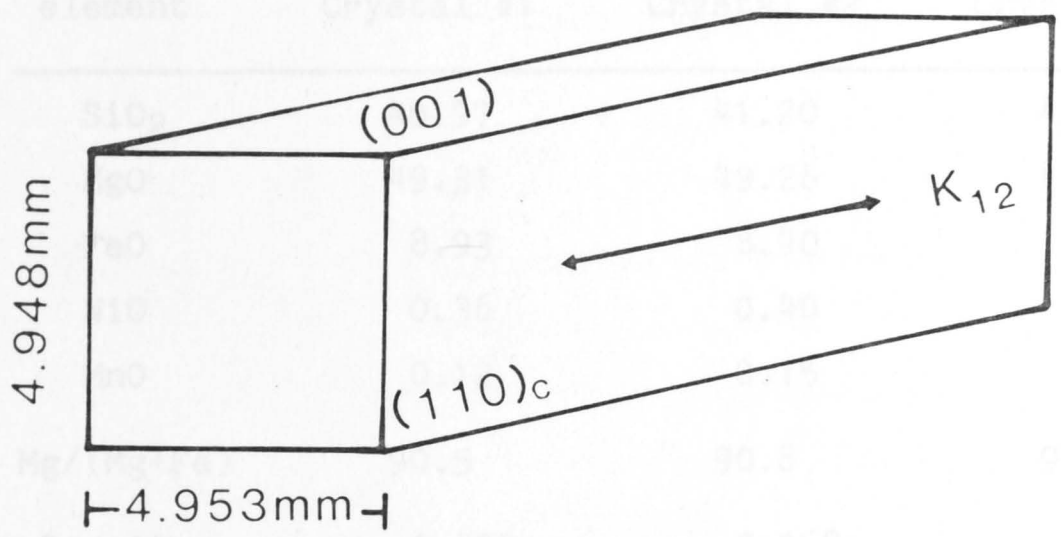

San Carlos # 3

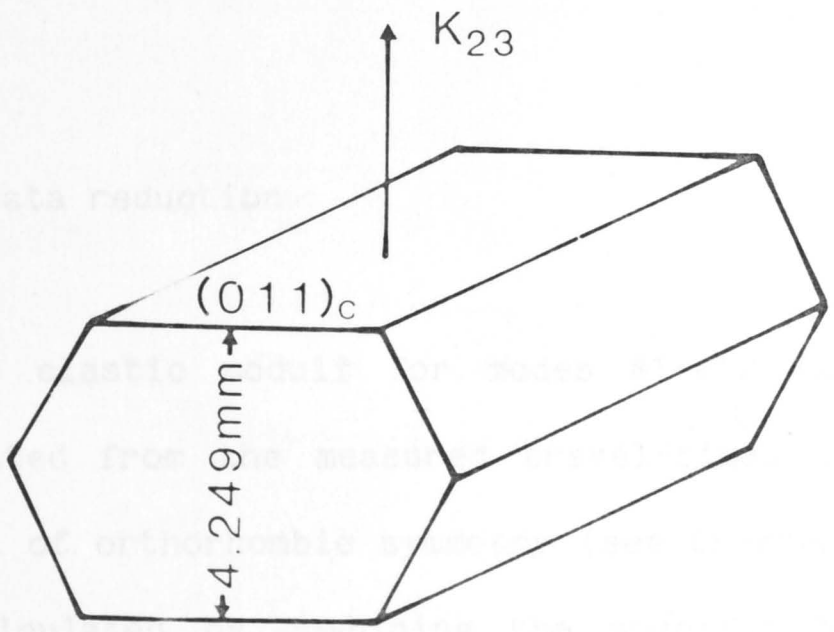

San Carlos # 4

Figure 4.6 Propagation and polarization directions for the elastic moduli determined on the San Carlos olivine crystals #2, #3 and #4.

minor inclusions and cracks; however, each had a region of gem quality through which the ultrasonic signal could be propagated. Figure 4.7 illustrates typical travel-time versus frequency plots for these crystals over the 3 GPa pressure range.

Table 4.7 Microprobe analyses and densities of the four single-crystals of San Carlos olivine.

element	Crystal #1	Crystal #2	Crystal #3	Crystal #4
SiO_2	40.97	41.20	41.19	40.95
MgO	49.31	49.26	49.24	49.15
FeO	8.93	8.90	8.84	8.84
NiO	0.36	0.40	0.40	0.40
MnO	0.12	0.15	0.14	0.00
Mg/(Mg+Fe)	90.5	90.8	90.6	90.6
Density g cm^{-3}	3.325	3.368	3.347	3.349

4.3.2 Data reduction

The elastic moduli for modes #1-#12 (see Eqns. 2.45-2.52) were calculated from the measured travel-times using Cook's method for a crystal of orthorhombic symmetry (see Chapter 2). The specific heat c_p was calculated by combining the specific heats for the end-members forsterite (118.6 J mol^{-1} K^{-1}, Robie et al., 1982b) and fayalite (131.9 J mol^{-1} K^{-1}, Robie et al., 1982a) to give the specific heat

$$c_p = 817 \text{ J kg}^{-1} \text{ K}^{-1} \qquad (4.5)$$

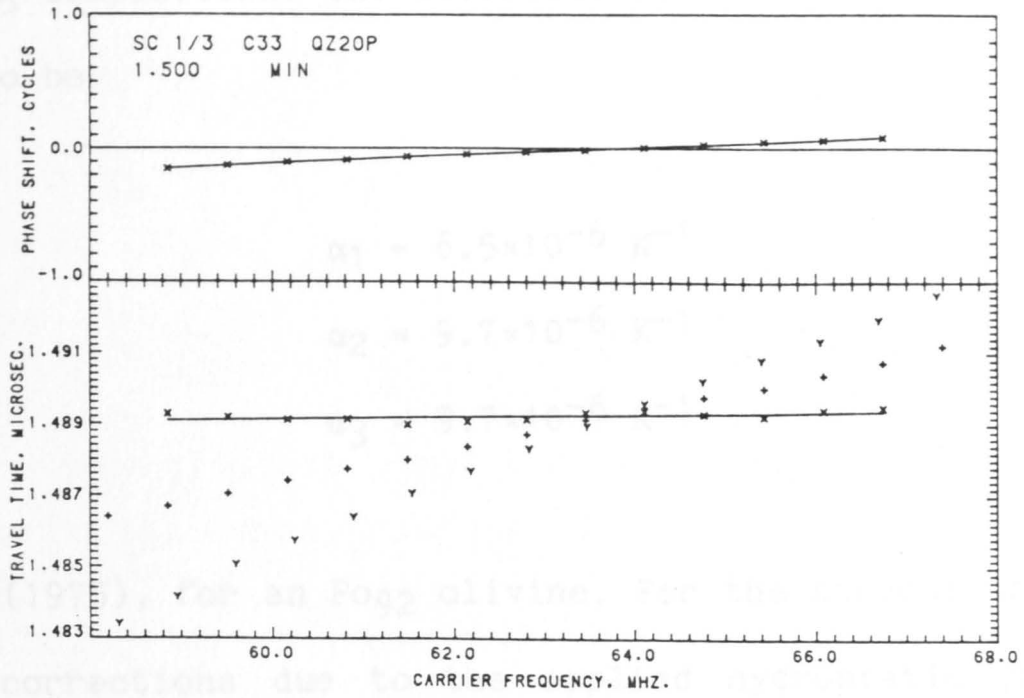

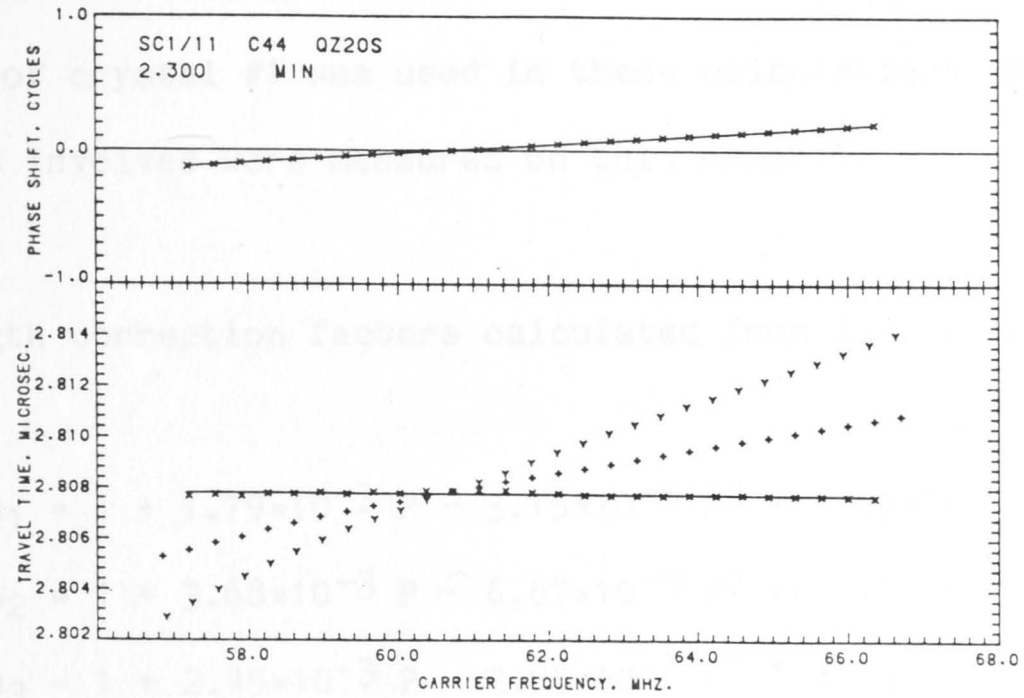

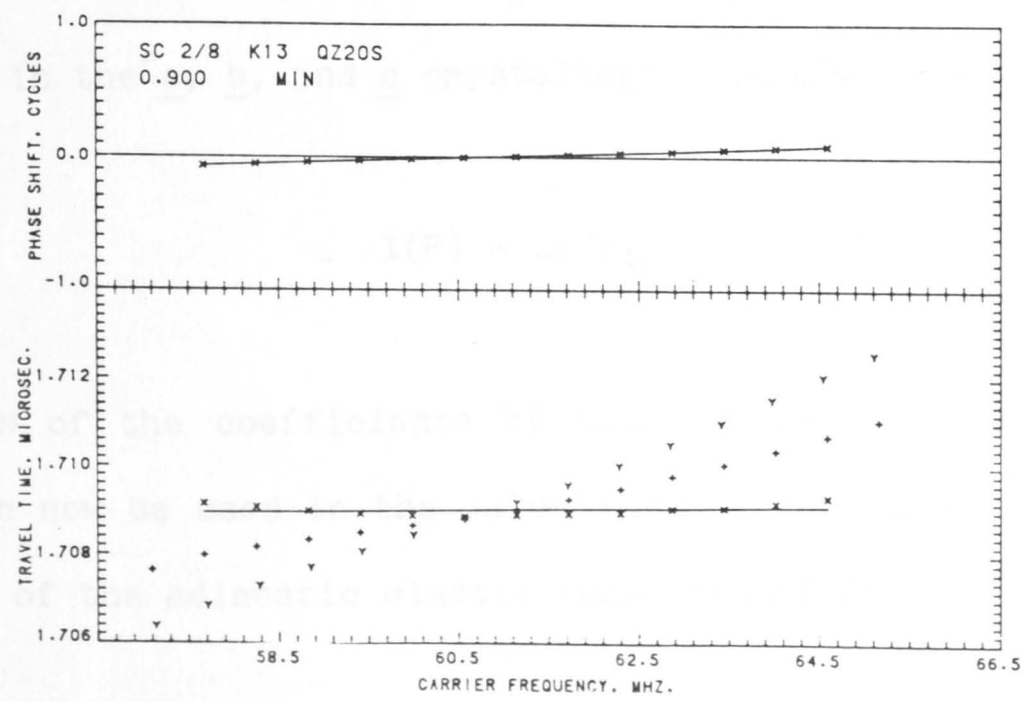

Figure 4.7 Phase comparison data for the compressional modulus C_{33}, the shear modulus C_{44} (mode 11) and the quasi-shear modulus K_{13} of olivine at 1.50 GPa, 2.30 GPa and 0.90 GPa respectively.

for an $Fo_{90.5}$ composition. The coefficients of linear thermal expansion were taken to be

$$\alpha_1 = 6.5\times10^{-6}\ K^{-1}$$
$$\alpha_2 = 9.7\times10^{-6}\ K^{-1}$$
$$\alpha_3 = 9.7\times10^{-6}\ K^{-1} \qquad (4.6)$$

from Suzuki (1975), for an Fo_{92} olivine. For the purpose of calculating the length corrections due to the applied hydrostatic pressure, all four crystals were assumed to have the same density and composition. The density of crystal #1 was used in these calculations as nine of the twelve modes involved were measured on this crystal.

The length correction factors calculated from Eqn. 2.56 are:

$$s_1 = 1 + 1.79\times10^{-3}\ P - 3.15\times10^{-5}\ P^2 + 9.85\times10^{-7}\ P^3$$
$$s_2 = 1 + 3.68\times10^{-3}\ P - 6.67\times10^{-5}\ P^2 + 2.11\times10^{-6}\ P^3$$
$$s_3 = 1 + 2.45\times10^{-3}\ P - 3.95\times10^{-5}\ P^2 + 1.69\times10^{-6}\ P^3 \qquad (4.7)$$

for lengths in the a, b, and c crystallographic directions, where

$$l(P) = l_0/s_i \qquad i = 1,2,3. \qquad (4.8)$$

These values of the coefficients of axial strains due to hydrostatic pressure can now be used in the calculation of the isothermal pressure derivatives of the adiabatic elastic constants of San Carlos olivine.

The calculated moduli for each of the 12 modes at room pressure, with the first and second pressure derivatives of the moduli also calculated at room pressure are tabulated in Table 4.8. The moduli

(C_{ij}, $i \neq j$) calculated from the quasi-compressional and quasi-shear modes K_{ij} are also tabulated. Figures 4.8-4.11 illustrate the behaviour of the moduli with increasing pressure.

Table 4.8 The zero-pressure elastic moduli of $Fo_{90.5}$ olivine with the first and second pressure-derivatives calculated at zero-pressure.

Crystal/Mode	Modulus	Cij /Gpa	$\partial C/\partial P$	$\partial^2 C/\partial P^2$ /GPa^{-1}
1/ 1	C_{11}	320.2±0.4	7.40±0.06	-0.40±0.04
1/ 2	C_{22}	195.9±0.3	5.53±0.04	-0.20±0.03
1/ 3	C_{33}	233.7±0.3	6.08±0.04	-0.36±0.04
1/ 4	C_{44}	63.5±0.1	2.20±0.03	-0.19±0.02
1/11	C_{44}	63.6±0.1	2.26±0.03	-0.19±0.01
1/ 5	C_{55}	77.5±0.2	1.71±0.02	-0.15±0.01
1/10	C_{55}	76.4±0.2	1.74±0.02	-0.15±0.01
1/ 6	C_{66}	78.1±0.1	2.67±0.05	-0.21±0.02
1/12	C_{66}	78.0±0.1	2.39±0.05	-0.21±0.01
3/ 7(S)	K_{12}	88.8±0.1	1.24±0.01	-0.05±0.01
2/ 8(S)	K_{13}	100.1±0.2	1.45±0.01	-0.12±0.01
4/ 9(P)	K_{23}	210.1±0.4	7.28±0.06	-0.48±0.04
7+ 6	C_{12}	67.8±0.3	4.18±0.04	-0.21±0.04
7+12	C_{12}	67.8±0.3	4.15±0.04	-0.21±0.04
9+ 5	C_{13}	70.6±0.3	3.89±0.04	-0.15±0.04
9+10	C_{13}	70.6±0.3	3.89±0.04	-0.16±0.04
8+ 4	C_{23}	77.0±0.4	4.43±0.07	-0.28±0.07
8+11	C_{23}	77.0±0.4	4.32±0.07	-0.29±0.07

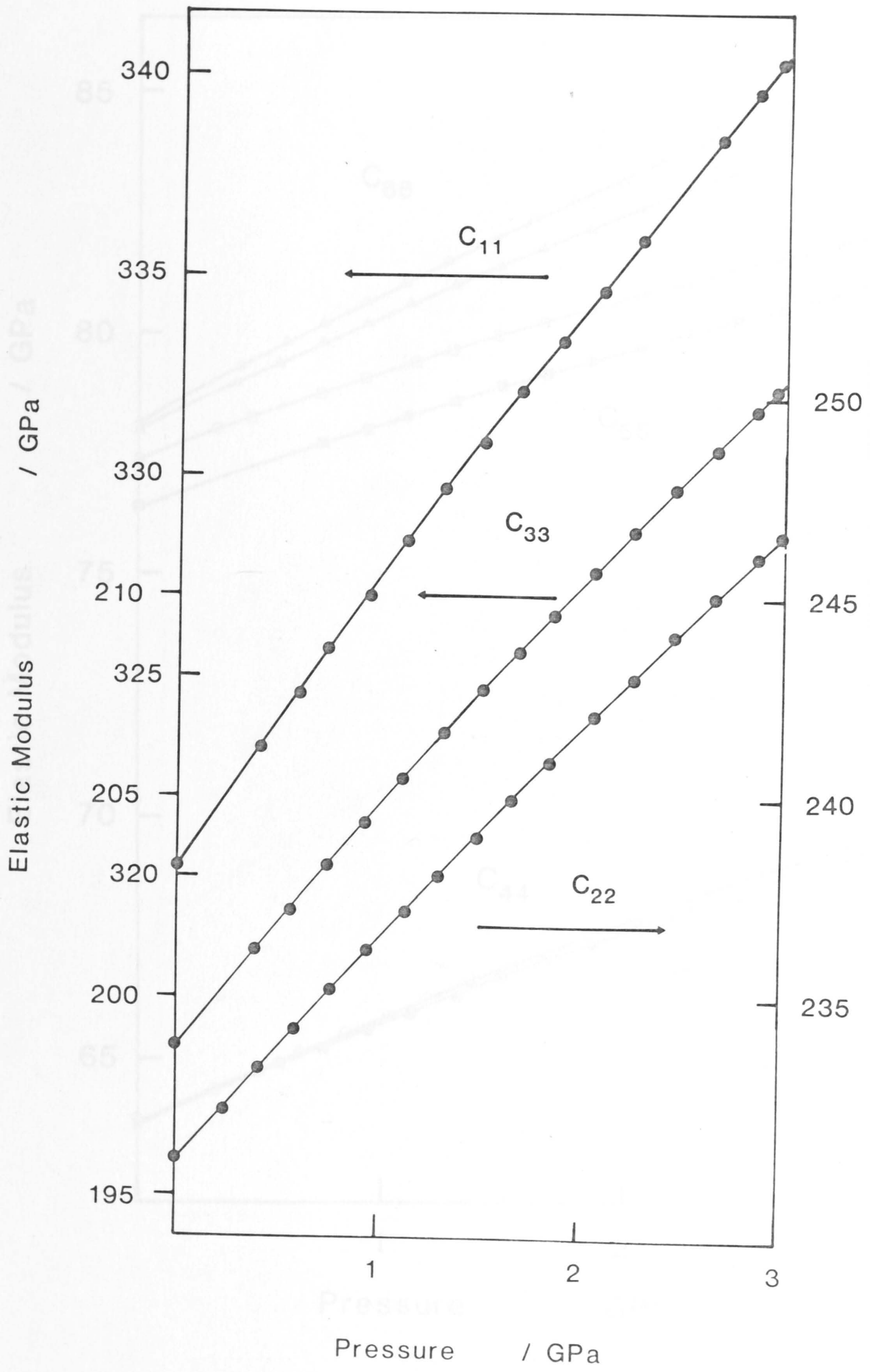

Figure 4.8 The variation with pressure of the compressional moduli C_{11}, C_{22} and C_{33} of olivine. The uncertainties in modulus are everywhere less than the diameter of the plotting symbols.

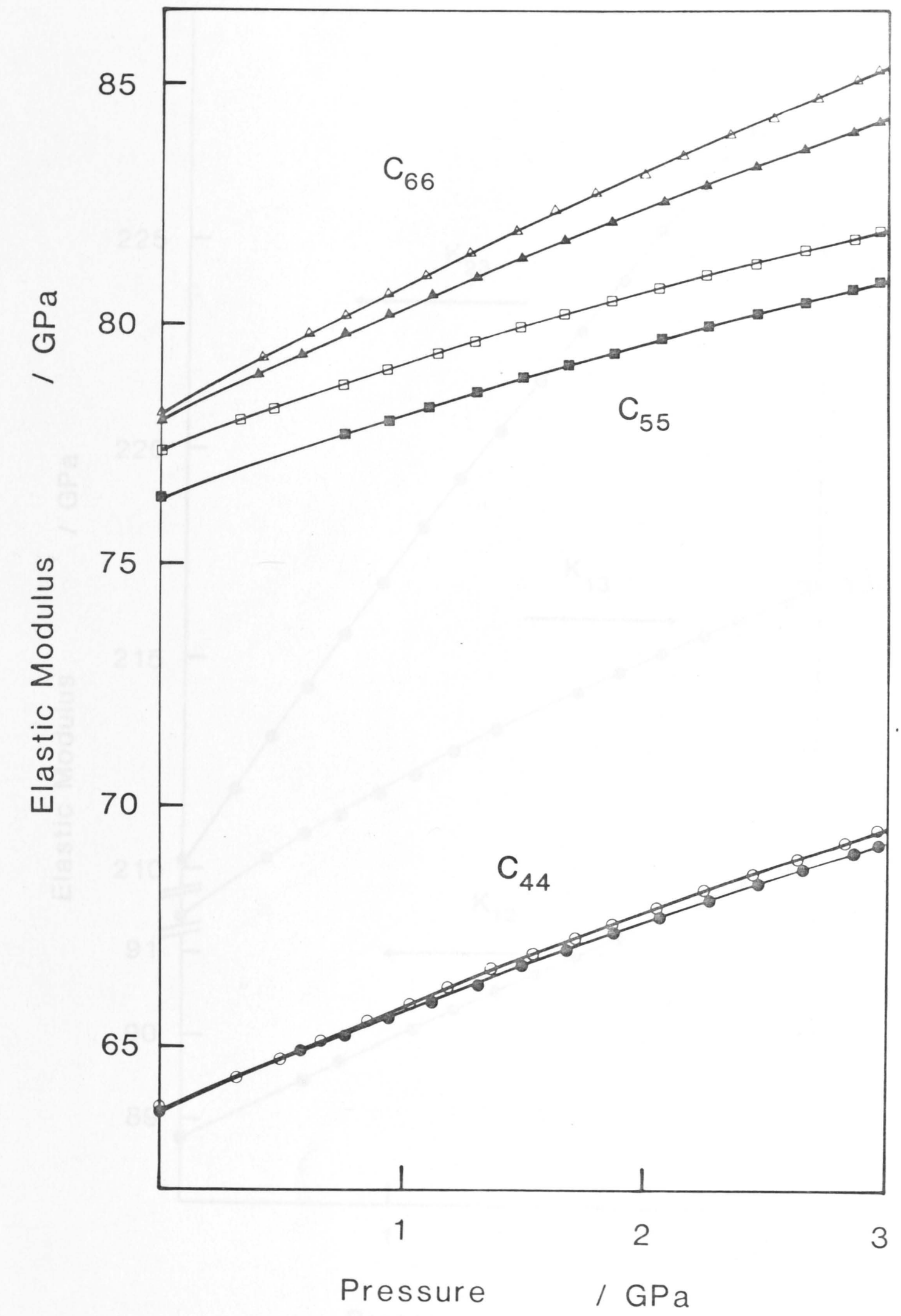

Figure 4.9 The variation with pressure of the shear moduli C_{44} (modes 4 - solid symbol, and 11 - hollow symbol), C_{55} (modes 5 - hollow symbol, and 10 - solid symbol) and C_{66} (modes 6 - hollow symbol, and 12 - solid symbol) of olivine. The uncertainties in modulus are everywhere less than the diameter of the plotting symbols.

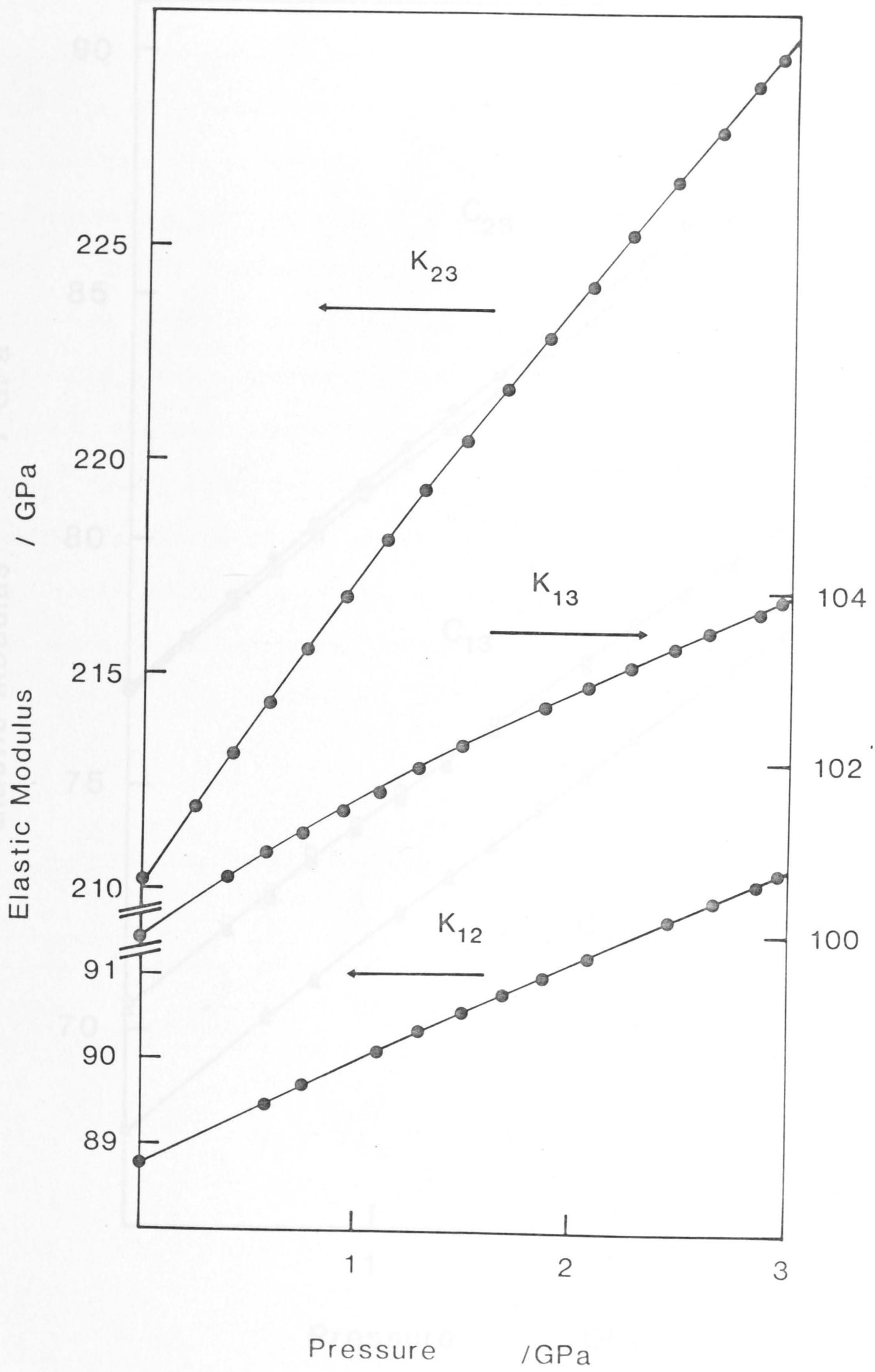

Figure 4.10 The variation with pressure of the quasi-shear modes K_{12} and K_{13}, and the quasi-compressional mode K_{23} of olivine. The uncertainties in modulus are everywhere less than the diameter of the plotting symbols.

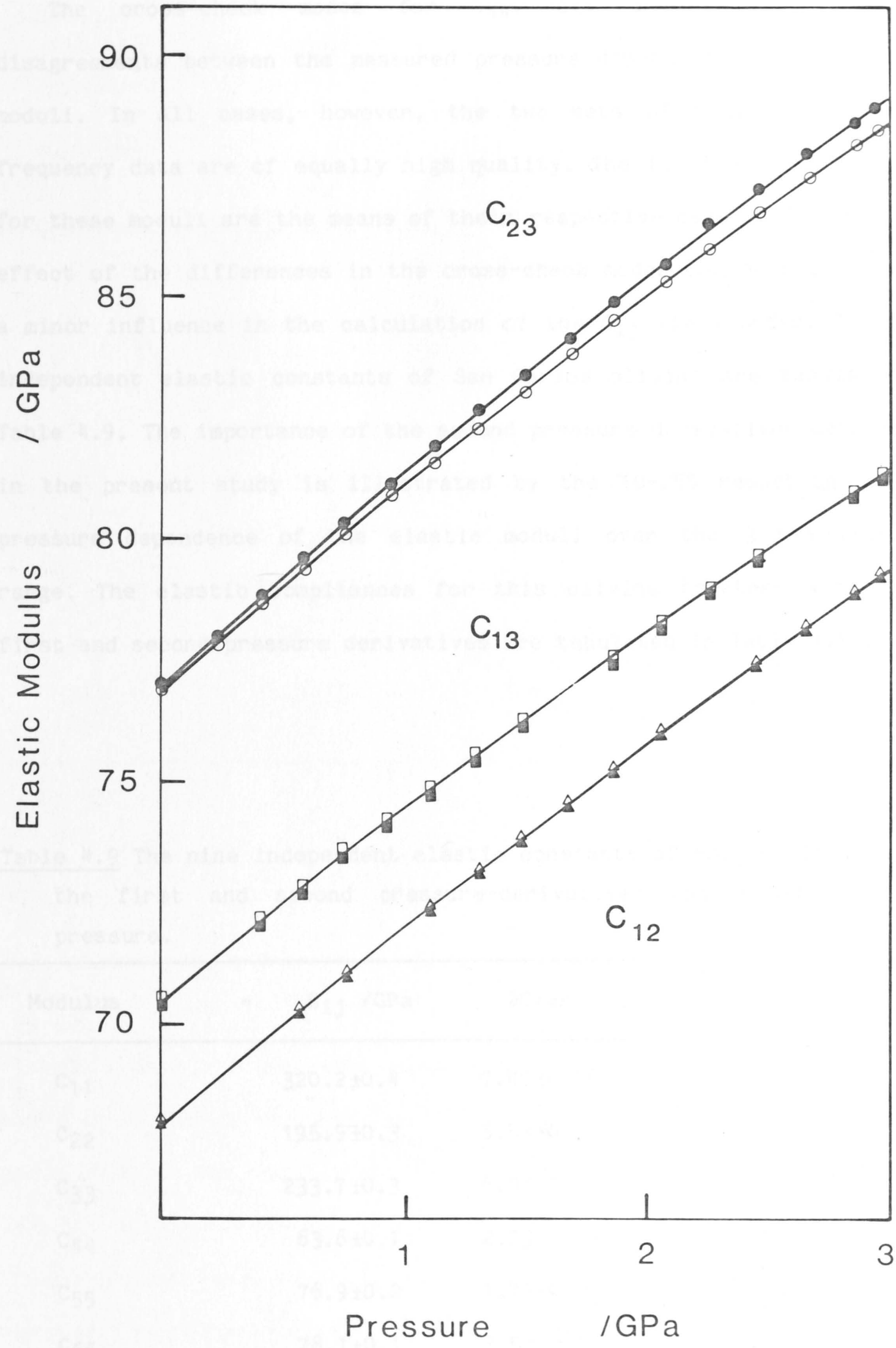

Figure 4.11 The variation with pressure of the moduli C_{12}, C_{13} and C_{23} of olivine. These moduli are calculated from the quasi-compressional and quasi-shear K_{ij} modes and the shear modes $C_{66}(6)$, $C_{55}(5)$ and $C_{44}(11)$ - hollow symbols, and $C_{66}(12)$, $C_{55}(10)$ and $C_{44}(4)$ - solid symbols, respectively.

The cross-check modes for C_{44}, C_{55} and C_{66} show slight disagreements between the measured pressure dependence of the elastic moduli. In all cases, however, the two sets of travel-time versus frequency data are of equally high quality. The final tabulated values for these moduli are the means of their respective measured values. The effect of the differences in the cross-check modes can be seen to have a minor influence in the calculation of the C_{ij} ($i \neq j$) modes. The nine independent elastic constants of San Carlos olivine are tabulated in Table 4.9. The importance of the second pressure derivatives determined in the present study is illustrated by the 10-25% reduction in the pressure dependence of the elastic moduli over the 3 GPa pressure range. The elastic compliances for this olivine together with their first and second pressure derivatives are tabulated in Table 4.10.

Table 4.9 The nine independent elastic constants of $Fo_{90.5}$ olivine with the first and second pressure-derivatives calculated at zero-pressure.

Modulus	C_{ij} /GPa	$\partial C/\partial P$	$\partial^2 C/\partial P^2$ /GPa^{-1}
C_{11}	320.2±0.4	7.40±0.06	-0.40±0.04
C_{22}	195.9±0.3	5.53±0.04	-0.20±0.03
C_{33}	233.7±0.3	6.08±0.04	-0.36±0.04
C_{44}	63.6±0.1	2.23±0.03	-0.19±0.02
C_{55}	76.9±0.2	1.73±0.02	-0.15±0.01
C_{66}	78.1±0.1	2.53±0.07	-0.21±0.01
C_{12}	67.8±0.3	4.17±0.04	-0.21±0.04
C_{13}	70.6±0.3	3.89±0.04	-0.16±0.04
C_{23}	77.0±0.4	4.38±0.07	-0.29±0.07

Table 4.10 The zero-pressure elastic compliances of $Fo_{90.5}$ olivine with the first and second pressure derivatives calculated at zero-pressure.

Modulus	S_{ij} /(10^{-3} GPa^{-1})	$\partial S/\partial P$ /(10^{-3} GPa^{-2})	$\partial^2 S/\partial P^2$ /(10^{-3} GPa^{-3})
S_{11}	3.48±0.05	-0.057±0.003	0.003±0.001
S_{22}	6.10±0.08	-0.103±0.005	0.003±0.001
S_{33}	5.08±0.08	-0.081±0.004	0.003±0.001
S_{44}	15.7 ±0.2	-0.54 ±0.04	0.034±0.001
S_{55}	13.0 ±0.3	-0.29 ±0.03	0.017±0.004
S_{66}	12.8 ±0.2	-0.41 ±0.05	0.025±0.007
S_{12}	-0.91±0.01	-0.012±0.001	0.011±0.003
S_{13}	-0.75±0.01	-0.000±0.001	0.001±0.001
S_{23}	-1.74±0.02	-0.016±0.001	-0.003±0.001

4.3.3 Elasticity and crystal chemistry

The elastic constants of single crystals of olivine and the end-members forsterite and fayalite have been measured previously (see Table 4.11). The room pressure elastic constants of single-crystal natural olivine ($Fo_{87.8}$) have been determined by Brillouin scattering (Yeganeh-Haeri and Vaughan, 1984), while the room pressure elastic constants of single-crystal fayalite (Fe_2SiO_4) have been determined by the rectangular parallelopiped resonance method (Sumino, 1979) and the pulse superposition method (Graham et al., 1982).

Kumazawa and Anderson (1969) measured the elastic constants of both

a natural olivine ($Fo_{92.7}$), and a synthetic forsterite (see Tables 4.11 and 4.12). The elastic constants were determined over a 0.2 GPa pressure range using the pulse superposition method to measure the repetition frequencies required to bring successive echoes into phase. The elastic constants were calculated from the relationship

$$C_i = 4\ L^2\ F_i^2\ \rho \qquad (4.9)$$

where F_i is the inverse of the two way travel-time. The measured crystal dimensions, density and travel-times, and the calculated elastic moduli were assumed to behave linearly with pressure, resulting in the linear pressure dependence of the elastic constant

$$C = C_0 + C_0(2b - 2\beta_j - B) \qquad (4.10)$$

for

$$C_0 = 4\ \rho_0\ (L_0)^2\ (F_{i0})^2 \qquad (4.11)$$

where the subscript '0' refers to the room pressure value, β_j is the isothermal linear compressibility, B is the isothermal volume compressibility, and

$$b = dF_i/dP\ F^{-1}. \qquad (4.12)$$

The elastic constants of a synthetic forsterite have also been measured by Graham and Barsch (1969) (see Tables 4.11 and 4.12). Once again a pulse superposition technique was used to determine the repetition delay times. These delay times measured over a 1 GPa pressure range were found to have a linear pressure dependence. The pressure dependence of the elastic moduli was calculated using an algorithm developed by Thurston and Brugger (1964). This involved calculating a natural wave-velocity for the crystal at pressure using

the zero pressure length and density measurements. This natural velocity has a pressure dependence

$$\left.\frac{\partial(\rho W^2)}{\partial P}\right|_{P=0} = (\rho_0 W^2)_0' = \frac{2\,\rho_0\,(V_0)^2}{P}\left(\frac{T_0 - 1}{T_r}\right) \qquad (4.13)$$

where T_r is the measured repetition delay time (two way travel-time) at pressure, and T_0 is the measured repetition delay time at room pressure. This pressure derivative of the natural velocity was then used to calculate the pressure derivative of the real velocity and hence the derivative of the elastic modulus;

$$-(\rho V^2)_0' = -(\rho_0 W^2)_0' + 2\,\rho_0\,(V_0)^2\,N_k N_m\,S^T_{kmaa} - \rho_0\,(V_0)^2\,S^T_{iiaa} \qquad (4.14)$$

where the S^T_{ijkl} are the isothermal elastic compliances, and the N_i are the direction cosines for the direction of propagation of the wave. This procedure adds correction terms for the effect of pressure on length and density to the measured velocity, in contrast to the algorithm develped by Cook (1957) and used in the present analysis in which the correction terms are applied to the measured travel-times, which are then used to calculate the velocities.

The close ageement between the zero-pressure elastic moduli determined by Kumazawa and Anderson (1969) for an $Fo_{92.7}$ olivine and the present study is illustrated in Tables 4.11 and 4.12. It is difficult to compare the first pressure derivatives between these two studies as the second pressure derivatives of the present study allow better resolution of the pressure dependences of the elastic moduli. However, the magnitudes of the first pressure derivatives observed in

both studies are in general accord.

The elastic constants of a synthetic forsterite have been determined to 4 GPa (see Tables 4.11 and 4.12) by Brillouin scattering in a gasketted diamond anvil cell (Bassett et al., 1982). The apparently different pressure derivatives obtained in this way (see Table 4.12) are of significantly lower accuracy than the ultrasonic determinations.

Table 4.11 The zero-pressure elastic moduli of a number of olivines of the forsterite-fayalite solid solution series.

Modulus	Fo †	Fo **	Fo ¶	$Fo_{92.7}$ †	$Fo_{90.5}$ ††	$Fo_{87.8}$ *	Fa ¶¶	Fa ***
C_{11}	328.4	329	331	323.7	320.2	315	267.4	267
C_{22}	199.8	200.5	191	197.6	195.9	194	159.8	174
C_{33}	235.3	236.3	230	235.1	233.7	237	220.9	239
C_{44}	65.9	67.2	65.7	64.6	63.6	64	31.6	32.4
C_{55}	81.2	81.4	83.8	78.1	76.9	81	46.7	46.7
C_{66}	80.9	81.1	82.4	79.0	78.1	72	57.3	57.3
C_{12}	63.9	66.3		66.4	67.8	73	93	95
C_{13}	68.8	68.4		71.6	70.6	67	82	99
C_{23}	73.8	72.8		75.6	77.0	80	87	98

† Kumazawa and Anderson (1969)

†† Present study

* Yeganeh-Haeri and Vaughan (1984)

** Graham and Barsch (1969)

¶ Bassett et al (1982)

¶¶ Graham et al. (1982)

*** Sumino (1979)

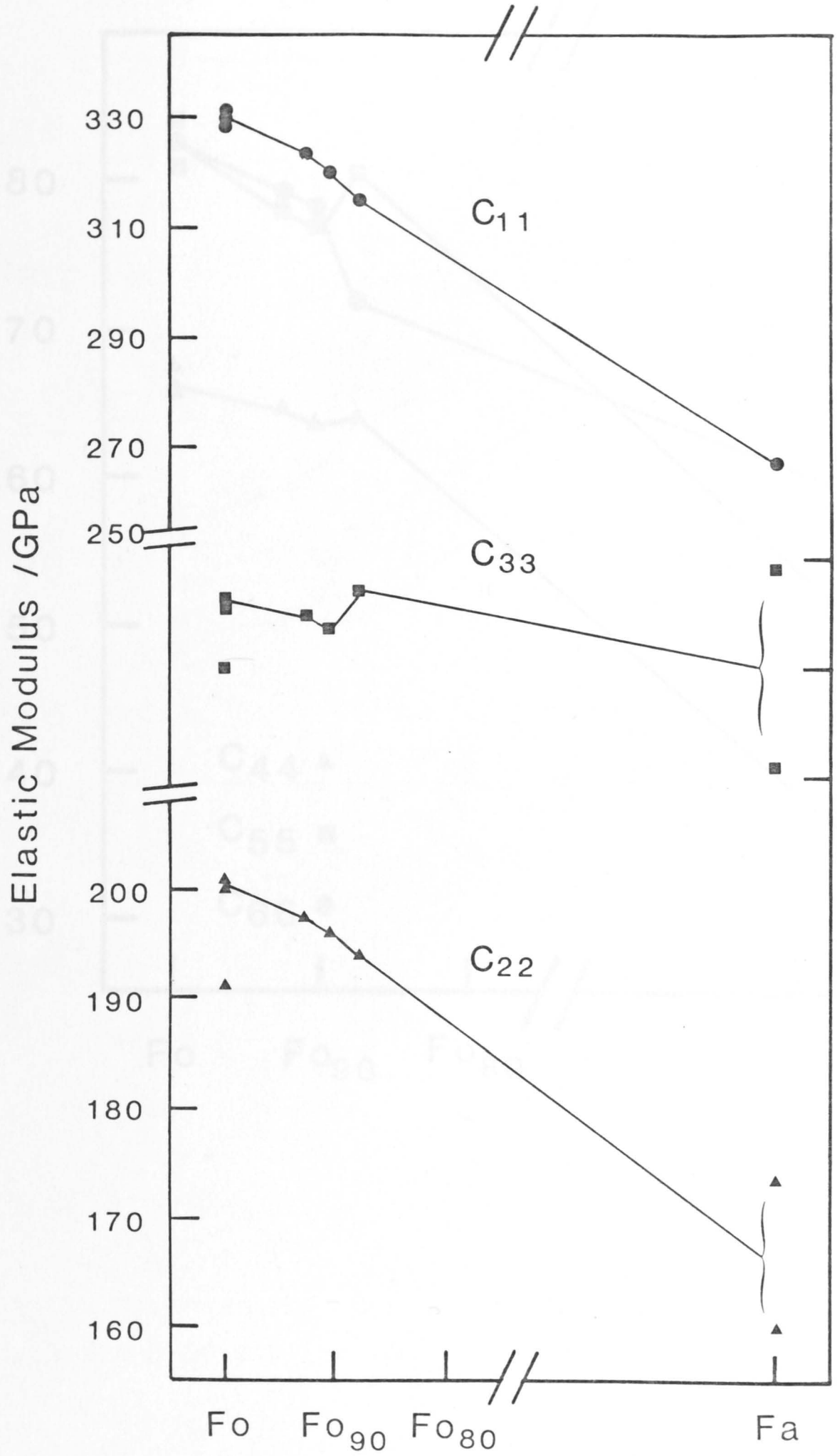

Figure 4.12 The variation with composition of the compressional moduli C_{11}, C_{22} and C_{33} of the ferro-magnesian olivines (see Table 4.11 for details).

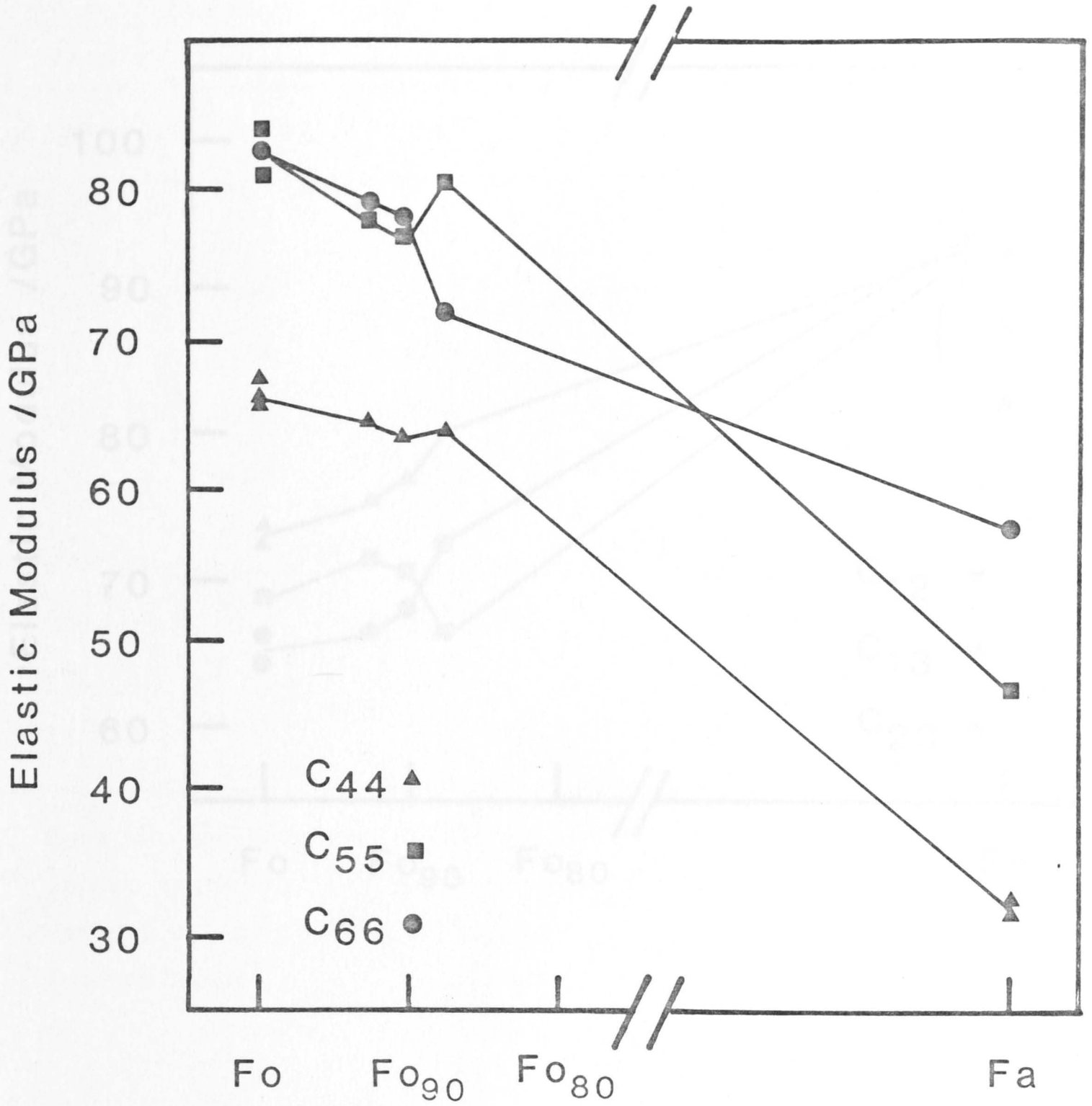

Figure 4.13 The variation with composition of the shear moduli C_{44}, C_{55} and C_{66} of the ferro-magnesian olivines (see Table 4.11 for details).

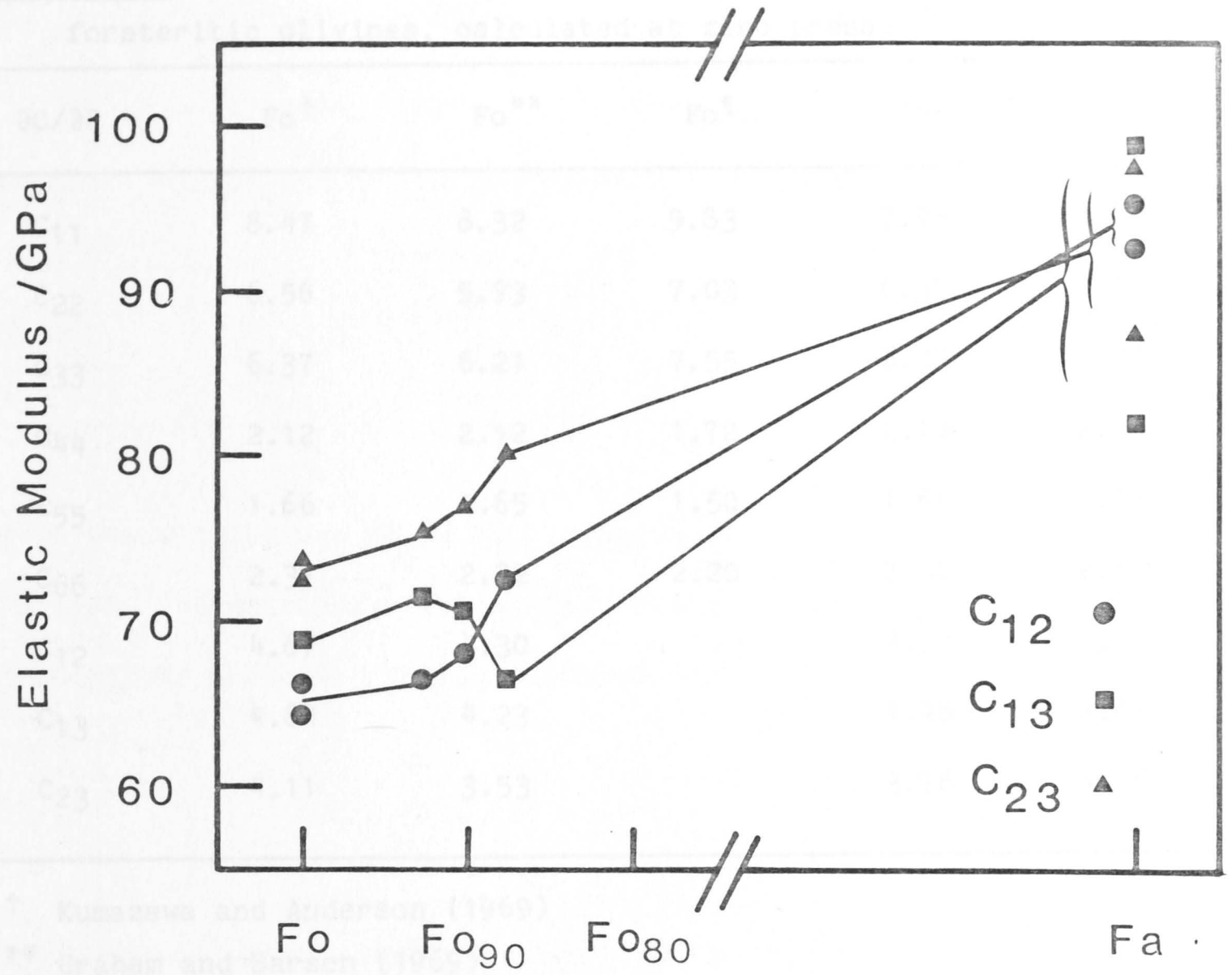

Figure 4.14 The variation with composition of the off-diagonal moduli C_{12}, C_{13} and C_{23} of the ferro-magnesian olivines (see Table 4.11 for details).

Table 4.12 The first pressure derivatives of a number of single crystal forsteritic olivines, calculated at zero pressure.

$\partial C/\partial P$	Fo†	Fo**	Fo¶	$Fo_{92.7}$†	$Fo_{90.5}$††
C_{11}	8.47	8.32	9.83	7.98	7.40
C_{22}	6.56	5.93	7.03	6.37	5.53
C_{33}	6.37	6.21	7.55	6.38	6.08
C_{44}	2.12	2.12	1.72	2.17	2.23
C_{55}	1.66	1.65	1.50	1.64	1.73
C_{66}	2.37	2.32	2.20	2.31	2.53
C_{12}	4.67	4.30		4.74	4.17
C_{13}	4.84	4.23		4.48	3.89
C_{23}	4.11	3.53		3.76	4.38

† Kumazawa and Anderson (1969)

** Graham and Barsch (1969)

¶ Bassett et al. (1982)

†† Present study

Figures 4.12-4.14 illustrate the effect of increasing Fe content in the forsterite end-member. There are some inconsistencies in the measured elastic constants of both the forsterite and fayalite end-members. In the case of forsterite, the agreement between the measurements of Kumazawa and Anderson (1969) and Graham and Barsch (1969) is taken to indicate the correct values of the elastic moduli.

The substitution of Fe for Mg in olivine has the effect of reducing the magnitude of the compressional and shear moduli while increasing the magnitude of the off-diagonal moduli. The measurement of the modulus C_{33} by Graham et al. (1982) is preferred to that of Sumino (1979) as it is difficult to reconcile Sumino's high values of C_{33} with

the trends observed for the other compressional moduli.

Throughout the forsterite-fayalite solid solution series the relative magnitudes of the on-diagonal moduli remain constant with

$$C_{11} > C_{33} > C_{22} \tag{4.15}$$

and

$$C_{66} \approx C_{55} > C_{44} \tag{4.16}$$

with the modulus C_{33} being the least sensitive to addition of Fe to the lattice. The observed off-diagonal moduli show a more complex behaviour between the various studies, although a general trend

$$C_{23} > C_{13} > C_{12} \tag{4.17}$$

is observed among the ultrasonic measurements. The first pressure derivatives of a number of forsteritic olivines have also been measured (see Table 4.12). Here, the small range of compositions over which the pressure dependence of the moduli has been determined together with the variations in measurements between studies creates difficulties in the observation of consistent trends with increasing Fe content. However, the relative magnitudes of the pressure derivatives remains constant, with

$$\partial C_{11}/\partial P > \partial C_{33}/\partial P \approx \partial C_{22}/\partial P \tag{4.18}$$

and

$$\partial C_{66}/\partial P > \partial C_{44}/\partial P > \partial C_{55}/\partial P; \tag{4.19}$$

with the off-diagonal pressure-derivatives showing no consistent trends in the relative magnitudes. The maintenance of the same relative magnitudes of the elastic moduli of these olivines with changing crystal chemistry indicates that these relative magnitudes are controlled mainly by the crystal structure, with substitution of the

octahedrally coordinated atoms (Mg,Fe) causing only minor variations in the lattice elasticity. This observation forms the basis of structural interpretations of the major trends in olivine elasticity (Bass et al., 1984;Au and Weidner, 1985;see Chapter 5)

4.4 Orthopyroxene

4.4.1 Specimen description

Four single crystals of orthopyroxene (see Figure 4.15) (space group Pbca) were required in order to measure the twelve modes of propagation necessary for the calculation of the nine independent elastic constants of a crystal of orthorhombic symmetry.

All four crystals were natural specimens of unknown provenance. In their uncut state they appeared badly weathered and cracked. However, when the outer 1-2 mm of material was removed, each crystal revealed an interior of gem quality material suitable for our use. Each crystal was deep yellow-brown in colour and slightly pleochroic. These pyroxenes were bronzites with Mg/(Mg+Fe) ratios of 78-82.5 (see Table 4.13). One crystal was cut in half and examined for possible zonation in crystal growth by comparing electron-microprobe analyses obtained at 0.5 mm intervals along a traverse across the cut face of the crystal. No change (within the error of the analyses) in the composition was observed.

Irregular semi-coherent needles of amphibole (see Figure 4.16a) were observed by electron-microscopy to be present in these crystals - comprising ~0.1 vol % of each crystal. These needles of hornblende are ~0.2 μm in width (see Figure 4.16b), elongate parallel to [001] in the orthopyroxene lattice, and apparently responsible for [001] interference fringes observed when the crystals are viewed along [010]. These needles are too small to interact directly with the elastic waves of this study (wavelength ~0.1 mm) although scattering from larger heterogeneities associated with the strain fields of the amphibole

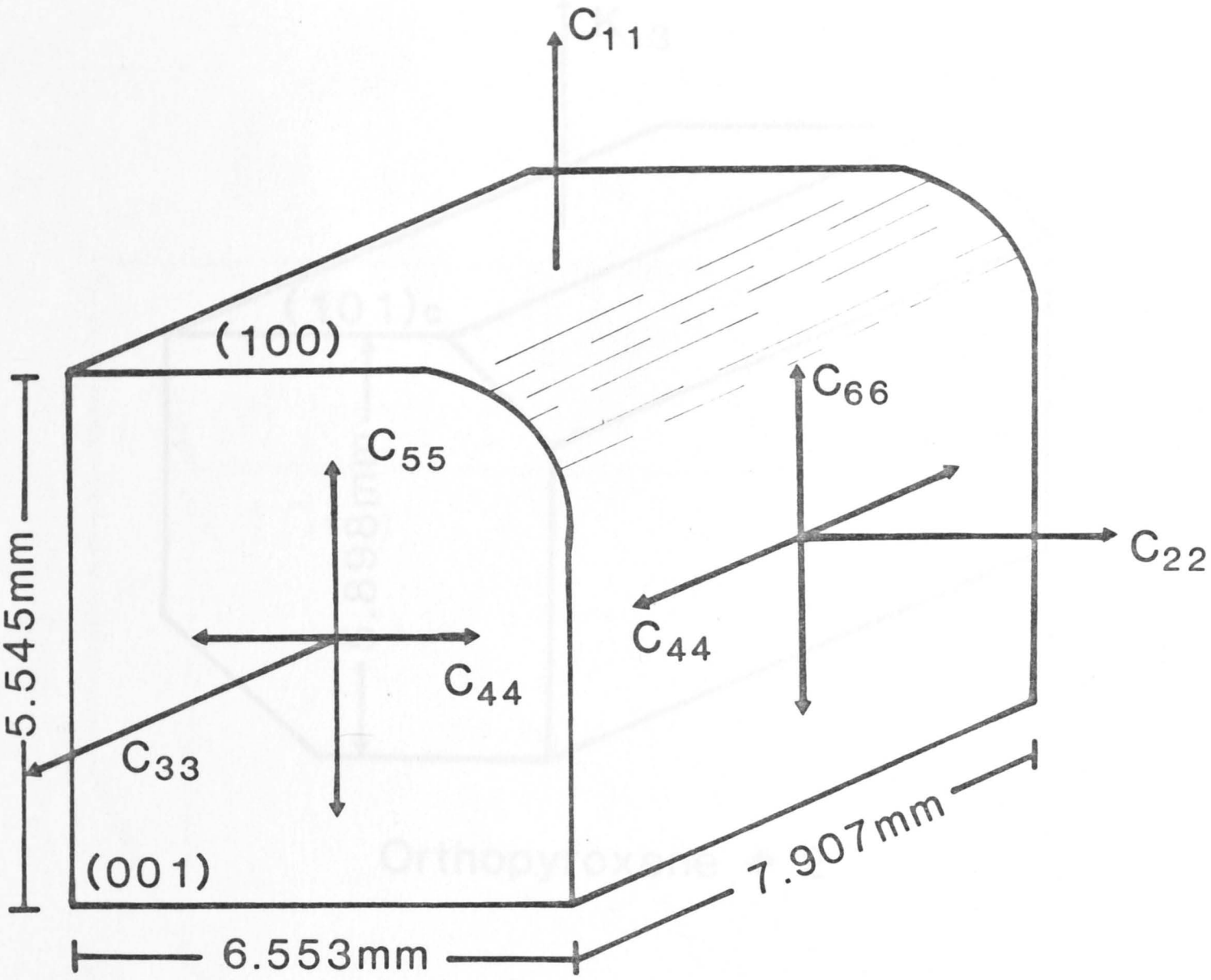

Orthopyroxene # 1

Figure 4.15a Propagation and polarization directions for the elastic moduli determined on the orthopyroxene crystal #1.

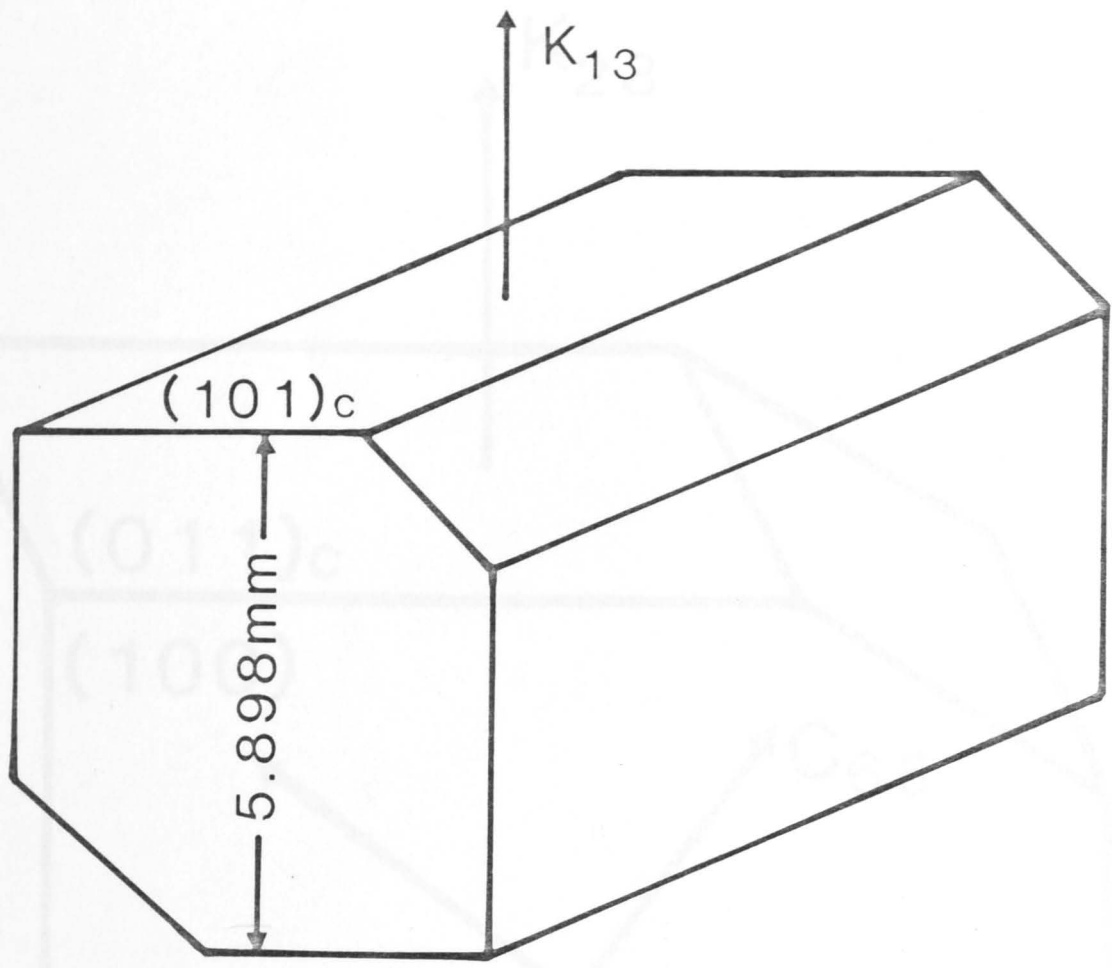

Orthopyroxene # 2

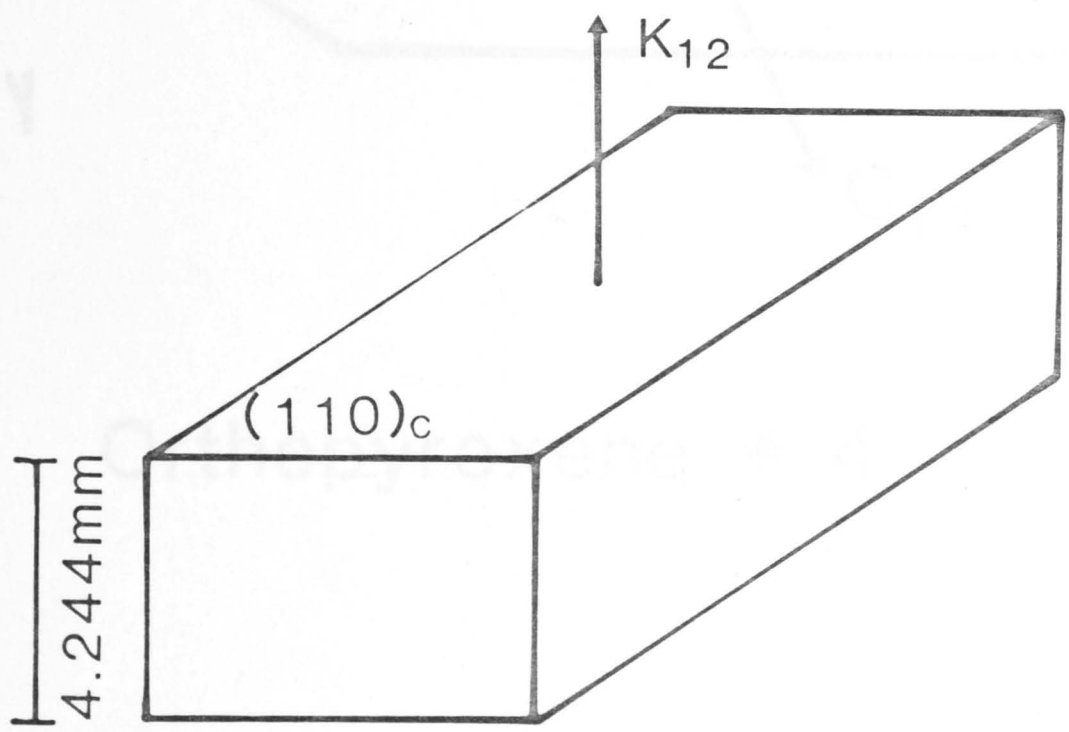

Orthopyroxene # 3

Figure 4.15b Propagation and polarization directions for the elastic moduli determined on the orthopyroxene crystals #2 and #3.

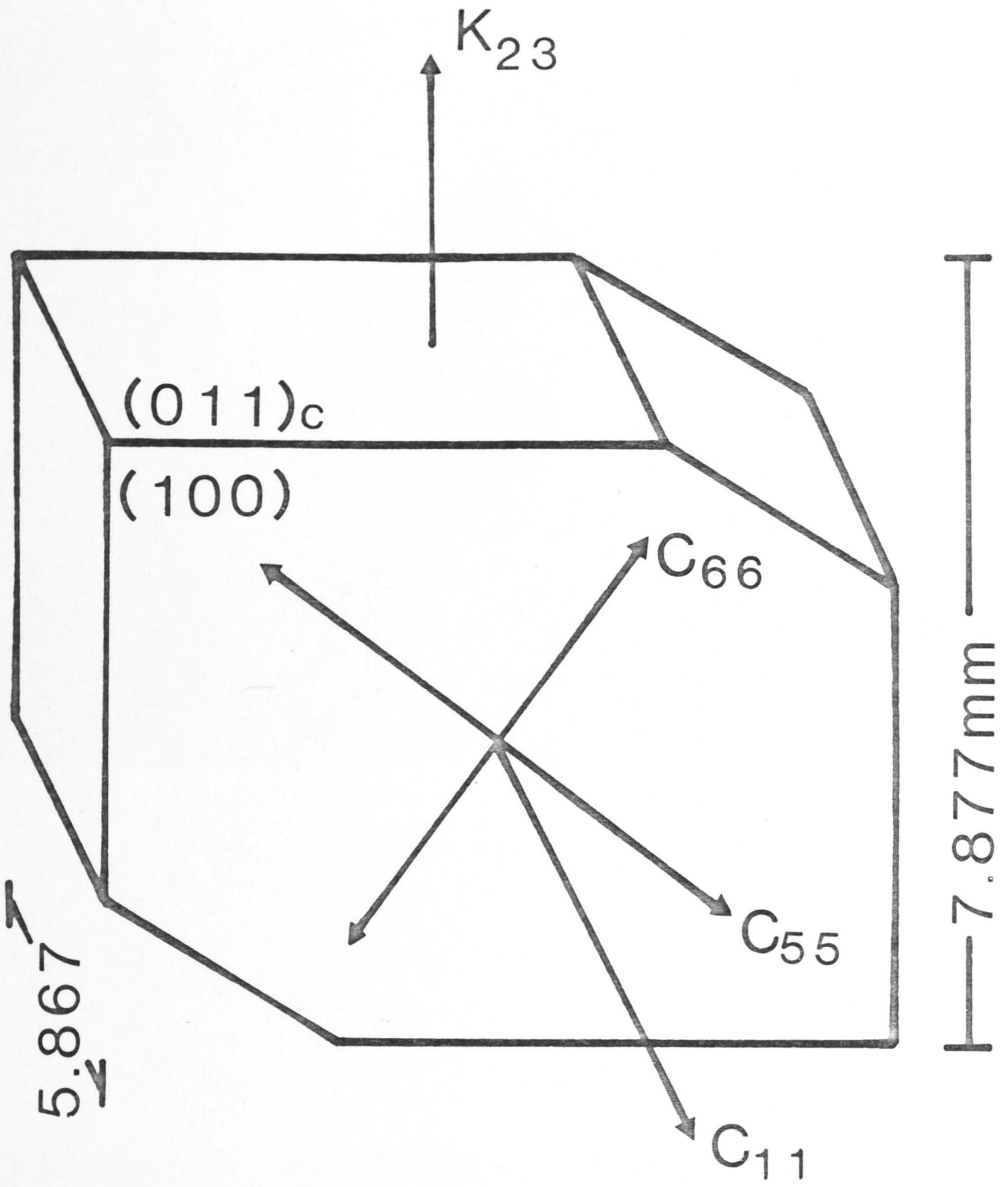

Orthopyroxene # 4

Figure 4.15c Propagation and polarization directions for the elastic moduli determined on the orthopyroxene crystal #4.

Figure 4.16a Election diffraction pattern of orthopyroxene, with the diffraction pattern of the twinned amphibole superimposed on it. (Courtesey of J. Fitz Gerald)

Figure 4.16b Twinned amphibole needles ~0.2μm in width, elongate parallel to [001] of orthopyroxene. (1μm = 6cm)

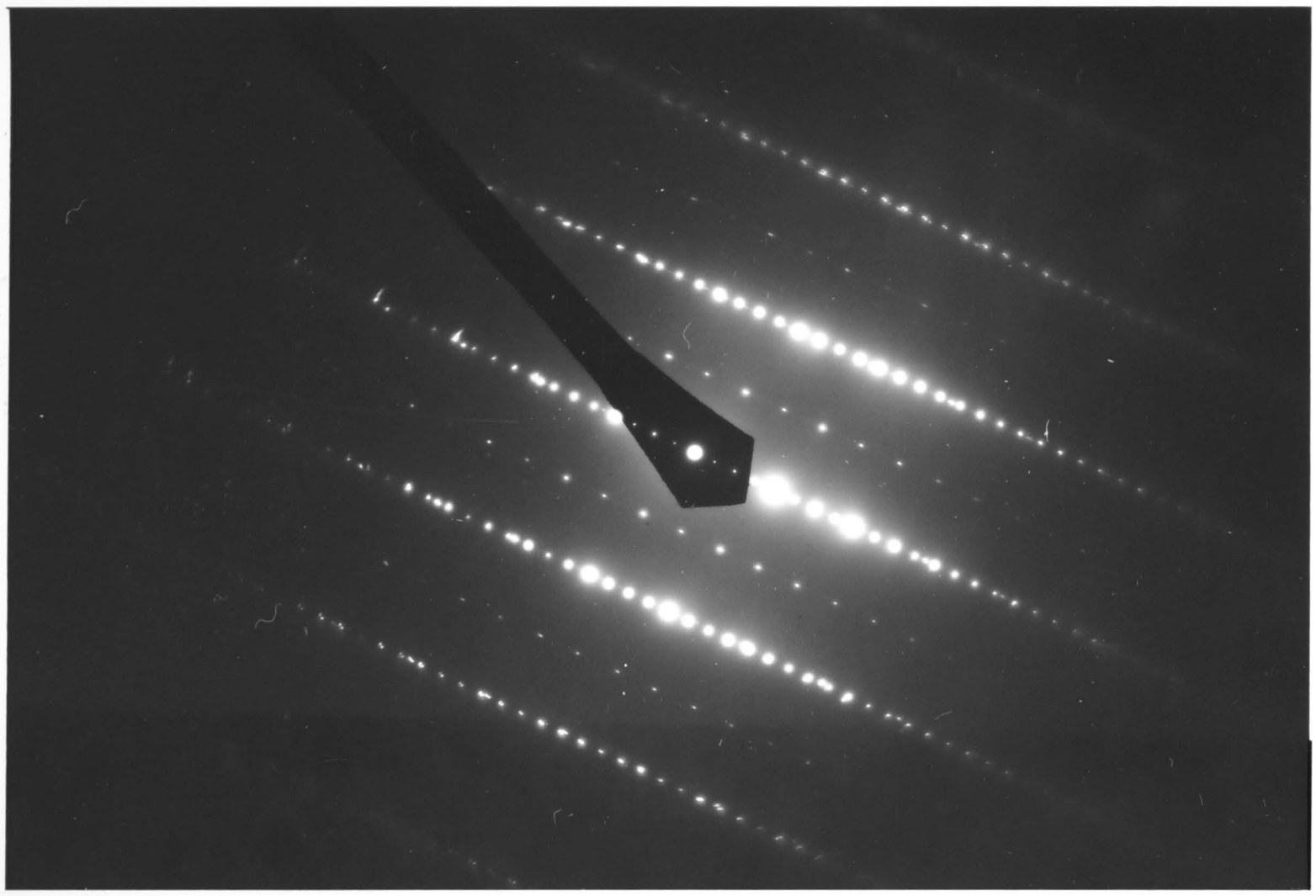

inclusions may account for the observation of relatively high apparent attenuation at the third harmonic frequencies (~60 MHz).

Table 4.13 Electron microprobe analyses and densities of the four bronzites.

element	Crystal #1	Crystal #2	Crystal #3	Crystal #4
SiO_2	56.10	55.40	55.41	55.17
MgO	30.88	29.93	28.80	29.24
FeO	11.68	13.06	14.54	13.69
Al_2O_3	0.90	1.00	1.02	1.20
MnO	0.17	0.20	0.12	0.24
CaO	0.12	0.30	0.17	0.17
Mg/(Mg+Fe)	82.7	80.2	78.0	79.4
Density g cm^{-3}	3.366	3.369	3.395	3.362

The crystal faces were oriented to within 0.5° using the Laue back-reflection technique. Some slight ambiguity remained between the b and c crystallographic directions. This ambiguity was removed by orienting a thin section of one crystal from its electron diffraction pattern and using this as a cross-check for the X-ray orientation.

4.4.2 Data reduction

The elastic constants were calculated from the measured travel-times of the modes of propagation #1-#12 using Cook's algorithm (Eqns. 2.45-2.52) for crystals of orthorhombic symmetry. The signal echoes propagating at the third harmonic (60 MHz) were greatly

attenuated, possibly for the reasons discussed above, and the travel-times measured at this frequency were not of a reproducibly high quality. Therefore, all of the travel-time measurements for waves propagating through the orthopyroxene crystals were made within the fundamental response envelope (20 MHz) of the transducers. Figure 4.17 illustrates typical travel-time versus frequency plots for these crystals at various pressures.

The length correction terms for the effects of hydrostatic pressure were calculated for a crystal density of 3.366 g cm^{-3}. The specific heat was taken as

$$c_p = 768 \text{ J kg}^{-1} \text{ K}^{-1} \qquad (4.20)$$

from JANAF Thermochemical Tables (1971) for an enstatite end-member, $MgSiO_3$. The linear thermal expansion coefficients were

$$\begin{aligned} \alpha_1 &= 1.64\times10^{-5} \text{ K}^{-1} \\ \alpha_2 &= 1.45\times10^{-5} \text{ K}^{-1} \\ \alpha_3 &= 1.68\times10^{-5} \text{ K}^{-1} \end{aligned} \qquad (4.21)$$

from Frisillo and Buljan (1972) for an En_{80} bronzite. The length correction factors calculated from Eqn. 2.56 are;

$$\begin{aligned} s_1 &= 1 + 2.21\times10^{-3} P - 9.78\times10^{-5} P^2 + 1.00\times10^{-5} P^3 \\ s_2 &= 1 + 3.98\times10^{-3} P - 1.31\times10^{-4} P^2 + 5.43\times10^{-6} P^3 \\ s_3 &= 1 + 3.09\times10^{-3} P - 1.88\times10^{-4} P^2 + 1.64\times10^{-5} P^3 \end{aligned} \qquad (4.22)$$

for lengths in the a, b, and c crystallographic directions, where

$$l(P) = l_0/s_i \qquad i = 1,2,3. \qquad (4.23)$$

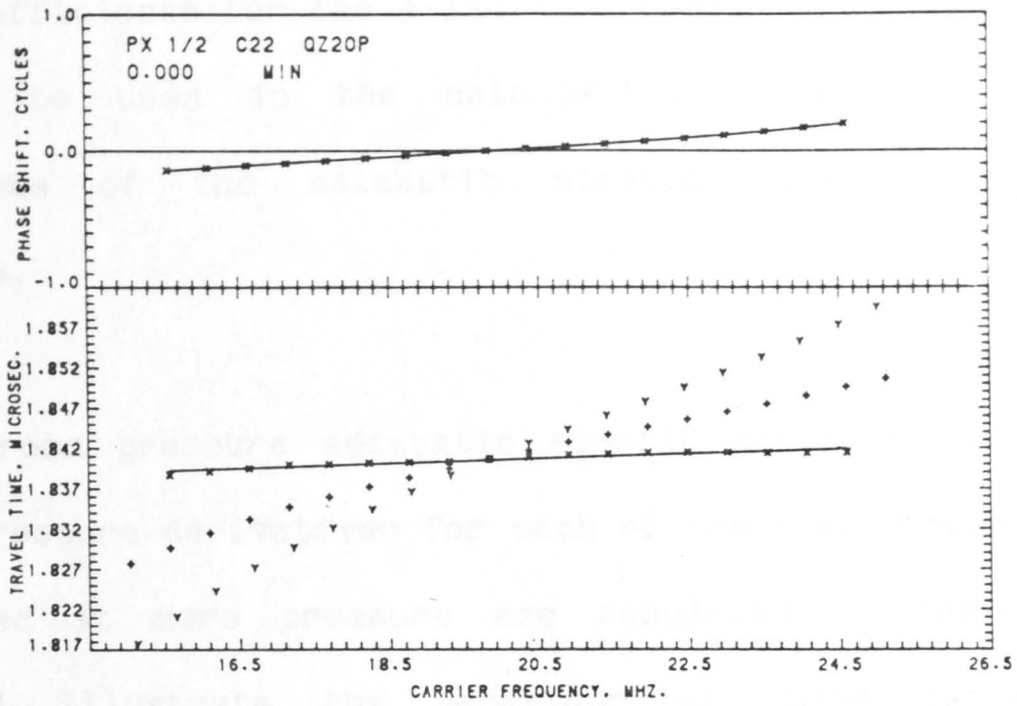

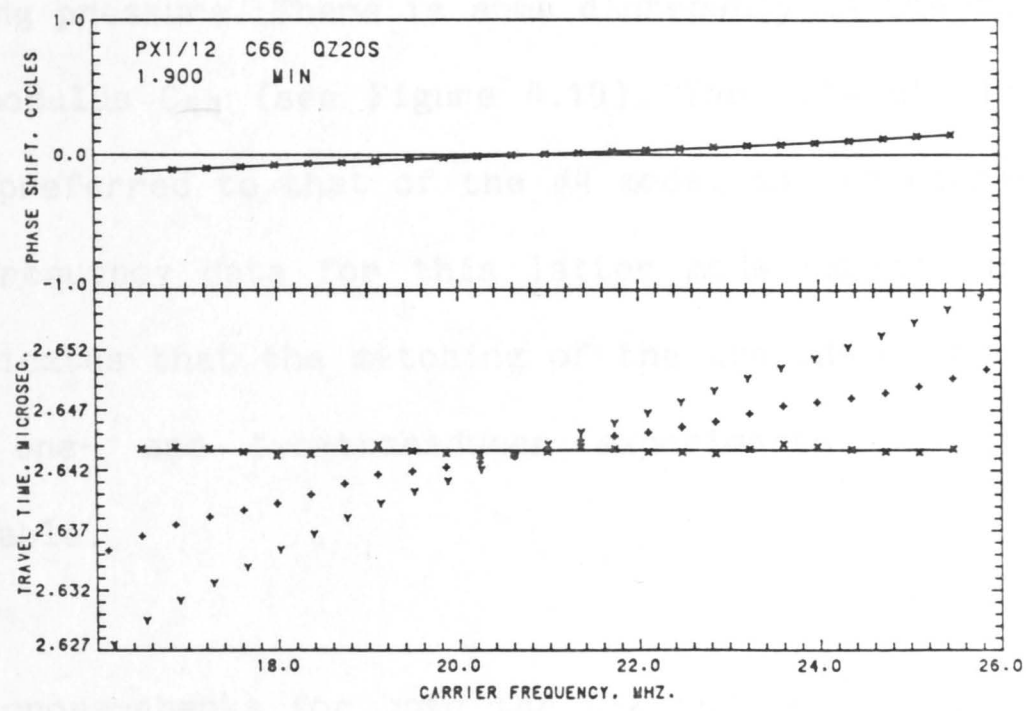

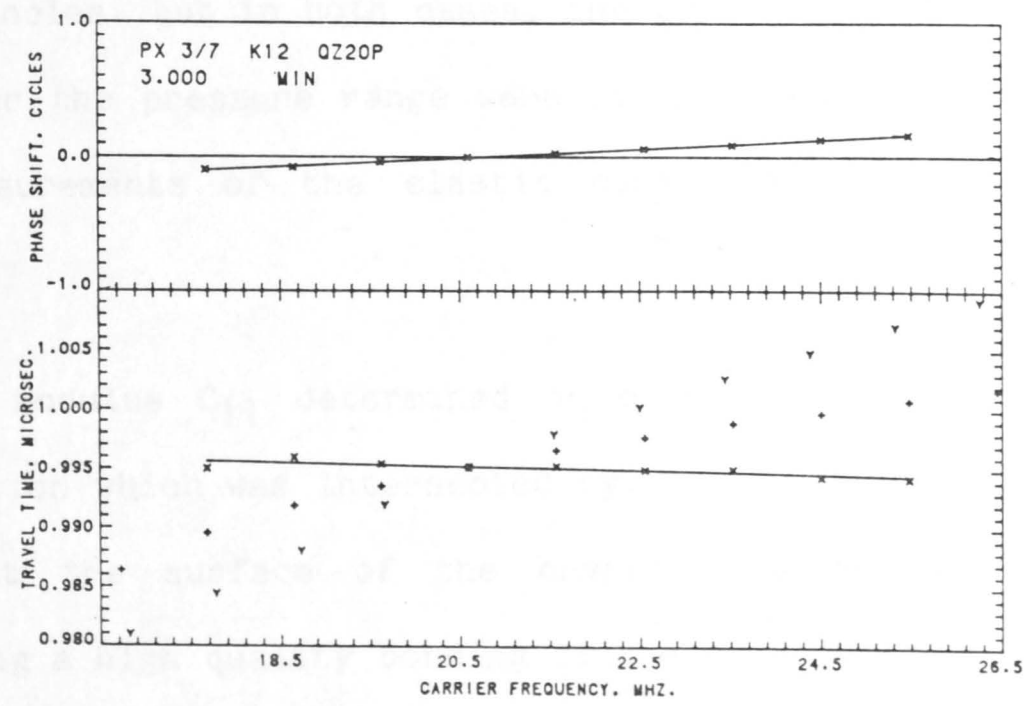

Figure 4.17 Phase comparison data (at 20 MHz) for the compressional modulus C_{22}, the shear modulus C_{66} (mode 12) and the quasi-compressional modulus K_{12} of orthopyroxene, at 0.00 GPa, 1.90 GPa and 3.00 GPa respectively.

These coefficients for the axial compression due to increasing pressure can now be used in the calculation of the isothermal pressure derivatives of the adiabatic elastic constants of the present bronzites.

The room pressure adiabatic elastic constants and the first and second pressure derivatives for each of the twelve modes of propagation calculated at zero pressure are tabulated in Table 4.14. Figures 4.18-4.21 illustrate the behaviour of these twelve moduli with increasing pressure. There is some dicrepancy in the observed behaviour of the modulus C_{44} (see Figure 4.19). The data obtained from the #11 mode is preferred to that of the #4 mode, as the corrected travel-time versus frequency data for this latter mode exhibit a non-zero slope. This indicates that the matching of the transducer and bond conditions in the one- and two-transducer experiments for the #4 mode was questionable.

The cross-checks for both the C_{55} and C_{66} moduli show some slight discrepancies, but in both cases, the two sets of corrected travel-time data over the pressure range were of high quality. The average of the two measurements of the elastic constants is taken as the correct value.

The modulus C_{11} determined on crystal #1 was in a direction of propagation which was intersected by a large crack. The effect of this crack at the surface of the crystal was to create difficulty in achieving a high quality bonding of the transducer to the crystal. This data is however, in good agreement with the modulus C_{11} measured on crystal #4 despite the greater scatter of the calculated moduli about the fitted curve.

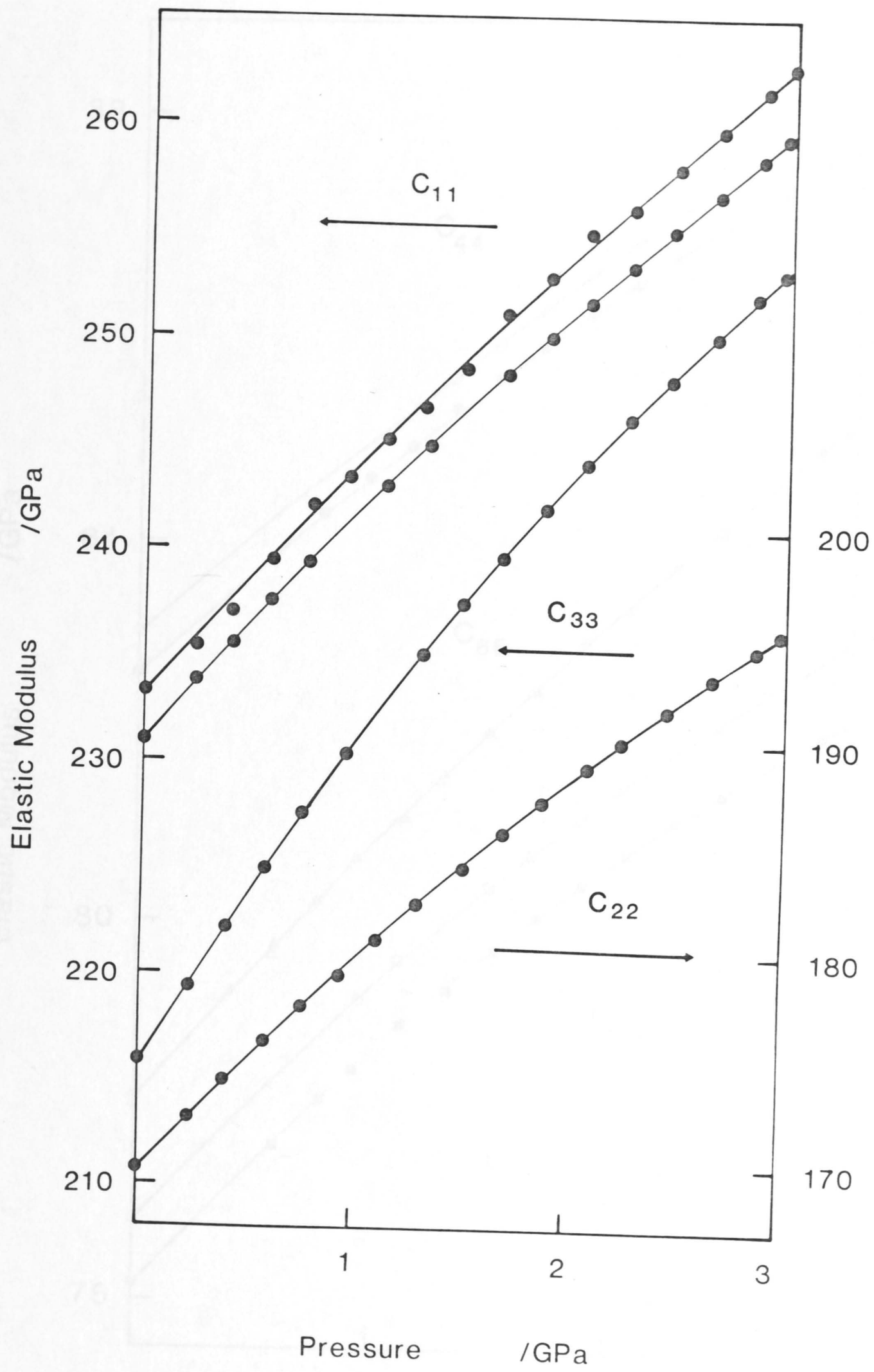

Figure 4.18 The variation with pressure of the compressional moduli C_{11} (determined on crystals #1 and #4, respectively), C_{33} and C_{22} of orthopyroxene. The uncertainties in modulus are everywhere less than the diameter of the plotting symbols.

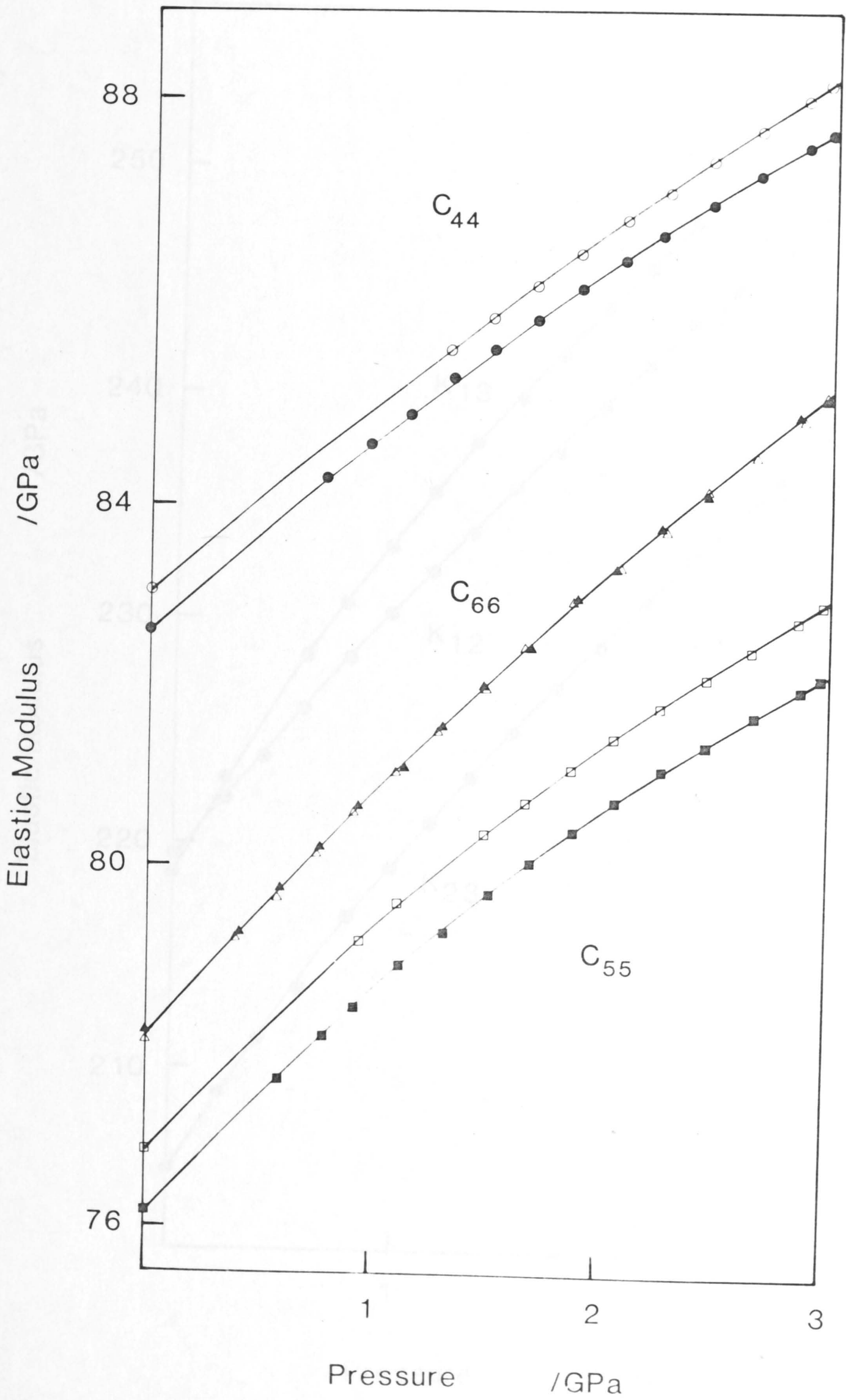

Figure 4.19 The variation with pressure of the shear moduli $C_{44}(4)$, $C_{55}(10)$ and $C_{66}(6)$ - hollow symbols, and $C_{44}(11)$, $C_{55}(5)$ and $C_{66}(12)$ - solid symbols, of orthopyroxene. The uncertainties in modulus are everywhere less than the diameter of the plotting symbols.

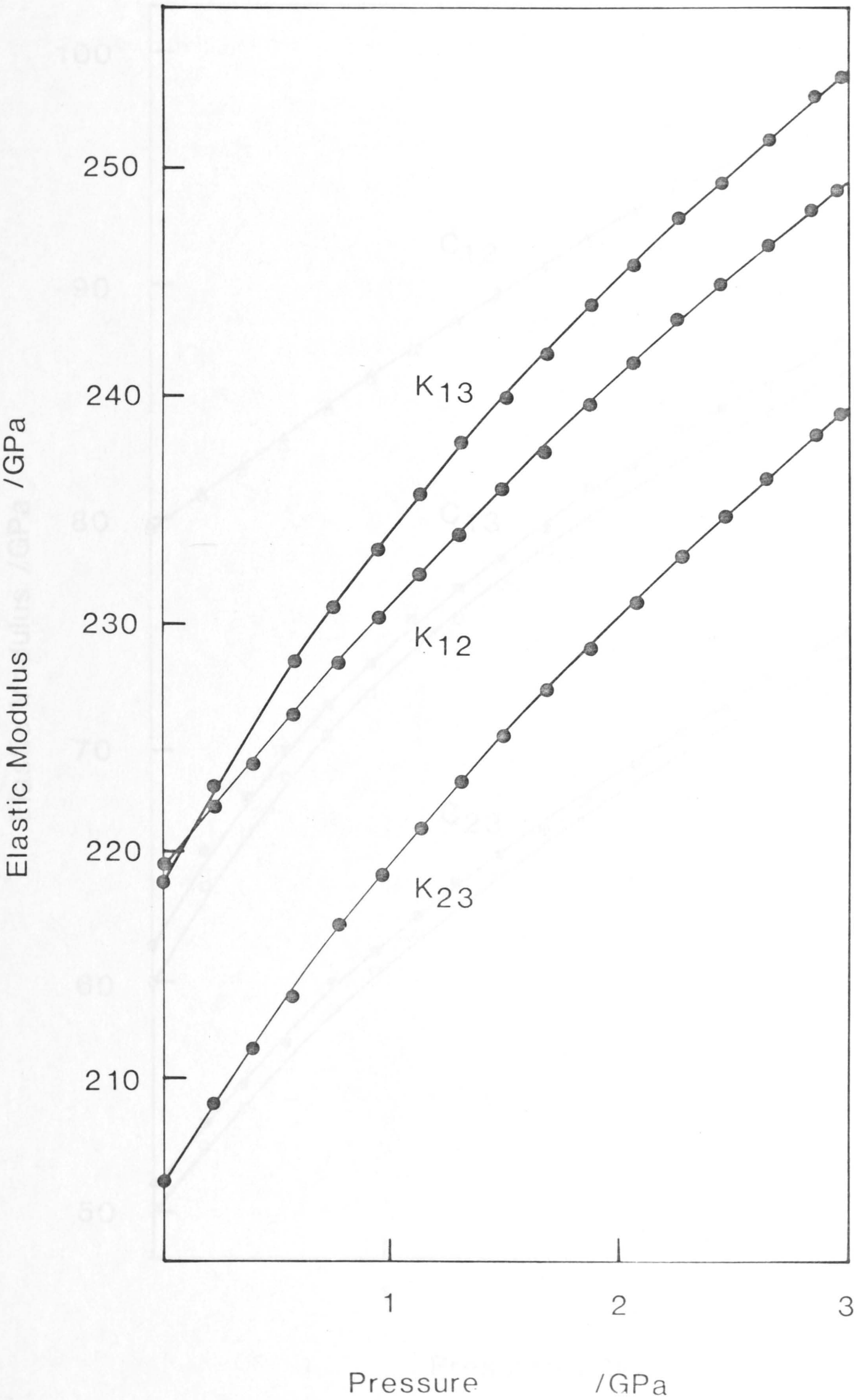

Figure 4.20 The variation with pressure of the quasi-compressional modes K_{13}, K_{12} and K_{23} of orthopyroxene. The uncertainties in modulus are everywhere less than the diameter of the plotting symbols.

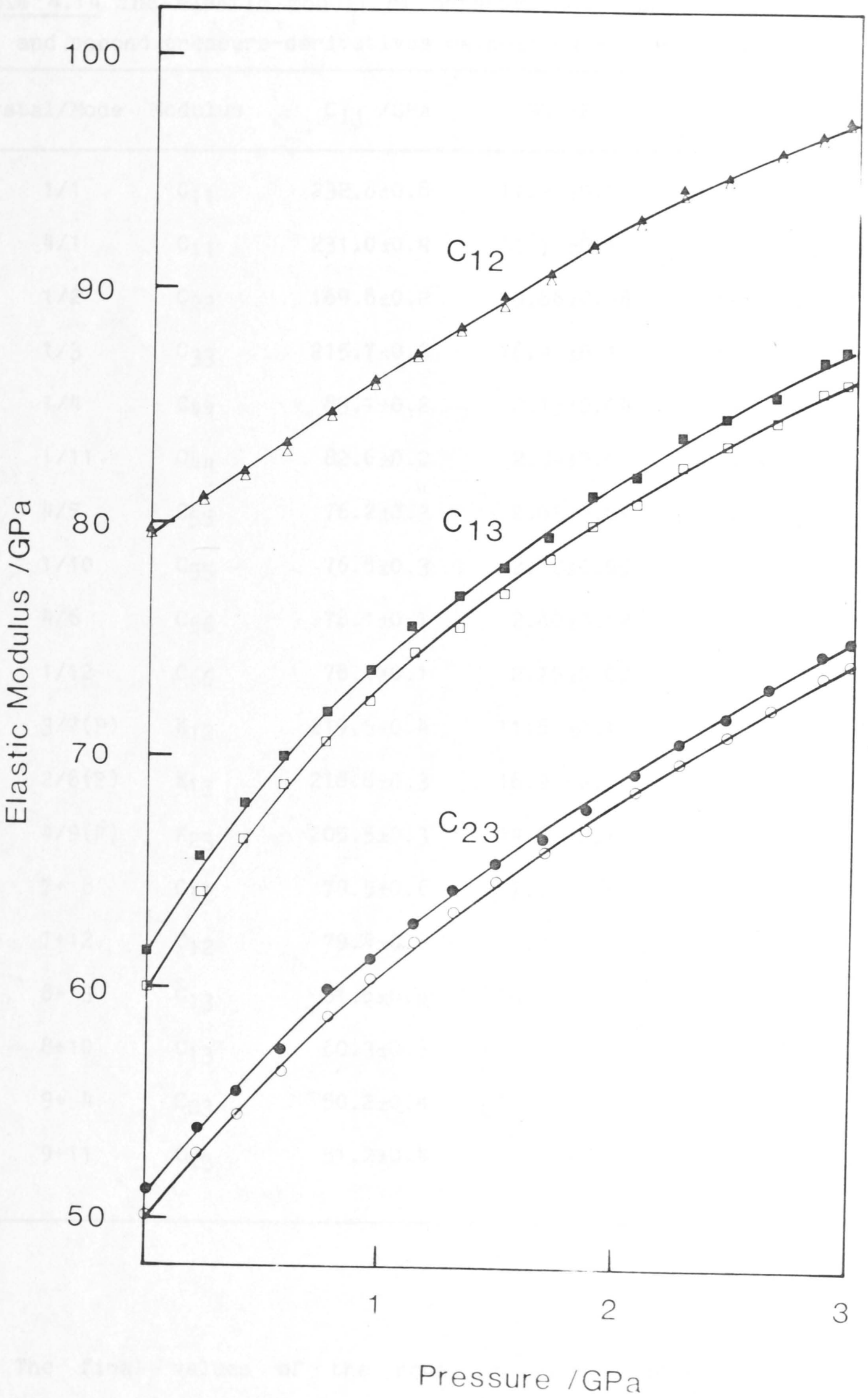

Figure 4.21 The variation with pressure of the moduli C_{12}, C_{13} and C_{23} of orthopyroxene. These moduli are calculated from the quasi-compressional K_{ij} modes, and the shear moduli $C_{66}(6)$, $C_{55}(10)$ and $C_{44}(11)$ - hollow symbols, and $C_{66}(12)$, $C_{55}(5)$ and $C_{44}(11)$ - solid symbols, respectively. Everywhere the errors in modulus are ± the size of the symbols again.

Table 4.14 The elastic moduli of orthopyroxene (En_{80}) with the first and second pressure-derivatives calculated at zero-pressure.

Crystal/Mode	Modulus	C_{ij} /GPa	$\partial C/\partial P$	$\partial^2 C/\partial P^2$ /GPa^{-1}
1/1	C_{11}	232.6±0.8	11.9 ±0.6	-1.3 ±0.1
4/1	C_{11}	231.0±0.4	11.2 ±0.1	-1.14±0.08
1/2	C_{22}	169.8±0.2	10.86±0.08	-1.30±0.07
1/3	C_{33}	215.7±0.3	16.4 ±0.1	-2.6 ±0.1
1/4	C_{44}	83.1±0.2	2.13±0.04	-0.17±0.02
1/11	C_{44}	82.6±0.2	2.34±0.04	-0.31±0.01
4/5	C_{55}	76.2±0.3	2.63±0.04	-0.43±0.02
1/10	C_{55}	76.8±0.3	2.72±0.05	-0.46±0.02
4/6	C_{66}	78.1±0.1	2.80±0.02	-0.25±0.02
1/12	C_{66}	78.1±0.1	2.79±0.02	-0.26±0.02
3/7(P)	K_{12}	219.5±0.4	11.8 ±0.1	-1.21±0.07
2/8(P)	K_{13}	218.8±0.3	16.9 ±0.1	-3.5 ±0.1
4/9(P)	K_{23}	205.5±0.3	14.8 ±0.1	-2.4 ±0.1
7+ 6	C_{12}	79.5±0.6	7.2 ±0.1	-0.74±0.09
7+12	C_{12}	79.4±0.6	7.2 ±0.1	-0.72±0.09
8+ 5	C_{13}	61.6±0.6	15.0 ±0.3	-4.4 ±0.1
8+10	C_{13}	60.3±0.6	14.8 ±0.3	-4.4 ±0.1
9+ 4	C_{23}	50.2±0.4	11.5 ±0.3	-2.3 ±0.1
9+11	C_{23}	51.2±0.4	11.1 ±0.3	-2.1 ±0.1

The final values of the room pressure elastic constants for bronzite, together with their first and second pressure derivatives calculated at zero pressure are tabulated in Table 4.15. The zero pressure elastic compliances of these bronzites are presented together with their first and second pressure derivatives in Table 4.16.

Table 4.15 The elastic moduli of orthopyroxene (En_{80}) with the first and second pressure-derivatives calculated at zero-pressure.

Modulus	C_{ij} /GPa	$\partial C/\partial P$	$\partial^2 C/\partial P^2$ /GPa^{-1}
C_{11}	231.0±0.4	11.2 ±0.1	-1.14±0.08
C_{22}	169.8±0.2	10.9 ±0.1	-1.33±0.07
C_{33}	215.7±0.3	16.4 ±0.1	-2.6 ±0.10
C_{44}	82.6±0.2	2.34±0.04	-0.31±0.01
C_{55}	76.5±0.3	2.68±0.05	-0.45±0.02
C_{66}	78.1±0.1	2.80±0.02	-0.26±0.02
C_{12}	79.5±0.4	7.2 ±0.1	-0.74±0.09
C_{13}	61.0±0.6	14.9 ±0.3	-4.4 ±0.10
C_{23}	50.7±0.4	11.3 ±0.3	-2.2 ±0.10

Table 4.16 The zero-pressure elastic compliances of orthopyroxene with the first and second pressure derivatives calculated at zero-pressure.

Modulus	S_{ij} /(10^{-3} GPa^{-1})	$\partial S/\partial P$ /(10^{-3} GPa^{-2})	$\partial^2 S/\partial P^2$ /(10^{-3} GPa^{-3})
S_{11}	5.4 ±0.1	-0.11±0.01	0.005±0.001
S_{22}	7.2 ±0.1	-0.30±0.03	0.027±0.007
S_{33}	5.2 ±0.1	-0.18±0.02	0.007±0.001
S_{44}	12.1 ±0.2	-0.34±0.05	0.027±0.007
S_{55}	13.1 ±0.2	-0.45±0.05	0.04 ±0.01
S_{66}	12.8 ±0.2	-0.45±0.05	0.030±0.008
S_{12}	-2.21±0.04	0.08±0.01	-0.013±0.004
S_{13}	-1.00±0.03	-0.15±0.02	0.04 ±0.01
S_{23}	-1.08±0.03	-0.09±0.01	0.011±0.003

4.4.3 Elasticity and crystal chemistry

The elastic constants of bronzites of similar compositions (En_{80}) have previously been determined by Frisillo and Barsch (1972) to 1 GPa using the pulse superposition technique. Four single crystals of unknown microstructure were used in this study, with the crystals having an average density of 3.354±0.002 g cm^{-3}. The compressional moduli were found to increase linearly with pressure, while the shear and off-diagonal moduli were found to fit quadratic curves. The first and second pressure derivatives were calculated from the natural wave-velocity of Thurston and Brugger (1964),

$$\rho_0 W_2 = (\rho_0 W_0)^2 + (\rho_0 W^2)' \times P + (\rho_0 W^2)''/2 \times P^2 \qquad (4.24)$$

and the further development of this procedure for orthorhombic symmetry by Barsch and Frisillo (1973). The elastic constants measured in this study are tabulated in Table 4.17.

The room pressure moduli measured by Frisillo and Barsch (1972) are in general accord with those determined in the present study for crystals of similar compositions. However, there are significant differences which deserve comment. The moduli measured by Frisillo and Barsch are invariably lower than those of the present study: by ~1% for C_{11}, C_{44}, C_{55} and C_{66}; ~3% for C_{33}; ~5% for C_{22}; and by 9-10% for the C_{ij} $(i \neq j)$. This indicates there may be a need to be fully cognisant of the microstructure of each crystal in order to catalogue any possible microstructural effects on the measured travel-times.

Table 4.17 The elastic moduli and the first and second pressure derivatives calculated at zero pressure for the bronzites of Frisillo and Barsch (1972).

Modulus	C_{ij} /GPa	$\partial C/\partial P$	$\partial^2 C/\partial P^2$ /GPa^{-1}
C_{11}	228.6 ±0.1	11.04±0.06	-
C_{22}	160.5 ±0.1	9.19±0.08	-
C_{33}	210.4 ±0.1	16.42±0.04	-
C_{44}	81.74±0.09	2.38±0.03	-0.281±0.025
C_{55}	75.48±0.07	2.92±0.04	-0.595±0.022
C_{66}	77.66±0.05	2.75±0.01	-0.173±0.012
C_{12}	71.0 ±0.2	6.97±0.10	0.507†
C_{13}	54.8 ±0.2	9.09±0.10	0.663†
C_{23}	46.0 ±0.2	8.73±0.10	0.620†

† Calculated by assuming $\partial^2 C_{11}/\partial P^2$, $\partial C_{22}/\partial P^2$, and $\partial^2 C_{33}/\partial P^2$ to be zero.

The first pressure derivatives observed by Frisillo and Barsch are also generally consistent with the present measurements. The comparison between the pressure derivatives of the compressional moduli is extremely good, despite the linear pressure relationship observed by Frisillo and Barsch. The observed pressure dependences of the shear moduli are not in such close agreement, there being a significant discrepancy for $\partial C_{55}/\partial P$. The second pressure derivatives for these shear moduli, although varying between studies, have the same relative magnitudes. The pressure dependence of the off-diagonal moduli of Frisillo and Barsch are low by up to 38%, although the relative magnitudes are comparable to those observed in the present study. The calculated second pressure derivatives of these off-diagonal moduli of Frisillo and Barsch are complicated by the linear pressure dependence of the compressional moduli.

In both studies, the first pressure derivatives are much larger than those observed for the other mantle minerals garnet and olivine (see Tables 4.1 and 4.9). The original study of Frisillo and Barsch (1972) left this anomaly unresolved by finding linear relationships for the compressional moduli with pressure to 1 GPa. In the present study we have measured large negative second pressure derivatives for the on-diagonal compressional moduli and also the off-diagonal moduli; with second pressure derivatives for the on-diagonal shear moduli which are comparable to the pressure derivatives for the shear moduli of the other mantle minerals garnet and olivine.

The room pressure elastic constants of orthopyroxene and the end-members enstatite and orthoferrosilite have previously been measured. Kumazawa and Anderson (1969) measured the elastic constants of a small bronzite crystal $En_{84.5}$ using the pulse superposition technique. More recently, Weidner et al. (1978) and Bass and Weidner (1984) have measured the elastic constants of an orthoenstatite and an orthoferrosilite respectively by Brillouin scattering. The results of these studies are tabulated in Table 4.18. Figures 4.22, 4.23 and 4.24 illustrate the behaviour of the room pressure elastic constants of orthopyroxene with increasing substitution of Fe for Mg in the enstatite end-member.

The influence of Fe/Mg substitution on the elasticity of pyroxenes has been discussed by Bass and Weidner (1984). The substitution of Fe in the orthoenstatite end-member has the overall effect of reducing the magnitudes of the on-diagonal moduli C_{ii}, and increasing the magnitudes of the off-diagonal moduli C_{ij}. The substitution of $\leq$20% Fe in the enstatite end-member causes a slight increase in the moduli C_{11}, C_{22} and C_{44} against the overall trends, with C_{55} and C_{23} being insensitive

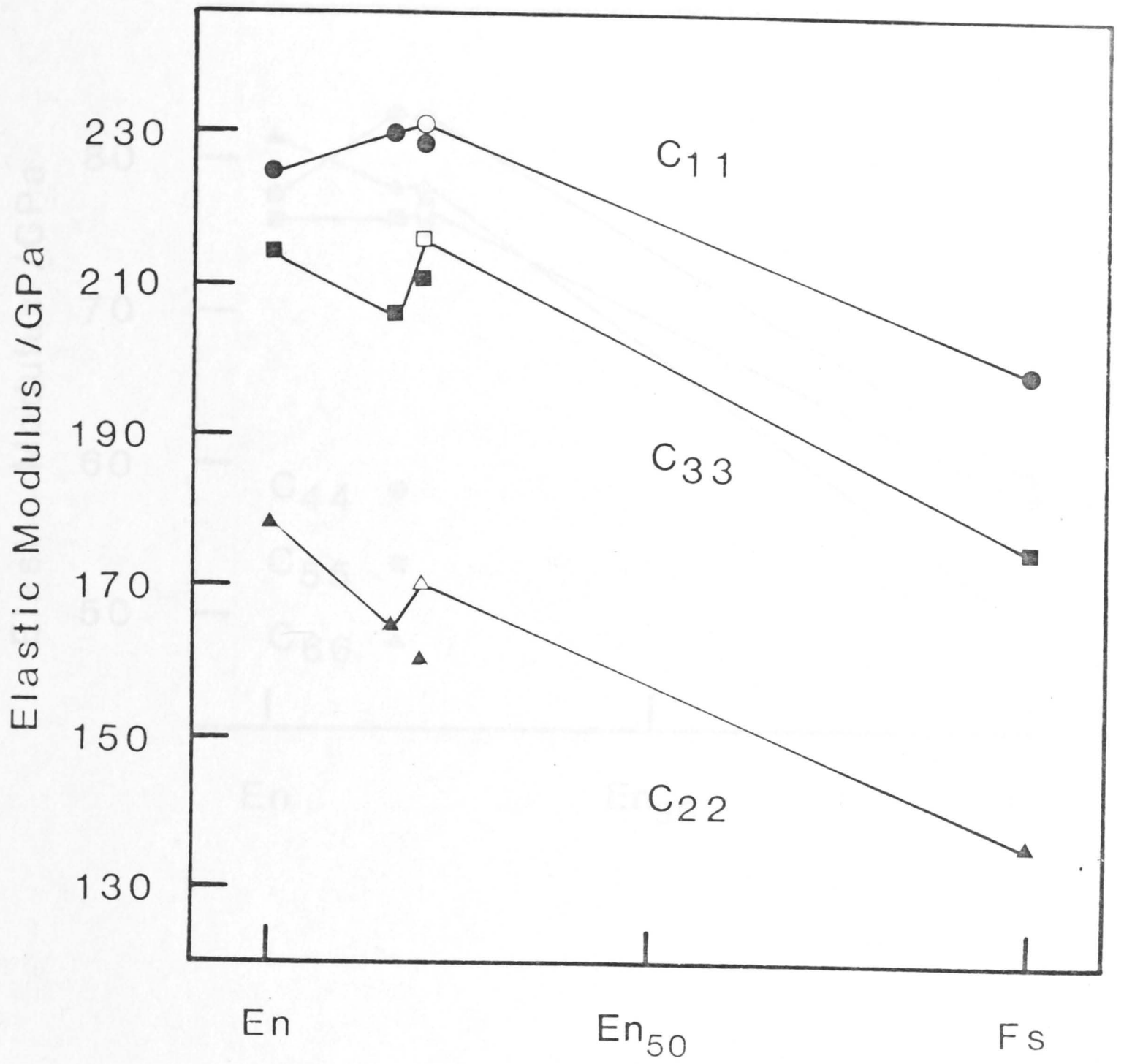

Figure 4.22 Variation with composition of the compressional moduli C_{11}, C_{22} and C_{33} for the orthoenstatite-orthoferrosilite solid solution series (see Table 4.18 for details). The hollow symbols represent the moduli determined in the present study.

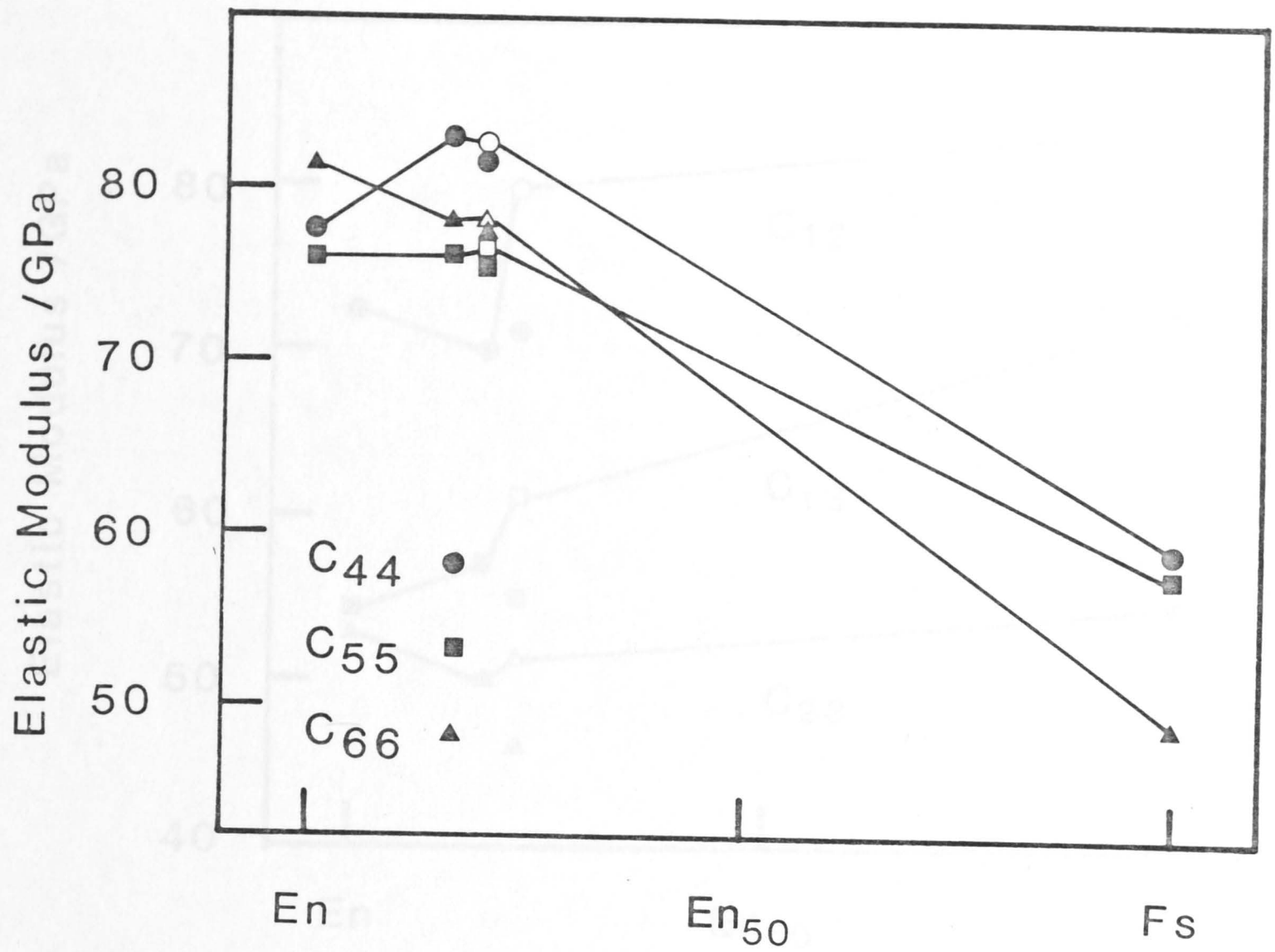

Figure 4.23 Variation with compositon of the shear moduli C_{44}, C_{55} and C_{66} for the orthoenstatite-orthoferrosilite solid solution series (see Table 4.18 for details). The hollow symbols represent the moduli determined in the present study.

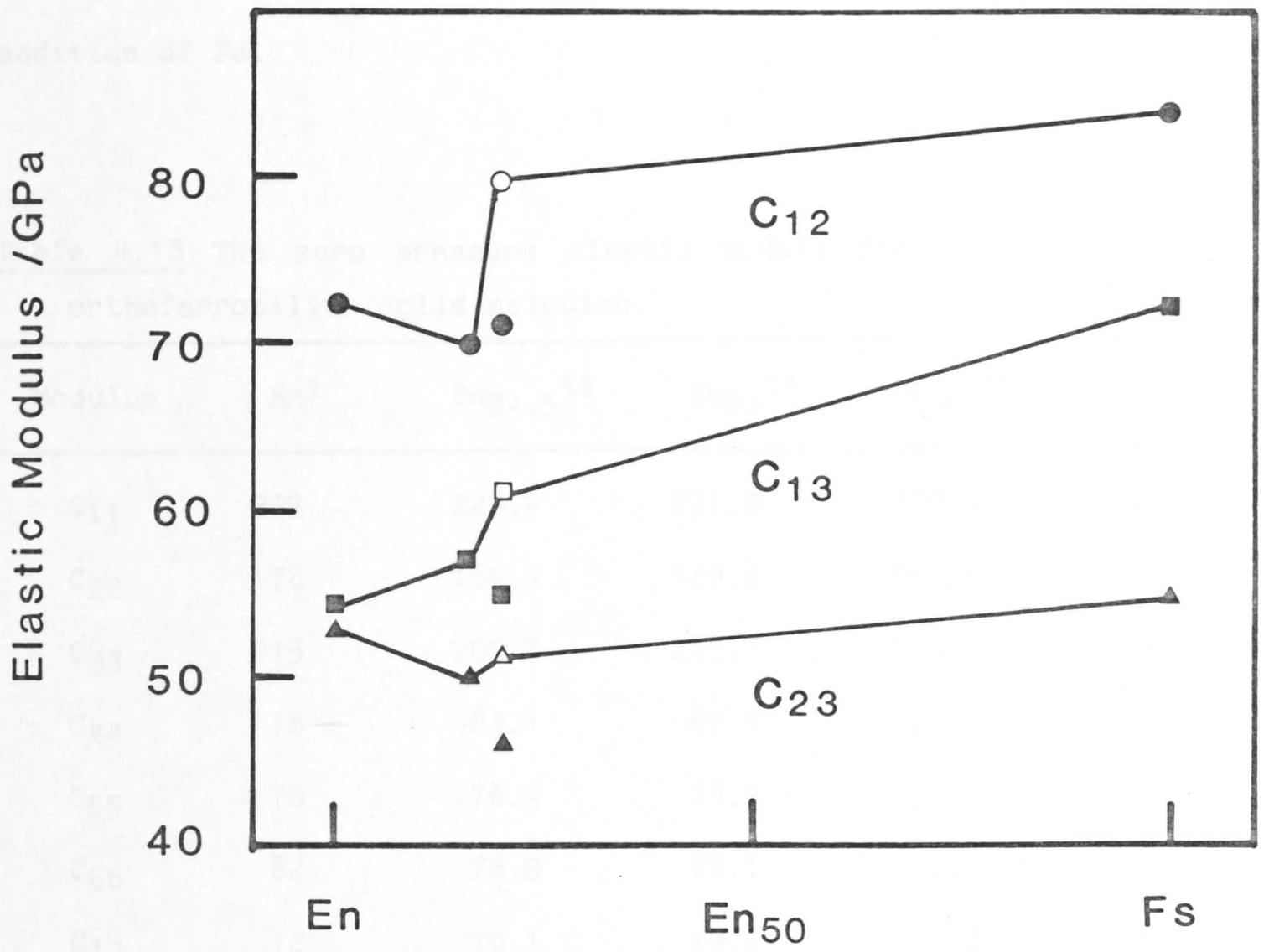

Figure 4.24 Variation with composition of the off-diagonal moduli C_{12}, C_{13} and C_{23} for the orthoenstatite-orthoferrosilite solid solution series (see Table 4.18 for details). The hollow symbols represent the moduli determined in the present study.

to small amounts of Fe, and C_{23} in general being insensitive to the addition of Fe.

Table 4.18 The zero pressure elastic moduli for the orthoenstatite-orthoferrosilite solid solution.

Modulus	En†	$En_{84.5}$¶¶	En_{80}††	En_{80}**	Fs*
C_{11}	225	229.9	231.0	228.6	198
C_{22}	178	165.4	169.8	160.5	136
C_{33}	215	205.7	215.7	210.4	175
C_{44}	78	83.1	82.6	81.74	59
C_{55}	76	76.4	76.5	75.48	58
C_{66}	82	78.5	78.1	77.66	49
C_{12}	72	70.1	79.5	71.0	84
C_{13}	54	57.3	61.0	54.8	72
C_{23}	53	49.6	50.7	46.0	55

† Weidner et al. (1978)

¶¶ Kumazawa and Anderson (1969)

* Bass and Weidner (1984)

** Frisillo and Barsch (1972)

In these studies of the elasticity of the orthoenstatite-orthoferrosilite solid solution, consistent trends in the relative magnitudes of the elastic moduli may be observed, with

$$C_{11} > C_{33} > C_{22} \tag{4.25}$$

$$C_{44} \approx C_{55} > C_{66} \tag{4.26}$$

and

$$C_{12} > C_{13} > C_{23}. \tag{4.27}$$

The immunity of these trends to chemical variation indicates that the elasticity of orthopyroxene is dominated by the elasticity of the lattice structure, with variation of the Mg/Fe occupancy of the octahedral site resulting in subsidiary changes in lattice elasticity.

4.5 The elasticity of single-phase isotropic aggragates

The elastic properties of single-phase isotropic aggregates were first considered by Voigt (1928) and Reuss (1929). Voigt assumed uniform strain throughout an aggregate and derived the effective elastic stiffnesses of the aggregate averaged over all possible orientations of the constituent crystals. The bulk and shear moduli calculated in this manner are;

$$K_V^* = (A + 2B)/3$$

and

$$G_V^* = (A - B + 3C)/5 \qquad (4.28)$$

where

$$A = (C_{11} + C_{22} + C_{33})/3$$

$$B = (C_{12} + C_{23} + C_{13})/3$$

$$C = (C_{44} + C_{55} + C_{66})/3. \qquad (4.29)$$

Reuss assumed uniform stress throughout the aggregate to derive expressions for the effective isotropic compliances in terms of the single crystal compliances averaged over all possible orientations. The bulk and shear moduli thus derived are;

$$K_R^* = (3(a + 2b))^{-1}$$

and

$$G_R^* = 5/(4a - 4b + 3c) \qquad (4.30)$$

where
$$a = (S_{11} + S_{22} + S_{33})/3$$
$$b = (S_{12} + S_{23} + S_{13})/3$$
$$c = (S_{44} + S_{55} + S_{66})/3. \qquad (4.31)$$

The use of these Voigt and Reuss expressions as bounds for the elastic properties of single phase aggregates is intuitively reasonable given the expectation that the boundary conditions for the behaviour of such aggregates must lie between those of uniform stress and uniform strain. Hill (1952) gave a rigorous proof of the bounding properties of these two averages and suggested the use of the arithmetic mean as an approximation to the effective moduli of the aggregate. This arithmetic mean of the the Voigt and Reuss bounds, the Voigt-Reuss-Hill (VRH) average has been widely used in discussions of the properties of polycrstals; however, this average is not physically meaningful as the actual moduli are known only to lie within these bounds (Thomsen, 1972).

In these models for the effective elastic moduli of an aggregate, Voigt and Reuss have replaced an aggregate of randomly orientated crystals with an equivalent isotropic homogeneous elastic medium. Hashin and Shtrikman (1962a, 1962b) have obtained more closely spaced bounds for the effective elastic moduli by deforming a homogeneous and isotropic elastic body and comparing its behaviour to that of a large polycrystalline quasi-homogeneous, quasi-isotropic reference-body of randomly orientated crystals. This reference-body is regarded as quasi-homogeneous and quasi-isotropic, in that the mean value of a physical quantity in a unit volume equals that of the whole body. Subject to the surface deformation of the homogeneous isotropic body, the stress and strain of the reference-body define the effective elastic moduli and the energy of the reference body. These effective

elastic moduli together with the energy of the reference body can then be used in the variational approach of Hashin and Shtrikman (1963) to calculate upper and lower bounds for the effective bulk and shear moduli of the polycrystal in terms of the moduli of the constituent single-crystals. This treatment requires no knowledge of the orientations of the crystals of the aggregate - only the single crystal moduli. The Hashin-Shtrikman bounds on the effective elastic moduli of single-phase aggregates of crystals of orthorhombic symmetry can be expressed as;

$$K^* \gtrless \frac{K_o + 3B_1 + 2B_2}{3 + \alpha(3B_1 + 2B_2)} \tag{4.32}$$

$$G^* \gtrless G_o + B_2(1 + 2\beta B_2)^{-1} \tag{4.33}$$

where K^* and G^* are the effective moduli, and G_o (and hence K_o) are chosen from the maximum and minimum energy requirements of the reference body. The initial moduli G_o and K_o are used to calculate the terms α and β,

$$\alpha = -3/(3K_o + 4G_o)$$

$$\beta = -3(K_o + 2G_o)(5G_o(3K_o + 4G_o))^{-1} \tag{4.34}$$

while B_1 and B_2 are related to the conditions necessary for the maximum and minimum energy conditions (see Watt, 1979) of the reference body. These equations collapse to the appropriate equations for a crystal of cubic symmetry when the elastic constants of such a crystal are used as the input parameters.

The Hashin-Shtrikman bounds for the bulk and shear moduli of the garnet, olivine and orthopyroxene crystals have been calculated following the procedure of Watt (1979), and are presented in Table 4.19. The Voigt and Reuss bounds have also been calculated and are

compared with the Hashin-Shtrikman bounds in Table 4.19 and Figures 4.25 and 4.26. In all cases the Hashin-Shtrikman bounds lie between the Voigt and Reuss bounds (as expected), and the VRH average lies within the Hashin-Shtrikman bounds. These bounds have been calculated across the 3 GPa pressure range by calculating the elastic constants of each mineral from the $C_{ij}(P)$ quadratics and using these values to calculate the bounds at pressure. The bounds calculated for the bulk modulus of garnet are equal using both the Voigt and Reuss and the Hashin-Shtrikman methods of calculation, as is expected for a crystal of cubic symmetry. The bounds on the shear modulus of garnet were also found to be equal using both bounding procedures, due to the near isotropy of the present pyrope-rich garnet.

Table 4.19 Hashin-Shtrikman bounds on the elastic moduli for single phase aggregates of the garnet, olivine and orthopyroxene crystals characterized in this study (see Tables 4.1, 4.9 and 4.15). The values quoted are the average of the Hashin-Shtrikman bounds with the errors giving the spacing of the bounds; the terms in brackets give the spacing of the Voigt–Reuss bounds.

Mineral	M /GPa	$\partial M/\partial P$	$\partial^2 M/\partial P^2$ /GPa^{-1}
Garnet			
K	173.6	4.97	-0.32
G	94.9	1.59	-0.11
Olivine			
K	129.1±0.3(±2.0)	4.87±0.01(±0.01)	-0.27±0.01(±0.01)
G	77.7±0.3(±1.6)	1.76±0.01(±0.01)	-0.13±0.01(±0.01)
Orthopyroxene			
K	109.9±0.3(±1.5)	11.62±0.01(±0.05)	-1.46±0.01(±0.01)
G	75.0±0.3(±0.7)	1.97±0.01(±0.05)	-0.33±0.01(±0.01)

Table 4.19 illustrates the effectiveness of the Hashin-Shtrikman method in the calculation of tight bounds on the bulk and shear moduli of single-phase polycrystals, and compares this with the more widely spaced Voigt and Reuss bounds.

For a model mineralogy dominated by olivine, we see that the room pressure bulk and shear moduli of garnet are substantially higher than those of the olivine phase, while the moduli for orthopyroxene are slightly lower. The pressure dependence of these moduli however is not as straightforward. The first pressure derivative of the bulk modulus of garnet is slightly higher than that of the dominant phase olivine, while the first pressure derivative of orthopyroxene is more than twice that of olivine. The pressure derivatives of the shear moduli however are not so divergent, with the pressure dependence of the shear modulus of garnet being slightly lower than that of olivine, while the derivative of the shear modulus of orthopyroxene is slightly higher.

For these three mantle minerals, the importance of the second pressure derivatives in decreasing the pressure dependence of the bulk and shear moduli of garnet, olivine and orthopyroxene becomes obvious (see Figures 4.25, 4.26 and Table 4.19). At 3 GPa, the values of the pressure derivatives of the bulk and shear moduli of garnet and olivine are comparable, while the pressure dependence of the bulk modulus of orthopyroxene has decreased by 38% and the pressure dependence of the shear modulus of orthopyroxene has decreased by 50%, and is less than that of both garnet and olivine. At 6 GPa, not only are the extrapolated pressure derivatives for the bulk and shear moduli of garnet and olivine comparable, but the extrapolated derivatives for the moduli of orthopyroxene are lower than those of garnet or olivine. This quadratic extrapolation from 3 to 6 GPa for orthopyroxene however is

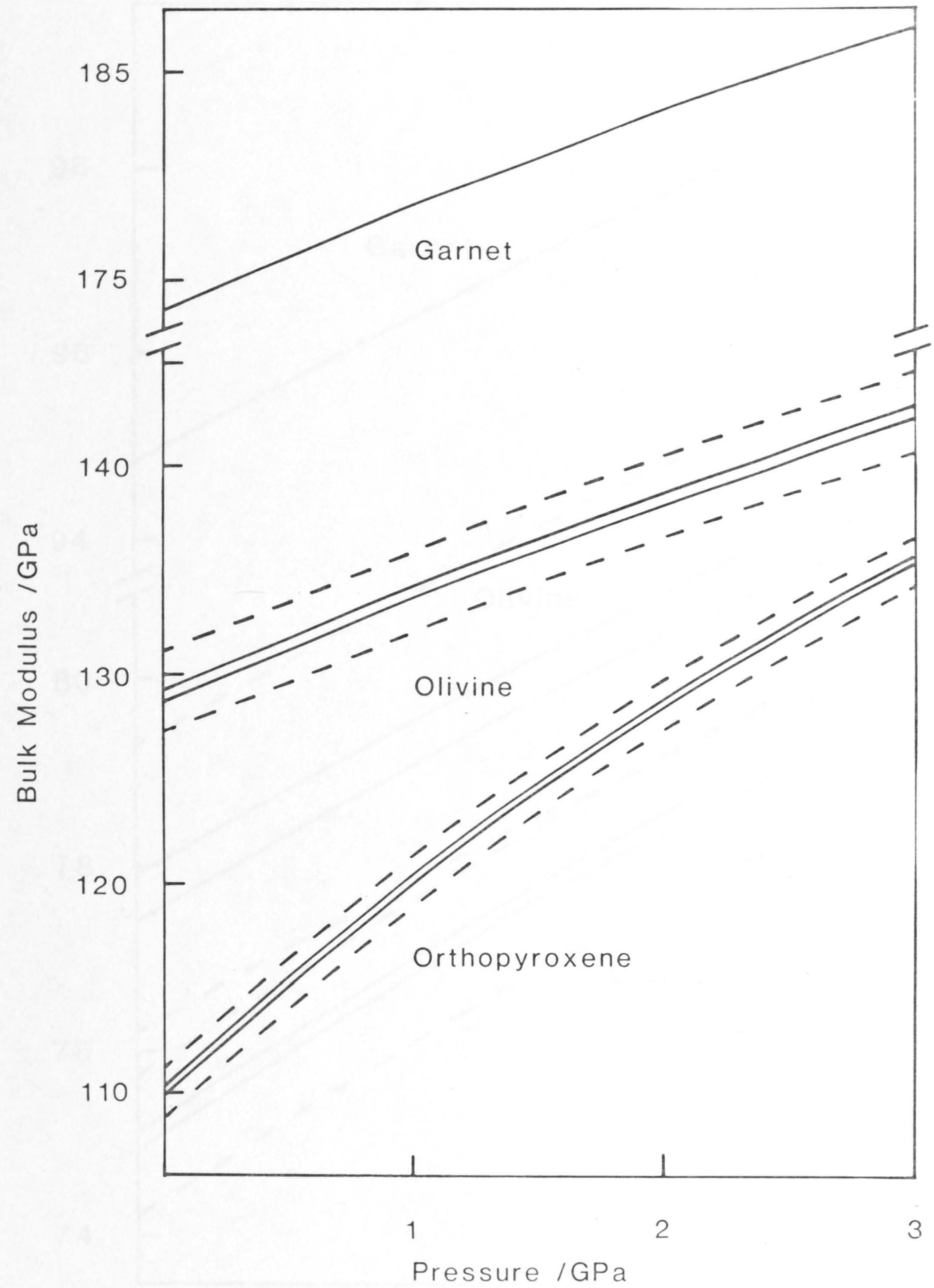

Figure 4.25 The Hashin-Shtrikman bounds on the bulk moduli for single phase aggregates of olivine, garnet and orthopyroxene (solid lines), together with the Voigt and Reuss bounds (broken lines) (see Table 4.19 for details).

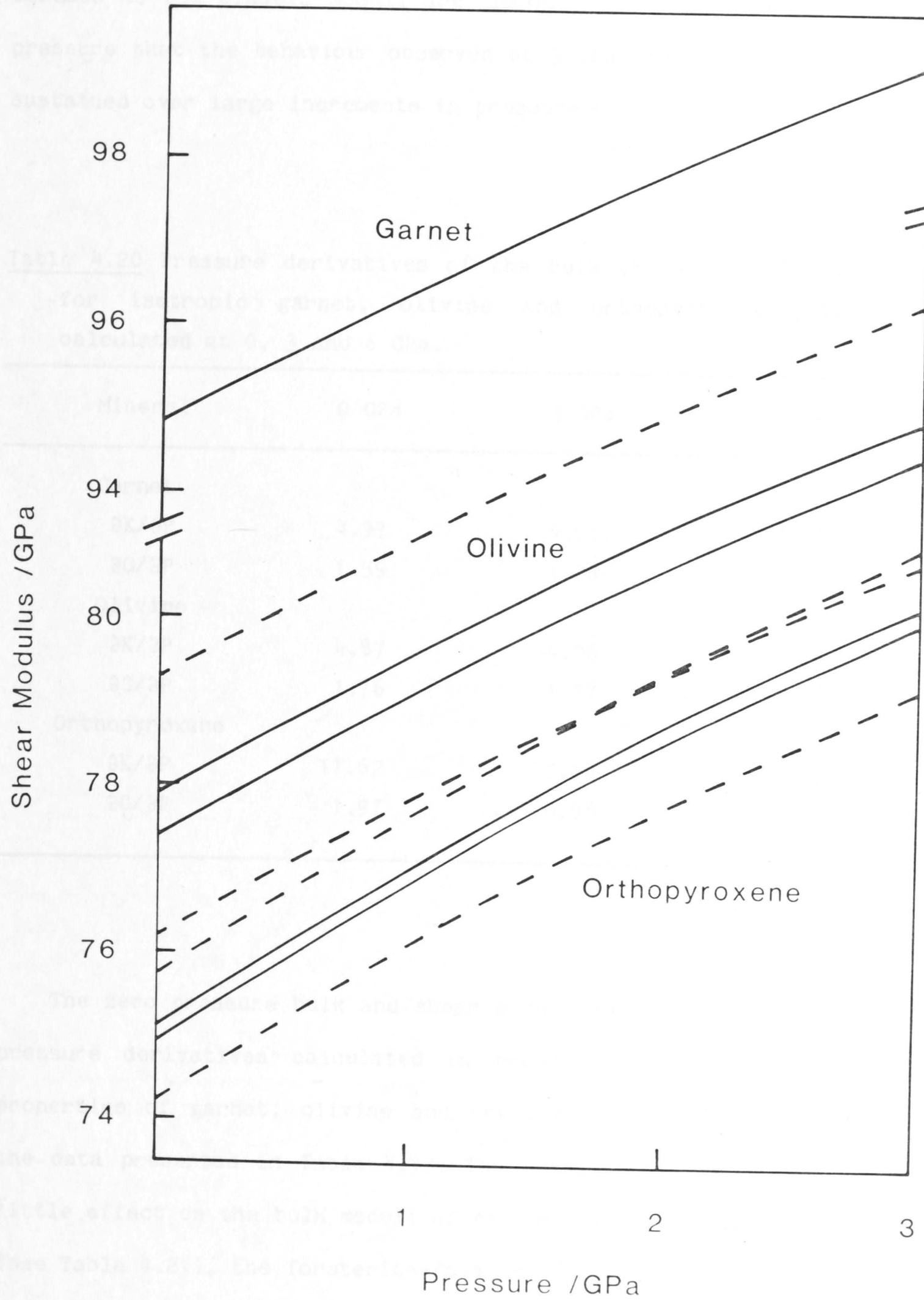

Figure 4.26 The Hashin-Shtrikman bounds on the shear moduli for single phase aggregates of olivine, garnet and orthopyroxene (solid lines), together with the Voigt and Reuss bounds (broken lines) (see Table 4.19 for details).

tenuous as the elastic moduli are changing so rapidly with increasing pressure that the behaviour observed at 3 GPa cannot be expected to be sustained over large increments in pressure.

Table 4.20 Pressure derivatives of the bulk (K) and shear (G) moduli for isotropic garnet, olivine and orthopyroxene polycrystals calculated at 0, 3 and 6 GPa.

Mineral	0 GPa	3 GPa	6 GPa
Garnet			
$\partial K/\partial P$	4.97	4.01	3.05
$\partial G/\partial P$	1.59	1.26	0.93
Olivine			
$\partial K/\partial P$	4.87	4.06	3.25
$\partial G/\partial P$	1.76	1.37	0.98
Orthopyroxene			
$\partial K/\partial P$	11.62	7.24	2.86
$\partial G/\partial P$	1.97	0.98	-0.01

The zero pressure bulk and shear moduli and their first and second pressure derivatives calculated in previous studies of the elastic properties of garnet, olivine and orthopyroxene can be compared with the data presented in Table 4.19. The substitution of Fe for Mg has little effect on the bulk moduli of either the pyrope-almandine garnets (see Table 4.21), the forsterite-fayalite olivines (see Table 4.22), or the orthoenstatite-orthoferrosilite pyroxenes (see Table 4.23). The addition of Fe does however, result in ~10% increase in shear modulus across the pyrope-almandine solid solution series, while the shear moduli of olivine and orthopyroxene experience a decrease of approximately 35% with the substitution of Fe for Mg (Jackson et al., 1978; Leitner et al., 1980).

Table 4.21 The bulk and shear moduli and their first pressure derivatives for the pyrope-almandine solid solution.

Modulus	Pyrope†	~$Py_{63}Al_{37}$††	~$Py_{22}Al_{78}$*	Almandine†
K	176.6	173.6	177.0	177
∂K/∂P	–	4.97	5.43	–
G	89.6	94.9	94.32	98.6
∂G/∂P	–	1.59	1.40	–

† Leitner et al. (1980)

†† Present study

* Soga (1967)

Table 4.22 The Hashin-Shtrikman bulk and shear moduli together with their and their first pressure deivatives for the forsterite-fayalite solid solution.

Modulus	Fo†	Fo**	$Fo_{92.7}$†	$Fo_{90.5}$††	$Fo_{87.8}$*	Fa¶¶	Fa***
K	128.5	129.0	129.3	129.1	129.0	127.7	138.1
∂K/∂P	5.35	4.85	5.14	4.87	–	–	–
G	81.0	81.5	78.9	77.7	76.8	50.3	51.0
∂G/∂P	1.80	1.82	1.78	1.76	–	–	–

† Kumazawa and Anderson (1969)

** Graham and Barsch (1969)

†† Present study

* Yeganeh-Haere and Vaughan (1984)

¶¶ Graham et al. (1982)

*** Sumino (1979)

Table 4.23 The bulk and shear moduli and their first pressure derivatives for the orthoenstatite-orthoferrosilite solid solution

	En†	$En_{84.5}$¶¶	En_{80}††	En_{80}**	Fs*
K	108	107.1	109.9	103.5	102
∂K/∂P	–	–	11.62	9.54	–
G	76	74.3	75.0	74.8	52
∂G/∂P	–	–	1.97	2.37	–

† Weidner et al. (1978)

¶¶ Kumazawa and Anderson (1969)

†† Present study

** Frisillo and Barsch (1972)

* Bass and Weidner (1984)

CHAPTER 5

ELASTICITY AND CRYSTAL STRUCTURE

5.1 Introduction

The considerable expansion of the single-crystal elasticity dataset for silicate minerals which has resulted from the application of Brillouin spectroscopy to microcrystals by Weidner and his colleagues (Weidner et al., 1978;Vaughan and Bass, 1983;Bass et al., 1984) has provided a clearer picture of the relative roles of crystal structure and chemical composition as determinants of crystal elasticity. It has been demonstrated, particularly for olivines and pyroxenes (Weidner and Vaughan, 1982;Vaughan and Bass, 1983;Bass et al., 1984), that the relative magnitudes of the stiffness or compliance moduli tend to be controlled primarily by gross features of the crystal structure with cation composition playing a subsidiary role.

Another important development in the last decade has been the

advent of high-pressure and high-temperature crystal structure refinements which have provided a firmer basis for the polyhedral view of crystal structures, along with detailed information concerning polyhedral compressibilities and expansivities e.g.Hazen and Finger, 1978, 1980, 1981;Levien and Prewitt, 1981).

These factors along with the inherent difficulty of ab initio and atomistic approaches to the elasticity of these complex crystal structures have led to both qualitative (Weidner and Vaughan, 1982; Vaughan and Bass, 1983) and quantitative (Au and Weidner, 1985) discussion of crystal elasticity in terms of polyhedral models.

Cation- and Si-centred polyhedra of known relative rigidities and compressibilities are thus regarded as the basic building blocks for the structure, and are linked (eg by corner, edge and face sharing) to form structural elements (such as chains, columns and layers) whose mechanical properties provide at least a qualitative explanation of many of the major features of crystal elasticity.

The elasticity of a crystal may be described in terms of either the compliances or the stiffnesses of the structural elements. The elastic stiffness moduli arise naturally in the context of wave propagation because of their close relationship to the wave-velocity eigen-values (see Chapter 2). The C_{ij} describe the stresses required to produce a simple one-component strain ε_j, since

$$\sigma_i = C_{ij}\varepsilon_j \qquad i,j=1,2..6. \tag{5.1}$$

However, it is more appealing in the present discussion to emphasize the elastic compliances, which yield the strain components arising from

the application of a single stress component. Thus an applied uniaxial stress, σ_1, results in the strains

$$\varepsilon_1 = S_{11}\sigma_1 \tag{5.2}$$

$$\varepsilon_2 = S_{12}\sigma_1 \tag{5.3}$$

$$\varepsilon_3 = S_{13}\sigma_1. \tag{5.4}$$

Similarly, the shear stress, σ_6, produces the strain

$$\varepsilon_6 = S_{66}\sigma_6. \tag{5.5}$$

In their discussions of the elastic properties of polyhedral models for crystal structures, Vaughan and Weidner (1978), Bass (1982) and Weidner and Vaughan (1982) formulated the following set of basic rules for the relationships between the lattice compliances and the compliances of the major structural elements. When the compliance of a lattice is measured parallel to a set of structural elements, the least compliant element will determine the overall compliance in that direction. However, when compliance is measured normal to a set of structural elements, the compliance is determined by the most compliant element. The lattice compliances defined in this manner, can be increased by the introduction of polyhedral linkages with rotational degrees of freedom.

An attempt will be made in the following sections to identify the important structural elements and to assess their influence upon the elasticity of the olivine, orthopyroxene and garnet structures. The approach follows that of Weidner and colleagues except that attention is focussed on the elastic compliances rather than stiffnesses. Many of the principal conclusions concerning the relative magnitudes of the

compressional and shear moduli have previously been drawn by Weidner and his collaborators. However, the arguments concerning the off-diagonal moduli and the anomalous pressure dependence of the orthopyroxene compressional moduli represent a significant extension of this earlier work.

5.2 Polyhedral models of garnet, olivine and orthopyroxene

5.2.1 Garnet

The cubic garnet structure (space group Ia3d, Figure 5.1) consists of a three-dimensional network of alternate corner-linked SiO_4 tetrahedra and AlO_6 octahedra with divalent atoms M(Mg,Fe,Ca) in dodecahedrally (8-fold) co-ordinated interstices (Novak and Gibbs, 1971). The major structural elements in this lattice are the kinked chains of corner-sharing tetrahedra and octahedra which run parallel to the crystallographic axes. These chains are linked to form a three dimensional framework which is braced against further kinking by the edge sharing of both tetrahedra and octahedra with the large distorted MO_8 dodecahedra. Each tetrahedron shares two edges with dodecahedra, and each octahedron shares six edges with dodecahedra. Each dodecahedron shares four edges with octahedra, two edges with tetrahedra, and four edges with other dodecahedra. The edge sharing of the dodecahedra with eachother and with the tetrahedra and octahedra comprising the axial chains, restricts any possible rotation of polyhedra within the chains. The SiO_4 tetrahedra are the least compliant polyhedra in this structure, with the dodecahedra being the most compliant (Hazen and Finger, 1978)

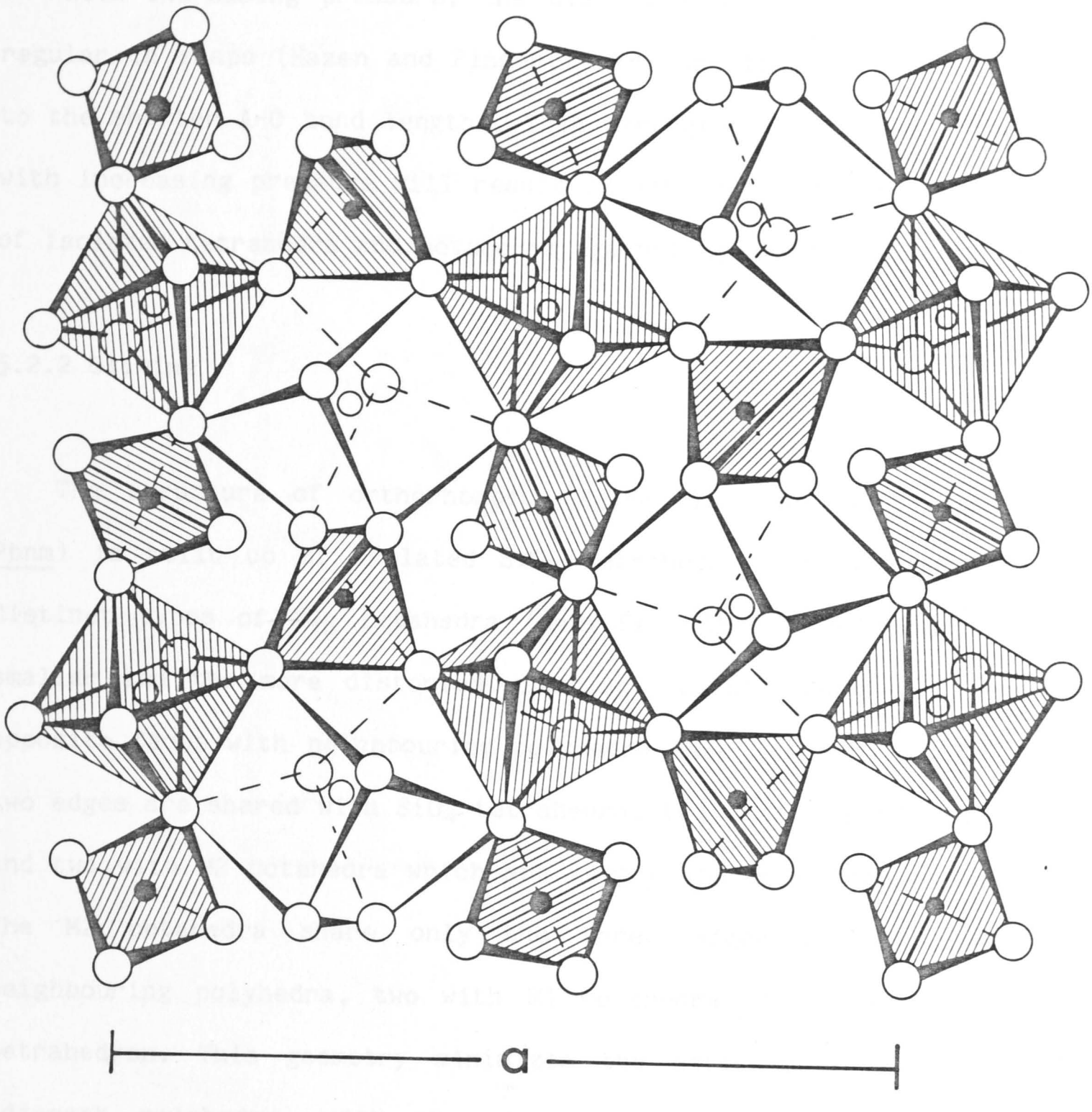

Figure 5.1 The crystal structure of garnet viewed down [001].
(redrawn after Novak and Gibbs, 1971)

With increasing pressure, the distorted MO_8 polyhedra become more regular in shape (Hazen and Finger, 1978) and thus less compliant due to the shorter A-O bond lengths. This strengthening of the dodecahedra with increasing pressure will result in stronger bracing of the chains of isolated tetrahedra and octahedra against deformation.

5.2.2 Olivine

The structure of orthorhombic $(Mg,Fe)_2SiO_4$ olivine (space group Pbnm) is built up of isolated SiO_4 tetrahedra and two symmetrically distinct types of MO_6 octahedra (M=Mg,Fe). The M1 octahedron is the smaller and the more distorted, sharing the six edges in a pair of opposite faces with neighbouring polyhedra (see Figure 5.3). Of these, two edges are shared with SiO_4 tetrahedra, two with other M1 octahedra, and two with M2 octahedra which are larger and more regular in shape. The M2 octahedra share only the three edges of one face with neighbouring polyhedra, two with M1 octahedra, and one with an SiO_4 tetrahedron. This geometry minimizes the cation-cation repulsion in adjacent polyhedra, with the shared edges shorter and thus less compliant than unshared edges. The SiO_4 tetrahedron is the least compliant polyhedron in the lattice (Hazen and Finger, 1980), with the average compressibility of the M1 octahedron being larger than that of the M2 octahedron.

There are three major structural elements in the olivine lattice. The least compliant of these are columns (see Figure 5.2) parallel to [100] of alternate SiO_4 tetrahedra and triangular clusters of edge-sharing octahedra (2M1,1M2). Each tetrahedron shares its basal plane edges with the three octahedra of the cluster below and its apical corner with the three octahedra of the culster above. The shared edges

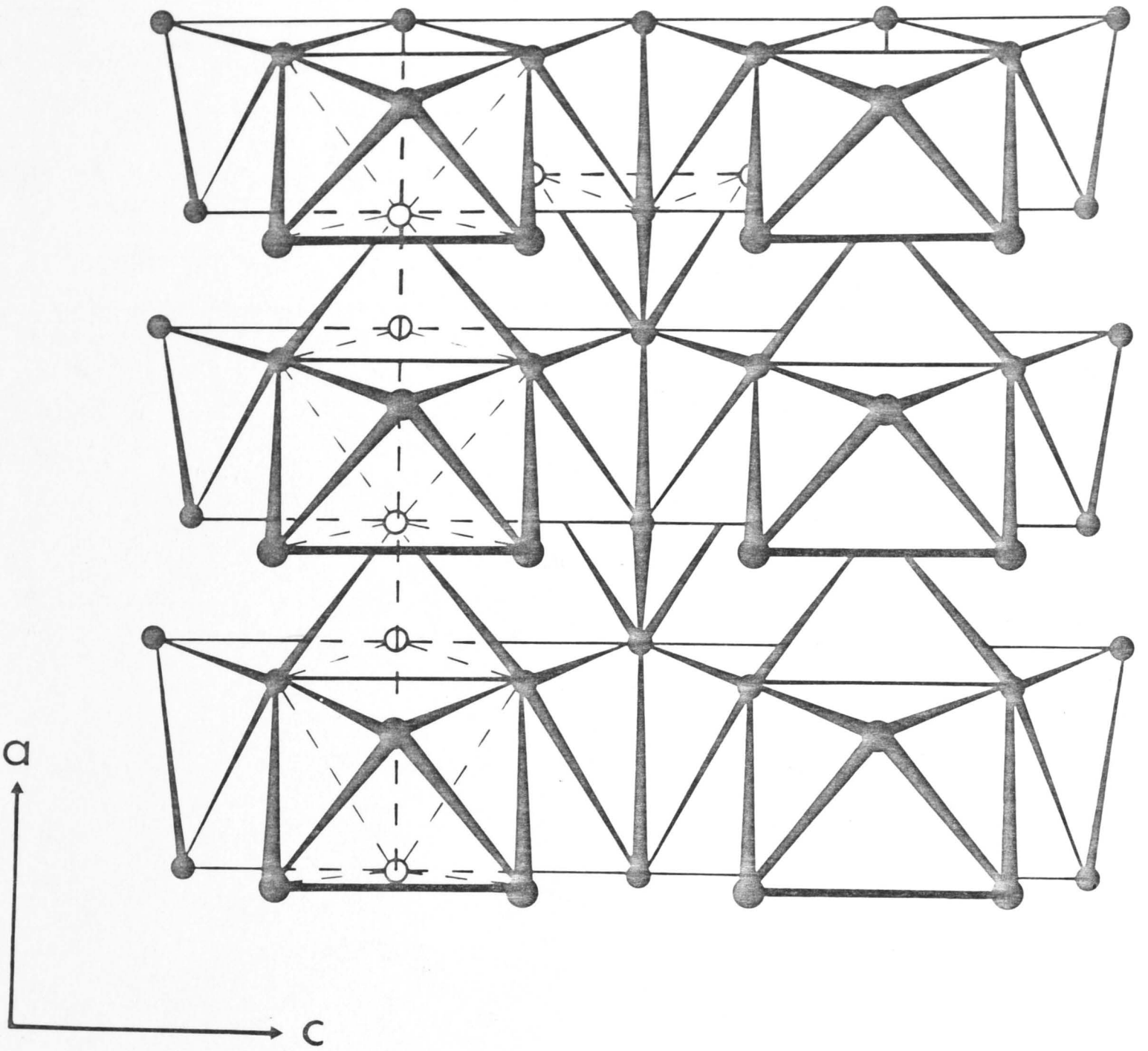

Figure 5.2 A schematic view of the polyhedral linkages in the olivine structure, viewed approximately down [010]. (Bass, 1982)

Figure 5.3 The crystal structure of olivine projected down [100].
(redrawn after Bass, 1982)

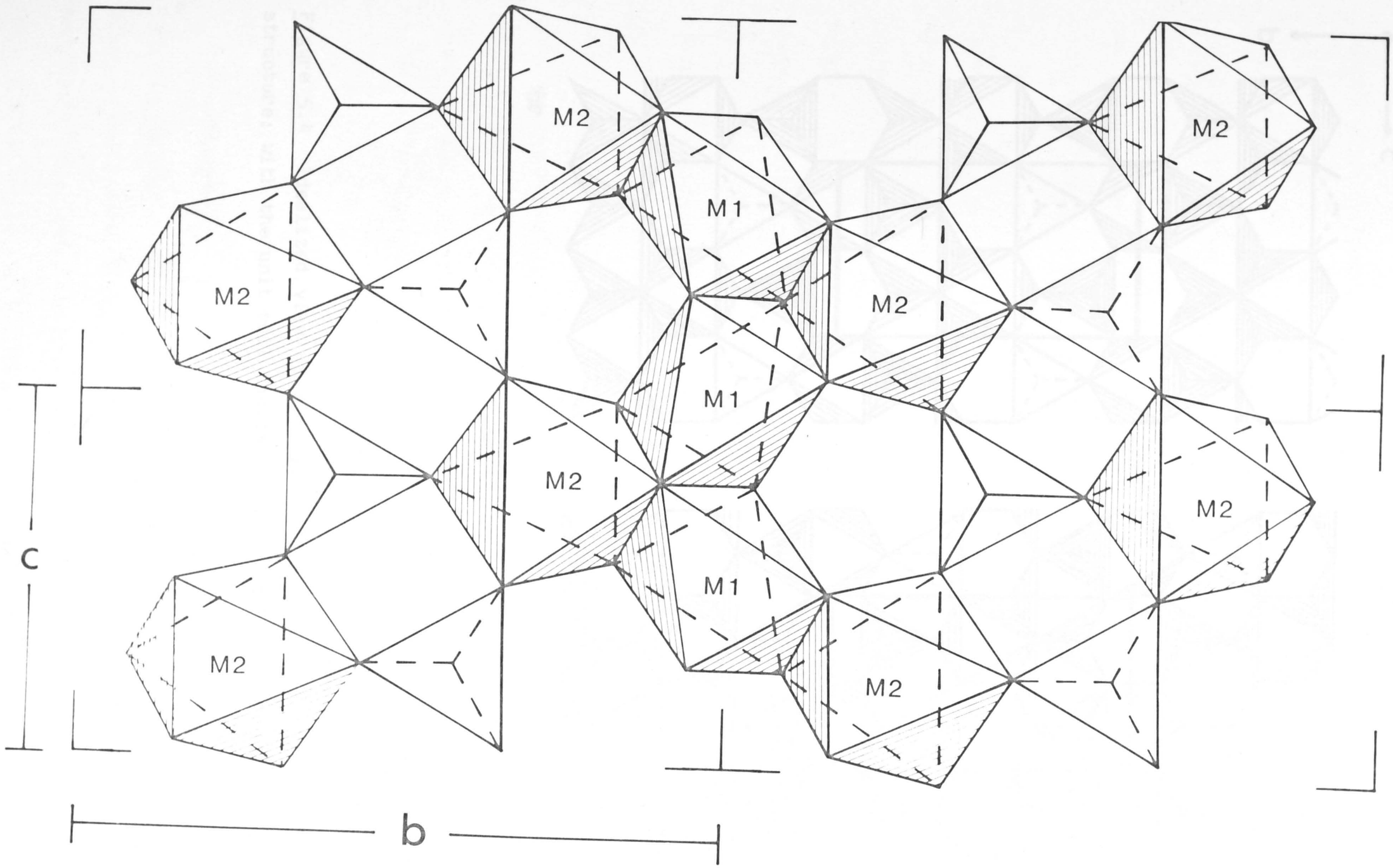
M2
M1
M2
M2
M1
M2
M2
M1
M2
M2
M2
M2
c
b

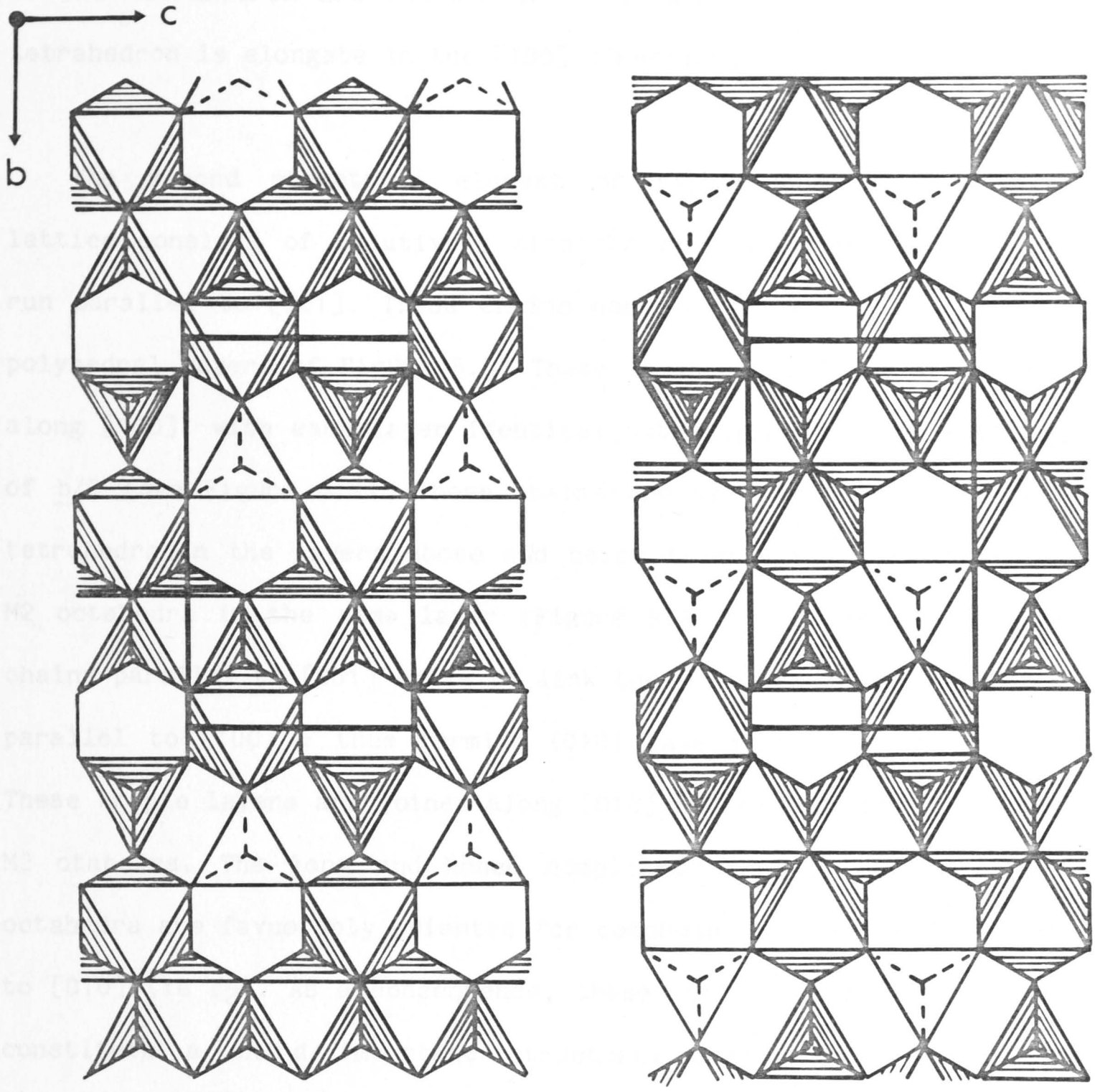

Figure 5.4 Idealized view of successive (100) layers of the olivine structure; with the unit cell indicated (after Morimoto et al., 1974).

of the tetrahedron are shorter than the unshared edges and hence the tetrahedron is elongate in the [100] direction.

The second structural element of significance in the olivine lattice consists of relatively straight chains of M1 octahedra which run parallel to [001]. These chains can be seen clearly in the (100) polyhedral layers of Figure 5.3. These layers of polyhedra are stacked along [100], with each layer identical but displaced by an [010] glide of b/2 (see Figure 5.4). These chains are well braced by the linking tetrahedra in the layers above and below (Figure 5.2) and also by the M2 octahedra in the same layer (Figure 5.3). These braced octahedral chains parallel to [001] serve to link the previously mentioned columns parallel to [100] - thus forming (010) layers three polyhedra thick. These triple layers are joined along [010] by the sharing of a layer of M2 otahedra. The long and hence compliant unshared edges of the M2 octahedra are favuorably oriented for compression or extension parallel to [010] (ie ε_2). As a consequence, these (010) layers of M2 octahedra constitute a third important structural element with considerable compliance parallel to [010]. Hazen and Finger (1980) have shown the MO_6 octahedra in the olivine lattice are compressed with increasing pressure, while the SiO_4 tetrahedra remain relatively incompressible. The M1 and M2 octahedra are most compressible in the [010] direction.

5.2.3 Orthopyroxene

The orthorhombic structure of orthopyroxene (space group Pbca) consists of alternate (100) layers of SiO_4 tetrahedra and MO_6 octahedra (Cameron and Papike, 1981) (see Figures 5.5 and 5.6). In each layer of tetrahedra, adjacent tetrahedra share corners to form kinked chains running parallel to [001]. There are two symmetrically distinct kinked

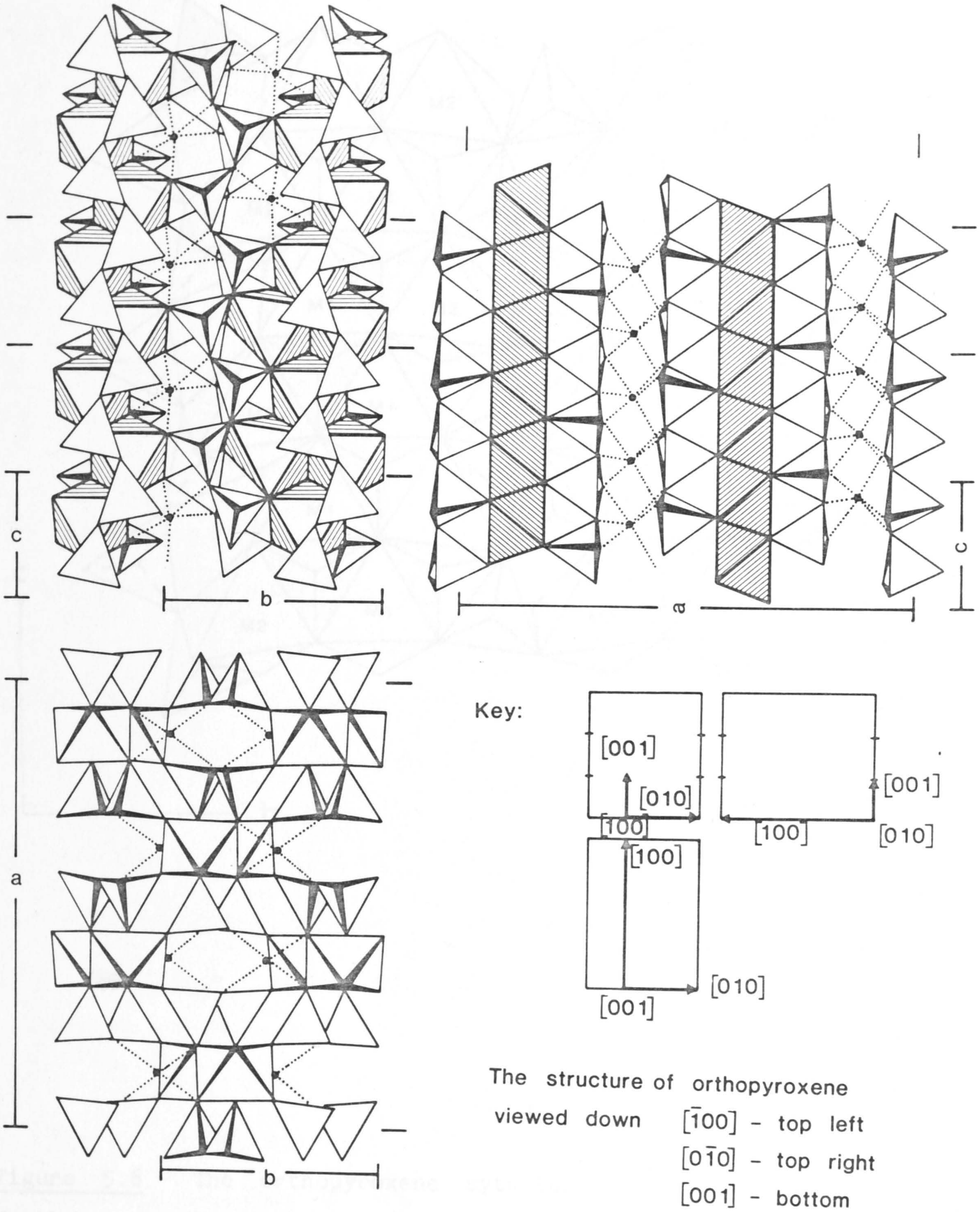

Figure 5.5 The structure of orthopyroxene (after Miyamoto et al., 1975); illustrating the serrated [001] chains of M1 octahedra braced by edge sharing M2 octahedra and capped by pairs of opposed kinked and puckered chains of tetrahedra - top left; the alternate layers of edge sharing octahedra and tetrahedra forming [100] I-beams - bottom; and the long bonds of the distorted M2 octahedra connected to the bridging corners of the puckered and kinked [001] chains of tetrahedra capping the I-beams - top right. The M2 octahedra are indicated by their M-O bonds.

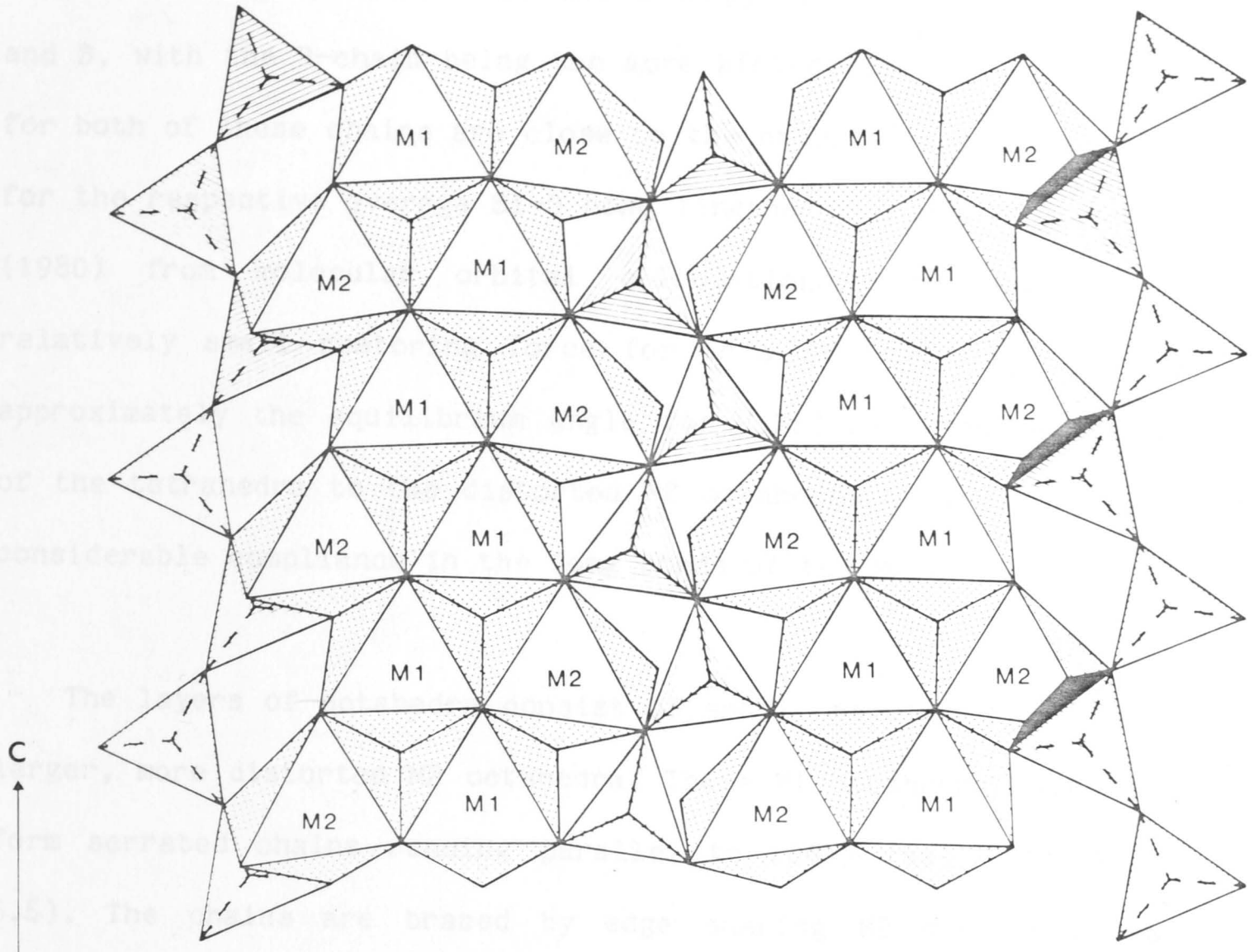

Figure 5.6 The orthopyroxene sytucture viewed down [100] (after Hawthorne and Ito, 1977).

chains of SiO_4 tetrahedra in the orthopyroxene structure, labelled A and B, with the B-chain being the more kinked. The Si-O-Si kink angles for both of these chains are close to the calculated equilibrium angles for the respective average Si-O bond lengths obtained by Newton et al. (1980) from molecular orbital calculations. The ability of the relatively small restoring force for this Si-O-Si angle to maintain approximately the equilibrium angle for $H_3SiOSiH_3$ despite the bonding of the tetrahedra to the distorted M2 octahedra is indicative of very considerable compliance in the long bonds of the M2 octahedra.

The layers of octahedra consist of small, regular M1 octahedra and larger, more distorted M2 octahedra. These M1 octahedra share edges to form serrated chains running parallel to [001] (see Figures 5.5 and 5.6). The chains are braced by edge sharing M2 octahedra. Each M1 octahedron shares an edge with two adjacent M1 octahedra, and two edges with bracing M2 octahedra. All six corners of each M1 octahedron are shared with tetrahedra - two are apical oxygens (O1B) and one is a non-bridging oxygen (O2B) in the B-chain above; two are apical oxygens (O1A) and one a non-bridging oxygen (O2A) in the A-chain below (terminology of Miyamoto et al., 1975).

The M2 octahedra are situated on the outer edges of the chains of M1 octahedra. All six corners of each M2 octahredron are shared with tetrahedra - the upper three being an apical oxygen (O1B), a non-bridging oxygen (O2B) and a bridging oxygen atom (O3B) of the B-chain; the lower three corners are the corresponding oxygen atoms of the A-chain. In addition, one of the M2 octahedral edges is shared (O2A-O3A) with a tetrahedron of the A-chain. The tetrahedral basal planes are constrained to approximate parallelism with the (100) plane by their corner linkages to the M1 and M2 octahedra.

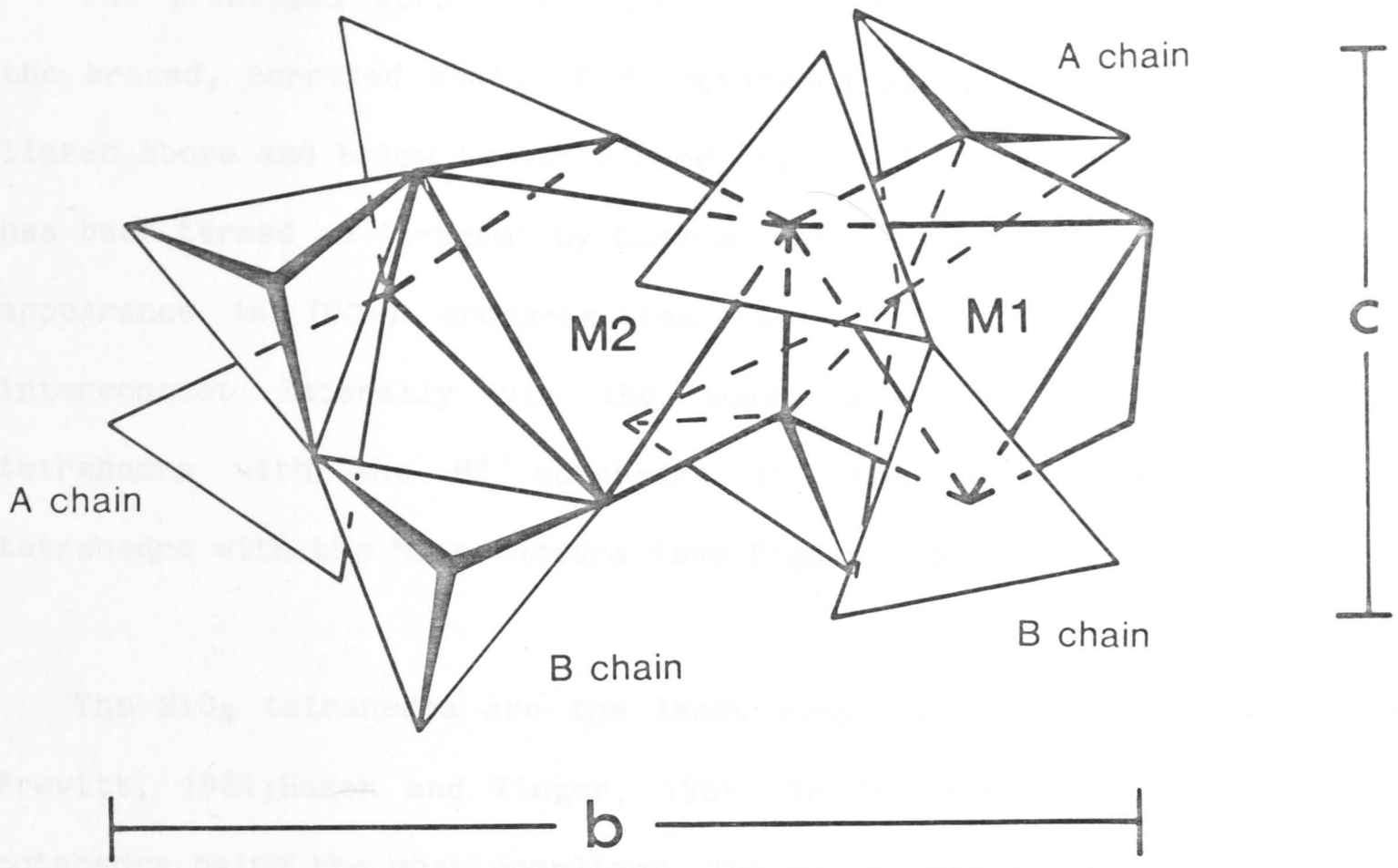

Figure 5.7 The linkages of the A- and B-chains of tetrahedra to the M1 and M2 octahedra.

The principal structural element of the orthopyroxene lattice is the braced, serrated chain of M1 octahedra parallel to [001] which is linked above and below to two kinked chains of tetrahedra. This element has been termed an 'I-beam' by Cameron and Papike (1981) because of its appearance in (001) cross-section (see Figure 5.5). These I-beams interconnect laterally via the edge- and corner-sharing of the tetrahedra with the M2 octahedra and the corner-sharing of the tetrahedra with the M1 octahedra (see Figure 5.5).

The SiO_4 tetrahedra are the least compliant polyhedra (Levien and Prewitt, 1981;Hazen and Finger, 1981) in the structure, with the M2 octahedra being the most compliant. The orthopyroxene structure is made up of deformed and unsymmetrical polyhedral linkages and therefore the effects of rotational degrees of freedom and polyhedral distortion must be included in the qualitative discussion of the lattice compliances. Rotational freedom within a structural element has the potential to increase the compliance of the element more than distortion of the component polyhedra (Vaughan and Bass, 1983;Bass and Weidner, 1984).

The deformed B-chain kinks more with increasing pressure than the A-chain (Ralph and Ghose, 1980). This kinking is accompanied by compression of the long bonds of the distorted M2 octahedra which therefore become more regular with increasing pressure. This B-chain is linked by corner-sharing only to the chains of M1 octahedra and to the M2 octahedra, while the A-chain is similarly linked to the chains of M1 octahedra and to the M2 octahedra by corner sharing, but also by edge-sharing with the M2 octahedra Thus, the B-chain has silghtly more rotational freedom than the A-chain.

5.3 Zero-pressure compliances

5.3.1 Compressional compliances

The dominant influence of crystal structure upon the relative magnitudes of the elastic moduli of garnet, olivine and orthopyroxene has been demonstrated in Chapter 4. Uniaxial stresses σ_i (i=1,2,3) and the associated strains ε_i determined by the compressional compliances S_{ii} are the easiest to envisage and will be discussed first. these compressional compliances for the three structures olivine, garnet and orthopyroxene are listed in Table 5.1 in order of increasing compliance, along with information concerning the principal structural element parallel to $\underline{x}_i$ for each case. It is immediately evident that there is an impressive correlation between increasing measured compliance down the table and increasing inferred compliance of the principal structural element. The directions of the compressive stresses in the upper part of the table correspond to sturdy columns or well-braced chains of relatively incompressible polyhedra whereas the lower entries have compressive stresses acting normal to unusually compliant layers. A number of the compliances in the centre of the table are comparable and the relatively small differences among them are probably beyond the resolution of this qualitative analysis. On the other hand the low values of S_{11} for olivine and garnet and the high value of S_{22} for orthopyroxene deserve special consideration.

Table 5.1 The zero-pressure compressional compliances together with their first and second pressure derivatives, and the principal structural elements of the garnet, olivine and orthopyroxene lattices. Units for S_{ii}, $\partial S_{ii}/\partial P$ and $\partial^2 S_{ii}/\partial P^2$ are 10^{-3} GPa^{-1}, 10^{-3} GPa^{-2} and 10^{-3} GPa^{-3} respectively.

S_{ii}	S	$\partial S/\partial P$	$\partial^2 S/\partial P^2$	Principal structural element
S_{11}(ol)	3.5	-0.06	0.006	columns of rigid triangular clusters of three edge-sharing octahedra (2M1,1M2) capped by isolated SiO_4 tetrahedra sharing basal plane edges and apical corners with the clusters of octahedra
S_{11}(gt)	4.1	-0.08	0.006	chains of alternate corner-sharing SiO_4 tetrahedra and AlO_6 octahedra braced by edge-sharing distorted MO_8 dodecahedra
S_{33}(ol)	5.1	-0.10	0.006	relatively straight chains of M1 octahedra well braced by edge-sharing with SiO_4 tetrahedra and M2 octahedra
S_{33}(opx)	5.2	-0.18	0.014	serrated chains of M1 octahedra braced by edge sharing M2 octahedra and capped by pairs of opposed kinked and puckered A- and B-chains of tetrahedra
S_{11}(opx)	5.4	-0.10	-0.010	alternate layers of octahedra (M1 and M2 edge-sharing and hence relatively densely packed within the layer) and of tetrahedra (layer of tetrahedra may have finite compliance due to presence of the degree of freedom of movement inherent in the puckering of the chains)
S_{22}(ol)	6.1	-0.10	0.004	alternate layers of M2 octahedra (corner shared and thus not densely packed within the layer) and of tetrahedra and M1 octahedra (the latter edge share with the tetrahedra)
S_{22}(opx)	7.2	-0.30	0.054	long bonds of the distorted M2 octahedra connected to the bridging corners of the tetrahedra in the kinked and puckered chains capping the I-beams

(ol)-olivine, (gt)-garnet, (opx)-orthopyroxene

The repeat unit in the [100] columns of olivine is a triangluar cluster of three edge-sharing octahedra capped by an SiO_4 tetrahedron sharing a basal plane edge with each of the octahedra in the cluster (Figure 5.2). Most of the compliance of this umit would be expected to come from the triangular cluster of octahedra rather than the capping tetrahedron. However, the very symmetrical arrangement of short shared octahedral/octahedral and octahedral/tetrahedral edges (they define an empty tetrahedron) must confer unusually low compliance on the cluster of octahedra.

The load-bearing element associated with the next lowest compliance - S_{11} for garnet - is a chain of alternate corner-sharing SiO_4 tetrahedra and AlO_6 octahedra, braced by edge-sharing with MO_8 dodecahedra. The lesser compressibility of SiO_4 tetrahedra and AlO_6 octahedra relative to MgO_6 octahedra, along with the dodecahedral bracing explains why S_{11} for garnet is less than S_{ii} for braced chains of MO_6 octahedra (eg S_{33} for olivine and orthopyroxene).

The large compressional compliance of the orthopyroxene structure parallel to [010] is related to the nature of the lateral linkages between the I-beams which are the principal structural elements running parallel to [001]. The I-beams are linked mainly by corner-sharing between M1 and M2 octahedra associated with a given I-beam and tetrahedra belonging to the kinked and puckered chains of adjacent I-beams. The substantial compliance of the longest M2-O bonds and the rotational degrees of freedom associated with kinking and puckering of the tetrahedral chains account qualitatively for the high value of S_{22}.

The intermediate compressional compliances of Table 5.1 are associated with principal structural elements intermediate in character

between the sturdy columns and well braced chains of incompressible polyhedra at the top of the table and the long bonds and rotational degrees of freedom at the bottom.

5.3.2 Off-diagonal compliances

The relative magnitudes of the off-diagonal moduli can now be discussed in terms of the magnitudes of the respective compressional compliances. For example, the application of a uniaxial compressive stress σ_1 to the olivine structure results in a small strain ε_1 (S_{11} is small) which is concentrated in the clusters of edge-sharing octahedra in the stiff [100] columns. The increase in internal energy of the octahedra due to this shortening parallel to [100] is partially compensated by extensional strains ε_2 and ε_3, related to the moduli S_{12} and S_{13} respectively. The relative magnitudes of ε_2 and ε_3 and hence S_{12} and S_{13} can be inferred from the relative compressional compliances of the structural elements parallel to [010] and [001]. Accordingly it is expected that more extensional strain will appear across the compliant layers of M2 octahedra parallel to [010] than along the [001] braced chains of octahedra, and thus, that $|S_{12}| > |S_{13}|$. Similarly, a uniaxial compressive stress σ_2 results in thinning of the compliant layer of M2 octahedra. This deformation is accompanied by extensional strains ε_1 and ε_3 in the M2 octahedra. The fact that $S_{11} < S_{33}$ guarantees that $\varepsilon_1 < \varepsilon_3$ and hence that $|S_{21}| = |S_{12}| < |S_{23}|$. In the same way, the deformation experienced by the chain of M1 octahedra due to the application of a uniaxial stress σ_3 is compensated by the thickening of the layers of linking M2 octahedra, with the rigid [100] columns accommodating little strain, and thus $|S_{23}| > |S_{13}|$. These three predictions of the relative magnitudes of the off-diagonal moduli form a consistent trend with

$$|S_{23}| > |S_{12}| > |S_{13}|; \qquad (5.6)$$

which is in accord with the observed magnitudes of the off-diagonal moduli for olivine (see Table 5.2).

Table 5.2 The off-diagonal compliances of garnet, olivine and orthopyroxene together with their first and second pressure derivatives.

S_{ij}	S_{ij} /(10^{-3} GPa^{-1})	$\partial S/\partial P$ /(10^{-3} GPa^{-2})	$\partial^2 S/\partial P^2$ /(10^{-3} GPa^{-3})
S_{13}(ol)	-0.75	-0.000	0.001
S_{12}(ol)	-0.91	-0.012	0.022
S_{13}(opx)	-1.00	-0.153	0.084
S_{23}(opx)	-1.08	-0.087	0.022
S_{12}(gt)	-1.10	0.012	-0.001
S_{23}(ol)	-1.74	-0.016	-0.006
S_{12}(opx)	-2.21	0.084	-0.026

(ol)-olivine, (gt)-garnet, (opx)-orthopyroxene

The relative magnitudes of the compressional compliances of the orthopyroxene structure can now be employed in the discussion of the off-diagonal moduli. A compressive stress σ_2 will result in shortening of the long compliant bonds of the M2 octahedra and associated increased kinking of the chains of tetrahedra. However, increased kinking of a chain of incompressible tetrahedra contributes equally to ε_2 and ε_3 and would therefore result in $S_{23} > 0$ - in conflict with the observations. In an alternative scenario, the high compliance S_{22} might be related to the other rotational degree of freedom which is associated with puckering of the chains of tetrahedra (ie relative rotation about edges joining bridging oxygen atoms). Extension parallel

to [100] accompanies shortening parallel to [010] achieved by puckering - so that one might expect $|S_{12}| < |S_{23}|$.

Similarly, a strain ε_1 resulting from the application of a compressive stress σ_1 may be accommodated by reduction of the puckering of the chains of tetrahedra, with significant extensional strain ε_2, and thus $|S_{12}| > |S_{13}|$. The stress σ_3 is resisted by the rigid chains of M1 octahedra which are braced against compression by the M2 octahedra. The isolation of the [100] puckered and kinked chains of tetrahedra and deformed M2 octahedra from the strained M1 octahedra indicates $S_{13} \approx S_{23}$. Thus, given the initial constraint of negative S_{23} and the structural behaviour necessary for this observation, the off-diagonal compliances form a consistent trend, with

$$|S_{12}| > |S_{13}| \approx |S_{23}|. \qquad (5.7)$$

This trend in the relative magnitudes of the off-diagonal moduli is comparable with the observed moduli tabulated in Table 5.2.

It is the distorted M2 bonds to the kinked and puckered chains of tetrahedra together with the control exerted by the chains of M1 octahedra which results in the anomalous compliances of the orthopyroxene lattice. With increasing pressure, however, the distorted M2 octahedra are known to become regular (Ralph and Ghose, 1980) with further kinking of the chains of tetrahedra.

5.3.3 Shear-mode compliances

Resistance to shear (low compliance) implies bracing of the unit cell; that is incompressible, inextendable structural elements

approximately parallel to the diagonals of the unit cell. Table 5.3 lists the shear-mode compliances of garnet, olivine and orthopyroxene in order of increasing compliance down the table. It is evident that the majority of the shear compliances are comparable, with S_{44} of garnet being the least compliant, and S_{44} of olivine being the most compliant.

The magnitudes of the shear compliances S_{55} and S_{66} of both olivine and orthopyroxene (see Figures 5.2 and 5.5) are controlled by the structural elements parallel to the ~[101] and ~[110] diagonals respectively. The structural elements in these directions are braced against compression or extension by rigid tetrahedra fixed in the (100) plane by either edge or corner sharing with octahedra. The shear ε_4 in orthopyroxene (see Figure 5.5) is resisted by the linkages of the chains of M1 octahedra and the chains of tetrahedra with rotational freedom about [100]. This rotational freedom however, is restricted by the resistance to deformation of the M1 octahedral edge which links the apices of neighbouring tetrahedra. The shear compliance S_{44} of orthopyroxene is comparable in magnitude with the compliances S_{55} and S_{66} of both olivine and orthopyroxene.

The modulus S_{44} of garnet is the least compliant. The garnet lattice (see Figure 5.1) is well braced against shear by the space filling and edge sharing dodecahedra which act effectively as bracing components. The most compliant shear modulus is S_{44} for olivine. The ~[011] diagonals of the olivine lattice (see Figure 5.3) consist of small chains of three octahedra connected by tetrahedra. These tetrahedra share their basal edges with three octahedra in the (100) layer below. This would imply only moderate compliance, contrary to the observations (see Table 5.3). Thus, the shear compliance S_{44} must be

increased by the freedom of the tetrahedra to rotate about [100], deforming the edge-sharing octahedra in the (100) layer below.

Table 5.3 The shear-mode compliances of garnet, olivine and orthopyroxene, together with their first and second pressure derivatives.

S_{ij}	S /(10^{-3} GPa^{-1})	$\partial S/\partial P$ /(10^{-3} GPa^{-2})	$\partial^2 S/\partial P^2$ /(10^{-3} GPa^{-3})
S_{44}(gt)	10.60	-0.174	0.018
S_{44}(opx)	12.11	-0.337	0.054
S_{66}(opx)	12.80	-0.451	0.060
S_{66}(ol)	12.80	-0.409	0.050
S_{55}(ol)	13.00	-0.290	0.034
S_{55}(opx)	13.07	-0.446	0.086
S_{44}(ol)	15.72	-0.542	0.068

(ol)-olivine, (gt)-garnet, (opx)-orthopyroxene

5.4 The anomalous elasticity of orthopyroxene - pressure dependence of the compressional compliances

With increasing pressure, the deformed compliant dodecahedra of the garnet lattice become more regular and thus less compliant. This strengthening of the bracing of the chains of tetrahedra and octahedra will reduce the already low compliance S_{11}. As these AO_8 dodecahedra (and BO_6 octahedra) compress regularly, the rate of change of the pressure derivative is negligible. Similarly, for the olivine lattice, increasing pressure causes the slightly deformed octahedra to become more regular and thus less compliant. The regular compression of these

octahedra is mirrored in the small rate of change of the pressure derivatives of the compressional moduli of olivine. In comparing the pressure dependences of the compressional compliances for these three minerals (see Table 5.1), it can be seen that the moduli S_{22}, and to a lesser extent S_{33}, of orthopyroxene have anomalously large pressure derivatives.

For the orthopyroxene lattice, increasing pressure causes the longest bond of the distorted M2 octahedra to shorten significantly in association with further kinking of the kinked chains of tetrahedra (Ralph and Ghose, 1980). The modulus S_{11} however, is determined by the compliances of the alternate layers of octahedra and tetrahedra in the direction normal to the layer. Pressure-induced kinking operates in the plane of the layer and is therefore unlikely to have a significant influence on S_{11}, for which a normal pressure derivative is expected.

The behaviour required of the kinked and puckered chains of tetrahedra in response to the shortening of the long bonds of the distorted M2 octahedra has been analysed with respect to the effects of hydrostatic pressure.

This analysis reveals that distances in the b-c plane are changed uniformly by kinking. However, for the b and c lattice parameters to be equally affected by the kinking of the A- and B-chains requires the A-chain to change its kink angle by about twice the change in the kink angle of the B-chain. This is contrary to the observations of Ralph and Ghose (1980).

If both kinking and puckering are allowed in the orthopyroxene lattice, the b lattice parameter is reduced by both kinking and

puckering, the c lattice parameter is reduced by kinking and the a lattice parameter is increased by puckering. The long M2 edge length is the dimension most sensitive to kinking of the chains, while it is insensitive to puckering.

Therefore, the initial compression of the orthopyroxene lattice can be accommodated by the kinking and puckering of the chains of tetrahedra with the shortening of the long M2 bonds in response to the kinking. This combination of kinking and puckering is controlled by the resistance of the appropriate M1 octahedral edge, which links the apical corners of the tetrahedra, to deformation

This unusually large rearrangement of the three-dimensional network of polyhedra with increasing pressure causes the lattice to very rapidly lose its compliance in the [010] and [001] directions as these are the directions are most affected by the kinking of the chains. The puckering of the chains with pressure does not appear to greatly affect the compliance of the [100] I-beams. Thus S_{22} and S_{33} have large pressure derivatives due to the loss of compliance in the [010] and [001] directions accompanying the kinking of the chains and the shortening of the dominantly corner-shared lateral linkages between the I-beams. However, the compression of the deformed M2 octahedra quickly reaches an equilibrium with the kinking and puckering of the chains of tetrahedra, with further kinking becoming energetically unfavourable. At this point the pressure derivatives of the moduli S_{22} and S_{33} must be comparable with those observed for the S_{11} modulus and the compressional moduli of olivine. Hence, not only are the first pressure derivatives of S_{22} and S_{33} of orthopyroxene large, but the second pressure derivatives are also anomalously large. The anomalous rate of change of the pressure derivative of the S_{11} modulus for orthopyroxene

may be due to the complex interaction of the puckering of the chains of tetrahedra with increasing pressure affecting the compliance of the lateral corner-sharing bonding of the I-beams.

CHAPTER 6

GEOPHYSICAL IMPLICATIONS

6.1 Introduction

Models for the mineralogy of the mantle have been based primarily upon natural samples of the upper mantle provided by basaltic lavas and the dominantly peridotitic xenoliths carried by magmas of deep-seated origin. The geochemical and petrological information provided by these samples of upper mantle melt and the complementary residue, together with laboratory studies of the relevant phase equilibria has facilitated the development of a pyrolite model for the chemical composition of the upper mantle (Ringwood, 1966). At depths between ~70 and 200 km, the pyrolite composition crystallizes into an olivine, Al-poor pyroxene and pyrope-rich garnet mineralogy. At shallower depths the aluminous phase garnet is replaced by spinel and Al-rich pyroxenes, and at depths in excess of ~200 km the Al-poor pyroxenes begin to dissolve in complex garnet solid solutions featuring partial octahedral

co-ordination of silicon.

The physical properties of these mineral constituents of the upper mantle determine the velocities of seismic waves travelling through the mantle. Therefore, laboratory measurements of the velocities of ultrasonic pulses propagating at approximate mantle conditions through rocks representative of the proposed upper mantle mineralogy should reproduce the observed seismic velocities.

However, there are a number of sources of error associated with this laboratory measurement of velocities through upper mantle specimens. It is important to ensure that the physical properties of the necessarily small ($<10^{-1}$ m) rock samples on which the wave velocities are measured are statistically representative of the properties of the mantle (with heterogeneities $>10^{1}$ m); and furthermore that velocity differences between samples are due to mineralogical variations and not to the physical competance of the samples or to the variable effects of mineral alteration within the aggregates. Difficulties arise in the determination of the wave velocities due to the changing effects of cracks, pore spaces and pore fluids on the propagating signal with increasing temperature and pressure. A further source of error lies in the extrapolation of these laboratory measurements to the high temperature and high pressure conditions of the upper mantle.

Most of these technical and theoretical hazards can be sidestepped by the measurement of the elastic properties of single crystals of representative upper mantle minerals at temperature and pressure. The resulting single crystal data may then be combined via aggregate theory to produce bounds on the velocities of waves propagating through

hypothetical isotropic aggregates of specified compositions, with no spurious effects introduced by the presence of pore spaces or cracks in the samples. This mathematical approach does however, leave the resulting velocity models at the mercy of the assumptions and limitations of the mathematical theory.

In the present study, the elastic constants of single crystals of garnet, olivine and orthopyroxene of approximate mantle compositions have been determined at high pressures and room temperature with sufficient precision to provide accurate determination of the first pressure derivatives, and the first measurements of the second pressure derivatives of the elastic moduli. These new data facilitate the immediate computation of bounds on the elastic properties of a model 'garnet harzbergite' mantle at 295 K and pressures to 3 GPa, where previously data existed for these minerals only to pressures ~1 GPa. As observed previously (see Chapter 4), the effects of these second pressure derivatives become important with increasing pressure, especially in the case of orthopyroxene. The 3 GPa pressure capability of the present study substantially shortens the extrapolation to upper mantle pressures. Temperature derivatives of elastic moduli from the literature permit the further extrapolation to upper mantle temperatures to be made and thus facilitate calculation of bounds for upper mantle velocity profiles for specified mineralogies. The velocites calculated in this manner may be slight over-estimates (1-5%) of the seismic velocities due to possible dispersion occurring across the frequency range between the seismic (~0.1 Hz) and ultrasonic (~100 MHz) frequencies (Goetze, 1977).

6.2 The elasticity of multiphase composites

There are a number of mathematical treatments for the calculation of the effective elastic moduli of composites of two or more isotropic phases. The simplest approach is that of Hill (1963) in which the average stresses and strains of a body with prescribed boundary conditions are defined in terms of the average stresses and strains of the constituent phases;

$$\langle \varepsilon \rangle = \sum_{i=1}^{n} v_i \langle \varepsilon_i \rangle \tag{6.1}$$

and

$$\langle \sigma \rangle = \sum_{i=1}^{n} v_i \langle \sigma_i \rangle \tag{6.2}$$

where v_i is the volume fraction of the i^{th} phase and σ_i and ε_i are the stress and strain respectively for the i^{th} phase. The effective moduli can then be defined as

$$\langle \sigma \rangle = C^* \langle \varepsilon \rangle . \tag{6.3}$$

The Voigt and Reuss bounds on the effective elastic properties can then be found by assuming uniform stress and uniform strain respectively throughout the body to give the bounds on the moduli of the composite;

$$M_R^* = \left(\sum_{i=1}^{n} v_i / M_i \right)^{-1} \leq M^* \leq \sum_{i=1}^{n} v_i M_i = M_V^* \tag{6.4}$$

where M_i is the bulk or shear modulus of the i^{th} phase and M^* is the effective modulus of the composite.

Hashin and Shtrikman (1963) have derived bounds for an isotropic composite which are much tighter than those derived using the Voigt and Reuss assumptions. This approach replaces a heterogeneous body of modulus $C(\underline{x})$, stress $\sigma(\underline{x})$, and strain $\varepsilon(\underline{x})$, with a reference body of C', σ' and ε'; where the internal stress field $\sigma'(\underline{x})$ does not alter the strain $\varepsilon(\underline{x})$ and

$$\sigma'(\underline{x}) = (C - C')\varepsilon(\underline{x}); \tag{6.5}$$

where $\underline{x}$ is the position vector; or alternatively, the strain field $\varepsilon'(\underline{x})$ leaves the stress $\sigma(\underline{x})$ unchanged

$$\varepsilon'(\underline{x}) = (S' - S)\sigma(\underline{x}). \tag{6.6}$$

The bounding process involves choosing either σ' or ε' in the reference body subject to the constraints of Equations 6.5 and 6.6. This treatment produces the following equations for the lower and upper bounds on the bulk and shear moduli respectively;

$$K_-^* = K_1 + A_1/(1 + \alpha_1 A_1) \tag{6.7}$$

$$K_+^* = K_n + A_n/(1 + \alpha_n A_n) \tag{6.8}$$

where

$$\alpha_1 = -3/(3K_1 + 4G_1)$$

$$\alpha_n = -3/(3K_n + 4G_n) \tag{6.9}$$

and

$$A_1 = \sum_{i=2}^{n} v_i/((K_i - K_1)^{-1} - \alpha_1)$$

$$A_n = \sum_{i=1}^{n-1} v_i/((K_i - K_n)^{-1} - \alpha_n) \tag{6.10}$$

and

$$G_-^* = G_1 + B_1/(2(1 + \beta_1 B_1)) \tag{6.11}$$

$$G_+^* = G_n + B_n/(2(1 + \beta_n B_n)) \tag{6.12}$$

where $$\beta_1 = -3(K_1 + 2G_1)/(5G_1(3K_1 + 4G_1))$$

$$\beta_n = -3(K_n + 2G_n)/(5G_n(3K_n + 4G_n)) \qquad (6.13)$$

and $$B_1 = \sum_{i=2}^{n} v_i/((2(G_i - G_1))^{-1} - \beta_1)$$

$$B_n = \sum_{i=1}^{n-1} v_n/((2(G_i - G_n))^{-1} - \beta_n) \qquad (6.14)$$

where $$K_-^* \leqq K^* \leqq K_+^* \qquad (6.15)$$

and $$G_-^* \leqq G^* \leqq G_+^* \qquad (6.16)$$

with K_1 and G_1 being the smallest moduli (in the present case those of orthopyroxene) and K_n and G_n being the largest moduli (in the present case those of garnet). The bounds thus calculated on the bulk modulus of two-phase aggregates have been shown by Hashin (1962) to coincide with the bulk moduli of the special composite which is formed by incorporation of spherical inclusions of one phase in a matrix of the other phase. This result demonstrates that the Hashin-Shtrikman bounds are the closest possible bounds given only the volume fractions of the phases and the single crystal elastic moduli. There exist treatments which will produce bounds tighter than those of Hashin and Shtrikman (eg Miller, 1969;Kuster and Toksöz, 1974;Berryman, 1980) but knowledge of the distribution of orientations and shapes of the grains making up the aggregate is required.

The calculation of the bounds on the bulk and shear moduli for single-phase polycrystals, followed by the calculation of the bounds for the bulk and shear moduli of multiphase composites of isotropic phases is a procedure which has been widely used in the geophysical literature (eg Davies, 1974;Watt and O'Connell, 1978;Jackson, 1983), and for which there exists some observational support (Watt and

O'Connell, 1979) - yet it is far from obvious that it results in rigorous bounds on the elastic properties of the most general multiphase aggregate. Rather, the bounds for the elastic properties of an isotropic composite which is an aggregate of isotropic polycrystals (not single crystals) have been calculated. It is possible therefore that bounds calculated in this way actually bound the elastic moduli of a subset only of the complete set of polycrystalline aggregates.

6.3 The elasticity of composites of upper mantle phases

6.3.1 Composites of the measured olivine (Fo_{90}), orthopyroxene (En_{80}) and garnet (Py_{63}) phases

The bounds on the elastic moduli of isotropic polycrystals of the measured garnet, olivine and orthopyroxene phases calculated in Chapter 4, can now be used in the calculation of the bounds for the bulk and shear moduli of specific composites of these mantle minerals to 3 GPa at 295 K. Three composites of non-equilibrium mineralogies have been chosen in a simplified MgO-FeO-SiO_2-Al_2O_3 system. The first is a dunite whose bulk and shear moduli were calculated from the single crystal moduli of the San Carlos olivine. The other composites are a 'harzburgite' and a 'garnet harzburgite' - the latter with fractions of olivine, orthopyroxene and garnet similar to pyrolite (see Table 6.1). For the purposes of the present calculation the compositions of the olivine, orthopyroxene and garnet phases are those of the measured crystals and obviously do not necessarily constitute an equilibrium assemblage under any conditions of pressure and temperature. In Section 6.3.2 the properties of equilibrium assemblages will be calculated. The bulk and shear moduli for these three mantle models were calculated

using the garnet, olivine and orthopyroxene bulk and shear modulus data presented in Table 6.2

Table 6.1 Compositions, densities and Mg/(Mg+Fe) ratios for the three composites of the measured phases.

Model	Dunite	'Garnet Harzburbite'	'Harzburgite'
Garnet			
Mg/(Mg+Fe)		63	63
vol %	-	10.9	1.5
Olivine			
Mg/(Mg+Fe)	91	91	91
vol %	100.0	59.1	75.4
Orthopyroxene			
Mg/(Mg+Fe)		80	80
vol %	-	30.0	23.1
Density g cm^{-3}	3.325	3.393	3.342

Table 6.2 The average Hashin-Shtrikman bounds on the elastic moduli for single phase aggregates of the garnet, olivine and orthopyroxene crystals characterized in the present study (see Tables 4.1, 4.9, 4.15 and 4.19)

Mineral	M /GPa	$\partial M/\partial P$	$\partial^2 M/\partial P^2$ / GPa^{-1}
Garnet			
K	173.6	4.97	-0.32
G	94.9	1.59	-0.11
Olivine			
K	129.1	4.87	-0.27
G	77.7	1.76	-0.13
Orthopyroxene			
K	109.9	11.62	-1.46
G	75.0	1.97	-0.33

The Voigt and Reuss bounds for the elastic properties of the composites were defined as the lower (Reuss) bound for a composite of isotropic polycrystals whose bulk and shear moduli were calculated using the Reuss method (see Table 4.19), and the upper (Voigt) bound for a composite whose bulk and shear moduli were calculated using the Voigt method (see Table 4.19). The Hashin-Shtrikman bounds for the composites were calculated using the averages of the Hashin-Shtrikman bounds on the bulk and shear moduli of the various polycrystals since these bounds were in all cases very closely spaced.

The calculated Hashin-Shtrikman bounds for the multiphase composites were found to be co-incident within the uncertainties in the elastic moduli of the aggregates. The Voigt and Reuss bounds on the bulk and shear moduli were ±(2-3)% and ±(1-2)% respectively about the Hashin-Shtrikman values. The comparison of these Hashin-Shtrikman bounds and Voigt and Reuss bounds for the shear and bulk moduli of both single-phase aggregates and multiphase composites illustrates the greater effectiveness of the Hashin-Shtrikman variational approach in producing tight constraints on the moduli of an aggregate. Figures 6.1 and 6.2 illustrate the Hashin-Shtrikman effective bulk and shear moduli for the isotropic dunite, 'harzburgite' and 'garnet harzburgite' composites at 295 K, with the pressure dependence extrapolated from the observed 3 GPa range to 6 GPa.

At zero pressure, the relative magnitudes of the bulk and shear moduli of these garnet, olivine and orthopyroxene polycrystals are 1.34:1:0.85 and 1.22:1:0.97 respectively. Thus, for a mineralogy dominated by olivine, the addition of equal volumes of garnet and orthopyroxene will result in a small increase in the bulk modulus and a substantial increase in the shear modulus, by virtue of the magnitudes

of the garnet moduli. For the 'garnet harzburgite' and 'harzburgite' mineralogies the volume ratio of orthopyroxene to garnet is at least 3:1. This large volume of orthopyroxene swamps the effects of the high bulk modulus of the garnet phase in both of these assemblages and results in bulk moduli for the 'garnet harzburgite' and the 'harzburgite' which are lower than that of the dunite (see Figure 6.1). Despite this volume disparity, the high shear modulus of the garnet phase of the 'garnet harzburgite' results in a modest increase in the modulus of the composite with respect to that of dunite. The shear modulus of the 'harzburgite' composite, however, is lower than that of the dunite.

The first pressure derivative of the bulk modulus of the isotropic orthopyroxene phase (and to a lesser degree, the pyrope-rich garnet phase), which is high with respect to that of olivine (see Table 6.2), results in the bulk moduli for the 'harzburgite' and 'garnet harzburgite' composites increasing more rapidly with increasing pressure than the bulk modulus of the dunite. This effect of the high pressure-dependence of the bulk modulus of orthopyroxene is illustrated in Figure 6.1, where the bulk moduli of all but the most pyroxene rich assemblage (and therefore the composite with the lowest zero pressure bulk modulus), are higher than that of the dunite at ~6 GPa. The large negative pressure derivative measured in the present study results in significantly lower bulk moduli at 3-6 GPa than has previously been inferred by linear extrapolation of the lower pressure data of Frisillo and Barsch (1972).

The three isotropic mineral phases comprising these composities have more similar first pressure derivatives for the shear moduli. The second pressure derivative for the shear modulus of orthopyroxene

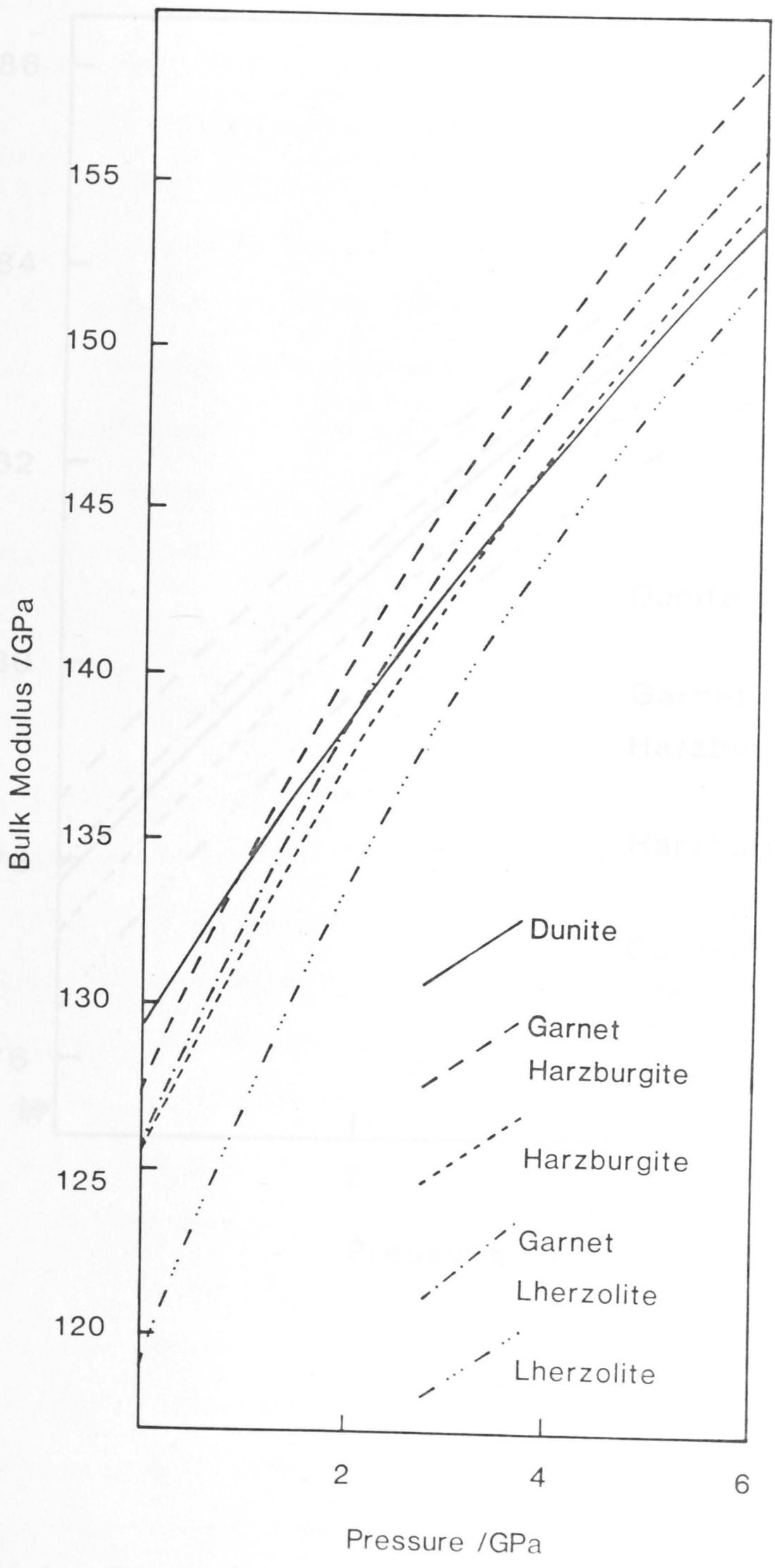

Figure 6.1 The variation with pressure of the bulk moduli of mulitphase composites of specific compositions and mineralogies (see text for details).

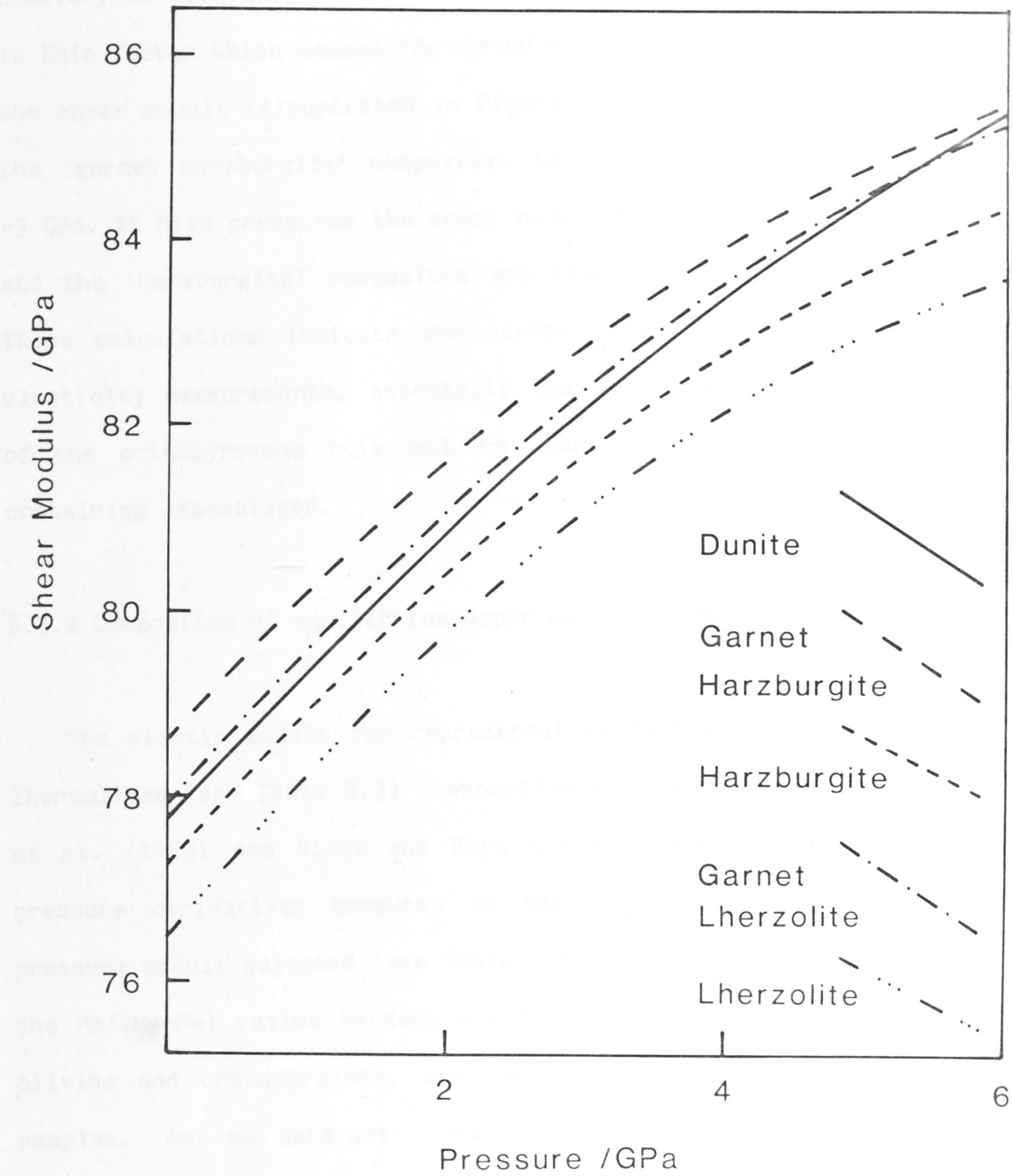

Figure 6.2 The variation with pressure of the shear moduli of mulitphase composites of specific compositions and mineralogies (see text for details).

however, is much larger than than that of either garnet or olivine. It is this factor which causes the curvature in the pressure dependence of the shear moduli (illustrated in Figure 6.2) for the 'harzburgite' and the 'garnet harzburgite' composites to be apparent even at pressures ~3 GPa. At high pressures the shear moduli for the 'garnet harzburgite' and the 'harzburgite' composites are lower than that for the dunite. These calculations indicate the general impact of the high pressure elasticity measurements, especially the anomalous pressure dependence of the orthopyroxene bulk modulus upon the moduli of orthopyroxene containing assemblages.

6.3.2 Composites of equilibrium upper mantle assemblages

The elastic moduli for representative fertile and depleted garnet lherzolites (see Table 6.3) (respectively PHN1611 and PHN1569 of Nixon et al. (1963) and Nixon and Boyd (1973)) were calculated using the pressure derivatives measured in the present study, with the zero pressure moduli adjusted (see Table 6.4 and Chapter 4) for variation in the Mg/(Mg+Fe) ratios between the measured single crystals of garnet, olivine and orthopyroxene, and the phases which comprise these rock samples. As no data are available for the elastic moduli of clinopyroxene, it was assumed, due to the similarity of the crystal structure (see Chapter 5.), that the elastic moduli of clinopyroxene together with their pressure derivatives are the same as those observed for orthopyroxene. The dunite discussed in the previous section has a plausible upper mantle composition and therefore is included in the present discussion of composites of mantle mineralogies and composition. These lherzolites are probably not genetically related - otherwise less orthopyroxene would be expected in the lherzolite than in the garnet lherzolite.

Table 6.3 Compositions, densities and Mg/(Mg+Fe) ratios for the three upper mantle composites.

Model	Dunite	Garnet Lherzolite	Lherzolite
Garnet			
Mg/(Mg+Fe)		81	84
vol %	-	9.3	0.7
Olivine			
Mg/(Mg+F e)	91	88	93
vol %	100.0	58.9	52.1
Pyroxene			
Mg/(Mg+Fe)		89	94
vol %	-	31.8	47.2
Density g cm^{-3}	3.325	3.39	3.30

The increase in the Mg/(Mg+Fe) ratios from those of the garnet and orthopyroxene measured in the present study (see Table 6.2) to those of the minerals comprising the garnet lherzolite and the lherzolite (see Table 6.4) has the effect of decreasing the shear modulus of garnet and the bulk modulus of pyroxene, while increasing the bulk modulus of garnet, with the shear modulus of pyroxene remaining unchanged. These zero pressure moduli have been calculated from measurements of the elastic moduli of the various solid solution members by previous authors. The garnet moduli were calculated from Leitner et al.'s (1980) systematics for members of the pyralspite solid solution series. The olivine moduli and the bulk moduli for the pyroxenes were calculated from linear regressions of the moduli determined by previous authors for crystals of varying compositions (see Tables 4.22 and 4.23). The shear moduli of the pyroxenes were calculated from a linear regression of the data obtained for the magnesium-rich orthopyroxenes in Table 4.23.

Table 6.4 The average zero-pressure Hashin-Shtrikman effective bulk and shear moduli for the garnet, olivine and pyroxene polycrystals which are used in the calculation of the bounds of the elastic properties of the dunite, garnet lherzolite and lherzolite.

Mineral	Present Study	Dunite	Garnet Lherzolite	Lherzolite
Garnet				
K /GPa	173.6	-	175.4	175.3
G /GPa	94.9	-	91.8	91.5
Olivine				
K /GPa	129.1	129.1	129.1	129.1
G /GPa	77.7	77.7	77.3	77.3
Pyroxene				
K /GPa	109.9	-	107.4	107.7
G /GPa	75.0	-	75.2	75.5

These compositionally adjusted bulk and shear moduli (Table 6.4) affect the elastic properties of the olivine rich composites in the same manner as previously observed for the non-equilibrium assembalges (see Figures 6.1 and 6.2). Again the large volume of pyroxene swamps the competing effect of garnet and decreases the bulk modulus of the composites with respect to that of the dunite. The shear modulus of the garnet-rich mineralogy is higher than that of the dunite despite the high pyroxene/garnet volume ratio. As can be seen from Table 6.4, the increase in Mg content between the fertile garnet lherzolite and the depleted lherzolite has little effect on the bulk and shear moduli of the various phases of the aggregates, and it is the loss of garnet and the addition on pyroxene which causes the bulk and shear moduli of the lherzolite to decrease with respect to the moduili of the garnet lherzolite.

The 'garnet harzburgite' and the garnet lherzolite differ essentially by Mg/(Mg+Fe) ratios. Figures 6.1 and 6.2 illustrate that the effect of the change in composition from the 'garnet harzburgite' to the garnet lherzolite composite is to decrease both the bulk and shear moduli. Such a decrease must be due to the effect of the large increase in magnesium content (see Tables 6.2 and 6.4) from that of the present crystals (of approximate upper mantle compositions) to that of the phases of the garnet lherzolite. Comparison of Tables 6.2 and 6.4 reveals the shear modulus of garnet and the bulk modulus of pyroxene for the garnet lherzolite composition are reduced with respect to the moduli for the 'garnet harzburgite'.

6.4 Velocity models for the upper mantle

The compressional- and shear-mode velocities of waves propagating through these isotropic composites have been calculated from the bulk and shear moduli and the densities of the composites at high pressure and room temperature, where the compressional velocity is

$$v_p = \sqrt{(K + (4/3)G)/\rho} \qquad (6.17)$$

and the shear velocity is

$$v_s = \sqrt{G/\rho}. \qquad (6.18)$$

These velocities have be extrapolated to ~6 GPa (200 km depth) using the quadratics determined over the observed 3 GPa pressure range. The temperature dependence of these velocities has been introduced to the calculations as

$$\Delta v_i = 0.5\sqrt{(M_i/\rho)}\ ((\partial M_i/\partial T)/M_i + \alpha))\ \Delta T \qquad (6.19)$$

where M_i and ρ are the zero pressure modulus and density and α is the thermal volume expansion coefficient at 295 K. For the purposes of the present study and in an effort not to introduce the possibly misleading high linear temperature dependence of the elastic moduli of orthopyroxene (Frisillo and Barsch, 1972), the temperature dependence of the bulk and shear moduli of the dominant phase olivine, with $\partial K/\partial T = -0.016$ GPa K^{-1} and $\partial G/\partial T = -0.013$ GPa K^{-1} (Kumazawa and Anderson, 1969) and the thermal volume expansion coefficient of olivine $\alpha = 26\times10^{-6}$ K^{-1} (Suzuki, 1975), have been used in Eqn. 6.19.

The oceanic and shield geotherms of Clark and Ringwood (1964) have been used in these calculations - being plausible upper and lower bounds on the upper mantle temperature profile. The pressure dependence of the calculated room temperature velocities has been converted into a depth dependence by a conversion factor of 31.15 km GPa^{-1} (from PREM, Dziewonski and Anderson, 1981). Figures 6.3 and 6.4 illustrate the resulting compressional and shear velocity profiles for the upper 200 km of the mantle for these two temperature gradients.

Figure 6.3 illustrates the effectiveness of the large volumes of orthopyroxene in the garnet lherzolite and lherzolite mineralogies in reducing (by ~2%) the low temperature, low pressure compressional velocities from that of the dunite, despite the presence of significant amounts of garnet (which will tend to cause the compressional velocity to increase) in the garnet lherzolite aggregate. The initial large temperature gradient of the oceanic geotherm produces a zone of low velocity at ~75 km depth (Figure 6.3), reducing the calculated

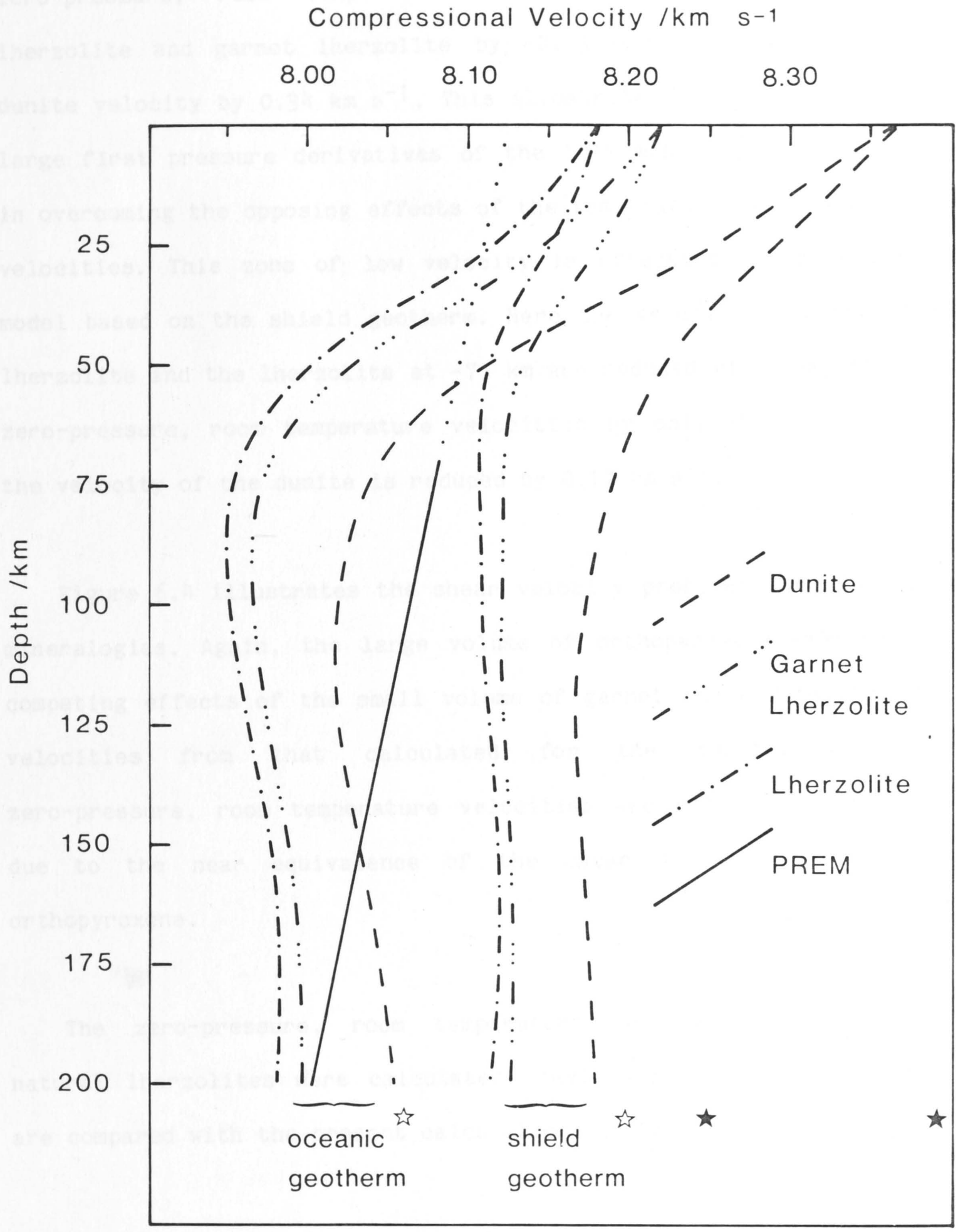

Figure 6.3 The variation with depth and temperature of the compressional velocity profiles for specific upper mantle assemblages, together with the average upper mantle velocity profile of Dziewonski and Anderson (1981). The solid stars indicate the velocities calculated for the orthopyroxene-rich mineralogy, assuming a linear pressure dependence of the elastic moduli of orthopyroxene. The hollow stars indicate the velocities calculated assuming a linear pressure dependence of the elastic moduli of orthopyroxene for depths greater than 100 km. In both cases, the velocity profiles to about 100 km depth are similar.

zero-pressure, room temperature compressional velocities of the lherzolite and garnet lherzolite by ~0.23 km s^{-1}, and reducing the dunite velocity by 0.34 km s^{-1}. This illustrates the importance of the large first pressure derivatives of the bulk modulus of orthopyroxene in overcoming the opposing effects of the temperature dependence of the velocities. This zone of low velocity is effectively absent for the model based on the shield geotherm. Here the velocities of the garnet lherzolite and the lherzolite at ~75 km are reduced with respect to the zero-pressure, room temperature velocities by only ~0.10 km s^{-1}, and the velocity of the dunite is reduced by 0.17 km s^{-1}.

Figure 6.4 illustrates the shear velocity profiles for these three mineralogies. Again, the large volume of orthopyroxene overcomes the competing effects of the small volume of garnet and reduces the shear velocities from that calculated for the dunite. Here, the zero-pressure, room temperature velocities are reduced by only ~0.5% due to the near equivalence of the shear moduli of olivine and orthopyroxene.

The zero-pressure, room temperature velocities for these two natural lherzolites were calculated previously by Jordan (1979), and are compared with the present calculations in Table 6.3.

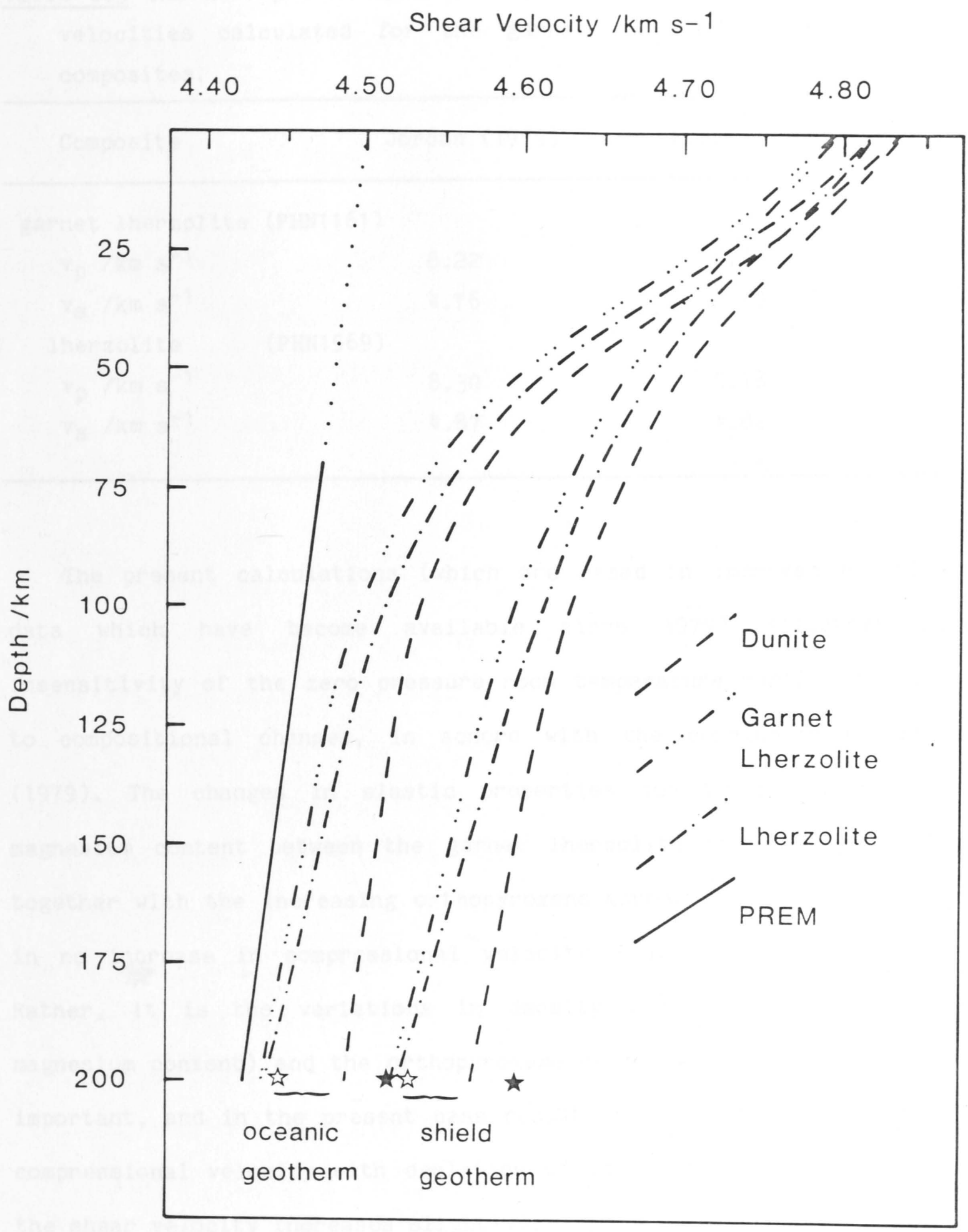

Figure 6.4 The variation with depth and temperature of the shear velocity profiles for specific upper mantle assemblages, together with the average upper mantle velocity profile of Dziewonski and Anderson (1981). The solid stars indicate the velocities calculated for the orthopyroxene-rich mineralogy, assuming a linear pressure dependence of the elastic moduli of orthopyroxene. The hollow stars indicate the velocities calculated assuming a linear pressure dependence of the elastic moduli of orthopyroxene for depths greater than 100 km. In both cases, the velocity profiles to about 100 km depth are similar.

Table 6.3 The zero-pressure, room temperature shear and compressional velocities calculated for the garnet lherzolite and lherzolite composites.

Composite	Jordan (1979)	Present study
garnet lherzolite (PHN1161)		
v_p /km s^{-1}	8.22	8.22
v_s /km s^{-1}	4.76	4.79
lherzolite (PHN1569)		
v_p /km s^{-1}	8.30	8.18
v_s /km s^{-1}	4.87	4.82

The present calculations (which are based on improved elasticity data which have become available since 1979) illustrate the insensitivity of the zero pressure room temperature mantle velocities to compositional changes, in accord with the conclusion of Jordan (1979). The changes in elastic properties due to the increase in magnesium content between the garnet lherzolite and the lherzolite, together with the increasing orthopyroxene/garnet volume ratio, result in no increase in compressional velocity - as calulated by Jordan. Rather, it is the variations in density (due to the increase in magnesium content) and the orthopyroxene/garnet volume ratio which are important, and in the present case result in a slight decrease in the compressional velocity with depletion of the garnet lherzolite (while the shear velocity increases slightly).

The global average seismic velocities for an isotropic upper mantle are presented in the 'preliminary reference Earth model' of Dziewonski and Anderson (1981). These velocity profiles are plotted in Figures 6.3 and 6.4. The compressional velocities predicted by PREM for the upper mantle are bounded by the present velocities calculated with the shield

geotherm and the lower velocities calculated with the oceanic geotherm. The slope of the PREM compressional velocity profile is -0.62×10^{-3} km s^{-1} per km, which can be compared with the linear fit to the present velocity profiles from 25-200 km depth. The slopes for the dunite, garnet lherzolite and lherzolite composites range from -0.88 to -0.48×10^{-3} km s^{-1} per km for the oceanic geotherm, to -0.51 to -0.10×10^{-3} km s^{-1} per km for the shield geotherm. Thus, the rate of change of velocity with depth for the average PREM upper mantle compressional velocity is also bounded by the profiles calculated for the dunite and the lherzolite composites.

The present well-defined first pressure derivatives and the second pressure derivatives are especially important in the comparison of these compressional velocities. Use of the high first pressure derivative of the bulk modulus of orthopyroxene, without the large, negative second pressure derivative results in the compressional velocities calculated at 200 km depth being ~0.2 km s^{-1} higher than the present velocities (see Figure 6.3). This results in substantial positive velocity gradients between 100 and 200 km depth, for profiles calculated with both geotherms. Therefore not only are reliable first pressure derivatives required in the calculation of the upper mantle velocity profiles, but also second pressure derivatives are necessary for reliable extrapolation to high pressure. These second pressure derivatives have not been available previously, resulting in over-estimates of the compressional velocities for models of the upper mantle. The velocity profiles have also been calculated assuming $\partial^2M/\partial P^2=0$ from 100-200 km depth for orthopyroxene. This results in an increase in velocities at 200 km, ~0.1 km s^{-1}, with the largest increases occurring for the orthopyroxene-rich compositions (see Figure 6.3).

The average upper mantle shear velocities predicted by PREM (see Figure 6.4) are 1-4% lower than the velocity profiles calculated using either the oceanic or the shield geotherms. This may be due in part to frequency dispersion of the measured elastic moduli, or the presence some of partial melt in this region of the mantle. The slope of the PREM model shear velocity is -0.37×10^{-3} km s^{-1} per km, compared to the profiles for the dunite, garnet lherzolite and lherzolite composites for depths of 100-200 km, which range from -0.45 to -0.81×10^{-3} km s^{-1} per km for the oceanic geotherm and -0.62 to -0.97×10^{-3} km s^{-1} per km for the shield geotherm. Thus, the rate of change of velocity with depth for the PREM model shaer velocity is also lower than that of the profiles calculated for the present three composites of upper mantle mineralogies and compositions.

The effect of neglecting the second pressure derivatives of orthopyroxene is less spectacular for the shear velocities. The velocities at 200 km depth would be ~0.05 km s^{-1} higher if the second pressure derivatives of orthopyroxene were neglected. The effect of assuming $\partial^2 M/\partial P^2 = 0$ at 100 km is to increase the velocities by ~0.02 km s^{-1} (see Figure 6.4).

Thus we can see that with the inclusion of the second pressure derivatives of the elastic moduli of garnet, olivine and especially orthopyroxene determined in this study, the compressional velocities calculated for the three isotropic equilibrium assembalges are close approximations to the average upper mantle compressional velocity calculated in PREM, with the calculated 200 km velocities for the lherzolites being ~2-3% lower than if the second pressure derivatives of orthopyroxene were neglected. The compressional velocity calculated for the dunite however, tends to be slightly higher than the PREM

velocity. The calculated shear velocities for these compositions tend to be higher than predicted by PREM. The large second pressure derivatives of the shear modulus of orthopyroxene however, tends to reduce the shear velocities towards that of the PREM model at depths approaching 200 km.

CHAPTER 7

CONCLUSION

Improved techniques of high-pressure ultrasonic interferometry have been applied in the characterization of a number of mantle minerals and their structural analogues. A procedure for the elimination of the unwanted transducer-bond phase shift provides for more accurate measurement of elastic-wave travel-times than has previously been possible. The combination of more precise ultrasonic interferometry and a 3 GPa hydrostatic pressure capability has allowed the determination not only of more reliable first pressure derivatives (within ±1%), but also the first measurements of the second pressure derivatives (±10%) of the elastic moduli for these relatively incompressible minerals.

These experimental techniques have been applied in three distinct areas of geophysical interest:

(i) the elasticity of the major upper mantle minerals olivine, orthopyroxene and garnet,

(ii) the study of the transition-metal monoxide MnO as an analogue for $Fe_{1-x}O$ wüstite, and

(iii) a search for possible shear-mode softening premonitory to the olivine→spinel phase transformation in Fe_2SiO_4 fayalite.

7.1 Elasticity of the major upper mantle minerals

In general, the results of this study of the elasticity of magnesian forsteritic olivine (~Fo_{90}), and enstatitic orthopyroxene (~En_{80}) and pyrope-rich garnet (~Py_{63}) confirm and significantly refine the findings of previous investigations. Remeasurement of the density of a previously studied crystal of pyrope-rich garnet (Bonczar et al., 1977) has resolved an apparent discrepancy in the otherwise systematic variation of the elastic moduli with composition for garnet solid solutions (Leitner et al., 1980). Of particular interest is the confirmation of very high pressure derivatives for some of the compressional moduli (and hence the bulk modulus, K) for single-crystal orthopyroxene (Frisillo and Barsch, 1972). However, it has also been demonstrated that these moduli display unusually large second pressure derivatives. An explanation is offerred for the anomalous elasticity of orthopyroxene - in terms of an internal degree of freedom of the lattice arising from the interplay between the kinking of tetrahedral chains and distortion of the M2 octahedra.

These new data for the pressure dependences of the bulk and shear moduli of the major upper mantle minerals can be used to construct better-constrained velocity-depth profiles for specific mantle assemblages. These profiles illustrate the sensitivity of the calculated mantle velocity to the volume fractions of the various

phases and to the assumed geotherm. Jordan's (1979) earlier conclusion concerning the insensitivity of wave velocities to the degree of depletion of garnet lherzolites is reinforced. The large negative second pressure derivative of the bulk modulus of orthopyroxene reduces the 200 km compressional velocity calculated for a typical garnet lherzolite mineralogy from that which would be calculated from a linear pressure dependence of the modulus, by about 2%, and has the overall effect of reducing calculated velocity gradients between 100 and 200 km depth. Calculated shear-wave velocities are higher than those of the PREM model (Dziewonski and Anderson, 1981) for both continental and oceanic geothems and all plausible chemical compositions. This discrepancy might reflect significant dispersion (1-5% in shear velocity) between ultrasonic and seismic frequencies.

7.2 The elasticity of the wüstite analogue MnO

The pressure dependence of the elastic moduli of the wüstite analogue MnO have been determined for the first time. The determination of $\partial K/\partial P$ and a more reliable value of K for MnO help constrain the calculation of the bulk moduli of the 3d B1-structured transition-metal monoxides based upon the model of Ohnishi and Mizutani (1978) for the incorporation of the crystal-field stabilization energy. A bulk modulus of 177 GPa is inferred for stoichiometric wüstite, in good agreement with the bulk modulus predicted for FeO from the measurements of Jackson et al. (1978) on polycrystalline $(Mg_xFe_{1-x})O$ and the recent static compression measurements of Yagi et al. (1985) for $Fe_{0.98}O$. Inspection of the experimental data for non-stoichiometric wüstite ($Fe_{0.95}O$) indicates that the bulk modulus for this composition is much lower than predicted by the present systematics.

The investigation of the pressure dependence of the elastic moduli of MnO has also resulted in the observation of C_{44} shear-mode softening - the pressure derivative becoming negative for $P \geq 1$ GPa. The connection between C_{44} mode softening and the B1→B2 phase transformation in the alkali halides and the alkaline earth oxides is well documented (Demarest et al., 1977). However, pronounced softening of the modulus C_{44} has also been observed in the paramagnetic phase of MnO within ~50° of the room pressure Néel point in response to the nearest-neighbour exchange interactions accompanying the development of short-range magnetic order (Seino, 1982). Thus, the negative pressure dependence of the shear modulus C_{44} in MnO may be indicative of short-range magnetic order developing as pressure raises the Néel temperature towards room temperature, or it may simply be shear-mode softening characteristic of the B1 lattices at high pressure. Hence, there are two likely modes of high pressure phase transformation for MnO: the paramagnetic→antiferromagnetic phase transformation which would occur if pressure were to raise the Néel point to room temperture, or the B1→B2 transition which is so common in the alkali halides and the alkaline earth oxides with increasing pressure.

7.3 Search for shear-mode softening premonitory to the olivine→spinel transition

The shear modulus C_{55} of fayalite has been measured to pressures in excess of the equilibrium olivine→spinel transition pressure. This modulus is one of the shear moduli which might be expected to soften prior to a martensitic olivine→spinel phase transition (Poirier, 1981a). No softening of the modulus C_{55} was observed over this pressure range. In fact, the first and second pressure derivatives of the

modulus C_{55} of fayalite are comparable to those of the modulus C_{55} of the forsteritic olivine discussed earlier, despite the much closer proximity of fayalite to the high pressure boundary of its stability field. There is however, the possible need for substantial thermal activation of the martensitic transition and hence the shear-mode softening associated with it. Measurements of the wave velocity of polycrystalline fayalite under simultaneous high pressure and high temperature (Fukizawa and Kinoshita, 1982) to the point of transition however, has failed to observe an anomalous decrease in velocity. Thus, there is no evidence for the pressure-induced shear mode softening in fayalite which might have been expected prior to a martensitic olivine→spinel phase transition.

REFERENCES

Akimoto, S.I., E. Komada and I. Kushiro, Effect of pressure on the melting of olivine and spinel polymorph of Fe_2SiO_4, J. Geophys. Res., 72, 679-686, 1967.

Akimoto, S., Y. Matsui and Y. Syono, High-pressure crystal chemistry of orthosilicates and the formation of the mantle transition zone, in The Physics and Chemistry of Minerals and Rocks, R. Strens (ed), Wiley, New York, 1976.

Anderson, D.L. and O.L. Anderson, The bulk modulus-volume relationship for oxides, J. Geophys. Res., 75, 3494-3500, 1970.

Anderson, O.L., Elastic constants of the central force model for three cubic structures: pressure derivatives and equations of state, J. Geophys Res., 75, 2719-2740, 1970.

Anderson, O.L. and H.H. Demarest, Elastic constants of the central force model for cubic structures: polycrystalline aggregates and instabilities, J. Geophys. Res., 76, 1349-1369, 1971.

Anderson, O.L. and R.C. Liebermann, Equations for the elastic constants and their pressure derivatives for three cubic lattices and some geophysical applications, Phys. Earth Planet Int., 3, 61-85, 1970.

Anderson, O.L. and J.E. Nafe, The bulk-modulus-volume relationship for oxide compounds and related geophysical problems, J. Geophys. Res., 70, 3951-3963, 1965.

Au, A.Y. and D.J. Weidner, Theoretical modelling of the elastic properties of forsterite: A polyhedral approach, in John C. Jameison Memorial Volume, J. Geophys. Res., 1985.

Babić, B., N.B. Nesković and J. Konstantinović, Spin correlations in MnO, Fizika, 8, 257-259, 1976.

Babuska,V., J. Fiala, M. Kumazawa, I. Ohno and Y. Sumino, Elastic properties of garnet solid solution series, Phys. Earth Planet. Int., 16, 157-176, 1978.

Barsch, G.R. and A.L. Frisillo, Determination of second pressure derivatives of elastic constants from elastic wave velocities for orthorhombic, tetragonal, trigonal, hexagonal and cubic symmetry, J. Acoust. Soc. Am., 46, 1973.

Barsch, G.R. and H.E. Shull, Pressure dependence of elastic constants and crystal stability of alkali halides: NaI and KI, Phys. Stat. Sol., 43, 637, 1971.

Bartels, R.A. and D.E. Schuele, Pressure derivatives of the elastic constants of NaCl and KCl at 295 K and 195 K, J. Phys. Solids, 26, 537-549, 1965.

Bass, J.D. The relationship between elasticity and crystal chemistry for some mantle silicates and aluminates, Ph.D. Thesis, State University of New York, 1982.

Bass, J.D. and D.J. Weidner, Elasticity of single-crystal orthoferrosilite, J. Geophys. Res., 89, 4359-4371, 1984.

Bass, J.D., D.J. Weidner, N. Hamaya, M. Ozima and S. Akimoto, Elasticity of the olivine and spinel polymorphs of Ni_2SiO_4, Phys. Chem. Min., 10, 261-272, 1984.

Bassett, W.A., H. Shimizu and E.M. Brody, Pressure dependence of elastic moduli of forsterite by Brillouin scattering in a diamond anvil cell, in High-pressure research in geophysics, S. Akimoto and M.H. Manghnani (eds), pp 115-124, Tokyo, 1982.

Bassett, W.A., T. Takahashi, H. Mao and J.S. Weaver, Pressure-induced phase transformations in NaCl, J. Appl. Phys., 39, 319-325, 1968.

Berger, J., J. Berthon, A. Revcolevshi and E. Jolles, Elastic constants of $Fe_{1-x}O$ single crystals, Comm. Am Ceram. Soc., C153-C154,1981.

Berger, J., F. Thomas, J. Berthon and A. Revcolevschi, Elastic properties of $Fe_{1-x}O$ near the antiferromagnetic phase transition, Solid State Comm., 48, 231-233, 1983.

Berryman, J.G., Long-wavelength propagation in composite elastic media 1. Spherical inclusions, J. Acoust. Soc. Am., 68, 1809-1819, 1980.

Berlincourt, D.A., D.R. Curran and H. Jaffe, Piezoelectric and piezomagnetic materials and their functions in transducers, in Physical Acoustic, 1, W.P. Mason (ed), Academic Press, 1964.

Bevington, P.R., Data reduction and error analysis for the physical sciences, McGraw-Hill, New York, 1969.

Birch, F., Elasticity and constitution of the Earth's interior, J.Geophys. Res., 57, 227-286, 1952.

Bloch D., C. Vettier and P. Burlet, Phase transition in manganese oxide at high pressure, Phys. Lett., 75A, 301-303, 1980.

Boehler, R., I.C. Getting and G.C. Kennedy, Grüneisen parameter of NaCl at high compressions, J. Phys. Chem. Solids, 38, 233-236, 1977.

Bonczar, L.J., E.K. Graham and H. Wang, The pressure and temperature dependence of the elastic constants of pyrope garnet, J. Geophys. Res., 82, 2529-2534, 1977.

Born, M., On the stability of crystal lattices, 1., Proc. Cambridge. Phil. Soc., 36, 100-165, 1940.

Burns, R.G., Mineralogical applications of crystal field theory, Cambridge University Press, 1970.

Cameron, M. and J.J. Papike, Structural and chemical variations in pyroxenes, Am. Min., 66, 1-50,1981.

Chang, Z.P. and G.R. Barsch, Pressure dependence of the elastic constants of RbCl, RbBr and RbI, J. Phys. Chem. Solids, 32, 27-40, 1971.

Chang, Z.P. and E.K. Graham, Elastic properties of oxides in the NaCl structure, J. Phys. Chem. Solids, 38, 1355-1362, 1977.

Christensen, N.I., Compressional wave velocities in rocks at high temperatures and pressures, critical thermal gradients, and crustal low-velocity zones, J. Geophys. Res., 84, 6849-6857, 1979.

Clark, S.P. and A.E. Ringwood, Density distribution and constitution of the mantle, Rev. Geophys., 2, 35-88, 1964.

Cook, R.K., Variation of elastic constants and static strains with hydrostatic pressure: A method for calculation from ultrasonic measurements, J. Acoust. Soc. Am., 29, 445-449, 1957.

Cracknell, M.F. and R.G. Evans, Elastic moduli and the order of the antiferromagnetic transition in MnO, Solid State. Commun., 8, 359-361, 1970.

Davies, G.F., Limits on the constitution of the lower mantle, Geophys. J. R. astr. Soc., 38, 479-504,1974.

Davies, G.F., and R.J. O'Connell, Transducer and bond phase shifts in ultrasonics, and their effect on measured pressure derivatives of elastic moduli, in High-pressure Research: applications in geophysics, M.H. Manghnani and S. Akimoto (eds), Academic Press, pp. 533-565, 1977.

Demarest, H.H., Extrapolation of elastic properties to high pressure in the alkali halides, J. Geophys. Res., 77, 848-856, 1972.

Demarest, H.H., R. Ota and O.L. Anderson, Prediction of high pressure phase transitions by elastic constant data, in High-Pressure Research: Applications in Geophysics, M.H. Manghnani and S.I Akimoto (eds) Academic Press, pp. 281-301, 1977.

Dziewonski A.M. and D.L. Anderson, Preliminary reference Earth model, Phys Earth Planet Int., 25, 297-356, 1981.

Frisillo, A.L. and G.R. Barsch, Measurement of single-crystal elastic constants of bronzite as a function of pressure and temperature, J. Geophys. Res., 77, 6360-6384,1972.

Frisillo, A.L. and S.T. Buljan, Linear thermal expansion coefficients of orthopyroxene to 1000° C, J. Geophys. Res., 77, 7115-7117,1972.

Fukizawa, A., and H. Kinoshita, Shear wave velocity jump at the olivine-spinel transformation in Fe_2SiO_4 by ultrasonic measurements in situ, J. Phys. Earth., 30, 245-253, 1982.

Goetze, C., A brief summary of our present day understanding of the effect of volatiles and partial melt on the mechanical properties of the upper mantle, in High-pressure research: Applications in Geophysics., M.H. Manghnani and S. Akimoto (eds.) Academic Press, New York, 1977.

Graham, E.K. and G.R. Barsch, Elastic constants of single-crystal forsterite as a function of temperature and pressure, J. Geopyhs. Res., 74, 5949-5960,1969.

Graham, E.K., S.M. Sopkin and W.E. Resley, Elastic properties of fayalite, Fe_2SiO_4, and the olivine solid solution series, EOS, 63, 1090, 1982.

Green D.H., Composition of basaltic magmas as indicators of conditions of origin: Application to oceanic vulcanism, Phil. Trans. Roy. Soc. London, A206, 707-725, 1971.

Green, D.H., W.O. Hibberson and A.L. Jaques, Petrogenesis of mid-ocean ridge basalts, in The Earth: Its origin, structure and evolution, M.W. McElhinny (ed), 265-299, Academic Press, 1979.

Green, D.H. and A.E. Ringwood, Mineral assemblages in a model mantle composition, J. Geophys. Res., 68, 937-945, 1963.

Green, D.H. and A.E. Ringwood, The genesis of basaltic magmas, Contrib. Mineral. Petrol., 15, 103-190, 1967.

Halleck, P.M. The compression and compressibility of grossularite garnet: A comparison of X-ray and ultrasonic methods, Ph.D. Thesis, Univ. of Chicago, Chicago, Ill., 1973.

Hashin, Z., The elastic modulus of heterogeneous materials, J. Appl. Mech., 29, 143-150, 1962.

Hashin, Z. and S. Shtrikman, On some variational principles in anisotropic and nonhomogeneous elasticity, J. Mech. Phys Solids., 10, 335-342, 1962a.

Hashin, Z. and S. Shtrikman, A variational approach to the theory of the elastic behaviour of polycrystals, J. Mech. Phys. Solids, 10, 343-352, 1962b.

Hashin, Z. and S. Shtrikman, A variational approach to the theory of the elastic behaviour of multiphase materials, J. Mech. Phys. Solids, 11, 127-140, 1963.

Hawthorne, F.C. and J. Ito, Synthesis and crystal-structure refinement of transition-metal orthopyroxenes. 1:orthoenstatite and (Mg,Mn,Co) orthopyroxene, Can. Min., 15, 321-338,1977.

Hazen, R.M., Effects of temperature and pressure on the crystal structure of forsterite, Am. Min., 61, 1280-1293, 1976.

Hazen, R.M. and L.W. Finger, Crystal structure and compositional variation of Angra dos Reis Fassite, Earth Planet Sci. Lett., 35, 357-362, 1977.

Hazen, R.M. and L. Finger, Crystal structures and compresibilities of pyrope and grossular to 60 kbar, Am. Min., 63, 297-303, 1978.

Hazen, R.M. and L.W. Finger, Crystal structure of forsterite at 40 kbar, Carnegie Inst. Wash. Y.B., 79, 364-369, 1980.

Hazen, R.M. and L.W. Finger, Crystal structure of diopside at high temperature and pressure, Ann. Rep. Geophysics. Lab., 373-375, 1981.

Heinz, D.L. and R. Jeanloz, Phase equilibria of $Fe_{0.94}O$ wüstite at high-pressures and temperatures, EOS, 64, 847, 1983.

Heydemann, P.L.M., The Bi I→II transition pressure measured with a dead-weight piston gauge, J. Appl. Phys., 38, 2640-2644, 1967.

Hill, R., The elastic behaviour of a crystalline aggregate, Proc. Phys. Soc. London., A65, 349-354,1952.

Hill, R., Elastic properties of reinforced solids: some theoretical principles, J. Mech. Phys. Solids, 11, 357-372, 1963.

Hush, N.S. and M.H.L. Pryce, Influence of the crystal-field potential on interionic separation in salts of divalent iron-group ions, J. Chem. Phys., 28, 244-249, 1958.

Isaak, D.G. and Graham, E.K., The elastic properties of an almandine-spessartine garnet and elasticity in the garnet solid solution series, J. Geophys. Res., 81, 2483-2489, 1976.

Ito, E., Y. Matsui, K. Suito and N. Kawai, Synthesis of γ-Mg_2SiO_4, Phys. Earth Planet, Inter., 8, 342-344, 1974.

Ito, E., T. Matsumoto, K. Suito, and N. Kawai, High-pressure break-down of enstatite, Proc. Jpn. Acad., 48, 412-415, 1972.

Jackson, I., Some geophysical constraints on the chemical composition of the Earth's lower mantle, Earth Planet. Sci. Lett., 62, 91-103.

Jackson, I., R.C. Liebermann and A.E. Ringwood, The elastic properties of $(Mg_xFe_{1-x})O$ solid solutions, Phys. Chem. Min., 3, 11-31, 1978.

Jackson, I., and H. Niesler, The elasticity of periclase to 3GPa and some geophysical implications, in High-Pressure Research in Geophysics, S. Akimoto and M.H. Manghnani (eds), Adv. Earth. Planet Sci, 12, 93-113, 1982.

Jackson, I., H. Niesler and D.J. Weidner, Explicit correction of ultrasonically determined elastic wave velocities for transducer-bond phase shifts, J. Geophys. Res., 86, 3736-3748, 1981.

Jackson, I. and A.E. Ringwood, High-pressure polymorphism of the iron oxides, Geophys. J.R. astr. Soc., 64, 767, 1981.

Jackson, I., S.L. Webb and A. Revcolevschi, The elasticity of single-crystal wüstite, EOS, 1985, in press.

JANAF, Thermochemical tables, 1971.

Jeanloz, R., T.J. Ahrens, H.K. Mao and P.M. Bell, B1→B2 transition in calcium oxide from shock-wave and diamond-cell experiments, Science, 206, 829-830, 1979.

Jeanloz, R. and T. Ahrens, Equations of state of FeO and CaO, Geophys. J.R. astr. Soc., 62, 505-528, 1980.

Jeanloz, R. and R. Hazen, Wüstite ($Fe_{1-x}O$): Compression, non-stoichiometry and bulk viscosity, Nature, 304, 620-622, 1983.

Jordan, T.H., Mineralogies, densities and seismic velocities of garnet lherzolites and their geophysical implications, in The Mantle Sample: Inclusions in lherzolites and other volcanics, F.R. Boydana and H.O.A. Meyer (eds), AGU, Wash., 1979.

Kieffer, S.W., Thermodynamics and lattice vibrations of minerals: 4. Application to chain and sheet silicates and orthosilicates, Rev. Geophys. Space Phys., 18, 862-886,1980.

Koliwad, K.M., P.B. Ghate and A.L. Ruoff, Pressure derivatives of the elastic constants of NaBr and KF, Phys. Status. Solidi, 21, 507-516, 1967.

Kumazawa, M., The elastic constants of single crystal orthopyroxene, J. Geophys. Res., 74, 5973-5981, 1969.

Kumazawa, M. and O.L. Anderson, Elastic moduli, pressure derivatives, and temperature derivatives of single-crystal olivine and single-crystal forsterite, J. Geophys. Res., 74, 5961-5972, 1969.

Kuster, G.T. and M.N. Toksöz, Velocity and attenuation of seismic waves in two-phase media: Part 1. Theoretical formulations, Geophysics, 39, 587-606, 1974.

Leitner, B.J., D.J. Weidner and R.C. Liebermann, Elasticity of single crystal pyrope and implications for garnet solid solution series, Phys. Earth Planet. Int., 22, 111-121,1980.

Levien, L. and C.T. Prewitt, High-pressure structural study of diopside, Am. Min., 66, 315-323,1981.

Liebermann, R.C., Elasticity of olivine (α), beta (β) and spinel (γ) polymorphs of germanates and silicates, Geophys. J.R. astr. Soc., 42, 899-929, 1975.

Liu, L., Post oxide phases of olivine and pyroxene and minerology of the mantle, Nature, 258, 510-512, 1975.

Liu, L. and A.E. Ringwood, Synthesis of a perovskite-type polymorph of $CaSiO_3$, Earth Planet. Sci. Lett., 28, 209-211, 1975.

Lloyd, E.C., C.W. Beckett and F.R. Boyd, Measurements in the high-pressure environment, Science, 164, 860-862, 1969.

McCammon, C.A., Aspects of the high-pressure behaviour of iron oxides and sulphides, Ph.D. Thesis, ANU, 1983.

McCammon, C.A., I. Jackson, A.E. Ringwood and J.D. Cashion, (Fe,Mn)S and (Fe,Mg)S solid solutions. I. Mossbauer study of the B1 phase. II. High-pressure phase relations of the binary systems, Phys. Chem. Min., 11, 182-193, 1984.

McCammon, C.A., A.E. Ringwood and I. Jackson, Thermodynamics of the system Fe-FeO-MgO at high pressure and temperature and a model for formation of the Earth's core, Geophys. J.R. astr. Soc., 72, 577-595, 1983.

McSkimmin, H.J., Ultrasonic measurement techniques applicable to small solid specimens, J. Acoust. Soc. Am., 22, 413-418, 1950.

Miller, M.N., Bounds for effective bulk modulus of heterogeneous materials, J. Math, Phys., 10, 2005-2013, 1969.

Miyamoto, M, H. Takeda and Y. Takano, Crystallographic studies of a bronzite in the Johnstown achondrite, Fortschr. Miner., 52, 389-397, 1975.

Morimoto, N., M. Tokonami, W. Watanabe and K. Koto, Crystal structures of three polymorphs of Co_2SiO_4, Am. Min., 59, 475-485, 1974.

Morosin, B., Exchange striction effects in MnO and MnS, Phys. Rev. B., 1, 236-243, 1970.

Navrotsky, A., and P.K. Davies, Cesium chloride vs. nickel arsenide as possible structures for (Mg,Fe)O in the lower mantle, J. Geophys. Res., 86, 3689-3694, 1981.

Newton, M.D., M. O'Keefe and G.V. Gibbs, Ab initio calculation of interatomic force constants in $H_6Si_2O_7$ and the bulk modulus of α quartz and α cristobalite, Phys. Chem. Min., 6, 305-312, 1980.

Niesler, H., M.Sc. Thesis, ANU, 1985.

Nixon, P.H. and F.R. Boyd, Petrogenesis of the granular and sheared ultrabasic nodule suite in kimberlites, in Lesotho kimberlites, P.H. Nixon (ed) Lesotho, 1973.

Nixon, P.H., O. von Knorring and J.M. Rooke, Kimberlites and associated inclusion of Basutoland: a mineralogical and geochemical study, Am. Min., 48, 1090-1132, 1963.

Notis, M., R. Spriggs and W. Hahn, Elastic moduli of pressure-sintered nickel oxide, J. Geophys. Res., 76, 7052, 1971.

Novak, G.A., and G.V. Gibbs, The crystal chemistry of the silicate garnets, Am. Min., 56, 791-825, 1971.

Nye, J.F. Physical properties of crystals, Oxford University Press, London, 1957.

Ohnishi, S. and H. Mizutani, Crystal field effects on bulk moduli of transition metal oxides, J. Geophys. Res., 83, 1852-1856, 1978.

Oliver, D.W., The elastic moduli of MnO, J. Appl. Phys., 40, 893,1969.

Papadakis, E.P., Ultrasonic phase velocity by the pulse-echo-overlap method incorporating diffraction phase corrections, J. Acoust. Soc. Am., 42, 1045-1051, 1967.

Paterson, M.S., Creep in transforming polycrystalline materials, Mech. Mater., 2, 103-109, 1983.

Peerdeman, S.A.G., N.J. Trappeniers and J.A. Schouten, Temperature coefficients of the bismuth I-II and the bismuth II-III transition pressures from 20 to 175° C, High Temperature-High Pressures, 12, 67-73, 1980.

Pistorius, C.W.F.T., Melting curves of the potassium halides at high pressures, J. Phys. Chem. Solids., 26, 1543-1548, 1965a.

Pistorius, C.W.F.T., Melting curves of the rubidium halides at high pressures, J. Chem. Phys., 43, 1557-1562, 1965,b.

Poirier, J.P., Martensitic olivine-spinel transformation and plasticity of the mantle transition zone, Anelastic Properties and Related Processes in the Earth's Mantle, Am. Geophys. Union Monograph, IUGG General Assembly, F.D. Stacey, M.S. Paterson and A. Nicholas (eds), 1981a.

Poirier, J.P., On the kinetics of olivine-spinel transition, Phys. Earth. Planet. Int., 26, 179, 1981b.

Ralph, R.L. and S. Ghose, Enstatite, $Mg_2Si_2O_6$: Compressibility and crystal structure at 21 kbar, EOS, 61, 409, 1980.

Reddy, P.J. and A.L. Ruoff, Pressure derivatives of the elastic constants in some alkali halides, in Physics of Solids at High Pressures, C.T. Tomizuka and R.M. Emrick (eds), Academic Press, 1965.

Reuss, A., Berechnung der Fliessgrenze von Mischkristallen auf Grund der Plastizitätsbedingung für Einkristalle, Z. Angew. Math. Mech., 9, 49-58, 1929.

Ricoult, D.L. and D.L. Kohlstedt, Structural width of low-angle grain boundaries in olivine, Phys. Chem. Min., 9, 133-138, 1983.

Ringwood, A.E., A model for the upper mantle, J. Geophys. Res., 67, 857-866, 1962.

Ringwood, A.E., Mineralogy of the mantle, in Advances in Earth Science, P.M. Hurley (ed), M.I.T. Press, Cambridge, Mass., pp. 357-399, 1966.

Ringwood, A.E., Composition and petrology of the Earth's Mantle, McGraw-Hill, New York, 1975.

Ringwood, A.E., Composition of the core and implications for the origin of the Earth, Geochem. J., 11, 111-136, 1977.

Ringwood, A.E. and A. Major, High pressured transformations in pyroxene II, Earth Planet. Sci. Lett., 5, 76-78, 1968.

Ringwood, A.E. and A. Major, The system Mg_2SiO_4-Fe_2SiO_4 at high pressures and temperatures, Phys. Earth Planet. Int., 3, 89-108, 1970.

Ringwood, A.E. and A. Major, Synthesis of majorite and other high pressure garnets and perovskites, Earth Planet. Sci. Lett., 12, 411-418, 1971.

Robie, R.A., C.B. Finch and B.S. Hemingway, Heat capacity and entropy of fayalite (Fe_2SiO_4) between 5.1 and 383K: comparison of calorimetric and equilibrium values for the QFM buffer reaction, Am. Min., 67, 463-469, 1982.

Robie, R.A., B.S. Hemingway and H. Takei, Heat capacities and entropies of Mg_2SiO_4, Mn_2SiO_4, and Co_2SiO_4 between 5 and 380 K, Am. Min., 67, 470-480, 1982.

Sammis, C.G., The pressure dependence of the elastic constants of cubic crystals in the NaCl and spinel structures from a lattice model, Geophys. J. R. astr Soc., 19, 285-297, 1970.

Sato, Y. and R. Jeanloz, Phase transition in SrO, J. Geophys. Res., 86, 11773-11778, 1981.

Schubert, G. and D.L. Turcotte, Phase changes and mantle convection, J. Geophys. Res., 76, 1424-1432, 1971.

Seino, D., Effect of distance-dependent exchange interactions in MnO on elastic constants and magnetic susceptibility, J. Magn. Magn. Mater., 128, (1-2), 55-63, 1982.

Sittig, E.K., Effects of bonding and electrode layers on the transmission parameters of piezoelectric transducers used in ultrasonic digital delay lines, IEEE Trans. Sonics and Ultrasonics, SU-16, 2-10, 1967.

Skinner, B.J., Physical properties of end-members of the garnet group, Am. Min., 48, 428-436, 1956.

Soga, N., Elastic constants of garnet under pressure and temperature, J. Geophys. Res., 72, 4227-4234, 1967.

Spetzler, H., C.G. Sammis and R.J. O'Connell, Equation of state of NaCl: Ultrasonic measurements to 8 kbar and 800°C and static lattice theory, J. Phys. Chem. Solids, 33, 1727-1750, 1972.

Sumino, Y., The elastic constants of Mn_2SiO_4, Fe_2SiO_4 and Co_2SiO_4 and the elastic properties of olivine group minerals at high temperature, J. Phys. Earth., 27, 209-238, 1979.

Sumino, Y., M. Kumazawa, O. Nishizawa and W. Pluschkell, The elastic constants of single crystal $Fe_{1-x}O$, MnO, and CoO, and the elasticity of stoichiometric magnesiowüstite, J. Phys. Earth., 28, 475–495, 1980.

Sung, C.M. and R.G. Burns, Kinetics of high-pressure phase transformations; implications to the evolution of the olivine→spinel transition in the down-going lithosphere and its consequences on the dynamics of the mantle, Tectonophysics, 31, 1-32, 1976.

Suzuki, I., Thermal expansion of periclase and olivine, and their anharmonic properties, J. Phys. Earth., 23, 145-159, 1975.

Suzuki, I., S-I. Okajima and S. Kiyoshi, Thermal expansion of single-crystal manganosite, J. Phys. Earth, 27, 63-69, 1979.

Takei, H., Growth of fayalite (Fe_2SiO_4) single crystals by the floating-zone method, J. Cryst. Growth, 43, 463-468, 1978.

Thomsen, L., Elasticity of polycrystals and rocks, J. Geophys. Res., 77, 315-327, 1972.

Thurston, R.N. and K. Brugger, Third order elastic constants and the velocity of small amplitude elastic waves in homogeneously stressed media, Phys. Rev., 133, A1604-A1610, 1964.

Toksöz, M.N., J. Minear and B. Julian, Temperature field and geophysical effects of a downgoing slab, J.Geophys. Res., 76, 1113-1138, 1971.

Truell, R., C. Elbaum and B. Chick, Ultrasonic Methods in Solid State Physics, Academic Press, 1969.

Uchida, N. and S. Saito, Elastic constants and acoustic absorption coefficients in MnO, CoO and NiO single crystals at room temperature, J. Acoust. Soc. America, 51, 1602-1605,1972.

Vassilou, M.S. and T.J. Ahrens, Hugoniot equation of state of periclase to 200 GPa, Geophys. Res. Lett., 8, 729-732, 1981.

Vaughan, M.T. and J.D. Bass, Single crystal elastic properties of protoenstatite: a comparison with orthoenstatite, Phys. Chem. Min., 10, 62-68, 1983.

Vaughan, M.T. and D.J. Weidner, The relationship of elasticity and crystal structure in andalusite and sillimanite, Phys. Chem. Min., 3, 133-144,1978.

Voigt, W., Lehrbuch der Kristallphysik, Teubner, Leipzig, 1928.

Wang, H. and K. Huang, Elastic constants of natural pyrope, EOS, 56, 601, 1975.

Wang, H. and G. Simmons, Elasticity of some mantle crystal structures, 3. Spessartine-almandine garnet, J. Geophys. Res., 79, 2607-2613, 1974.

Warner, A.W., M. Onoe and G.A. Coquin, Determination of elastic and piezoelectric constants for crystals in class (3m), J. Acoust. Soc. Am., 42, 1223-1231, 1967.

Waterman, P.C. Orientation dependence of elastic waves in single crystals, Phys. Rev., 113, 1240-1253, 1959.

Watt, J.P., Hashin-Shtrikman bounds on the effective elastic moduli of polycrystals with orthorhombic symmetry, J. Appl. Phys., 50, 6290-6295, 1979.

Watt, J.P., G.F. Davies and J. O'Connel, The elastic properties of composite materials, Rev. Geophys. Space Phys., 14, 541-563, 1976.

Watt, J.P. and R.J. O'Connell, Mixed-oxide and perovskite-structure model mantles from 700-1200 km, Geophys. J. R. astr. Soc., 54, 601-630, 1978.

Watt, J.P. and R.J. O'Connell, An experimental investigation of the Hashin-Shtrikman bounds on two-phase aggregate elastic properties, Phys. Earth Planet. Inter., 1979.

Weidner, D.J., J.D. Bass and M.T. Vaughan, The effect of crystal structure and composition on elastic properties of silicates, High Pressure Research in Geophysics, S. Akimoto and M. Manghnani (eds), Centre for Academic Publication, Japan, Tokyo, 1982.

Weidner, D.J. and G. Simmons, Elastic properties of alpha quartz and the alkali halides based on an interatomic force model, J. Geophys. Res., 77, 826, 1972.

Weidner, D.J. and M.T. Vaughan, Elasticity of pyroxenes: effects of composition versus crystal structure, J. Geophys. Res., 87, 9349-9353, 1982.

Weidner, D.J., H. Wang and J. Ito, Elasticity of orthoenstatite, Phys. Earth Planet Int., 17, 7-13, 1978.

Winchell, A.N., Optical mineralogy II, Wiley and Sons, New York, 1933.

Yagi, T., H.K. Mao and P.M. Bell, Structure and crystal chemistry of perovskite-type $MgSiO_3$, Phys. Chem. Min., 3, 97-110, 1978.

Yagi, T., H.K. Mao and P.M. Bell, Hydrostatic compression of $MgSiO_3$ of perovskite structure, Carnegie Inst. Wash. Year Book, 78, 613-614, 1979.

Yagi, T., T. Suzuki and S. Akimoto, New high-pressure polymorphs in sodium halides, J. Phys. Chem. Solids, 44, 135-140, 1983.

Yagi, T., T. Suzuki and S. Akimoto, Static compression of wüstite ($Fe_{0.98}O$) to 120 GPa, J. Geophys. Res., 1985.

Yeganeh-Haere, A. and M.T. Vaughan, Single-crystal elastic constants of olivine, EOS, 65, 282, 1984.

Zeto, R.F. and H.B. Vanfleet, Interpretation of initiation pressure hysteresis phenomena for fixed-point pressure calibration, J. Appl. Phys., 42, 1001-1010, 1971.

Zou, G.T., H.K. Mao, P.M. Bell and D. Virgo, High-pressure experiments on the iron oxide wüstite ($Fe_{1-x}O$), Ann. Rep. Geophys. Lab., 79, 374-376, 1980.